ELECTROCHEMICAL AND SPECTROSCOPIC STUDIES OF PYRIDINE SURFACTANTS AT THE GOLD-ELECTROLYTE INTERFACE

A Thesis

Presented to

The Faculty of Graduate Studies

of

The University of Guelph

by

VLAD ZAMLYNNY

In partial fulfilment of requirements

for the degree of

Doctor of Philosophy

October, 2002

ABSTRACT

ELECTROCHEMICAL AND SPECTROSCOPIC STUDIES OF PYRIDINE SURFACTANTS AT THE GOLD-ELECTROLYTE INTERFACE

Vlad Zamlynny
University of Guelph, 2002

Advisor:
Professor Jacek Lipkowski

Two *in situ* infrared spectroscopic methods have been developed with the purpose of their application for quantitative studies of the potential-induced changes in the orientation and conformation of molecules of ultrathin organic films adsorbed at Au surfaces. Then, (i) subtractively normalized interfacial Fourier transform infrared spectroscopy (SNIFTIRS) was applied to study the dipole-field interactions of pyridine with an electrified Au(110) electrode surface while (ii) polarization modulation Fourier transform reflection absorption spectroscopy (PM FTIR RAS) was utilized to study the monolayers and bilayers of 4-pentadecylpyridine (C15-4Py) obtained at different stages of the transfer of this insoluble surfactant from the surface of the electrochemical cell to the electrode surface (*i.e.*, from the gas-solution (GS) interface to the metal-solution (MS) interface). Neutron reflectometry was utilized to determine the thickness and the structure of C15-4Py monolayers and bilayers while electrochemical methods (alternating current voltammetry and chronocoulometry) were applied to study kinetics of the C15-4Py transfer as well as the mechanism of the potential-induced phase transitions in the films adsorbed at the metal electrode.

SNIFTIRS studies of pyridine at Au(110) demonstrated that the electric field tends to orient pyridine molecules perpendicular to the metal surface while thermal motion prevents ordering. Electrochemical experiments demonstrated that the molecules of C15-4Py can move from the GS interface to the MS interface and spontaneously form a bilayer at the Au electrode surface. The transfer takes place regardless of whether the electrode is initially film-free or covered with a C15-4Py film deposited using the single horizontal touching (Langmuir-Schaefer) method. A nearly identical bilayer can also be deposited onto the electrode surface using the double horizontal touching technique. Studies of the transfer kinetics indicated that the crossing of the triple-phase line (the boundary of the GS, MS and gas-metal interfaces) by C15-4Py molecules is the rate-limiting step. Neutron reflectometry confirmed the monolayer state of the film, deposited using the single touching and the bilayer state of the film, produced by the double touching technique. Structural integrity of the C15-4Py bilayer was also indicated by this technique. PM FTIR RAS studies demonstrated that the bilayer remained in a fluid, liquid crystalline state in the whole range of applied potentials while the monolayer became condensed in a gel state at positive electrode polarizations. The outer leaflet of the bilayer was oriented with its pyridine moieties towards the solution and the inner leaflet was attached to gold *via* a nitrogen heteroatom. Both the monolayer and the bilayer displayed significant changes in orientation when the C15-4Py film was undergoing potential-induced adsorption and desorption. The concerted use of the complementary *in situ* surface analytical techniques demonstrated that C15-4Py is an excellent adhesive material for the fabrication of biomimetic membranes. In addition, this project demonstrated the feasibility of quantitative determination of the orientation of organic molecules in ultrathin films at metal electrodes inside an electrochemical cell.

DEDICATION

This work is dedicated to my teachers.

ACKNOWLEDGMENTS

While there are a number of individuals to whom I would like to express my utmost gratitude and appreciation, below I would like to single out those who made the most valuable contribution.

Dr. Jacek Lipkowski for a lake of knowledge I have inherited from him as well as for being an excellent teacher.

Dr. D. Thomas, Dr. A.R. Merrill, Dr. D. Irish and Dr. T Leung for being members of my advisory committee and for many valuable discussions during my studies and research.

Dr. M. Pézolet for agreeing to be my external examiner and for an extremely fruitful discussion during a CSC conference in Montreal.

Dr. D. Bizzotto for teaching me the basics of practical electrochemistry.

Dr. G. Szymanski for immense help in almost all aspects of this project.

Dr. S. Satija, Dr. R. Ivkov and Dr. J. Majewski for help with neutron reflectometry.

All members of our research team, especially those who co-authored papers: Mr. I. Burgess, Dr. S. Horswell, Dr. N. Li , Dr. H-Q. Li and Dr. I. Zawisza, for being friends and partners in research and beyond.

Staff members and secretaries of the Department of Chemistry, especially T. White, B. Morton, (machining) Y. Savoret, (glassblowing) I. Renaud, S. Seifried (electronics) and Dr. U. Oehler (programming) for assistance in various aspects of this project.

Most importantly, I would like to express my sincere gratitude to my wonderful wife Dr. Elena Ouvarova for patience and understanding as well as children Lydia and Anton for being a tremendous inspiration in my research. Finally, I would like to thank my parents for all I have ever achieved in my life.

TABLE OF CONTENTS

LIST OF ABBREVIATIONS

CHAPTER 1

SAM - self-assembling monolayer
FTIR RAS - Fourier transform infrared reflection absorption spectroscopy

CHAPTER 2

PM FTIR RAS - polarization modulation Fourier transform infrared spectroscopy
BLM - bilayer lipid membrane
C15-4Py - 4-pentadecylpyridine
pzc - potential of zero charge
GS - gas-solution
MS - metal-solution
IR RAS - infrared reflection absorption spectroscopy
ATR - attenuated total reflection
SNIFTIRS - subtractively normalized interfacial Fourier transform infrared spectroscopy
R - the reflectivity
E_1 - the base potential
E_2 - the sample potential
$\Delta R/R$ or $\Delta R/<R>$ - reflection absorption spectrum
R_s - reflectivity of s-polarized radiation
R_p - reflectivity of p-polarized radiation
FTIR - Fourier transform infrared
S/N - signal-to-noise ratio
MSEFS - mean squared electric field strength
SSD - synchronous sampling demodulator

CHAPTER 3

α - a phase
β - a phase
G - the Gibbs free energy
A - a unit area of surface
γ - the surface energy
T - the absolute temperature
p - the pressure
μ - the chemical potential
S - a thin interfacial layer
x_0 - a dividing plane
Γ - the surface (Gibbs) excess
i - a species i
N - the number of moles

π - the surface pressure
SC - the spreading coefficient
GL - gas (organic) liquid
SL - solution (organic) liquid
ESP (π_E) - the equilibrium spreading pressure
IPE - the ideally polarizable electrode
E - the electrode potential
σ_M - the charge density at the electrode
s - the entropy
V - the volume of electrochemical cell
$\mathfrak{m}$ - the surface stress
ε_e - the elastic surface strain
C - the differential capacity
E^* - the potential at which the surface tension $\gamma(E^*)$ is known
Θ - the degree of coverage of the electrode surface with an adsorbate
C_{true} - the true capacity
C_{pseudo} - the pseudo-capacity
L - a neutral organic species
R - the gas constant
Γ_{max} - the limiting surface excess
β_H - the adsorption coefficient
X_{bulk} - the mole fraction of adsorbate in the electrolyte solution
ΔG^0_{ads} - the Gibbs free energy of adsorption
v - the frequency of electromagnetic radiation
c - the velocity of electromagnetic radiation in vacuum
$\bar{\nu}$ - the wavenumber of electromagnetic radiation
I_i ,I_{r1} ,I_{t1} ,I_{r2} , I_{r3} and I_{out} - the infrared radiation inside a Michelson interferometer
$f_{\bar{\nu}}$ - the frequency of the detected signal
V_M - the velocity of the moving mirror
δ_r - retardation of the infrared radiation in a Michelson interferometer
$I(\delta_r)$ - the intensity of an interferogram
$B(\bar{\nu})$ - the intensity of the source (as a function of its wavenumber $\bar{\nu}$)
$\Delta\bar{\nu}$ - the resolution of the FTIR instrument
δ_{max} - the maximum retardation
η - the overall efficiency of the optical bench
Θ_{IR} - the optical throughput of the setup for the infrared beam
E - the electric field strength
H - the magnetic field strength
t - an arbitrary moment of time
x - a distance from the origin
E_0 - the amplitude of the electric field strength
λ - the wavelength of electromagnetic radiation
ω - the angular frequency of electromagnetic radiation

δ - the phase shift of electromagnetic radiation
Δx - displacement of the electric field strength amplitude with respect to the coordinate origin
n - the refractive index of a medium
k - the attenuation coefficient of a medium
$\hat{n}$ - the complex refractive index of a material
I - the intensity of electromagnetic radiation
$\left\langle E_0^2 \right\rangle$ - mean squared electric field strength
Θ_1^r - the angle of reflection
Θ_1^t - the angle of incidence
Θ_2^t - the angle of refraction inside the second phase
n_j - the refractive index of a phase j
r - the Fresnel amplitude reflection coefficient
t - the Fresnel amplitude transmission coefficient
ξ_j - the quantity defined by equation (3.4.13)
R - the reflectance (or reflectivity)
T - the transmittance
M_j - the characteristic matrix of a phase j
β_j - the quantity defined by equation (3.4.20)
M - the characteristic matrix of the whole stratified medium
U and V - the tangential (with respect to the propagation direction) fields
m_{jk} - the elements of the 2×2 characteristic matrix M of the whole stack.
N - the reciprocal matrix of M
I - the unit matrix.
PEM - photoelastic modulator
v - speed of light in a material
dx - a distance
dt - a time interval
P - a static polarizer
n - a phase shift imposed by the PEM
I_D - the intensity of the radiation at the detector
I_p - the intensity of p-polarized radiation
I_s -the intensity of s-polarized radiation
ω_m - the frequency of the PEM
φ_0 - the maximum phase shift introduced by the PEM,
V_m - the voltage that is applied to the PEM
G - the proportionality factor
λ_o - the wavelength at which half-wave retardation is observed
ΔI - the intensity difference signal
$\langle I \rangle$ - the intensity average signal

$I_D(2\omega_m)$ - the detector signal at the second harmonic of the PEM frequency

$J_2(\varphi_0)$ - the second order Bessel function of φ_0

$I_D(0)$ - the signal at the terminal of a low pass filter

$J_0(\varphi_0)$ - the zero order Bessel function of φ_0

$I_D^{Ave}(2\omega_m)$ - the intensity average signal at the SSD terminal

$I_D^{Diff}(2\omega_m)$ - the intensity difference signal at the SSD terminal

S - the PM FTIR spectrum

(d)- the spectrum of the analyte

(0) - the spectrum of the background

γ - the optical setup efficiency for p-polarized light, normalized by the efficiency for the s-polarized light

A - the absorbance of the analyte

C_{PP} and C_{SP} - the calibration spectra

g - the gain of the electronics during collection of experimental spectra

g' - the gain of the electronics during collection of calibration spectra

CHAPTER 4

SCE - the saturated calomel electrode

r.m.s - root mean square

RC - resistance and capacitance

i_R - the real component of the measured current

i_Q - the quadrature (imaginary) component of the measured current

E_{ac} - the root-mean-square voltage of the applied alternating current perturbation

ω - the angular frequency of the applied alternating current perturbation

E_b - the base potential

t_b - the equilibration time at the base potential

E_v - the variable potential

ΔE_v - an increment of the variable potential

E_{vN} - the maximum potential

t_v - the equilibration time at the variable potential

MCT - mercury cadmium telluride

E_1 - the base potential in SNIFTIRS

E_2 - the sample potential in SNIFTIRS

$R(E_1)$- the electrode reflectivity at the base potential E_1

$R(E_2)$ - the electrode reflectivity at a sample potentials E_2

n_w - the refractive index the optical window

α_1 - the angle of incidence inside the optical window

α_2 - the angle of incidence outside of the optical window

R - the normalized (by the incident flux) intensity of specularly reflected neutrons

Q_z - the momentum transfer vector
σ_R - the standard deviation
$\Delta Q_z/Q_z$ - an instrumental resolution

CHAPTER 5

$\bar{\nu}$ - the wavenumber
α - the angle of convergence
Θ - the angle of incidence
n - the refractive index
k - the attenuation coefficient
h - the thickness of a layer of a stratified medium
r - radius of a hemisphere or hemicylinder
FWHM - full width at half maximum
Γ_{max} -the limiting surface concentration
I - the intensity of the beam reflected from the Window/ D_2O / Au interface
I_0 - the intensity of the beam reflected from the Window /Air interface
I_p - the intensity of the p-polarized light that passes through the whole optical bench
CJ_0 - the zero order calibration spectrum
CJ_2. - the second order calibration spectrum
ΔI_γ - the intensity difference signal (uncorrected for γ)
$\langle I \rangle_\gamma$ - the intensity average signal (uncorrected for γ)
$\gamma = C_p/C_s$ - the ratio of the optical throughput of the experimental setup for p- and s- polarized radiation
A - the integrated absorbance of the analyte film at the metal surface
$\vec{\mu}$ – the transition dipole
$\vec{E}$ - the electric field of the photon
$|\mu|$ - the absolute value of the transition dipole moment
$\langle E^2 \rangle$ - the mean squared electric field strength (MSEFS) of the photon
1 - the angle between the directions of the electric field of the photon and the transition dipole of a vibration in the molecule
A^R - the integrated absorbances of a preferentially oriented analyte film at the metal mirror (obtained using the reflection absorption technique)
A^T - the integrated absorbance of an isotropic sample of analyte (measured using transmittance spectroscopy).
$A^R{}_{Exp}$ - the experimental integrated absorbance of the analyte film at the metal, recorded using reflectance absorbance spectroscopy
$A^R{}_{Theor}$ - the simulated integrated absorbance
ΔN - the number of the interference fringes
$\bar{\nu}_1 - \bar{\nu}_2$ - the frequency range

d - the transmittance cell thickness
n_∞ - the average refractive index of the medium within the cell
k_i - the attenuation coefficients of the analyte
I - the intensity of radiation transmitted through the thin layer cell filled with the analyte solution
I_o - the intensity of radiation transmitted through the thin layer cell filled with the pure solvent
i.- a component of the solution
f_i - the volume fraction of the analyte in the sample
x_i - the mole fraction of the analyte in the solution
M_i - the molar mass the analyte in the solution
ρ_i - the density of the analyte in the solution
n_i - refractive indices of pure analyte
ρ - the density of the solution
n - the refractive indices of the solution
k -the attenuation coefficients of the solution
$R(\Gamma_S)$ - the reflectivity of the stratified medium (window / electrolyte / metal) that contains a homogeneous solution of Γ molecules of the analyte in the electrolyte
$R(0)$ - the reflectivity of the stratified medium (window / electrolyte / metal) in the absence of the analyte.
$R(\Gamma_M)$ - the reflectivity of the stratified medium (window / electrolyte / metal) that contains a film of Γ molecules of the analyte at the metal electrode

CHAPTER 6

E - the electrode potential
F - the static electric field strength
φ - the electric potential
ε - the permittivity of a medium
n - the refractive index of a medium
ε_o - the permittivity of vacuum
C_{2v} - the symmetry group
C_2 - the axis of symmetry
a_1 - the vibrational mode
b_1 - the vibrational mode
α - the molar absorption coefficient
$\int \alpha d\bar{\gamma}$ - the integrated molar absorption coefficient
$L(a)$ - the Langevin function
$a = pF/kT$
p - the permanent dipole moment of the molecule
kT - the thermal energy

CHAPTER 7

Θ - the fraction of the metal-solution interface covered by the film
C_0 - the differential capacities at zero equilibration time
C_t - the differential capacities at equilibration time t
C_4 - the differential capacities at infinitely long (18 h) equilibration time
k - a proportionality constant
π_{GS} - the surface pressure of the film at the GS interface
Γ – the surface concentration of molecules transferred to the MS interface at a given equilibration time t
Γ_4 – the surface concentration after an infinitely long period of equilibration time
r_o - radius of the electrode.
$\Gamma(r = r_o)$ - the surface concentration at the triple-phase line
n - the number of molecules crossing a unit length of the triple-phase line during time t
D - the diffusion coefficient
FP - the flow parameter
v - the rate of flow
k_r - the rate constant
SLD - the scattering length density
$\Delta\beta$ - the scattering length density difference between the lower and the upper media.
σ – the root mean square roughness factor
χ^2 - the value that characterizes the quality of the fit
f - the volume fraction of C15-4Py in the film
β_{film} -the scattering length density of the surfactant film
$\beta_{C15-4Py}$ - the scattering length density of the bulk C15-4Py
β_{D_2O} - the scattering length density of the bulk D_2O
Γ_{max} - the maximum surface concentration of a densely packed film
l -the thickness of the surfactant film
M - the molar mass of the surfactant
ρ - the bulk (mass) density of the surfactant
ΔG_{Ads} - the free energy of adsorption of the surfactant
vol. % - volume percent
wt. % - weight percent
sym. - symmetric
asym. - asymmetric
MMA -the mean molecular area

LIST OF TABLES

LIST OF FIGURES

CHAPTER 1

1. Introduction

Ultrathin films of surfactants are of practical and scientific interest [1]. They are used in industry as lubricants, corrosion inhibitors, levelling agents, *etc*. Films of insoluble surfactants also have applications in electrocatalysis, active optics, information storage and molecular electronics devices [2], as well as in chemical, biochemical, and physical sensors [3][4]. One of the scientific interests in these films stems from their close resemblance to biological cell membranes. Natural membranes contain many components that accomplish different functions, making these systems difficult to study [5]. Therefore, simplified models of these membranes are used in research. These models mimic the natural environment of biological membranes allowing incorporation of a particular type of a membrane polypeptide in order to study its many functions in an environment similar to a natural cell membrane. Many processes that take place in cell membranes involve separation of charge and require precise control of the trans-membrane potential. They include photosynthesis, respiration, propagation of nerve impulses and many other biological mechanisms.

1.1. Motivation

It is beneficial to deposit biomimetic membranes on the surface of a solid metal electrode for several reasons. First of all, such a configuration allows for precise control or measurement of the potential across model films. The second reason is that a plethora of atomic resolution *in situ* surface analytical techniques can be applied to study biomimetic films with molecular resolution. Finally, the knowledge, gained during such research, can be

directly applied for the design of novel biosensors and other molecular devices.

The most suitable metal for biomimetic research is gold because it is thermodynamically stable in a broad range of applied potentials. The best material for the biomimetic matrix is a lipid or a lipid-cholesterol mixture because such a matrix is both simple and relevant to a natural polypeptide environment. There is a difficulty, however, in the use of this matrix on gold, because lipids tend to form poor quality, patchy films when deposited directly on the metal surface. This is the consequence of a weak interaction of lipid molecules with the metal substrate. To overcome this obstacle, self assembling monolayers of thiols (SAMs) have been deposited on the surface of gold first, and then lipids have been deposited as a second layer [5]. Bilayers formed in this way are still far from providing an adequate environment for polypeptides because SAMs are quite rigid and often have permanent defects in the form of pinholes, due to strong binding to gold of thiol molecules.

In the present thesis it will be demonstrated that pyridine-based surfactants are superior candidates for application as adhesive layers to attach lipids to the gold substrate. In contrast to SAMs, these surfactants form mobile fluid films that not only can better accommodate polypeptides but also spontaneously self-heal small defects in the supported membrane model.

The structure of ultrathin films of insoluble surfactants has already been studied quantitatively using Fourier transform infrared reflection absorption spectroscopy (FTIR RAS). These studies, however, were performed either at the gas-solid or gas-liquid interfaces. This thesis describes novel methodology that was developed in order to perform *in situ* quantitative FTIR RAS studies of ultrathin films at the metal-liquid interface under potential

control. The information gained during studies of such systems is directly relevant to the fabrication of biosensors. In future, the developed techniques may be applied to study biomimetic films containing membrane polypeptides and allow one to determine molecular level information concerning the influence of the trans-membrane potential on the processes that take place in living cell membranes.

1.2. Research Objectives

The current project pursued two major research objectives. Our first intention was to develop the Fourier transform infrared reflection absorption spectroscopy (FTIR RAS) to the level that would allow quantitative studies of ultrathin organic films at the metal-solution interface. The second goal was to apply the FTIR RAS to study the potential-induced phase transitions of the surfactant films at the metal electrode surface.

1.3. Scope of the Thesis

This thesis consists of eight chapters. An introduction to the project is given in this chapter. Chapter 2 is a literature review on the major achievements in the development of biomimetic films at metal electrodes and interfacial infrared spectroscopy of relevant systems. Chapter 3 presents a brief review of the theory related to insoluble surfactants, electrochemistry and FTIR RAS. The emphasis is on the description of polarization modulation FTIR RAS. Chapter 4 contains technical information concerning the electrochemical and spectroscopic experiments that were performed, while Chapter 5 describes several spectroscopic procedures that were developed during the realization of this

project. The influence of the electric field on the orientation of pyridine molecules at the metal-solution interface is described in Chapter 6. The spontaneous formation of a bilayer of 4-pentadecylpyridine at the gold electrode is discussed in Chapter 7. The kinetics of the film formation, the structure, the orientation and the conformation of the surfactant molecules in the ultrathin films at the gold electrode are presented in separate sections of this chapter. Finally, the most important achievements of this project are summarized in Chapter 8.

References

1. E. Sackmann, Science 271 (1996) 43.

2. L.M. Goldenberg, J. Electroanal. Chem. 379 (1994) 3.

3. J.D. Swalen, D.L. Allara, J.D. Andrade, E.A. Chandross, S. Garoff, J. Israelachvili, T.J. McCarthy, R. Murray, R.F. Pease, J.F. Rabolt, K.J. Wynne, and H. Yu, Langmuir 3 (1987) 932.

4. A. Ulman, An Introduction to Ultrathin Organic Films: From Langmuir-Blodgett to Self-Assembly, Academic Press, New York (1991) 339.

5. R. Guidelli, G. Aloisi, L. Becucci, A. Dolfi, M.R. Moncelli, F.T. Buoninsegni, J. Electroanal. Chem. 504 (2001) 1.

CHAPTER 2

2. Literature Review

This review provides a brief description of the most significant achievements and challenges in studies of metal-supported biomimetic films. In addition, it contains an introduction to modern infrared techniques that are employed to characterize the orientation of ultrathin organic films at electrified interfaces. Finally, selected applications of the polarization modulation Fourier transform infrared spectroscopy (PM FTIR RAS), the technique that was advanced in this project, for biomimetic research at the air-water interface will be reviewed.

2.1. Achievements and Challenges of Biomimetic Research

Membranes of living cells have complex structure and comprise many components that fulfil their multiple functions [1]. Various simplified models are used to mimic biological membranes in order to study specific functions of the membrane constituents [2] and the knowledge gained during this biomimetic research can be very useful for fabrication of biosensors [3][4]. The first successful biomimetic model was a bilayer lipid membrane BLM [5]. It was prepared by spreading a lipid solution across a small aperture in a hydrophobic septum and a number of biochemical and physiological studies have been performed on polypeptides incorporated in these membrane models [6]. The major problem of BLMs stems from their long term instability which makes these films unsuitable for development of biosensors [7]. Consequently, supported biomimetic films have gained more attention in recent years [8].

Miller *et al.* [9][10] initiated research of metal-supported biomimetic films. They monitored the formation of lipid films at the Hg surface by observation of a characteristic decrease in the differential capacity [11][12] of the dropping Hg electrode. The group also studied the interactions of polypeptides with the phospholipid molecules in the biomimetic matrix [13][14].

Further advances in this field were made by Nelson *et al*. [15] who studied phospholipid monolayers deposited on a hanging mercury drop electrode. Figure 2.1 shows a typical dependence of the differential capacity on the potential when the electrode is coated with a lipid film. Theoretical modelling, using a self-consistent field approach [16][17] revealed that the pseudo-capacitance peaks 1 and 2 can be attributed to the displacement of the hydrocarbon tails of lipid molecules by their polar heads (flip-flop of the molecules), followed by the formation of a lipid bilayer at the interface. This behaviour was explained as resulting from the potential-induced change of the electrode surface affinity for water. The peak at -1.25 V was attributed to the desorption of the bilayer from the electrode surface. Nelson and coworkers utilized this model membrane to carry out research that involved studies of the influence of electrolyte composition [18] and the presence of chelating agents [19] as well as the effect of micropollutants [20] and toxins [21] on the permeability of the film to ions. In addition, Nelson *et al.* studied the effect of incorporation of cholesterol [22], retinal (a photon-activated proton pump) [23] and gramicidin A (a channel-forming membrane polypeptide) [24][25][26][27] on the electrochemical properties of the lipid film. Recently, Nelson and Bizzotto performed quantitative studies of these biomimetic membranes using chronocoulometry [28] and chronoamperometry [29].

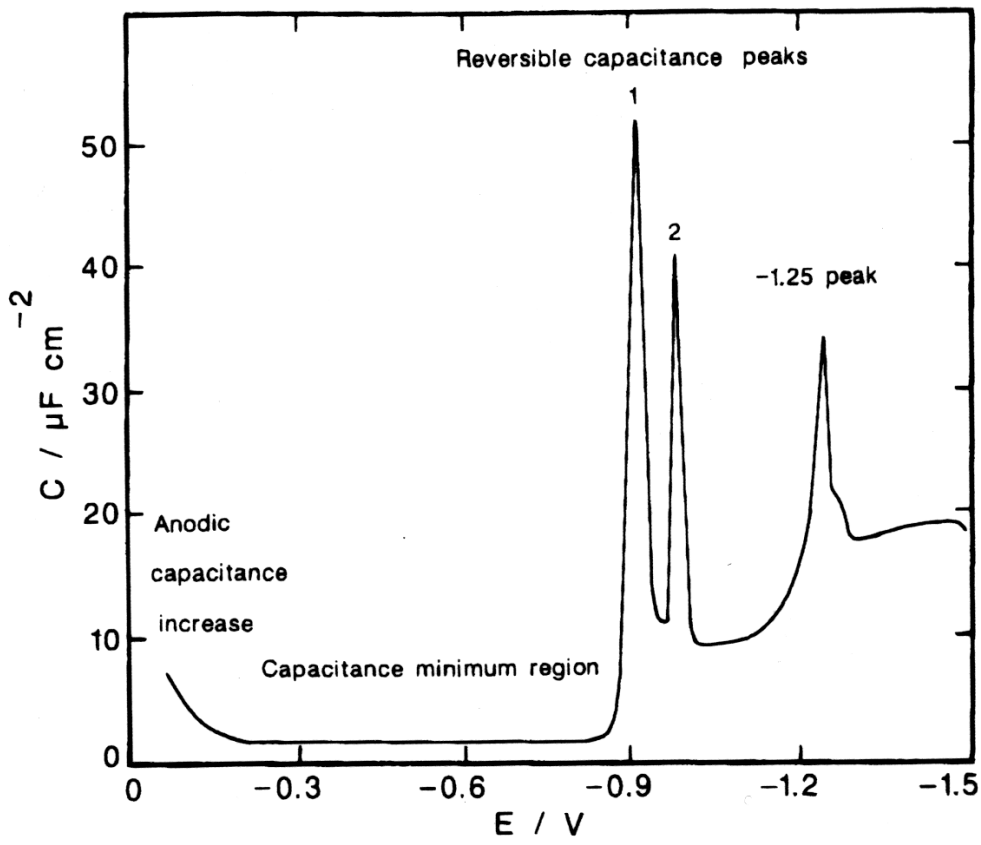

Figure 2.1. Dependence of the capacity of the hanging mercury drop electrode covered with a monolayer of dioleoylphosphatidylcholine on the applied potential.
Electrolyte solution: 0.55 M KCl.
Taken from [22].

Similar studies have been performed by a group led by Guidelli and Moncelli who made further advances in electrochemical studies of biomimetic materials. They used a lipid-covered mercury-electrolyte interface to test the Gouy-Chapman theory [30] and to determine the values of pK_a for several lipids [31] and phosphatidic acid [32]. In addition, the group employed a lipid-covered mercury electrode to study the presence of amphiphilic species in electrolyte [33], the transport of lipophilic ions [34][35][36] and chelating agents [37] across the membrane as well as the mechanism of the electro-reduction of ubiquinone-10 (the primary transporter of protons across the mitochondrial membrane) [38][39] and the influence of anti-cancer drugs on the surface potential of the model membrane [40].

The above-mentioned studies demonstrate the diversity of tasks that have been addressed using model films deposited on a mercury electrode. Most of these studies were performed using electrochemical techniques only and mercury is an ideal material for such studies. There are, however, several limitations of the mercury electrode for biomimetic research. First, the liquid state and spherical shape of this electrode do not allow for application of spectroscopic and surface microscopic techniques to investigate molecular properties and structure of membrane models. In addition, it is difficult to form bilayers of lipids on a mercury electrode and to fabricate biosensors using this electrode material. For these reasons, biomimetic films formed on solid electrodes have become more attractive in recent years. Solid electrodes offer the possibility to employ an array of modern *in situ* spectroscopic and surface imaging techniques to study the properties of biomimetic membranes at the molecular level. Gold is perhaps the most suitable metal for such studies because of its high stability to oxidation in a broad potential range. Unfortunately,

phospholipid films transferred directly onto the surface of this metal tend to form defect-filled, patchy films that make poor matrices to study the permeation of the membrane to ions [41]. To overcome this problem, the surface of gold has been modified with hydrophobic films of self assembled monolayers of thiols (SAMs) and then the lipid has been deposited onto the monolayer of the thiol. Such bilayers were produced by fusion of phospholipid vesicles [42][43], by Langmuir-Blodgett [44][45] deposition and by painting and paint freezing methods [46]. Their properties have already been studied using electrochemistry [47][48], Raman spectroscopy [49], surface plasmon resonance [50][51] and scanning tunnelling microscopy [52].

SAMs on gold were first prepared by Nuzzo *et al.* [53][54]. Porter *et al.* [55] characterized these monolayers using ellipsometry, infrared spectroscopy and electrochemistry. It was found that long-chain thiol molecules form densely-packed, crystalline-like assemblies with fully extended alkyl chains tilted from the surface normal by $20\text{-}30^0$. Krysinski *et al.* [56] demonstrated that adsorption of thiols on Au results in a partial electron transfer and the mechanism of their chemisorption was explained as the reduction-oxidation reaction that may involve the release of hydrogen gas [57]

$$R\text{-}S\text{-}H + Au^0_{surf} = R\text{-}S^-\text{-}Au^+_{surf} + \tfrac{1}{2}\, H_2$$

and the formation of the covalent S-Au bond, the strength of which was estimated to be ~ 180 kJ mol^{-1} [58]. Such a high affinity of thiols for gold results in rigid, condensed films with restricted lateral mobility that often exhibit defects in the form of pinholes [59][60][61][62]. These properties severely affect the usefulness of these matrices to build a model of a biological membrane that must be fluid to accommodate membrane polypeptides and provide

an adequate environment for their function [63].

2.2. The Search for New Biomimetic Materials

One of the objectives of the current project was to find an adhesive material that would be better than SAMs of thiols for preparation of the biomimetic films supported on a gold electrode. Since the main problem associated with SAMs arises from their strong chemisorption to gold, our efforts were to find materials that would have lower affinity for this metal. It was learned from previous research performed in our laboratory that pyridine is weakly chemisorbed on gold single crystals [64][65][66][67][68], having a free energy of adsorption of approximately 40 kJ mol^{-1}. This number is 4.5 times lower than the corresponding value for thiols and yet about 4 times higher than the values characteristic for aliphatic molecules, physisorbed at a gold electrode [69]. It is most important that this value exceeds the free energy of adsorption of water since experimental evidence demonstrates that close packed films of pyridine are formed at all the faces of gold single crystals studied.

Taking the above information into consideration, a pyridine-based surfactant, 4-pentadecylpyridine (C15-4Py), was synthesised and studied [70]. Results of preliminary experiments, performed in our laboratory by Bizzotto *et al.*, demonstrated that a C15-4Py film, transferred onto a Au(111) electrode using the double horizontal touching (Langmuir Schaefer [71]) technique, has excellent barrier properties at potentials close to the potential of zero charge (pzc), where the surfactant forms a compact film. Addition of 25 mol% of 10-decyl-9-[2-(4-pyridyl)ethyl]anthracene, a surfactant dye, to the C15-Py film only slightly modified its properties but allowed the use of fluorescence and elastic light scattering

spectroscopies to study the mechanism of adsorption of C15-4Py on a gold electrode [72]. The results of these studies are summarized in Figure 2.2. At potentials near the pzc (250 mV), the surfactant is strongly adsorbed at the electrode surface as a compact film. When a progressively more negative potential is applied to the electrode, electroporation is observed at moderately negative potentials followed by full desorption of the film at the most negative potentials. At potentials of desorption, the surfactant remains in the vicinity of the electrode in the form of micelle-like aggregates. Bizzotto *et al.* [73][74] have previously observed similar aggregates formed by stearic acid tagged with anthracene (12-(9-anthroloxy)stearic acid) at negative electrode polarizations with the aid of fluorescence spectroscopy. Interestingly, these aggregates do not diffuse away from the interface and are readily re-adsorbed when the potential attains less negative values. The re-spreading of the micellar aggregates probably occurs in a fashion similar to the spreading of organic droplets on a mercury pool electrode observed by ðutif *et al*.[75][76][77]. Initially, the micelles adhere to the metal surface and form hemimicelles. The shape of the hemimicelles is controlled by the magnitude of the contact angle. The contact angle changes from 90^0 to 0^0 as the electrode potential becomes more positive and the film pressure at the metal increases. At potentials where the surface pressure at the metal-solution interface is higher than the interfacial tension of the liquid-water interface, hemimicelles spread onto the metal surface to form initially a loose, and eventually a more compact film. The formation of hemimicelles as the first step in a surfactant adsorption onto a solid-liquid interface has been recently observed by neutron scattering [78] and atomic force microscopy [79].

The mechanism of the potential-induced spreading of C15-4Py on a metal electrode

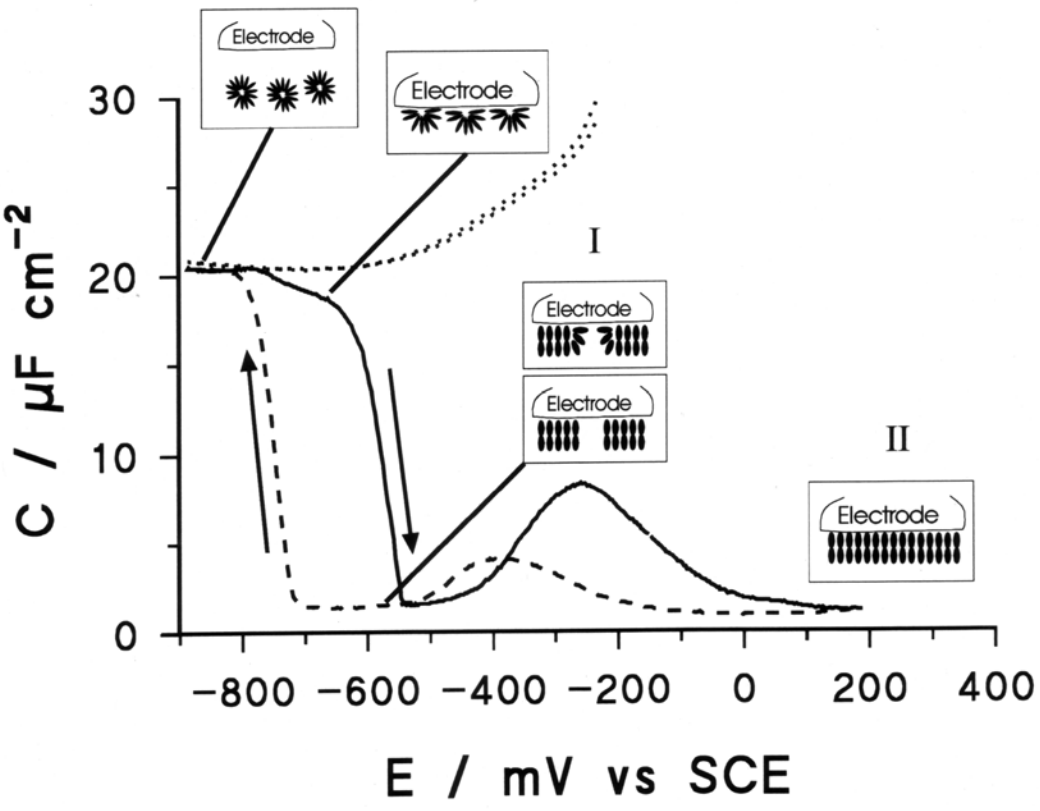

Figure 2.2. Schematic description of the adsorption and desorption of C15-4Py film deposited onto a Au(111) electrode using the double horizontal touching procedure.
Electrolyte: 0.05 M $KClO_4$.
Taken from [72].

is typical for the whole family of insoluble surfactants that includes SAMs of thiols and lipids. Indeed, Bizzotto and Lipkowski [80] have reported similar electrochemical behaviour for octadecanol and octadecanoic acid while Yang *et al*. [81][82] showed that the reductive desorption of SAMs of thiols at very negative electrode polarizations and high pH also involves a similar mechanisn. Recently, Horswell *et al.* [83] described similar potential-driven desorption and readsorption of phospholipid films on gold. In all the above experiments the insoluble films are detached from the electrode at sufficiently high negative electrode polarization and quantitatively re-spread at the metal when the potential is set to values close to the potential of zero charge, and exhibit a similar pattern in the dependence of the interfacial capacity on the electrode potential. Thus, studies of C15-4Py generate knowledge that is useful for understanding of the influence of the electrode potential on the behaviour of ultrathin films formed at the electrode by the whole class of insoluble surfactants, including phospholipids.

Early studies of equilibrium of an insoluble surfactant between the gas-solution (GS) and the metal-solution (MS) interfaces were performed in our laboratory using differential capacity and charge density measurements [84][85][86]. These experiments were completed in a time scale on the order of minutes and no evidence of surfactant molecules moving from the GS interface to the MS interface was observed within this short experiment time. It has been concluded that once deposited on the metal electrode surface, the film at the MS interface is not affected by a change in the physical state of the film spread at the GS interface. Recently, Steel *et al.* [87] reported that Langmuir monolayers can flow across the triple-phase line from the GS interface to the MS interface of an organothiol-modified gold electrode.

Independently, we have presented preliminary results [88] to show that C15-4Py can also move from the GS interface to the MS interface of a Au(111) electrode to spontaneously form a bilayer.

This section has demonstrated that the mechanism of potential-induced spreading of C15-4Py at gold electrodes was characterized quite comprehensively using electrochemical and ultraviolet-visible spectroscopic techniques. The current project is thus aimed at extracting molecular level information about the orientation of C15-4Py films at the gold electrode using infrared spectroscopy that would complement the information gained in the preceding studies. The focus is on a spontaneous transfer of the surfactant from the GS interface to the MS interface, particularly on the structure, fluidity and orientation of the obtained films. In addition, the influence of the electric field on the orientation of pyridine, which is the head group of the C15-4Py molecule, was investigated using infrared spectroscopy and the thickness and quality of the C15-4Py films was determined using neutron reflectometry.

Infrared spectroscopy has already been successfully applied to obtain the molecular orientation of metal-supported organic films [89]. Quantitative interpretation of the infrared spectra of these films is usually facile due to the anisotropy of the electric field of infrared radiation at the metal surface [90]. So far, most of these studies were performed *ex situ* at the gas-metal interface [91][92][93][94][95] and the studies involving *in situ* measurements at the MS interface inside a spectroelectrochemical cell [96][97] were limited to qualitative interpretation of the infrared spectra. In order to apply *in situ* FTIR RAS for the quantitative analysis of surfactant films at the metal electrode surface, it was necessary to develop a new

methodology. With the purpose to contrast the methodological advances made in this project to what has already been known in the literature, a brief review of developments in the field of electrochemical infrared spectroscopy will be presented below.

2.3. Introduction to Infrared Spectroscopy at the Metal-Electrolyte Interface

The history of infrared reflection absorption spectroscopy (IR RAS) begins from the work of Greenler [98][99][100] at the end of the 1960s. Greenler gave a theoretical background of the technique and studied infrared spectra of organic films adsorbed at metal mirrors. During the last three decades this technique was significantly expanded and presently it is used to study gas-solid, gas-liquid and solid-liquid interfaces. Ultrathin organic films adsorbed at electrified MS interfaces have been studied in this project, hence below the emphasis will be given on the development of IR RAS as a tool to study this particular interface.

The main challenge associated with IR RAS studies of organic film at the MS interface stems from the strong absorbance of infrared radiation by aqueous electrolyte. Presently, there are two experimental configurations that allow the overcoming of this difficulty. The first approach is to perform attenuated total reflection (ATR) spectroscopy using the Kretschmann cell [101]. This cell is equipped with an optical window (usually a Si or Ge hemisphere) that works in the regime of total reflection. A several nanometre-thin metal film, deposited directly onto the optical window, serves as an electrode in ATR spectroscopy. The most significant advantage of this method is a considerable enhancement of the electric field of the infrared beam at the window-electrolyte interface; *i.e.*, at the location of the adsorbate molecules. In

addition, this technique is very surface-selective because the electric field of the totally reflected infrared radiation rapidly decays inside the Kretschmann cell. However, the thin film electrode is not a single crystal, hence ATR cannot be used to study adsorption of organic molecules at single crystal surfaces.

The second approach is to apply IR RAS using a thin layer cell in which the electrode is pressed against the optical window until it is separated by a several micrometre-thick layer of electrolyte. This configuration allows for the use of metal single crystals. However, because the infrared beam penetrates the thin layer of electrolyte solution, the spectrum of an organic film is superimposed on a spectrum of the aqueous electrolyte. It is difficult (if possible) to acquire the background spectrum (the spectrum without an organic film) at exactly the same cavity thickness as that of the thin layer cell during the acquisition of the sample spectrum. Therefore, the background correction is made by either (i) potential modulation or (ii) polarization modulation. The first technique is presently called subtractively normalized Fourier transform interfacial infrared spectroscopy (SNIFTIRS) and the second technique is called polarization modulation Fourier transform infrared reflection absorption spectroscopy (PM FTIR RAS).

During SNIFTIRS, the electrode potential is modulated between the base (E_1) and the sample (E_2) values and the spectra of the reflected infrared radiation are measured. The reflection absorption spectrum ($\Delta R/R$) is obtained in the following way:

$$\frac{\Delta R}{R} = \frac{R(E_2) - R(E_1)}{R(E_1)} \qquad (2.3.1),$$

where $R(E_1)$ and $R(E_2)$ are the thin layer cell reflectivities at the base and the sample potentials, respectively. Due to subtraction, SNIFTIRS spectra are devoid of the common background signal due to the aqueous electrolyte. However, they represent the difference between the absorbances of organic molecules at potentials E_2 and E_1 rather than just absorbance at the sample potential E_2. Such spectra are difficult to use for quantitative interpretation and thus, SNIFTIRS has been primarily used as a qualitative tool. In this thesis it will be demonstrated how SNIFTIRS spectra can be converted to a form that can be employed for quantitative analysis.

During PM FTIR RAS the incident beam polarization is modulated between two orthogonal directions: (i) perpendicular (s-polarization) and (ii) parallel (p-polarization) to the plane of incidence of the infrared beam. Figure 2.3 shows the orientation of the electric field vectors of s- and p-polarized beams with respect to the metal surface. Due to destructive interference of the incident and reflected radiation in the vicinity of the metal surface, the electric field of the s-polarised infrared beam almost vanishes at the metal surface, while the electric field of the p-polarized beam is enhanced at the metal surface as the result of the constructive interference (see Figure 2.3). Thus, the first component of the modulated signal is insensitive to the surface species and can be used to obtain the background spectrum while the other component is attenuated due to absorption of the infrared beam by the surface species and thus can be utilized to obtain the sample spectrum. Modulation between s- and p-polarizations is made at a high frequency (100 kHz) and the reflection absorption spectrum $\Delta R/\langle R\rangle$ is obtained as

$$\frac{\Delta R}{\langle R\rangle} = \frac{\left|R_s - R_p\right|}{(R_s + R_p)/2} \qquad (2.3.2),$$

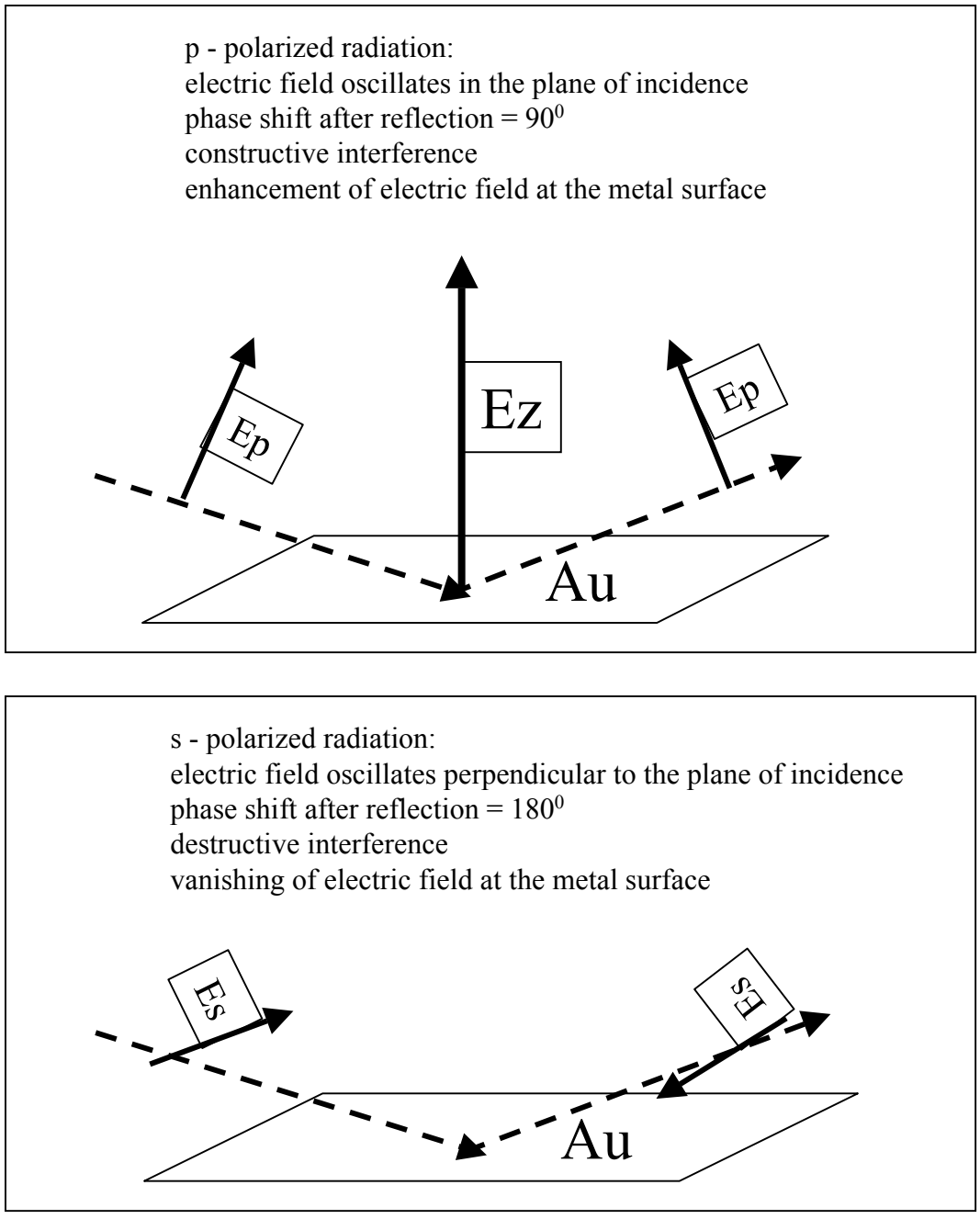

Figure 2.3. Diagrams of reflection of linearly polarized electromagnetic radiation by a metal mirror, showing the interaction of s- and p-polarized beams with the metal surface.
Dashed arrows show the direction of the incident and reflected beams and solid arrows indicate the directions of electric fields.

where R_s and R_p represent the reflectivities of the s- and p-components of the modulated infrared beam from the thin layer cell. It is evident from equation (2.3.2) that any common mode noise such as that due to atmospheric CO_2 and H_2O should be absent from the polarization modulation spectrum. Because there is no need to modulate the electrode potential, this method is particularly useful to study biological systems that are often destroyed by excessive perturbations due to potential modulation. It is important to note that PM FTIR RAS is sensitive not only to the surface species but also to the molecules that are in the vicinity of the metal surface at a distance which is less than 1 μm. Hence, the background due to the aqueous electrolyte cannot be completely removed from the $\Delta R/<R>$ spectrum.

2.4. Developments of SNIFTIRS and PM FTIR RAS

The first successful application of IR RAS for studies of the metal-solution interface were carried out in 1980 by Bewick, Kunimatsu and Pons [102][103]. The group used a thin layer cell and applied the potential modulation technique. These pioneering experiments were made using dispersive instruments and one year later the technique was advanced, employing Fourier transform infrared (FTIR) spectrometers [104][105]. Because of their superior performance, FTIR instruments completely replaced dispersive systems. Recently, Faguy *et al.* [106][107][108] demonstrated that an improvement in the signal-to-noise ratio (S/N) is achieved during SNIFTIRS experiments when a ZnSe hemisphere is used as an optical window. These researchers also described a design of a simple setup with two folding mirrors that has a superior optical throughput compared to systems that employ CaF_2 windows due

to the reduction in the number of reflecting metal surfaces.

The first polarization modulation IR RAS experiments on a metal mirror were done in 1981 by Golden *et al.* [109]. The authors acquired spectra of the sample that was housed in an ultrahigh vacuum chamber using a dispersive instrument and gave a theoretical background of this method, equivalent to the theoretical description of transmittance polarization modulation infrared spectroscopy given previously by Hipps and Crosby [110]. The first experiments that employed polarization modulation IR RAS for an electrochemical environment were carried out in 1982 by Russell *et al.* [111]. Two years later, Golden, Kunimatsu and Seki [112][113] used a Fourier transform spectrometer to perform the first PM FTIR RAS experiments. The last group also described the layout of their experimental setup and calculated the mean squared electric field strength (MSEFS) within the thin layer cell [114].The performance of dispersive and FTIR instruments was compared by Golden *et al.* [115] using an ultrahigh vacuum PM IR RAS setup. The group concluded that the use of FTIR instruments allows one to achieve a better resolution and S/N. The advantages of PM FTIR RAS over SNIFTIRS were demonstrated by Faguy *et al.* [116][117]. These researchers demonstrated experimentally that besides a superior S/N, the PM technique is almost insensitive to atmospheric H_2O and CO_2. An important advance in PM FTIR RAS was made in 1991 by Corn and coworkers [118][119], who introduced a novel method of the experimental signal demodulation. Their device, a synchronous sampling demodulator (SSD) allowed one to enhance the signal up to two times compared to the conventional lock-in technique.

The main difficulty of the PM FTIR RAS technique for quantitative analysis of

ultrathin films at metal electrodes stems from the broad-band background that is introduced to the spectra by the PEM as well as absorption and interference due to the thin layer of electrolyte sliced between the optical window and the electrode. Recently, Buffeteau *et al.* described methods to remove the artefacts introduced by the PEM *via* normalization by the spectrum of the film-free substrate [120] or by utilization of calibration spectra, acquired in an independent experiment [121]. This thesis will describe how to remove not only the spectral signature of the PEM but also the other artifacts, specific for the thin layer configuration of a spectroelectrochemical cell.

2.5. Optimization of Experimental Conditions

Since the birth of IR RAS, many efforts have been made to optimize the performance of the experimental setup. The first calculations aimed at the improvement of the S/N of IR RAS were carried out by Greenler [98][99][100]. He determined the optimal angles of incidence for IR RAS experiments at different metals. In addition, he demonstrated how the optical constants of the organic film affect the resulting spectra. Later Dluhy expanded IR RAS to study thin films adsorbed at the air-water interface [122]. He calculated the reflectivity and the MSEFS of infrared radiation at the air-water interface and compared these values with the corresponding data for the air-metal interface.(Calculation of the MSEFS allows one to estimate the absorbance of infrared radiation by an organic film, since absorbance is proportional to the MSEFS [123].) Seki *et al.* [114] have calculated the MSEFS distribution within a thin layer electrochemical cell. They demonstrated that absorption of radiation by an aqueous electrolyte has a profound effect on the MSEFS, and

consequently on the S/N. Roe *et al.* [124][125] have given detailed analysis of the influence of both the angle of incidence and the thin cavity thickness on the reflectivity of the spectroelectrochemical cell. These researchers demonstrated that the precise control of the thin cavity thickness is necessary for full optimization of the experimental setup. They also concluded that the best experimental conditions to perform IR RAS using p-polarized light are achieved when the reflectivity of the interface reaches a minimum. This last conclusion was recently challenged by Blaudez *et al.* [126] who showed that significant reduction in S/N is observed at these conditions.

The influence of the electrolyte solvent (water or deuterium oxide) on the spectra of organic films in the C-H stretch region has been described by Popenoe *et al.* [127]. The variation of the MSEFS with the angle of incidence and the thin cavity thickness for monochromatic infrared radiation has been shown by these authors. The data for CaF_2 and Si as the optical window materials have been presented. The influence of these and several other window materials such as ZnSe and Ge on the MSEFS were studied by Faguy *et al.*[106][107][108] who calculated the best angle at which to perform IR RAS using these materials. These researchers used very small values of thin cavity thickness of 0.25, 0.5, 1 and 5 μm [108] in their calculations of the angles corresponding to the maximum MSEFS. By averaging these angles they arrived on an optimum angle of incidence which was just above the critical angle. This conclusion, however, is inconsistent with the works of Roe *et al.* and Popenoe *et al.* Segmentation and partial discrepancy of the information presented above encouraged us to perform optimization of the experimental setup ourselves. The results of optimization are presented in Chapter 5 of this thesis.

2.6. Applications of PM FTIR RAS for Biomimetic Research

The exceptionally low sensitivity of PM FTIR RAS to atmospheric CO_2 and H_2O vapour prompted interest in the application of this technique to study insoluble surfactant monolayers at the air-water interface in a Langmuir trough. These films mimic the natural environment of the cell boundaries (single leaflets of lipid bilayers) and are the most relevant systems, studied by PM FTIR RAS, to the project described in this thesis. The first studies of such systems were reported in 1993 by Blaudez *et al.* [128]. The researchers recorded spectra of perdeuterated arachidic acid and arachidate monolayers spread at the air-water interface. These spectra were essentially free from absorption bands due to water vapour. Beginning with this pioneering work there was a lot of interest in studies of biomimetic films using PM FTIR RAS at the air-water interface. Blaudez *et al.* [129] applied this technique to study the orientation of dimyristoyl phosphatidylcholine monolayers and melittin (a cytotoxic polypeptide). A group led by Pézolet studied conformational changes of dipalmitoyl phosphatidylglycerol monolayers [130], formation of helices by a poly (L-lactide)/poly(D-lactide) stereocomplex [131] and the aggregate state of monolayers of behenic acid [132] in the Langmuir trough. PM FTIR RAS was also applied to study more sophisticated systems such as lipid/gramicidin [133] and photosystem II core complex (a pigment protein complex involved in electron transport during the photosynthetic process) [134].

In the present project, the successful application of PM FTIR RAS for studies of organic molecules at the air-water interface is extended to *in situ* studies of the influence of the electric potential on the orientation and conformation of insoluble surfactants deposited at the metal electrode surface.

References

1. J. Koryta, Ions, Electrodes and Membranes, John Wiley & Sons, New York (1991).

2. R. Guidelli, G. Aloisi, L. Becucci, A. Dolfi, M.R. Moncelli, F. T. Buoninsegni, J. Electroanal. Chem. 504 (2001) 1.

3. J.D. Swalen, D.L. Allara, J.D. Andrade, E.A. Chandross, S. Garoff, J. Israelachvili, T.J. McCarthy, R. Murray, R.F. Pease, J.F. Rabolt, K.J. Wynne and H. Yu, Langmuir 3 (1987) 932.

4. E. Sackmann, Science 271 (1996) 43.

5. P. Mueller, D.O. Rudin, H.T. Tien, W.D. Wescot, Nature 194 (1962) 979.

6. H.T. Tien, Bilayer Lipid Membranes, Marcel Dekker, New York (1974).

7. H.T. Tien and Z. Salamon, Biochemistry and Bioenergetics 22 (1989) 211.

8. A. Wardak and H.T. Tien, Biochemistry and Bioenergetics 24 (1990) 1.

9. I.R. Miller and D. Bach, J. Colloid Interface Sci. 29 (1969) 250.

10. R.E. Pagano and R.I. Miller, J. Colloid Interface Sci. 45 (1973) 126.

11. A.N. Frumkin, Potentials of Zero Charge, Moscow, Nauka (1979) (in Russian).

12. B.B. Damaskin, O.A. Petrii and V.V. Batrakov, Plenum Press, New York (1971).

13. I.R. Miller, J. Rishpon and A. Tenenbaum, Biochem. Bioenergetics 3 (1976) 528.

14. M.F. Lecompte and I.R. Miller, Biochem. Bioenergetics 6 (1979) 537.

15. A. Nelson and A. Benton, J. Electroanal. Chem. 202 (1986) 253.

16. F.A.M. Leermakers and A. Nelson, J. Electroanal. Chem. 278 (1990) 53.

17. A. Nelson and F.A.M. Leermakers, J. Electroanal. Chem. 278 (1990) 73.

18. A. Nelson and H.P. van Leeuwen, J. Electroanal. Chem. 273 (1989) 183.

19. A. Nelson and N. Auffret, J. Electroanal. Chem. 248 (1988) 167.

20. A. Nelson, N. Auffret and J. Readman, Analytica Chim. Acta 207 (1988) 47.

21. A. Nelson, N. Auffret and J. Borlakoglu, Biochim. Biophys. Acta 1021 (1990) 205.

22. A. Nelson and N. Auffret, J. Electroanal. Chem. 244 (1988) 99.

23. A. Nelson, J. Electroanal. Chem. 335 (1992) 327.

24. A. Nelson, J. Electroanal. Chem. 303 (1991) 221.

25. A. Nelson, Langmuir 12 (1996) 2058.

26. A. Nelson, Langmuir 13 (1997) 5644

27. A. Nelson, Biophys. J. 80 (2001) 2694.

28. D. Bizzotto and A. Nelson, Langmuir 14 (1998) 6269.

29. A. Nelson and D. Bizzotto, Langmuir 15 (1999) 7031.

30. M.R. Moncelli and R. Guidelli, J. Electroanal. Chem. 326 (1992) 331.

31. M.R. Moncelli, L. Belucci and R. Guidelli, Biophys. J. 66 (1994) 1969.

32. M.R. Moncelli and L. Becucci, J. Electroanal. Chem. 385 (1995) 183.

33. M.R. Moncelli and L. Becucci, Biochem. Bioenerg. 39 (1996) 227.

34. M.R. Moncelli, R. Herrero, L. Becucci and R. Guidelli, J. Phys. Chem. 99 (1995) 9940.

35. R. Herrero, M.R. Moncelli, L. Becucci and R. Guidelli, J. Electroanal. Chem. 425 (1997) 87.

36. R. Herrero, F.T. Buoninsegni, L. Belucci, M.R. Moncelli, J. Electroanal. Chem. 445 (1998) 71.

37. I. Zawisza, R. Bilewicz, M.R. Moncelli, R. Guidelli, J. Electroanal. Chem. 509 (2001) 31.

38. M.R. Moncelli, L. Becucci, A. Nelson and R. Guidelli, Biophys. J. 70 (1996) 2716.

39. M.R. Moncelli, R.Herrero, L. Belucci, R. Guidelli, Biochim. Biophys. Acta 1364 (1998) 373.

40. R. Herrero, M.R. Moncelli, R. Guidelli, M.Carlá, A. Arcangeli, M. Olivotto, Biochim. Biophys. Acta 1466 (2000) 278.

41. H.-Q. Li, Ph.D. Thesis, University of Guelph (2000)

42. A.L. Plant, Langmuir 9 (1993) 2764.

43. A.L. Plant, M.Gueguetchkeri and W.Yap, Biophys. J. 67 (1994) 1126.

44. I. Langmuir, Trans. Faraday Soc. 15 (1920) 62.

45. K.B. Blodgett, J. Am. Chem. Soc. 57 (1935) 1006.

46. L. Ding, J. Li, S. Dong and E. Wang, J. Electroanal. Chem. 416 (1996) 105.

47. P. Krysinski, M.R. Moncelli, F. Tadini-Buoninsegni, Electrochim. Acta 45 (2000) 1885.

48. P. Krysinski, A. Zebriwska, A. Michota, J. Bukowska, L. Belucci and M.R. Moncelli, Langmuir 17, (2001) 3852.

49. C.W. Meuse, G. Niaura, M.L. Lewis and A.L. Plant. Langmuir 14 (1998) 1604.

50. O.Pierrat, N. Lechat, C. Bourdillon and J.-M. Laval, Langmuir 13 (1997) 4112.

51. S. Lingler, I. Rubinstein, W. Knoll and A. Offenhäusser, Langmuir 13 (1997) 7085.

52. B.W. Gregory, R.A. Dluhy and L.A. Bottomley, J. Phys. Chem. 98 (1994) 1010.

53. R.G. Nuzzo and D.L. Allara, J. Am. Chem. Soc. 105 (1983) 4481.

54. R.G. Nuzzo, F.A. Fusco, D.L. Allara, J. Am. Chem. Soc. 109 (1987) 2358.

55. M.D. Porter, T.B. Bright, D.L. Allara and C.E.D. Chidsey, J. Am. Chem. Soc. 109 (1987) 3559.

56. P. Krysinski, R.U. Chamberlain II and M. Majda, Langmuir 10 (1994) 4286.

57. A. Ulman, An Introduction to Ultrathin Organic Films From Langmuir-Blodgett to Self-Assembly, Academic Press, Inc., New York (1991) 288.

58. R.G. Nuzzo, B.R. Zegarski and L.H. Dubois, J. Am. Chem. Soc. 109 (1987) 733.

59. H.O. Finklea, D.A. Snider and J. Fedyk, Langmuir 6 (1990) 371.

60. H.O. Finklea, D.A. Snider and J. Fedyk, Langmuir 9 (1993) 3660.

61. C. Schönenberger, J.A.M. Sondag-Huethost, J. Jorritsma and L.G.J. Fokkink, Langmuir 10 (1994) 611-614.

62. K. S»owi½ski, R. Bilewicz and M. Majda, Chem. Anal. (Warsaw) 40 (1995) 329.

63. R.R.C. New (Ed.), Liposomes, a Practical Approach, Oxford University Press, Oxford (1990).

64. D.F. Yang, L. Stolberg and J. Lipkowski, J. Electroanal. Chem. 329 (1992) 259.

65. L. Stolberg, J. Lipkowski and D.E. Irish, J. Electroanal. Chem. 296 (1990) 171.

66. L. Stolberg and J. Lipkowski, J. Electroanal. Chem. 322 (1992) 357.

67. L. Stolberg and J. Lipkowski, J. Electroanal. Chem. 238 (1987) 333.

68. L. Stolberg, S. Morin, J. Lipkowski and D.E. Irish, J. Electroanal. Chem. 307 (1991) 241.

69. J. Lipkowski, C. Nguen Van Huong, C. Hinnen, R. Parsons and J. Chevalet, J. Electroanal. Chem. 143 (1983) 375.

70. D. Bizzotto, A. McAlees, J. Lipkowski and R. McCrindle, Langmuir 11 (1995) 3243.

71. I. Langmuir and V.J. Schaefer, J. Am. Chem. Soc. 60 (1938) 1351.

72. T. Sagara, V. Zamlynny, D. Bizzotto, A. McAlees, R. McCrindle and J. Lipkowski, Israel J. Chem. 37 (1997) 197.

73. D. Bizzotto and J. Lipkowski, Progress Surf. Sci. 50 (1995) 237.

74. D. Bizzotto and J. Lipkowski, J. Electroanal. Chem. 409 (1996) 33.

75. V. ðutiƒ, S. Kova…, J. Tomiaƒ and V. Svetli…iƒ, J. Electroanal. Chem. 349 (1993) 173.

76. N. Ioševiƒ, J. Tomiaƒ and V. ðutiƒ, Langmuir 10 (1994) 2415.

77. N. Ioševiƒ and V. ðutiƒ, Langmuir 14 (1998) 231.

78. D.C. McDermott, J. McCarney, R.K. Thomas and A.R. Rennie, J. Colloid. Int. Sci. 162 (1994) 304.

79. I. Burgess, C.A. Jeffrey, X. Cai, G. Szymanski, Z. Galus and J. Lipkowski, Langmuir 15 (1999) 2607.

80. D. Bizzotto and J. Lipkowski, Progr. Colloid Polym. Sci. 103 (1997) 201.

81. D.-F. Yang, C.P. Wilde and M. Morin, Langmuir 12 (1996) 6570.

82. D.-F. Yang, C.P. Wilde and M. Morin, Langmuir 13 (1997) 243.

83. S.L. Horswell, V. Zamlynny, H-Q. Li, A.R. Merrill and J. Lipkowski, Faraday Disc. 121 (2002) 405.

84. J.J. Noël, D. Bizzotto and J. Lipkowski, J. Electroanal. Chem. 344 (1993) 343.

85. D. Bizzotto, J.J. Noël and J. Lipkowski, Thin Solid Films 248 (1994) 69.

86. D. Bizzotto, J.J. Noël and J. Lipkowski, J. Electroanal. Chem. 369 (1994) 259.

87. A.B. Steel, B.J. Cheek, C.J. Miller, Langmuir 14 (1998) 5379.

88. D. Bizzotto, V. Zamlynny, I. Burgess, C.A. Jeffrey, H-Q. Li, J. Rubinstein, Z. Galus, A. Nelson, B. Pettinger, A.R. Merrill, J. Lipkowski, "Amphiphilic and ionic surfactants at electrode surfaces", *In* " Interfacial Electrochemistry, theory, experiment and applications", A.Wieckowski (Ed.), Marcel Dekker, New York (1999).

89. D.L. Allara, R.G. Nuzzo, Langmuir 1 (1985) 52.

90. A.N. Parikh and D.L. Allara, J. Chem. Phys. 96 (1992) 927.

91. C.E. Jordan, B. L. Frey, S. Kornguth, and R. Corn, Langmuir 10 (1994) 3642.

92. Y. Sato, B. Frey, R. Corn and K. Uosaki, Bull. Chem. Soc. Jpn. 67 (1994) 21.

93. D.G. Hanken and R. Corn, Anal. Chem. 67 (1995) 3767.

94. B.L. Frey and R.M. Corn, Anal. Chem. 68 (1996) 3187.

95. E.A. Smith, M.J. Wanat, Y.C. Sérgio, V.P. Barreira, A.G. Frutos and R.M. Corn,

Langmuir 17 (2001) 2502.

96. W.N. Richmond and P. Faguy, R.S. Jackson and S.C. Weibel, Anal. Chem. 68 (1996) 621.

97. W.N. Richmond, P. Faguy, S.C. Weibel, J. Electroanal. Chem. 448 (1998) 237.

98. R.G. Greenler, J. Chem. Phys. 44 (1966) 310.

99. R.G. Greenler, J. Chem. Phys. 50 (1969) 1963.

100. R.G. Greenler, J. Vac. Sci. Technol. 12 (1975) 1410.

101. M. Osawa, M. Kuramitsu, A. Hatta, W. Suëtaka and H. Seki, Surf. Sci. 175 (1986) L787.

102. A. Bewick, K. Kunimatsu and B.S. Pons, Electrochim. Acta 25 (1980) 465.

103. A. Bewick and K. Kunimatsu, Surf. Sci. 101 (1980) 131.

104. T. Davidson, B.S. Pons, A. Bewick and P.P. Schmidt, J. Electroanal. Chem. 125 (1981) 237.

105. S. Pons, T. Davidson and A. Bewick, J. Am. Chem. Soc. 105 (1983) 1802.

106. P.W. Faguy and W.R. Fawcett, Appl. Spec. 44 (1990) 1309.

107. P.W. Faguy and N.S. Marinkovi*f*, Anal. Chem. 67 (1995) 2791.

108. P.W. Faguy and N.S. Marinkovi*f*, Appl. Spec. 50 (1996) 394.

109. W.G. Golden, D.S. Dunn and J. Overend, J. Catal. 71 (1981) 395.

110. K.W. Hipps and G.A. Crosby, J. Phys. Chem. 83 (1979) 555.

111. J.W.Russel, J. Overend, K. Scanlon, M. Severson and A. Bewick, J. Phys. Chem. 86 (1982) 3066.

112. W.G. Golden, K. Kunimatsu and H. Seki, J. Phys. Chem. 88 (1984) 1275.

113. K. Kunimatsu, H. Seki and W.G. Golden, Chem. Phys. Lett. 108 (1984) 195.

114. H. Seki, K. Kunimatsu and W.G. Golden, Appl. Spec. 39 (1985) 437.

115. W.G. Golden, D.D. Saperstein, M.W. Severson and J. Overend, J. Phys. Chem. 88 (1984) 574.

116. P.W. Faguy, W.N. Richmond, J. Electroanal. Chem. 410 (1996) 109.

117. P.W. Faguy, W.N. Richmond, R.S. Jackson, S.C. Weibel, G. Ball and J. Payer, Appl. Spec. 52 (1998) 557.

118. M.J. Green, B.J. Barner and R.M. Corn, Rev. Sci. Instrum. 62 (1991) 1426.

119. B.J. Barner, M.J. Green, E.I. Sáez and R.M. Corn, Anal. Chem. 63 (1991) 55.

120. T. Buffeteau, B. Desbat and J.M. Turlet, Appl. Spec. 45 (1991) 380.

121. T. Buffeteau, B. Desbat, D. Blaudez and J.M. Turlet, Appl. Spec. 54 (2000) 1646.

122. R.A. Dluhy, J. Phys. Chem., 90 (1986) 1373.

123. M. Moskovits, J. Chem. Phys., 77 (1982) 4408.

124. D.K. Roe, J.K. Sass, D.S. Bethune and A.C. Luntz, J. Electroanal. Chem. 216 (1987) 293.

125. D.S. Bethune, A.C. Luntz, J.K. Sass and D.K. Roe, Surf. Sci. 197 (1988) 44.

126. D. Blaudez, T. Buffeteau, B. Desbat, P. Fournier, A-M. Ritcey and M. Pézolet, J. Phys. Chem. B 102 (1998) 99.

127. D.D. Popenoe, S.M. Stole and M.D. Porter, Appl. Spec. 46 (1992) 79.

128. D. Blaudez, T. Buffeteau, J.C. Cornut, B. Desbat, N. Escafre, M. Pézolet and J.M. Turlet, Appl. Spec. 47 (1993) 869.

129. D. Blaudez, J.-M. Turlet, J. Dufourcq, D. Bard, T. Buffeteau and B. Desbat, J. Chem. Soc. Faraday Trans. 92 (1996) 525.

130. A. Dicko, H. Bourque, M. Pézolet, Chem. Phys. Lipids 96 (1998) 125.

131. H. Bourque, I. Laurin, M. Pézolet, J. Klass, R.B. Lennox and G.R. Brown, Langmuir 17 (2001) 5842.

132. I. Pelletier, H. Bourque, T. Buffeteau, D. Blaudez, B. Desbat and M. Pezolet, J. Phys. Chem. B 106 (2002) 1968.

133. W.-P. Ulrich and H.Vogel, Biophys. J. 76 (1999) 1639.

134. J. Gallant, B. Desbat, D. Vaknin and C. Salesse, Biophys. J. 75 (1998) 2888.

CHAPTER 3

3. Review of Theory

This work describes properties of insoluble surfactants adsorbed at an electrified interface. The purpose of this chapter is to provide the reader with an introduction to the theoretical topics related to this project. Spreading of insoluble surfactants at the gas-solution (GS) interface and their transfer onto solid substrates are discussed in the beginning of this chapter. The thermodynamics of the metal-solution (MS) interface and its application for studies of adsorption of neutral organic molecules at metal electrodes is presented next. A theoretical introduction to Fourier transform infrared (FTIR) spectroscopy is given at the end of this chapter. Such topics as principles of operation of the Michelson interferometer and the photoelastic modulator as well as the theory of reflection of electromagnetic radiation from a stratified medium are described in several sections dedicated to FTIR spectroscopy.

Since the emphasis of this work is on the infrared techniques, only essential material concerning the electrochemical techniques is given below. For the same reason, a theory of neutron reflectometry is not included in this chapter. However, a detailed description of neutron reflectometry can be found in a recent thesis [1], books [2][3] or journal publications [4][5].

3.1. Surfactants

Surfactant molecules are composed of two parts of dissimilar properties. The polar groups tend to confer water solubility, while the hydrophobic part prevents it [6]. The balance between these tendencies determines whether the molecule forms a lens or an insoluble

monolayer on the surface of water, or whether it is completely miscible with water. Solubility in water of surfactant molecules with the same head group decreases when the length of the hydrocarbon chain increases. Therefore, if the hydrophilicity of the head group is not very high (e.g. -Cl, -Br, -I, $-NO_3$), the molecules tend to float at the GS interface in the form of a lens or a crystal. In contrast, if the hydrophilicity of the head group is very high (e.g. $-SO_3^-$, $-OSO_3^-$, $-NR_3^+$) and the length of the hydrocarbon chain is relatively short (14-carbon atoms or less), the surfactants are completely water-soluble. However, if the length of the hydrocarbon tails is intermediate (14-20 carbon atoms) and the hydrophilicity of the polar head is also intermediate (e.g., $-CH_2OH$, -COOH, -CN, $-CONH_2$), the molecules spread at the GS interface to form an insoluble monolayer.

3.1.1. The Gibbs Adsorption Isotherm.

The thermodynamics of surfactants at an interface is described by the Gibbs adsorption isotherm which is presented in this section. At an interface the molecules of a phase α are neighbours of molecules of a different phase β. As a result, the balance of attractive and repulsive forces which is characteristic for the molecules in the bulk phase is altered. The lack of balance of intermolecular interactions is the property of a surface that can be expressed in the form of free energy G required to form a unit area of surface A

$$\gamma' (\partial G/\partial A)_{T,p,\mu} \qquad (3.1.1).$$

Gibbs approximated a thin interfacial layer S between the two neighbouring phases α and β with a dividing plane x_0 as shown in Figure 3.1.1 and derived the equation which bears

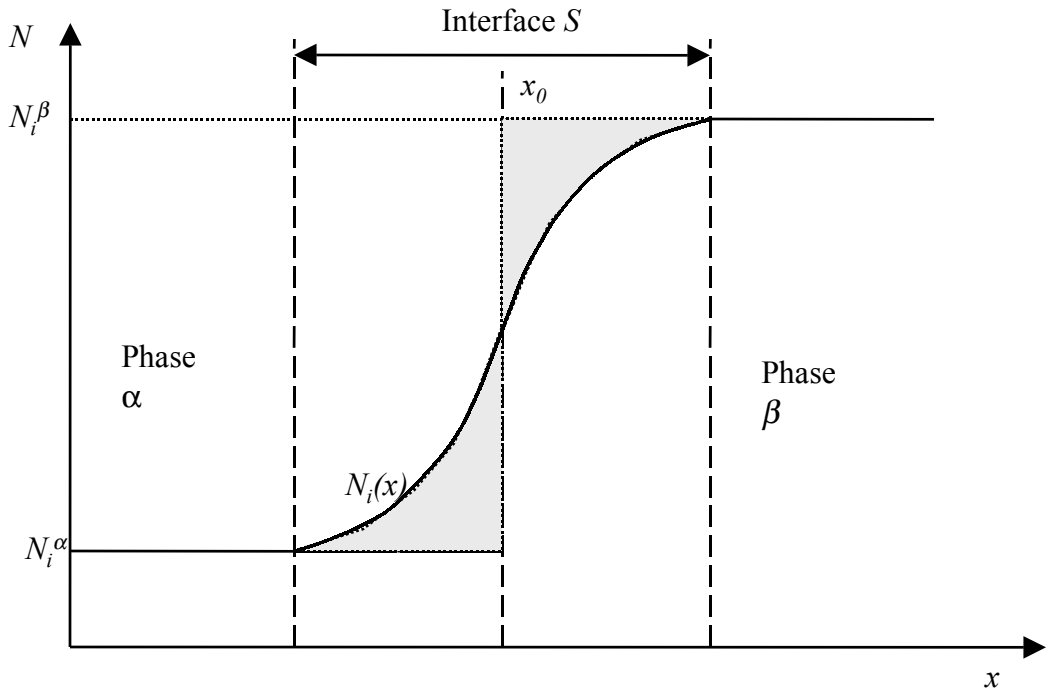

Figure 3.1.1 Gibbs model of an interface.
The change of the number of moles N_i of a species i across the interface S that separates two neighboring phases α and β.
The Gibbs excess is shown in grey.

his name

$$d\gamma = -\sum_i \Gamma_i d\mu_i \qquad (3.1.2)$$

where $d\gamma$ is the change of the surface energy, $d\mu_i$ is the change of the chemical potential of the species i, and Γ_i is the surface (Gibbs) excess of the species i defined as

$$\Gamma_i = N_i^S / A \qquad (3.1.3).$$

Here A is the surface area and N_i^S is the number of moles of a species i in the interfacial region S. Figure 3.1.1 demonstrates that

$$N_i^S = \int N_i(x)dx - (N_i^\alpha + N_i^\beta) \qquad (3.1.4)$$

The species i can be either in excess or in deficit at the interface, resulting in $\Gamma_i > 0$ or $\Gamma_i < 0$, respectively. The substances which are attracted to the interfaces are called surfactants. Consistently with the Gibbs adsorption isotherm, they decrease the surface energy γ because their Gibbs excess is positive.

3.1.2. Insoluble Surfactants

Insoluble surfactants have negligible bulk concentration, hence they cannot be described by the Gibbs equation. When spread at the interface, however, they lower the surface energy similarly to soluble surfactants. The change of the surface energy upon adsorption of insoluble surfactants is called the surface pressure

$$\pi = \gamma_W - \gamma_{GS} \qquad (3.1.5),$$

where γ_W and γ_{GS} are the surface energies at the GS interface in the absence (pure water) and in the presence of surfactant molecules, respectively. Insoluble surfactants can be deposited on the GS interface in a form of a small crystal or a droplet of a pure substance. However, some materials spread very slowly from condensed phases. Therefore, another deposition method is preferred in which a surfactant is first dissolved in a volatile water-immiscible solvent. When deposited, this surfactant solution stays at the interface in the form of a lens releasing the molecules quickly until the whole surface is covered with a monolayer. After evaporation of the solvent, the excess of the material remains in the form of a crystal or a lens of liquid in equilibrium with the monolayer. The driving force of spreading (spreading coefficient) is given by the following equation:

$$SC = dG / dA = \gamma_{GS} - \gamma_{GL} - \gamma_{SL} \qquad (3.1.6),$$

where γ_{GS}, γ_{GL} and γ_{SL} are the interfacial tensions for the gas-solution, the gas-organic liquid lens and the solution-organic liquid lens interfaces, respectively. At equilibrium $SC = 0$, and substitution of equation (3.1.5) into equation (3.1.6) yields the expression for the equilibrium spreading pressure (ESP):

$$\pi_E = \gamma_W - \gamma_{GL} - \gamma_{SL} \qquad (3.1.7)$$

Because the ESP is related to the surface energy, it remains constant at a constant temperature.

3.1.3. Transfer of Insoluble Surfactants

Transfer of insoluble surfactants takes place when a solid substrate is brought into contact with the film spread at the GS interface. The driving force for the transfer is the

difference between π at the GS interface and π at the substrate surface. Hence, to reach the highest coverage, π at the GS interface must be kept as high as possible, which is achieved at the ESP. Two methods of transfer of insoluble surfactant films are presently used: the Langmuir-Schaefer (horizontal touching) method [7], described in detail in Chapter 4 and the Langmuir-Blodgett method [8][9]. The principle of the Langmuir- Blodgett technique is that a (solid) substrate is moved through the surfactant-covered GS interface at an angle which is 90^0 with respect to the solution surface. It was found that efficient transfer of the surfactant film takes place when the contact angle between the advancing side of the substrate and the film-covered liquid surface is acute. The first layer of the film is transferred when a hydrophobic substrate is moved downwards and a hydrophilic substrate is moved upwards.

3.2. Electrified Interfaces

It is practically impossible to have two materials in contact without a separation of charge between the neighbouring phases, and consequently without a potential difference across the interface that is formed. Thus, most interfaces are electrified and their electrical properties have a pronounced influence on the interfacial processes.

3.2.1. Thermodynamics at an Electrified Interface

The electrical double layer theory [10] requires that the interface is in electrostatic equilibrium. This condition is applicable only to the ideally polarizable electrode (IPE), the electrode characterized by a lack of charge transfer across the interface. Mercury is an electrode material that not only displays the IPE behaviour in a wide region of applied

potentials but also allows for a direct measurement of the surface energy (surface tension). For these reasons, the mercury electrode has been widely used in electrochemical research.

In the middle of the nineteenth century, Lippman constructed a simple apparatus that measured the surface tension at the Hg capillary electrode as a function of potential and derived the famous equation which bears his name:

$$(\partial\gamma / \partial E)_{T,p,\mu} = -\sigma_M \qquad (3.2.1)$$

where γ is the interfacial tension at the mercury electrode, E is the potential and σ_M is the charge density at the electrode.

3.2.2. The Electrocapillary Equation

The electrocapillary equation [10][11] was derived for the mercury-electrolyte interface using the Gibbs model of an interface shown in Figure 3.1.1 and is essentially the extension of the Gibbs adsorption isotherm (equation (3.1.2)) for an electrified interface:

$$-d\gamma = sdT - Vdp + \sigma_M\, dE + \Sigma_i\, \Gamma_i\, d\mu_i \qquad (3.2.2)$$

where s, T, V and p are the entropy, temperature, volume and pressure in the electrochemical cell, respectively, while Γ_i and μ_i are the Gibbs excess and the chemical potential of the interfacial species i, respectively. If all the variables except γ and E are kept constant, the Lippman equation is obtained from equation (3.2.2). Equation (3.2.2) is an exact differential and thus, by cross-differentiation one can derive important expressions known as the Esin-Markov coefficient and the electrosorption valency. The Esin-Markov coefficient

$$(\partial E / \partial \mu_j)_{T,p,\sigma M,} = -(\partial \Gamma / \partial \sigma_M)_{T,p,\mu} \qquad (3.2.3)$$

is used to test the presence of specific adsorption at the interface and the electrosorption

valency

$$(\partial\sigma_M/\partial\Gamma_L)_{T,p,E,} = -(\partial\mu_L/\partial E)_{T,p,\Gamma} \qquad (3.2.4)$$

indicates the amount of charge transferred to the interface when a neutral or ionic species is adsorbed at a constant electrode potential. It is useful to note, however, that in the Gibbs model of an interface (see Figure 3.1.1), the dividing plane x_0 can be placed at any location within the interfacial region *S*, hence the exact location of the charge flowing to the interface per one adsorbed ion or molecule remains indeterminate.

The surface energy of a solid electrode is not a unique function of the surface area but depends on the path in which it was created. Specifically, the energies corresponding to the work of formation of a unit area by cleavage, called the superficial work γ, and by elastic stretching of the crystal, called the surface stress τ, are different. The Shuttleworth equation describes the relation between these two quantities

$$\tau = \gamma + \partial\gamma/\partial\varepsilon_e \qquad (3.2.5)$$

where ε_e is the elastic surface strain. Thus, the electrocapillary equation for a solid electrode should be presented as

$$-d\gamma = sdT - Vdp + \sigma_M\, dE + \Sigma_i\, \Gamma_i\, d\mu_i + (\gamma-\tau)d\varepsilon_e \qquad (3.2.6).$$

It was recently demonstrated [12] that the additional term in equation (3.2.6) has a very small value and can be neglected, allowing direct application of equation (3.2.2) as well as other relations derived from it for electrochemical studies carried out using solid electrodes.

3.2.3. Adsorption of Neutral Organic Molecules onto an Electrified Interface.

The electrocapillary equation has been widely used to study molecular adsorption at

a mercury electrode. The liquid state of the electrode allows for direct determination of the surface energy, and the Gibbs excess Γ_i can be calculated using equation (3.2.2)

$$\Gamma_i = (\partial\gamma/\partial\mu_i)_{T,p,E,\mu_{j\neq i}} \qquad (3.2.7).$$

The measurement of the surface tension is tedious and is frequently abandoned in favour of techniques which rely on measurements of charge density and differential capacity (C) of the interface. Because at constant temperature and pressure

$$\sigma_M = -\partial\gamma/\partial E \quad \text{and} \quad C = \partial\sigma_M/\partial E \qquad (3.2.8)$$

the surface energy can be calculated by integration of the charge density and the differential capacity according to

$$\gamma = \int_{E'}^{E} \sigma_M dE + \gamma(E') = \int_{E'}^{E}\int CdE^2 + \gamma(E') \qquad (3.2.9)$$

where E^* is the potential at which the surface tension $\gamma(E^*)$ is known. Using equations (3.2.7) and (3.2.9) the Gibbs excess of the species i can be found.

The differential capacity of the interface can be represented as follows [13]

$$C = \left(\frac{\partial\sigma_M}{\partial E}\right)_{\mu_L} = \left(\frac{\partial\sigma_M}{\partial E}\right)_{\Theta} + \left(\frac{\partial\sigma_M}{\partial\Theta}\right)_E \times \left(\frac{\partial\Theta}{\partial E}\right)_{\mu_L} = C_{true} + C_{pseudo} \qquad (3.2.10)$$

where Θ is the degree of coverage of the electrode surface with an adsorbate and μ_L is the chemical potential of the neutral organic species L in the electrolyte bulk. The first term in equation (3.2.10) is called the true capacity and the second term is called the pseudo-capacity.

The differential capacity is usually determined from the measurement of the electrode impedance when a small amplitude alternating voltage is applied to the electrode (details of this technique are given in Chapter 4). It has been shown that C_{pseudo} has an equilibrium value at zero frequency and drops to zero at infinite frequency. Measurements at sub-Hertz frequencies are difficult because of increased levels of electromagnetic noise in this frequency range. To overcome this problem the differential capacity is measured at several frequencies and then extrapolated to zero frequency to give the equilibrium values. Another option is to measure the charge density at the electrode using chronocoulometry [14] and then to calculate γ using the back integration technique described below.

3.2.4. The Back Integration Technique

One advantage of the mercury electrode is that the value of the interfacial tension at the electrode potential E^* (the integration constant in equation (3.2.9)) can be easily determined. Measurements of the surface energies for solid electrodes are much more difficult and as a rule the integration constant in equation (3.2.9) is not known. However, if the value of E^* is chosen such that the neutral or ionic species are desorbed from the electrode surface at this potential, the surface energy of the electrode in the pure electrolyte solution is equal to the surface energy of the electrode in the electrolyte that contains the adsorbate molecules. Hence, the surface pressure at the metal/solution interface π_{MS} can be calculated according to [15]:

$$\pi_{MS}(E) = \gamma(E)_{\theta=0} - \gamma(E)_{\theta} = \int_{E'}^{E} \sigma_M(\theta)\, dE - \int_{E'}^{E} \sigma_M(\theta=0)\, dE \qquad (3.2.11),$$

where θ is the coverage. The potential E^* is chosen so that $\theta(E^*) = 0$ and, therefore, the integration constants $\gamma(E^*)$ in equation (3.2.9) are the same and thus, disappear from equation (3.2.11).

The surface excess can be calculated using

$$\Gamma_i = (\partial\pi/\partial\mu_i)_{T,p,E,\mu_{j\neq i}} \qquad (3.2.12).$$

At low coverages of the electrode surface, the adsorption of neutral organic molecules can be described by the Henry isotherm

$$\pi = RT\,\Gamma_{max}\,\beta_H\,X_{bulk} \qquad (3.2.13)$$

where Γ_{max} is the limiting surface excess, β_H is the adsorption coefficient and X_{bulk} is the mole fraction of adsorbate in the electrolyte solution. The free energy of adsorption ΔG^0_{ads} can be calculated from β_H using the following relation

$$\Delta G^0_{ads} = -RT \ln \beta_H \qquad (3.2.14)$$

The standard state is unit mole fraction of adsorbate and unit coverage of the surface by ideal inert adsorbate molecules.

3.3. Fourier Transform Infrared Spectrometer

Infrared spectroscopy is nowadays one of the most popular tools to study organic compounds [16]. The first infrared instruments utilized prisms and diffraction gratings as monochromators. Beginning in the 1970s, dispersive spectrometers have been almost completely replaced by Fourier transform infrared (FTIR) instruments. The reason for such popularity stems from the following three advantages of FTIR spectrometers over the

dispersive instruments: (i) Fellgett's advantage,- reduction of measurement time due to simultaneous acquisition of the whole spectrum; (ii) Jacquinot's advantage,- increase in the optical throughput of the spectrometer due to absence of the slits; (iii) Conne's advantage,- superior accuracy of the acquired spectra due to the use of a subsidiary laser.

To fully benefit from these advantages of FTIR, full optimization of the optical bench is necessary, which requires a thorough understanding of the basic principles of its work. A description of the Michelson interferometer, which is the principal part of the FTIR spectrometer, is given below followed by a review of the most important concepts of FTIR spectroscopy.

3.3.1 Michelson Interferometer

The relationship between the frequency of electromagnetic radiation ν (Hz), its velocity (in vacuum) c (m s^{-1}) and wavenumber $\bar{\nu}$ (cm^{-1}) is given by equation

$$\nu = 100c\bar{\nu} \qquad (3.3.1).$$

In the mid infrared, the frequency of radiation that has $\bar{\nu}$ = 2000 cm^{-1} is equal to 6×10^{13} Hz. Such a high frequency is far beyond the detection capability of infrared detectors. To convert the high frequency electromagnetic radiation to a lower frequency signal that can be detected, the infrared beam is modulated using a Michelson interferometer. Figure 3.3.1 shows the diagram of the device. It consists of two mirrors and a beamsplitter. One of the mirrors has a fixed position and the other is moved between two extremes with a constant velocity. The collimated radiation that arrives from the broad band infrared source (I_i) is incident on the beamsplitter that divides it into two beams (I_{rI} and I_{tI}) of equal intensity. These two beams

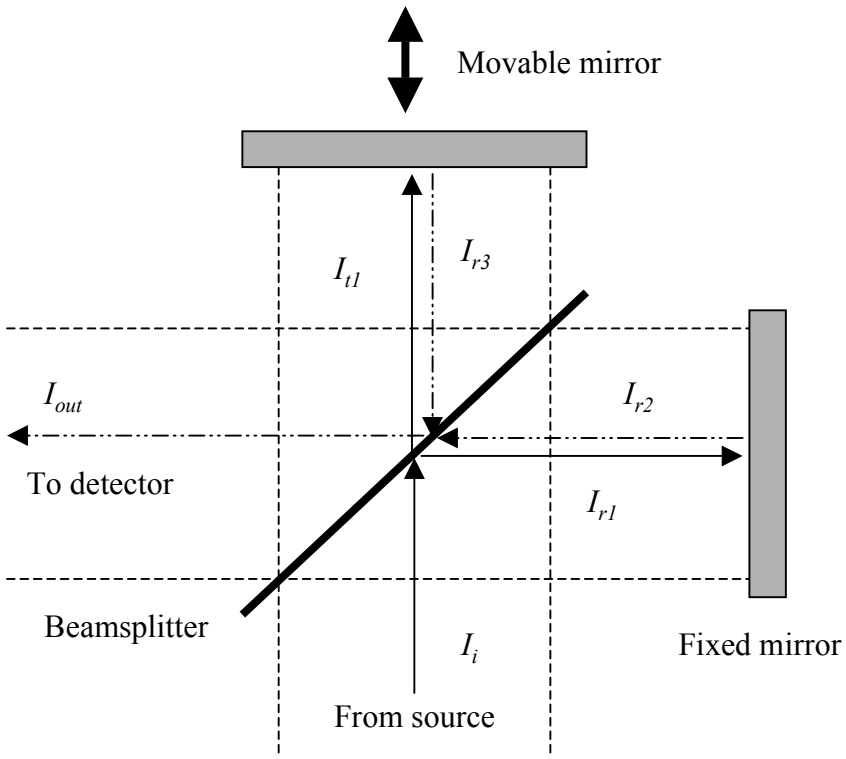

Figure 3.3.1. Schematic diagram of a Michelson interferometer.

are reflected from the fixed and the moving mirror yielding, respectively, I_{r2} and I_{r3} which recombine at the beamsplitter yielding the beam I_{out} that is directed to the sample and the detector. The intensity of the beam that reaches the detector is measured simultaneously with the measurement of the position of the movable mirror.

The modulation of the incident beam imposed by the Michelson interferometer significantly reduces the frequency of the detected signal $f_{\bar{\nu}}$ while preserving its proportionality to the wavenumber $\bar{\nu}$ of the incident beam:

$$f_{\bar{\nu}} = 2V_M\bar{\nu} \qquad (3.3.2),$$

where V_M denotes the velocity of the moving mirror (cm s^{-1}). Indeed, if the velocity of the moving mirror is 0.5 cm s^{-1} and the wavenumber of the incident beam is 2000 cm^{-1} , the frequency of the corresponding signal at the detector is only 2 kHz. Such signals are easy to monitor by conventional detectors. To understand how the signal at the detector, called an interferogram, is transformed to the corresponding spectrum, one needs to define a quantity called retardation and denoted as δ_r. Retardation attains the value that is equal to twice the difference between the two distances: (i) the distance from the beamsplitter to the stationary mirror and (ii) the distance from the beamsplitter to the moving mirror. When $\delta_r = 0$, the interferogram displays a maximum in intensity, due to constructive interference of all the frequency components of a broad band incident beam. When the retardation deviates from zero, only part of the incident beam interferes constructively and the interferogram intensity decreases. In general, the intensity of an interferogram $I(\delta_r)$ is a function of the moving mirror retardation δ_r and the wavenumber $\bar{\nu}$ of the incident radiation. It is given by equation [16]

$$I(\delta_r) = \int_0^{+\infty} B(\bar{\nu}) \cos(2\pi \bar{\nu} \delta_r) d\bar{\nu} \qquad (3.3.3),$$

where $B(\bar{\nu})$ is the intensity of the source (as a function of its wavenumber $\bar{\nu}$), corrected for the distortions imposed by the beamsplitter and the detector. Fourier transformation of equation (3.3.3) yields the spectrum:

$$B(\bar{\nu}) = 2\int_0^{+\infty} I(\delta_r) \cos(2\pi \bar{\nu} \delta_r) d\delta_r \qquad (3.3.4).$$

Since the path of the movable mirror from the point where $\delta_r = 0$ to the point where δ_r is at the maximum is finite, the experimental interferogram deviates from the dependence defined by equation (3.3.3). This deviation is diminished by combining the experimental interferogram with a mathematical function that reduces the effect of truncation of an interferogram at its extremes. Such a procedure is called apodization. The other problem that arises from truncation of an interferogram is that its symmetry around the point where $\delta_r = 0$ becomes distorted. This problem is especially acute when several interferograms are to be averaged. Fortunately, this complication can also be removed mathematically when a procedure called phase correction is executed.

The resolution $\Delta\bar{\nu}$ of the FTIR instrument is limited by the maximum retardation δ_{max} according to equation

$$\Delta\bar{\nu} = \left(2\delta_{\max}\right)^{-1} \qquad (3.3.5)$$

In addition, the resolution depends on the degree of the incident beam collimation, hence often smaller apertures, that assist in better beam collimation, are used for high resolution applications (2 cm^{-1} and higher).

The signal-to-noise ratio (*S/N*) of an FTIR spectrum is given by equation (3.3.6) (adapted from [16])

$$S/N \propto \eta \Theta_{IR} \Delta\bar{\nu} \sqrt{t} \qquad (3.3.6),$$

where η is the overall efficiency of the optical bench, Θ_{IR} is the optical throughput of the setup for the infrared beam, $\Delta\bar{\nu}$ is the resolution and t is the total time needed to complete the measurement. Relationships between the entities of equation (3.3.6) are also known as "trading rules" of FTIR spectroscopy [16]. The most important two rules are given below:

1. An increase of the total interval of experiment time by a factor of two results in an improvement of the *S/N* by a factor of $\sqrt{2}$. The experiment time can be increased twice either by averaging of two spectra (interferograms) or by acquiring a spectrum at a reduced (by a factor of two) mirror velocity.

2. Twofold enhancement of spectral resolution (eg. from 8 cm^{-1} to 4 cm^{-1}) at a constant mirror velocity and measurement time, degrades the *S/N* by a factor of two. Thus, to compensate for the degradation in *S/N*, the measurement time must be increased fourfold.

It is obvious that a better resolution is achieved at a very high cost due to reduction of the *S/N*. This is why optimal performance is achieved when the resolution is set to be equal or slightly smaller than the width of the most narrow feature on the collected spectrum.

To avoid a loss of the spectral information and a reduction of the *S/N* due to the

folding of high frequency noise onto the low frequency signal, the interferograms must be sampled such that the resulting spectra have at least two data points per resolution element. More narrow data spacing results in better quality spectra, however, a larger size of memory is required to store the spectra and longer computation times to process the interferograms. Interpolation is often used to fill-in the missing data points when more smooth spectra are desired. Usually it is done during Fourier transformation in a procedure called "zero-filling".

Fourier transformation is a procedure performed by a computer. This is why the analog signal from the detector must be digitized. To avoid the instrumental (digitization) noise the signal from the detector is amplified until it fills the dynamic range of the analog-to-digital converter such that the random noise at the detector is at least two times as large as the resolution of the converter.

The basic principles of the FTIR spectrometer outlined in this section were used in this project for acquisition of spectra. Specific settings that were used will be described in Chapter 4.

3.4. Physical Optics of a Stratified Medium

Quantitative analysis of experimental information determined using reflection absorption spectroscopy requires complete understanding of the physics of reflection and refraction of electromagnetic radiation. Reflection of light in a thin layer cell can be described theoretically using Fresnel equations in their analytical form. This approach provides a certain degree of insight into the physics of light reflection. However, the complexity of the equations increases significantly when stratified media consist of more then 3 layers [17]. The other

approach, first derived by Abelés [18][19], utilizes matrix algebra. It can be used to characterize reflection and refraction of light at unlimited number of phases that comprise a stratified medium using an elegant set of equations. Both methods are described in detail in an excellent paper by Hansen [20]. This paper is extensively cited by those who apply reflection absorption spectroscopy and the relationships presented below were adapted with minor changes from this source. (It should be noted, however, that there are two typing errors in the paper. Equations (90) and (100) on page 388 of reference [24] should have a positive sign in front of p_1 and q_1, respectively.)

The next section is a brief introduction to the reflection, refraction and absorption of electromagnetic radiation at a simple two-phase boundary. This introduction is written using material from an excellent book by Hecht and Zajac [21] as well as a paper by Hansen [20]. The section that follows will present Fresnel equations in the matrix form that describe the reflection and refraction of electromagnetic radiation at multilayer stratified media [20].

3.4.1. Reflection, Refraction and Absorption of Electromagnetic Radiation at a Simple Two-Phase Boundary

Infrared radiation is a transverse, electromagnetic wave that is characterized by the orthogonal electric and magnetic fields oscillating in the directions perpendicular to the direction of the wave propagation. Figure 3.4.1 shows a graphical depiction of an electromagnetic wave with the electric field oriented along the *y* axis. Such a wave with a well defined orientation of the electric and magnetic fields describes linearly polarized radiation and it is obvious from Figure 3.4.1 that non-polarized radiation can be regarded as composed

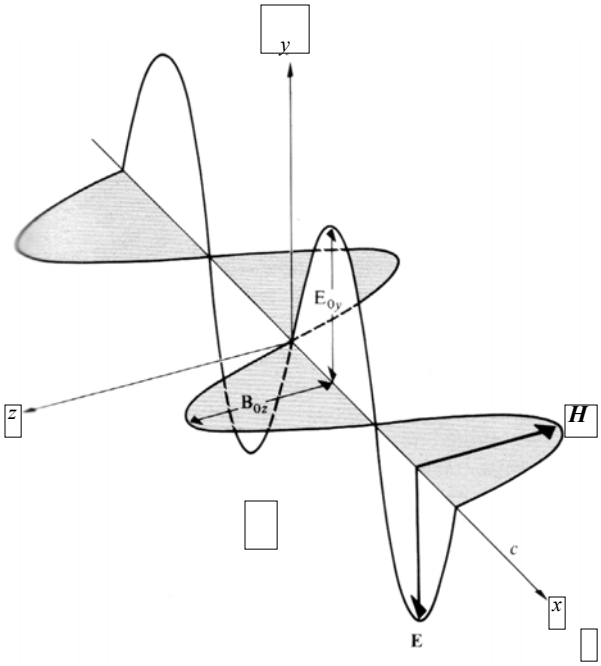

Figure 3.4.1. Direction of electric and magnetic fields with respect to the propagation direction of an electromagnetic wave.
Taken from [21].

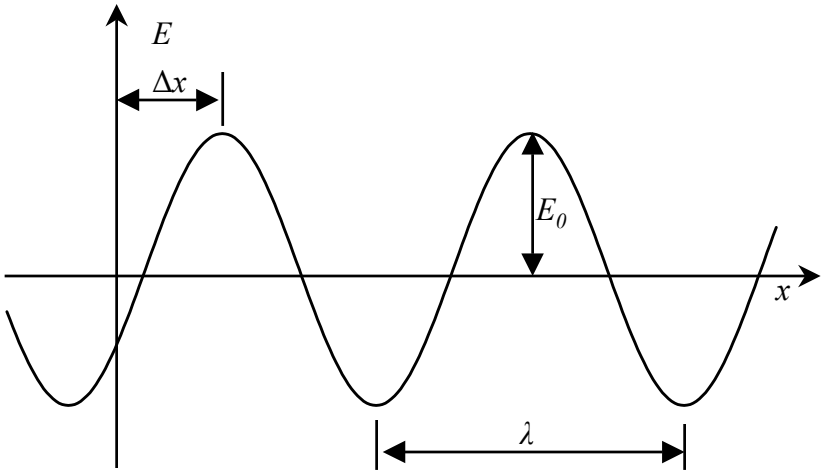

Figure 3.4.2. Spatial dependence of the electric field strength for an electromagnetic wave propagating along the *x* axis.

of two orthogonal linearly polarized components. The energy of the magnetic field is exactly equal to the energy of the electric field of an electromagnetic wave, hence it is convenient to consider only one (usually electric) field.

A planar electromagnetic wave (*i.e.*, the wave with a flat wavefront) that propagates along the *x* axis in vacuum can be described by a wave equation that relates the electric field strength *E* at an arbitrary moment of time *t* and a distance *x* from the origin:

$$E = E_0 \cos(\frac{2\pi}{\lambda} x + \delta - \omega t) = \mathrm{Re}\left(E_0 \exp\left[-i\left(\frac{2\pi}{\lambda} x + \delta - \omega t \right) \right] \right) \quad (3.4.1),$$

where E_0, denotes the amplitude of the electric field strength and λ, ω and δ are, respectively, the wavelength, the angular frequency and the phase shift. The last two quantities are, respectively, related to the frequency (number of waves per unit time) ν and the displacement of the electric field strength amplitude with respect to the coordinate origin Δx in the following fashion:

$$\omega = 2\pi\nu \qquad \text{and} \qquad \delta = \Delta x \cdot 2\pi / \lambda \qquad (3.4.2)$$

Figure 3.4.2 shows the spatial dependence of the electric field strength for the wave described by equation (3.4.1) and indicates its major parameters described in equation (3.4.2).

In a medium the wave equation (3.4.1) becomes

$$E = \mathrm{Re}\left\{ E_0 \exp\left[-i\left(\frac{2\pi n}{\lambda} x + \delta - \omega t \right) \right] \exp\left(-\frac{2\pi k}{\lambda} x \right) \right\} \quad (3.4.3)$$

or

$$E = \mathrm{Re}\left\{ E_0 \exp\left[-i\left(\frac{2\pi\hat{n}}{\lambda} x + \delta - \omega t \right) \right] \right\} \qquad (3.4.4),$$

where *n* and *k* denote the refractive index and attenuation coefficient of a medium which are components of the complex refractive index $\hat{n}$ of a material:

$$\hat{n} = n + ik \qquad (3.4.5).$$

It is important to note that there are two conventions about the sign of the imaginary part of $\hat{n}$, and the convention that regards k as a positive number is used throughout this thesis.

When infrared radiation is absorbed, the signal at a detector terminal is proportional to the energy dissipated per unit volume per unit time at the detector element. The time averaged value of this energy is called the intensity *I*. For nonmagnetic materials it is related to the amplitude of the electric field of the incident radiation in the following way:

$$I = nk\nu \cdot \left\langle E_0^2 \right\rangle \qquad (3.4.6),$$

where ν and $\left\langle E_0^2 \right\rangle = E_0^2 / 2$ are the frequency and the mean squared electric field strength (MSEFS) of the radiation incident on the detector, respectively.

When the electromagnetic radiation is incident at a boundary between two phases, part of the beam is reflected and part of it is refracted into the second medium. Figure 3.4.3 shows the plane of incidence profile of a boundary formed by a transparent and an absorbing phase. The coordinate system has the *x* and *z* axes in the plane of incidence and the *y* axis normal to

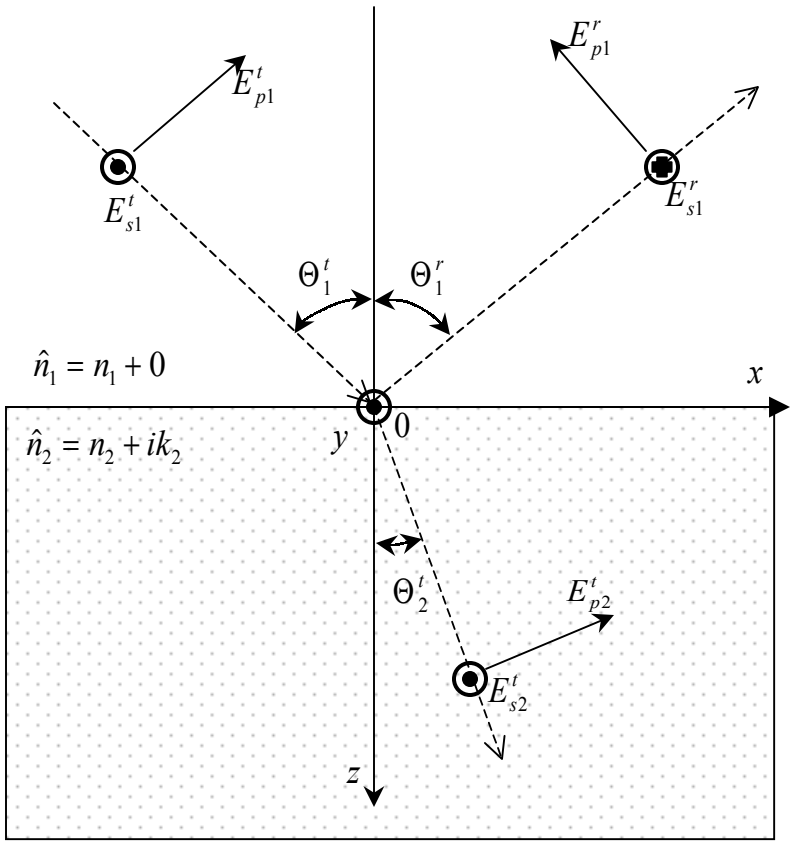

Figure 3.4.3. Reflection and refraction of electromagnetic radiation at the boundary between a transparent and an absorbing medium.
Dashed lines denote the direction of propagation of radiation.
Arrows indicate the electric field vector of p-polarized light which lies in the plane of incidence.
Symbols ⊙ and ⊕ indicate the advancing and retreating electric field vectors of s-polarized radiation (which is perpendicular to the plane of incidence).
In addition, symbol ⊙ shows the (advancing) direction of the *y* coordinate axis.

the plane of incidence, as shown in the figure. The propagation directions of the electromagnetic radiation are indicated by dashed lines. In accordance with the law of reflection

$$\Theta_1^r = \Theta_1^t \qquad (3.4.7)$$

and following Snell's law of refraction

$$n_2 \sin\Theta_2^t = n_1 \sin\Theta_1^t \qquad (3.4.8),$$

where n_j denotes the refractive index of a phase j. Equations (3.4.7) and (3.4.8) were discovered empirically, however they can be derived starting from Maxwell's equations for a linear isotropic substance and using the conditions of continuity of the electric and magnetic field components tangential to the phase boundary.

Fresnel equations (which relate the electric and magnetic field strength amplitudes of the incident, reflected and refracted waves) can also be derived from Maxwell's equations by applying the mentioned boundary conditions. Figure 3.4.3 shows that the incident beam can be envisaged as composed of two linearly polarized orthogonal components. These components, called p- and s-polarized components, are characterized by the directions of the electric field vectors in the plane of incidence and perpendicular to it, respectively. (The plane of incidence is the plane that contains the incident and reflected beams. Directions of p- and s-polarized beams with respect to the reflecting surface are shown in Figure 2.3.) It can be shown that for a plane boundary between two non-magnetic isotropic phases of infinite thickness, schematically depicted in Figure 3.4.3, the Fresnel amplitude reflection (r) and transmission (t) coefficients for s- and p-polarized light are given by the following equations:

$$r_s = \frac{E_{y1}^r}{E_{y1}^t} = \frac{\xi_1 - \xi_2}{\xi_1 + \xi_2} \quad (3.4.9) \qquad , \qquad t_s = \frac{E_{y2}^t}{E_{y1}^t} = \frac{2\xi_1}{\xi_1 + \xi_2} \quad (3.4.10),$$

$$r_p = \frac{H_{y1}^r}{H_{y1}^t} = \frac{\hat{n}_2^2\xi_1 - \hat{n}_1^2\xi_2}{\hat{n}_2^2\xi_1 + \hat{n}_1^2\xi_2} \quad (3.4.11) \text{ and } \quad t_p = \frac{H_{y2}^t}{H_{y1}^t} = \frac{2\hat{n}_2^2\xi_1}{\hat{n}_2^2\xi_1 + \hat{n}_1^2\xi_2} \quad (3.4.12),$$

where $$\xi_j = \hat{n}_j \cos\Theta_j^t = \sqrt{\hat{n}_j^2 - n_1^2 \sin^2 \Theta_1^t} = \mathrm{Re}\,\xi_j + i\,\mathrm{Im}\,\xi_j \quad (3.4.13),$$

and the symbols E_y and H_y denote the amplitudes of the electric and magnetic fields, oriented along the *y* axis, for s- and p-polarized radiation, respectively. Note that ξ_j can be calculated from experimentally available optical constants of the corresponding phase $\hat{n}_j$ and the angle of incidence Θ_1^t. Due to the choice of the sign convention for *k*, both $\mathrm{Re}(\xi_j)$ and $\mathrm{Im}(\xi_j)$ must always be taken as positive numbers when calculating the square root of the complex expression in equation (3.4.13).

The reflectance (or reflectivity) (*R*) and transmittance (*T*) are, respectively, given by the intensities of the reflected and transmitted radiation normalized by the intensity of the incident radiation. They are related to the Fresnel amplitude reflection and transmission coefficients in the following way:

$$R_{s,p} = \frac{I^r_{s,p1}}{I^t_{s,p1}} = \left|r_{s,p}\right|^2 \quad (3.4.14), \quad T_s = \frac{I^t_{s2}}{I^t_{s1}} = \frac{\mathrm{Re}(\xi_2)}{\xi_1}\left|t_s\right|^2 \quad (3.4.15)$$

and

$$T_p = \frac{\mathrm{Re}\left(\xi_2 / \hat{n}_2^2\right)}{\xi_1 / \hat{n}_1^2}\left|t_p\right|^2 \qquad (3.4.16).$$

Finally, the phase shift δ can also be determined from the amplitude coefficients using the following relationships:

$$\delta^r_{s,p} = Arg(r_{s,p}) \text{ and } \delta^t_{s,p} = Arg(t_{s,p}) \quad (3.4.17).$$

(Recall that argument of a complex number is given by $Arg(\hat{x}) = \tan^{-1}[\mathrm{Im}(x) / \mathrm{Re}(x)]$).

The above expressions denote the Fresnel equations in analytical form for a simple two-phase boundary. Below, the matrix algebra approach is presented that is used to determine the Fresnel coefficients of a stratified medium composed of a large number of phases.

3.4.2. Fresnel Equations in the Matrix Form

When electrochemical *in-situ* RAS experiments are performed, the analyte film is deposited on the metal surface which is then immersed in the electrolyte solution and pressed against the cell window, made of a material that is transparent for the infrared light. Such a system consists of four layers. The first medium is an infrared transparent window ($k_1 = 0$) and

the other three phases that represent electrolyte, an organic film and a metal electrode, respectively, may absorb light. The optical properties of a phase *j* are defined by its complex refractive index $\hat{n}_j$. The coordinate system shown in Figure 3.4.3, which has its origin at the interface formed by the first two phases (window and electrolyte), is also used in the matrix approach. The Fresnel equations presented below were derived assuming that the phases are nonmagnetic, isotropic, homogeneous and infinitely parallel with perfectly sharp boundaries. The first and the last phases are considered to be infinitely thick and all the intermediate phases *j* are characterized by the thicknesses h_j. The incident beam was regarded to be a planar wave of wavelength λ directed at an angle Θ_1^t with respect to the *z* axis which coincides with the normal to the planes of the phase boundaries.

For *N* phases with *N*-1 boundaries, one can define *N* -1 matrices M_j that fully characterize the electromagnetic radiation at each phase boundary *k*. These matrices are called characteristic matrices and are given by equations (3.4.18) and (3.4.19) for s- and for p-polarized electromagnetic radiation, respectively:

$$M_j^s = \begin{bmatrix} \cos\beta_j & \frac{-i}{\xi_j}\sin\beta_j \\ -i\xi_j \sin\beta_j & \cos\beta_j \end{bmatrix} \quad (3.4.18),$$

$$M_j^p = \begin{bmatrix} \cos\beta_j & \frac{-i\hat{n}_j^2}{\xi_j}\sin\beta_j \\ -i\frac{\xi}{\hat{n}_j^2}{}_j \sin\beta_j & \cos\beta_j \end{bmatrix} \quad (3.4.19),$$

where ξ_j is defined in equation (3.4.13) and

$$\beta_j = \frac{2\pi\xi_j h_j}{\lambda} \qquad (3.4.20),$$

where λ is the wavelength of the incident radiation and h_j is the thickness of a layer j. The characteristic matrix of the whole stratified medium is obtained by multiplication of individual characteristic matrices of all its constituents that are sandwiched between the first and the last phase

$$M = \prod_{j=2}^{j=N-1} M_j \qquad (3.4.21).$$

It relates the tangential (with respect to the propagation direction) fields U_1 and V_1 at the first interface where $z = z_1 = 0$ to those at the last interface U_{N-1} and V_{N-1} where $z = z_{N-1}$

$$\begin{bmatrix} U_1 \\ V_1 \end{bmatrix} = M \begin{bmatrix} U_{N-1} \\ V_{N-1} \end{bmatrix} \qquad (3.4.22).$$

For s-polarized radiation $U_1 = E_y$ and $V_1 = H_x$ while for p-polarized radiation $U_1 = H_y$ and $V_1 = E_x$, where E and H symbolize the amplitudes of electric and magnetic fields, respectively. Analogous relationships hold not only for the first but also for the other phase boundaries.

The amplitude reflection and transmission coefficients for the whole stack can be extracted from the characteristic matrix of the whole stratified medium using the following relationships:

$$r_{Es} = \frac{E_{y1}^r}{E_{y1}^t} = \frac{(m_{11} + m_{12}\xi_N)\xi_1 - (m_{21} + m_{22}\xi_N)}{(m_{11} + m_{12}\xi_N)\xi_1 + (m_{21} + m_{22}\xi_N)} \qquad (3.4.23),$$

$$t_{Es} = \frac{E_{yN}^t}{E_{y1}^t} = \frac{2\xi_1}{(m_{11} + m_{12}\xi_N)\xi_1 + (m_{21} + m_{22}\xi_N)} \qquad (3.4.24),$$

$$r_{Ep} = r_{Hp} = \frac{H_{y1}^r}{H_{y1}^t} = \frac{(m_{11} + m_{12}\,\xi_N/\hat{n}_N^2)\,\xi_1/\hat{n}_1^2 - (m_{21} + m_{22}\,\xi_N/\hat{n}_N^2)}{(m_{11} + m_{12}\,\xi_N/\hat{n}_N^2)\,\xi_1/\hat{n}_1^2 + (m_{21} + m_{22}\,\xi_N/\hat{n}_N^2)} \qquad (3.4.25),$$

$$t_{Hp} = \frac{H_{y1}^{r}}{H_{y1}^{t}} = \frac{2\,\xi_1 / \hat{n}_1^2}{(m_{11} + m_{12}\,\xi_N / \hat{n}_N^2)\,\xi_1 / \hat{n}_1^2 + (m_{21} + m_{22}\,\xi_N / \hat{n}_N^2)} \qquad (3.4.26),$$

$$t_{Ep} = \frac{E_p^t}{E_p^t} = \frac{n_1}{\hat{n}_N} t_{Hp} \qquad (3.4.27),$$

where m_{jk} are the elements of the 2×2 characteristic matrix M of the whole stack.

Reflectance of the whole assembly for s- and p-polarized light can be calculated from the corresponding amplitude reflection coefficients using equation (3.4.14) while transmittance of the whole stack for s- and p-polarized light can determined from the corresponding amplitude transmission coefficients using equations (3.4.15) and (3.4.16), respectively.

The matrix approach can be employed to model the reflectance of an experimental infrared cell during reflection absorption spectroscopy. Indeed, the equations that describe the three-phase system can be used to simulate the thin layer cell that contains the organic film in the desorbed state and the relationship governing the four-phase system can be utilized to model the cell when the film is adsorbed at the metal electrode. $\Delta R / R$ spectrum can be calculated using the reflectances of a thin layer cell composed of three and four layers in the following way [22]:

$$\frac{\Delta R}{R} = \frac{R_{1234}}{R_{123}} - 1 \qquad (3.4.28).$$

A similar approach can be used to simulate SNIFTIRS and PM FTIR RAS spectra that are needed for quantitative determination of the orientation of molecules in ultrathin films of organic molecules at the metal electrode.

3.4.3. Mean Squared Electric Field Strength

Quantitative analysis of the orientation of organic molecules at the metal electrode requires precise knowledge of the mean squared electric field strength (MSEFS) at the metal surface as well as in the electrolyte bulk. The matrix approach allows one to calculate the field strength at an arbitrary location z within the stratified medium. Before presenting the expressions that are used for calculation of the MSEFS, the concept of the reciprocal matrix should be recalled. A matrix N is reciprocal to M if $NM = I$, I being the unit matrix. If both sides of equation (3.4.22) are multiplied by N, one can obtain

$$\begin{bmatrix} U_{N-1} \\ V_{N-1} \end{bmatrix} = N \begin{bmatrix} U_1 \\ V_1 \end{bmatrix} \qquad (3.4.29).$$

This equation relates the field amplitudes at the N-1$^{\underline{\text{th}}}$ phase boundary to the field amplitudes at the first phase boundary, given by the amplitude reflection and transmission coefficients (equations (3.4.23)-(3.4.27)). A similar approach can be utilized to find the amplitude of electric field at any point within the stratified medium.

$$\begin{bmatrix} U_k(z) \\ V_k(z) \end{bmatrix} = N_k(z) \prod_{j=k-1}^{2} N_j \begin{bmatrix} U_1 \\ V_1 \end{bmatrix} \qquad (3.4.30),$$

where $U_k(z)$ and $V_k(z)$ denote the tangential fields at an arbitrary point within the stratified medium. Individual N_j for s- and p-polarized radiation can be determined using equations (3.4.18) and (3.4.19), respectively, if the negative sign of the elements m_{12} and m_{21} of the corresponding matrices is changed to positive. To use equation (3.4.30) one needs to define the explicit expressions of the other terms of this equation that are presented below.

For s-polarized light:

$$\begin{bmatrix} U_1 \\ V_1 \end{bmatrix} = \begin{bmatrix} E_{y1} \\ H_{x1} \end{bmatrix} = \begin{bmatrix} E_{y1}^t + E_{y1}^r \\ H_{x1}^t + H_{x1}^r \end{bmatrix} = \begin{bmatrix} 1 + r_s \\ \xi_1 (1 - r_s) \end{bmatrix} E_{y1}^t \qquad (3.4.31),$$

and $$N_k^s(z) = \begin{bmatrix} \cos\left(\frac{2\pi\xi_k (z - z_{k-1})}{\lambda}\right) & \frac{i}{\xi_k}\sin\left(\frac{2\pi\xi_k (z - z_{k-1})}{\lambda}\right) \\ i\xi_k \sin\left(\frac{2\pi\xi_k (z - z_{k-1})}{\lambda}\right) & \cos\left(\frac{2\pi\xi_k (z - z_{k-1})}{\lambda}\right) \end{bmatrix} \quad (3.4.32).$$

For p-polarized light:

$$\begin{bmatrix} U_1 \\ V_1 \end{bmatrix} = \begin{bmatrix} H_{y1} \\ E_{x1} \end{bmatrix} = \begin{bmatrix} H_{y1}^t + H_{y1}^r \\ E_{x1}^t + E_{x1}^r \end{bmatrix} = \begin{bmatrix} 1 + r_p \\ \frac{\xi_1}{n_1^2}(1 - r_p) \end{bmatrix} H_{y1}^t = \begin{bmatrix} n_1(1 + r_p) \\ \frac{\xi_1}{n_1^2}(1 - r_p) \end{bmatrix} E_{x1}^t \qquad (3.4.33),$$

and $$N_k^p(z) = \begin{bmatrix} \cos\left(\frac{2\pi\xi_k(z - z_{k-1})}{\lambda}\right) & \frac{i\hat{n}_k^2}{\xi_k}\sin\left(\frac{2\pi\xi_k(z - z_{k-1})}{\lambda}\right) \\ \frac{i\xi_k}{\hat{n}_k^2}\sin\left(\frac{2\pi\xi_k(z - z_{k-1})}{\lambda}\right) & \cos\left(\frac{2\pi\xi_k(z - z_{k-1})}{\lambda}\right) \end{bmatrix} \quad (3.4.34).$$

In equations (3.4.31-3.4.34), all the entities have already been defined, except z -the position within the thin cavity in which the electric field is calculated. The amplitude reflection coefficients can be calculated using equations from the preceding section. Using the values of the electric field strength determined from equation (3.4.30) and assuming that the amplitude of the electric field strength of the incident beam is equal to unity one can finally write expressions for the MSEFS:

For s-polarized radiation:

$$\left\langle E_{yk}^{s\,2} \right\rangle = \frac{1}{2}\left|U_k(z)\right|^2 \qquad (3.4.35).$$

For p-polarized radiation there are two relationships - for each component of the electric field vector oriented along the *x* and *z* coordinate axes:

$$\left\langle E_{xk}^{p\,2} \right\rangle = \frac{1}{2}\left|U_k(z)\right|^2 \qquad (3.4.36),$$

$$\left\langle E_{zk}^{p\,2} \right\rangle = \frac{1}{2}\left|\frac{n_1 \sin\Theta_1^t}{\hat{n}_k^2} U_k(z)\right|^2 \qquad (3.4.37).$$

Combined, they yield the total MSEFS for p-polarized light:

$$\left\langle E_k^{p2} \right\rangle = \left\langle E_{xk}^{p\,2} \right\rangle + \left\langle E_{zk}^{p\,2} \right\rangle \qquad (3.4.38).$$

The above relationships allow one to calculate the MSEFS using measurable quantities such as thicknesses and optical constants of the materials that constitute strata in a multilayer system as well as the wavelength and the angle of incidence of incoming radiation. These equations offer a tremendous help when the optimization of experimental conditions is undertaken. The specific applications of these relationships will be shown in Chapter 5.

3.5. Polarization Modulation FTIR Reflection Absorption Spectroscopy

Polarization Modulation FTIR spectroscopy was applied in this project to obtain quantitative information concerning the orientation of organic molecules at the metal electrode. Understanding of the quantitative relationships that govern the operation of a photoelastic modulator (PEM) is needed for optimization of the data acquisition procedure and for processing of the obtained spectra. This paragraph provides the reader with a brief introduction to propagation of light in matter. The focus is given on retardation of electromagnetic radiation, the phenomenon that is utilized in the PEM. The introduction is followed by the description of the work of the device and demodulation techniques. The methods of processing of experimental spectra that were described in literature are given in the end of this section.

3.5.1. Principles of Operation of a Photoelastic Modulator.

The element of the optical head changes its refractive index when the PEM is operated. A change of the phase of the incident beam is observed as the result. To understand the principle of operation of the PEM, one needs to understand the relationship of the refractive index of an optical element with the phase shift observed when the beam of electromagnetic radiation traverses this element. The refractive index of a material n is defined as the ratio of the speed of light in vacuum c to the speed of light in a material v :

$$n = \frac{c}{v} \qquad (3.5.1)$$

It follows from equation (3.5.1) that the velocity of a photon in an isotropic material,

characterized by a refractive index of 2, is two times slower than in vacuum. Apparently, the beam of light is retarded by the material. Figure 3.5.1 illustrates the retardation of electromagnetic radiation. If in vacuum (n = 1) the photon travels a distance dx in a time interval dt (it is convenient to choose dx equal to the wavelength of the radiation), in the material with refractive index of 2 it takes a two times longer period of time ($2dt$) to traverse the same distance. Since the frequency of the radiation is invariant with the refractive index, the wavelength of the radiation decreases by a factor of two. This is why the phase angle of the electromagnetic wave undergoes a two fold increase as shown in Figure 3.5.1. Thus, the phase of electromagnetic radiation in a condensed medium leads its phase in vacuum as the result of the retardation.

Certain materials, such as calcite for example, are anisotropic and the degree of retardation of electromagnetic radiation displayed by these materials strongly depends on the crystallographic orientation. This effect is called birefringence. If the linearly polarized light is incident on a birefringent material at an oblique angle with respect to its main optical axis, circularly polarized light is generated due to the different retardation imposed by the material on the two orthogonal components of the incident beam, oriented along two nonequivalent directions in an anisotropic crystal. Isotropic materials may also display birefringence if their symmetry is distorted due to mechanical stress [23]. This induced birefringence is called photoelastic effect and is utilized in the photoelastic modulator (PEM) to impose a periodic retardation on a beam of linearly polarized light.

A schematic diagram of the device is shown in Figure 3.5.2. It is made of two materials that are glued together [24]. One is a piezoelectric transducer that converts a periodic voltage

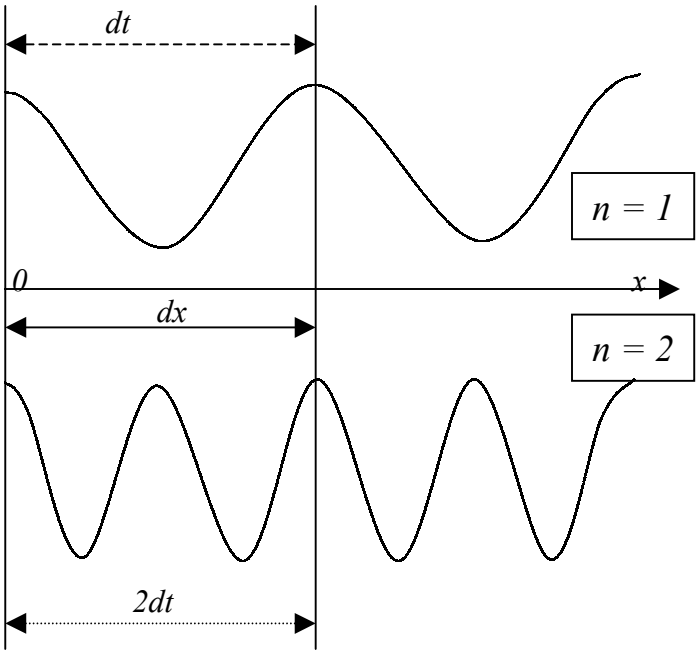

Figure 3.5.1. Retardation of an electromagnetic wave by materials.

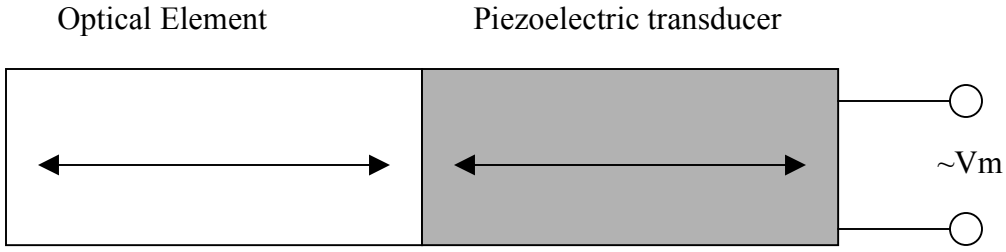

Figure 3.5.2. Diagram of a photoelastic modulator (PEM).

to a periodic mechanical (acoustic) wave. The other is an optical element that imposes a periodic retardation (or acceleration) on a component of the incident linearly polarized beam that is oriented along the main axis of the device, shown on the diagram by arrows. The other component of the incident beam, oriented perpendicular to the main axis of the PEM, remains unchanged. The PEM is operated at its resonant frequency that depends on the size of the device. The linearly polarized light is usually incident at an angle of 45^0 with respect to the main axis of the PEM in order to have two orthogonal components of the incident beam of equal intensity. Figure 3.5.3a demonstrates the direction of the electric fields of these two components, one being parallel to the main axis of the PEM. If the optical element is at rest, no change in the relative positions of the maxima of the electric fields is observed and, consequently, the polarization of the radiation remains unchanged. If the optical element undergoes compression or extension, retardation or acceleration occurs. Retardation results in a positive phase shift while acceleration yields a negative phase shift, relative to the component of the incident beam oriented perpendicular to the main axis of the PEM. The phase shifts are illustrated in parts b and c of Figure 3.5.3, respectively.

When the amplitude of the applied voltage is set such that the PEM imposes the maximum relative phase shift of 90^0 (half-wave retardation), the incident beam changes its polarization by 90^0 as illustrated in Figure 3.5.4 a. During one cycle of applied voltage the half-wave retardation occurs twice: once when the optical element becomes compressed and once when it becomes stretched. Both times the same net effect is observed since the polarization is changed by 90^0 regardless of whether retardation or acceleration takes place. When the optical element is at rest (between the compression and extension) no retardation occurs. Thus,

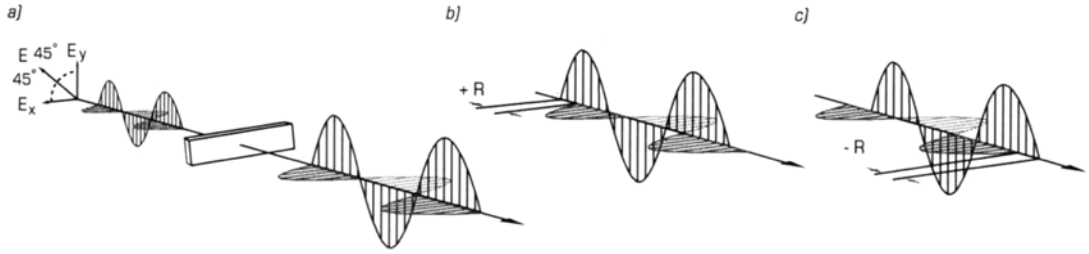

Figure 3.5.3. Retardation effect of compression and extension.
Photoelastic modulator: a) at rest, b) compressed, c) extended.
Figure was taken from [24].

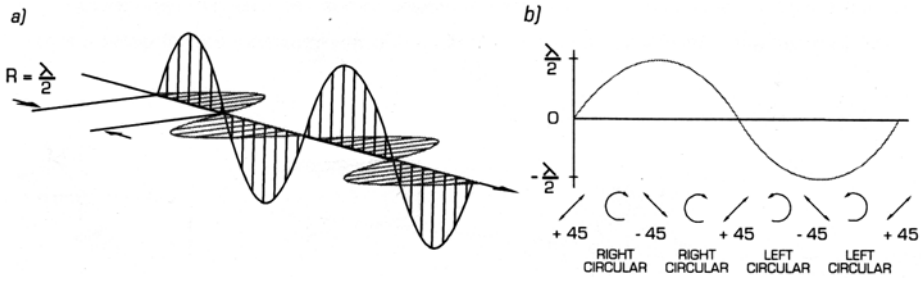

Figure 3.5.4. Half-wave retardation.
a) Relative orientation of the electric field components at half-wave retardation
b) Effect of retardation on the polarization of the beam that exits the PEM
Figure was taken from [24].

the PEM can be used to alter the polarization of the incident linearly polarized beam from 0^0 to 90^0 at a frequency that is twice the frequency of the voltage applied to the piezoelement. This property is used in reflection absorption spectroscopy and the quantitative relationships that describe the operation of the PEM applied in this spectroscopy are presented below.

3.5.2. Quantitative Relationships Describing Operation of the PEM

Figure 3.5.5 shows a diagram of a simplified experimental setup used in polarization modulation spectroscopy. This diagram is used to demonstrate the relationships that govern the operation of the PEM, hence some components that are not essential for this purpose are omitted. The setup consists of a static polarizer *P* and a photoelastic modulator *PEM*. The incoming radiation can be represented by two orthogonal components I_{0V} and I_{0H} that denote, respectively, the intensities of the vertical and the horizontal components of the incident beam with respect to the optical bench plane. When the beam crosses the static polarizer *P*, the vertical component is rejected and the radiation becomes linearly polarized in the direction parallel to the optical bench, indicated in Figure 3.5.5. as I_1. The modulator is mounted at an angle of 45^0 with respect to the optical bench plane. Hence, the beam of linearly polarized light I_1 can be regarded as composed of two orthogonal components I_{1x} and I_{1y} oriented along the main axis of the PEM and perpendicular to it, respectively (see Figure 3.5.5). The PEM imposes a phase shift n on the I_{1x} component and the I_{1y} component remains unchanged. Hipps and Crosby [25] derived an analytical expression that describes the signal at the detector measured using such a setup

$$I_D(\varphi) = \frac{I_s + I_p}{2} + \frac{I_s - I_p}{2}\cos\varphi \qquad (3.5.2).$$

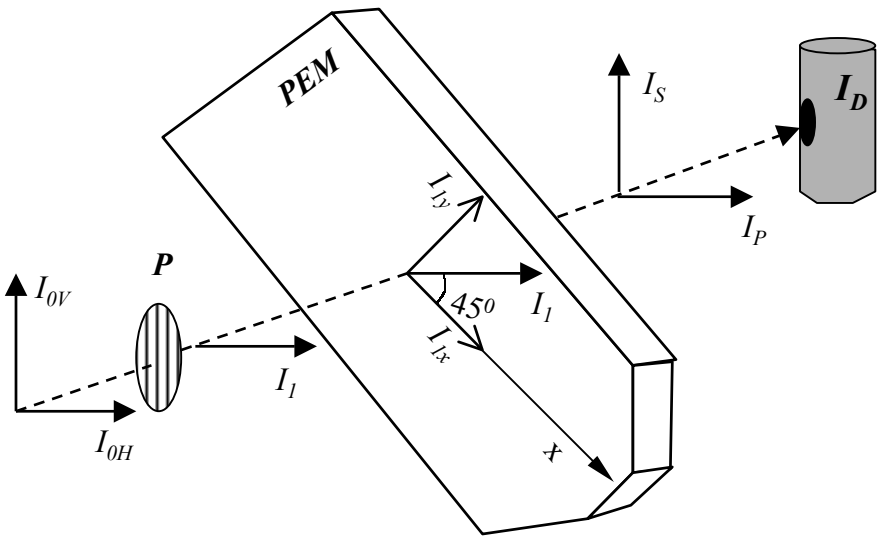

Figure 3.5.5. Simplified diagram of the experimental setup and orientations of the electric field vectors of the electromagnetic radiation.

Here I_D denotes the intensity of the radiation at the detector placed in the location shown in Figure 3.5.5. I_p and I_s represent the components of the beam in front of the detector that are oriented parallel and perpendicular to the optical bench, respectively. The notations were chosen to be consistent with the orientations of the s- and p-polarized beam at the metal electrode, which is not shown. The authors also demonstrated that the phase shift depends on the frequency of the PEM ω_m and time *t* in the following way:

$$\varphi = \varphi_0 \cos(\omega_m t) \quad (3.5.3).$$

Here φ_0 is the maximum phase shift introduced by the PEM, which depends on the magnitude of the voltage (V_m) that is applied to the PEM and the wavelength of the polarized radiation λ. This phase shift is given by

$$\varphi_0 = \frac{GV_m}{\lambda} \quad (3.5.4),$$

where *G* is the proportionality factor. The amplitude of the voltage V_m is usually optimized for a certain wavelength λ_o so that the maximum phase shift imposed by the PEM is equal to π. Substitution of λ for λ_o and φ_0 for π in equation (3.5.4) yields

$$GV_m = \pi\lambda_0 \quad (3.5.5).$$

Using equations (3.5.3-3.5.5), one can express the phase shift n introduced by the PEM to a beam of monochromatic light of wavelength λ as $\varphi = \frac{\lambda_0}{\lambda}\pi \cos(\omega_m t)$ (3.5.6).

Combining equations (3.5.2) and (3.5.6) one can finally write

$$I_D(t) = \frac{I_s + I_p}{2} + \frac{I_s - I_p}{2}\cos\left(\frac{\lambda_0}{\lambda}\pi\cos(\omega_m t)\right) \qquad (3.5.7).$$

Equation (3.5.7) demonstrates that:

1. $I_D(t) = I_P$ (3.5.8)

when $\omega_m t = \frac{\pi}{2} \pm N\pi, N = 0,1,2....$ (3.5.9),

2. $$I_D(t) = I_S + \frac{I_s - I_p}{2}\left\{1 + \cos\left(\frac{\lambda_0}{\lambda}\pi\right)\right\} \qquad (3.5.10)$$

when $\omega_m t = 0 \pm N\pi, N = 0,1,2....$ (3.5.11).

It is worth noting that when the condition (3.5.11) is fulfilled and when the wavelength of the incident beam $\lambda = \lambda_0$, the second term of equation (3.5.10) disappears resulting in

$$I_D(t) = I_S \qquad (3.5.12).$$

Thus, when the condition (3.5.9) is fulfilled, the polarization of the incident beam remains unchanged (I_P) regardless of its wavelength. When the condition (3.5.11) is fulfilled, the polarization of the incident beam undergoes a change. If the wavelength of the radiation is equal to λ_o (for which the PEM was optimized), the polarization of the incident beam is changed by 90^0 and linearly polarized (I_S) light is obtained at the exit of the PEM. If the wavelength of the incident beam departs from λ_o, the change in polarization of the incident

beam deviates from 90^0 and circularly polarized light (*i.e.*, light that has both s- and p-components) is received by the detector. The degree of contamination of s-polarized light with p-polarized light depends on the term in curly brackets in equation (3.5.10). Because broad band infrared radiation is used in FTIR spectroscopy one can fully optimize experiments for a single wavelength only.

3.5.3. Polarization Modulation Spectra

Theoretical spectra obtained using polarization modulation FTIR spectroscopy can be presented as

$$\left(\frac{\Delta I}{\langle I \rangle}\right)_{Theor.} = \frac{I_s - I_p}{(I_s + I_p)/2} \qquad (3.5.13)$$

where $\Delta I = I_s - I_p$ is the intensity difference signal and $\langle I \rangle = (I_s + I_p)/2$ is the intensity average signal. In order to avoid confusion it is important to note that equation (3.5.13) can be derived from equation (2.3.2) if both numerator and denominator of equation (2.3.2) are multiplied by the intensity of the incident beam I_0. The experimental signal received by the detector alternates between s- and p-polarizations according to equation (3.5.7). To obtain the spectrum given by equation (3.5.13) the signal from the detector should be decoded. There are two demodulation techniques: the first uses a lock-in amplifier and a low-pass filter while the second relies on the real-time sampling electronics to obtain the intensity difference and average signals. The theoretical background relevant to both these techniques is described below.

The first technique was used since the 1970s [25][26] and is still quite popular. It utilizes a lock-in amplifier to extract the detector signal $I_D(2\omega_m)$ at a frequency equal to the second harmonic of the voltage frequency applied to the PEM. Hipps and Crosby demonstrated [25] that this signal is related to the difference signal ΔI in the following fashion

$$I_D(2\omega_m) = \Delta I \cdot J_2(\varphi_0) \quad (3.5.14),$$

where $J_2(\varphi_0)$ is the second order Bessel function of the maximum phase shift φ_0 introduced by the PEM. They also derived the relationship between the signal at the terminal of a low pass filter $I_D(0)$ and the average signal $\langle I \rangle$:

$$I_D(0) = \langle I \rangle + \frac{\Delta I}{2} \cdot J_0(\varphi_0) \qquad (3.5.15).$$

Here $J_0(\varphi_0)$ is the zero order Bessel function of φ_0.

3.5.4. Application of a Lock-In Amplifier

If the output from the lock-in amplifier is used instead of a difference signal and the output from the low-pass filter as a substitute for the average signal, equation (3.5.13) becomes:

$$\left(\frac{\Delta I}{\langle I \rangle}\right)_{Exp.} = \frac{I_D(2\omega_m)}{I_D(0)} = \frac{\Delta I \cdot J_2(\varphi_0)}{\langle I \rangle + \frac{1}{2}\Delta I \cdot J_0(\varphi_0)} \qquad (3.5.16).$$

If a highly reflective metal is used in reflection absorption spectroscopy, the second term in the denominator of equation (3.5.16) could be ignored because in this case $\Delta I << \langle I \rangle$ and $J_0(\varphi_0) \leq 1$. The equation for the polarization modulation spectrum then becomes

$$\left(\frac{\Delta I}{\langle I \rangle}\right)_{Exp.} \approx \frac{\Delta I}{\langle I \rangle} \cdot J_2(\varphi_0) \qquad (3.5.17).$$

It is evident from equation (3.5.17) that instead of the desired spectrum of $\frac{\Delta I}{\langle I \rangle}$, experimentally one obtains a product of $\frac{\Delta I}{\langle I \rangle}$ and a function $J_2(\varphi_0)$ given by:

$$J_2(\varphi_0) = J_2\left(\frac{\lambda_0}{\lambda}\pi\right) \qquad (3.5.18).$$

Because $J_2(\varphi_0)$ is a function of wavelength, a systematic error is introduced to experimental $\frac{\Delta I}{\langle I \rangle}$ spectra if the change of $J_2(\varphi_0)$ with wavelength is ignored.

Fortunately, $J_2(\varphi_0)$ varies slowly with λ in the region of the spectrum where the wavelength is close to λ_o and this error can be neglected, especially if qualitative information is extracted

from the experimental spectra. It is important to note that the second order Bessel function has a maximum $J_2(\pi) \approx 0.5$ when $\lambda = \lambda_0$ and hence the maximum signal obtained using the lock-in technique is approximately two times smaller than the maximum theoretical signal given by equation (3.5.13).

3.5.5. Utilization of a Synchronous Sampling Demodulator

Recently Corn *et al.*[27][28] developed a new technique that utilizes the sampling electronics to detect not only the second but also higher harmonics of the modulator frequency. Consequently the signal measured at $\lambda = \lambda_0$ becomes considerably higher, approaching a theoretical maximum given by equation (3.5.13). Their device, the synchronous sampling demodulator (SSD), uses the reference signal from the PEM controller to sample the detector signal when conditions (3.5.9) and (3.5.11) are fulfilled and yields the following two signals at its terminals [28]:

1. the intensity average signal:

$$I_D^{Ave}(2\omega_m) = \langle I \rangle + \frac{\Delta I}{2}\left\{\frac{1+\cos\varphi_0}{2}\right\} \qquad (3.5.19).$$

2. the intensity difference signal

$$I_D^{Diff}(2\omega_m) = \Delta I\left\{\frac{1-\cos\varphi_0}{2}\right\} \qquad (3.5.20).$$

Both equations (3.5.19) and (3.5.20) can be derived from equations (3.5.8) and (3.5.10) after rearrangements. The polarization modulation reflection absorption spectrum acquired using the SSD can be written as:

$$\left(\frac{\Delta I}{\langle I\rangle}\right)_{Exp.} = \frac{\Delta I\left\{\left(1-\cos\varphi_0\right)/2\right\}}{\langle I\rangle + \frac{1}{2}\Delta I\left\{\left(1+\cos\varphi_0\right)/2\right\}} \qquad (3.5.21).$$

The similarity between equations (3.5.16) and (3.5.21) is obvious. Similarly to those obtained using the lock-in technique, the SSD spectra are superimposed on the periodic background caused by the terms in curly brackets. It should be noted, however, that when λ approaches λ_o, equation (3.5.21) approaches equation (3.5.13). Thus, a superior signal-to-noise ratio could be achieved using the novel technique [28].

3.5.6. Processing of PM FTIR RAS Spectra for Quantitative Analysis

Regardless of the choice of the demodulation technique, polarization modulation spectra must be further processed before they can be used to extract quantitative information. The aim of the data processing is to remove the artifacts introduced by the PEM. There are three methods to remove the contribution of the wavelength-dependent coefficients beside ΔI (Bessel functions or cosine terms depending on the demodulation technique) [29]:

1. The first approach is to calculate and remove these functions. It is not practical though, because there could be significant discrepancies between the theoretically calculated and experimental values of these coefficients, due to many factors that are hard to control or

reproduce (such as residual birefringence of the optical element of the PEM for example).

2. The second approach is to normalize the spectrum of the analyte to the background spectrum recorded at the same conditions. This approach has two weaknesses. One is that it is often very difficult to reproduce exactly the experimental conditions to collect the two spectra (the sample and the background). The other problem arises because another constant is introduced to the spectra as a consequence of such a treatment. Buffeteau *et al.* [29] have demonstrated that the normalized experimental signal obtained in reflection absorption experiments can be expressed as

$$\frac{\Delta S}{S} = \frac{S(d) - S(0)}{S(0)} = \frac{2\gamma R_P(0) R_S(0)}{R_S^2(0) - \gamma R_P^2(0)} A \qquad (3.5.22),$$

where S denotes the PM FTIR spectrum which is given by the ratio of the intensity difference signal to the intensity average signal that are obtained at the terminals of demodulation devices. Symbols (d) and (0) denote the spectra of the analyte and the background, respectively. R_S and R_P represent the reflectance of the metal substrate for s-and p-polarized light, respectively. γ is the optical setup efficiency for p-polarized light, normalized by the efficiency for the s-polarized light. Finally, A is the absorbance of the analyte. In principle, the constant in front of A can be calculated using the Fresnel equations. However, precise knowledge of the experimental conditions (such as the angle of incidence for example) is required for the calculation of this coefficient.

3. The third approach is to determine the coefficients beside ΔI in an independent experiment using a second static polarizer (analyzer) placed on the opposite (with respect to

the first polarizer) side of the PEM. This method requires additional equipment and time but is the best of the three methods. Following Buffeteau *et al.* [30] it could be demonstrated that

$$A = 1 - \frac{\gamma R_P(d)}{R_P(0)} \approx 1 - \frac{\gamma R_P(d)}{R_S(d)} = 1 - \frac{C_{PP}\left(\frac{g}{g'}C_{PS} - S(d)\right)}{C_{PS}\left(\frac{g}{g'}C_{PP} + S(d)\right)} \quad (3.5.23).$$

Here C_{PP} and C_{SP} are the calibration spectra obtained in a similar way as *S(0)*except that the analyzer was placed after the PEM and set to admit p- or s-polarized radiation, respectively. g and g' denote the gain of the electronics during collection of experimental and calibration spectra, respectively. The other notations are the same as in the second method. The authors used a lock-in amplifier to obtain the intensity difference spectrum and demonstrated that the calibration spectra are related to the Bessel functions in the following way:

$$C_{PP} = \frac{g'\left|J_2(\varphi_0)\right|}{1 + J_0(\varphi_0)} \quad (3.5.24)$$

and

$$C_{PP} = \frac{g'\left|J_2(\varphi_0)\right|}{1 - J_0(\varphi_0)} \quad (3.5.25).$$

The method similar to the third approach was developed and utilized in this project. Details concerning specific aspects of the experimental spectra conditioning are given in

Chapter 5, which describes the novel developments of FTIR RAS made as a part of this project.

References

1. I. Burgess, M.S. Thesis, University of Guelph (2000).

2. J. Lekner , Theory of Reflection of Electromagnetic and Particle Waves, Martinus Nijhoff Publishers, Boston (1987).

3. V.F. Sears, "Neutron Optics", Oxford University Press, Oxford (1989).

4. Ch.F. Majkrzak Mat. Res. Soc. Symp. Proc. 376 (1995) 143.

5. M.Tolan and W. Press, Z. Kristallogr. 213 (1998) 319.

6. G.L. Gaines, J. Insoluble Monolayers at Liquid-Gas Interfaces, Interscience, New York, (1966).

7. I. Langmuir and V.J. Schaefer, J.Am.Chem.Soc. 60 (1938) 1351.

8. I. Langmuir, Trans. Faraday Soc. 15 (1920) 62.

9. K.B. Blodgett, J. Am. Chem. Soc. 57 (1935) 1006.

10. D.M. Mohilner in A.J. Bard (Ed.), Electroanalytical Chemistry. Vol. 1, Marcel Dekker, New York (1966) 241.

11. R. Parsons in J.O'M. Bockris, B.E. Conway and E. Yeager (Eds.), Comprehensive Treatise of Electrochemistry, Plenum Press, New York (1980) 1.

12. J. Lipkowski, W. Schmickler, D.M. Kolb and R. Parsons, J.Electroanal.Chem. 452 (1998) 193.

13. B.B. Damaskin, O.A. Petrii and V.V. Batrakov, Adsorption of Organic Compounds on Electrodes, Plenum Press, New York (1971).

14. J. Richer and J. Lipkowski, J. Electrochem. Soc. 133 (1986) 121.

15. J. Lipkowski and L. Stolberg, in J. Lipkowski and P.N. Ross (Eds.), Adsorption of Molecules at Metal Electrodes, VCH Publishers (1992) 171.

16.P.R. Griffiths "Chemical Infrared Fourier Transform Spectroscopy" John Wiley & Sons New York (1975).

17. A.W. Crook, J. Opt. Soc. Am 38 (1948) 954.

18. F. Abelés, Ann. Phys. (Paris) 5 (1950) 596.

19. F. Abelés, in "Advanced Optical Techniques" A.C.S. Van Heel (Ed.), John Willey & Sons, New York (1967) 145.

20. W.N. Hansen, J. Opt. Soc. Am. 58 (1968) 380.

21. A. Hecht, A. Zajac, Optics, 2nd Ed. Addison-Wesley, Toronto (1975).

22. J.D.E. McIntyre in "Advances in Electrochemistry and Electrochemical Enineering", P. Delahay and Ch.W. Tobias (Eds.) John Wiley & Sons, New York, V9 (1973) 61.

23. M. Born and E. Wolf "Principles of Optics" Second Ed., Pergamon Press, New York (1964).

24. http://www.hindspem.com/LIT/PDF/HNDPEM90.PDF

25. K.W. Hipps and G.A. Crosby J. Phys. Chem. 83 (1979) 555.

26. W.G. Golden, D.S. Dunn and J. Overend, J. Cat. 71 (1981) 395.

27. M.J. Green, B.J. Barner and R.M. Corn Rev. Sci. Instrum. 62 (1991) 1426.

28. B.J. Barner, M.J. Green, E.I. Sáez and R.M. Corn, Anal. Chem. 63 (1991) 55.

29. T. Buffeteau, B.Desbat and J.M. Turlet, Appl. Spec. 45 (1991) 380.

30. T. Buffeteau, B. Desbat, D. Blaudez and J.M. Turlet Appl. Spec. 54 (2000) 1646.

CHAPTER 4

4. Materials and Experimental Methods

The purpose of this chapter is to describe the materials and equipment that were used during this research. In addition, the technical details of the applied experimental procedures will be presented. Electrochemical measurements of differential capacity and charge density as well as technical details of *in situ* techniques such as SNIFTIRS, PM FTIR RAS and neutron reflectometry are described in this chapter. The recent developments of the electrochemical FTIR spectroscopic methods, made during this project, will be given in Chapter 5.

4.1. Materials

Pyridine (>99.9%, HPLC grade, Aldrich) was added to an electrolyte of 0.1 M solution of $KClO_4$ (calcinated at 300 ^{0}C and twice re-crystallized, ACS certified AESAR) in D_2O (99.9 %D, Cambridge Isotope Laboratories) to obtain a 0.001 M solution of pyridine, used in SNIFTIRS experiments. In electrochemical measurements, a 0.05 M solution of $KClO_4$ in Milli-Q water was used and 0.1 mL of 0.4 M solution of $KHCO_3$ (BDH AnalaR, England) was added to this electrolyte to maintain a constant pH of ~ 9. Similar values of pH were achieved when a 0.1 M solution of NaF (Suprapur, EM Industries) in D_2O was used directly as electrolyte for PM FTIR RAS experiments. 4-pentadecylpyridine (C15-4Py) was synthesized and purified by McAlees and McCrindle as described in [1]. Figure 4.1 shows the model of this surfactant. The molecule of C15-4Py consists of a pyridine head group attached to the 15-atom hydrocarbon chain. 8 mg of C15-4Py was dissolved in 5 mL of chloroform

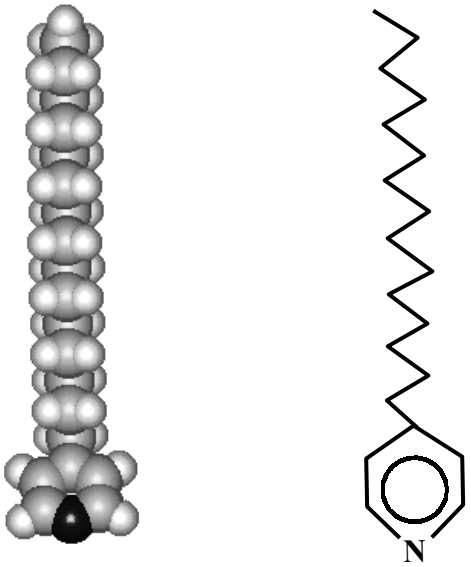

Figure 4.1 Model of 4-pentadecylpyridine (C15-4Py).

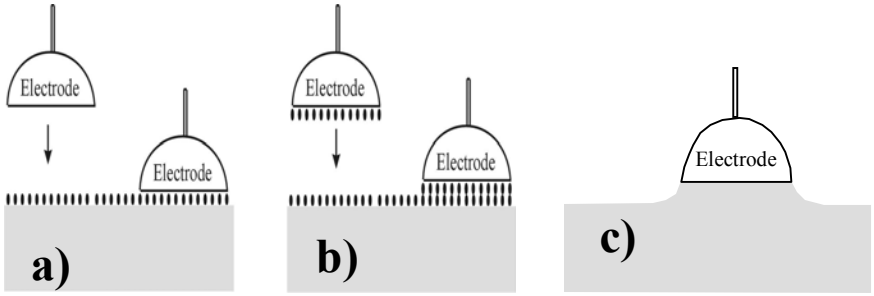

Figure 4.2 Schematic of the horizontal touching (Langmuir-Schaefer) deposition technique and the hanging meniscus configuration.
a) single horizontal touching,
b) double horizontal touching,
c) hanging meniscus configuration.

(ACS certified, spectroscopy grade, Fisher) resulting in a 0.0055 M stock solution of the surfactant. Gold single crystals in the shape of an inverted mushroom were prepared as described in [2]. All potentials reported in this project were measured with respect to the saturated calomel electrode (SCE) or converted to the SCE scale, unless specifically stated otherwise. All the glassware and Teflon parts used in the experiments were washed in a 1:3 mixture of nitric and sulfuric acids and rinsed in copious amounts of Milli-Q water. All experiments were performed at 22 ± 2 °C.

4.2. Deposition of Surfactant Films on the Working Electrode

Two variations of the Langmuir-Schaefer technique [3] were used to transfer C15-4Py from the GS interface to the metal surface. Single horizontal touching, shown schematically in Figure 4.2 a, was performed in the following way. Solution of C15-4Py in chloroform was delivered in small droplets onto the surface of the electrolyte using a 10 μL syringe (Hamilton) until the last droplet formed a lens that remained floating on the surface for at least a minute. The surfactant film thus formed maintained a constant equilibrium spreading pressure of 33 mNm^{-1} under these conditions. The film pressure was determined using a Wilhelmy plate [4]. To transfer the surfactant from the GS interface to the MS interface, the dry working electrode was adjusted to be parallel to the electrolyte surface and then slowly approached and brought in contact with the surfactant film. To perform the double horizontal touching, the electrode was withdrawn and a small spherical droplet of the electrolyte that usually adhered to the (hydrophobic) electrode surface was gently removed with a corner of a soft tissue. The electrode with a film obtained using the previous procedure was then

brought in contact with the surfactant film for the second time as shown in Figure 4.2 b. After deposition, the films of insoluble surfactants were analysed. To perform electrochemical measurements the electrode was positioned in hanging meniscus configuration schematically shown in Figure 4.2.c.

4.3 Electrochemical Measurements and Instrumentation

A Au(111) electrode of 3.5 mm diameter and a coil of gold wire were used as working electrode and a counter electrode, respectively, in electrochemical experiments. After assembling and filling with the electrolyte, the cell was deaerated with argon (BOC gases). The flame-annealed working electrode was introduced under the protection of a water drop and positioned in a hanging meniscus [5] configuration to check the cleanliness of the electrolyte using electrochemistry. If the interface was clean, the working electrode was withdrawn, re-annealed and re-introduced (dry) into the cell to cool down in an argon atmosphere. After cooling, the film of C15-4Py was deposited and the working electrode was elevated (*ca.* 2 mm) to assume a hanging meniscus configuration necessary for the electrochemical characterization of the surfactant-covered Au(111) surface.

A Heka potentiostat and a PAR model 129A lock-in amplifier were used to carry out electrochemical measurements. Data were digitized *via* an RC Electronics acquisition board and processed by a computer. The differential capacity of the interface was measured by superimposing a small sinusoidal perturbation of 5 mV r.m.s. and 25 Hz on a 0.005 V s^{-1} voltage ramp. The in-phase and out-of-phase components of the alternating current were then measured using a lock-in amplifier. Differential capacity was calculated assuming a simple

series RC equivalent circuit as the model of the electrode-solution interface, according to the equation

$$C = \frac{i_Q}{E_{ac}\omega}\left[1+\left(\frac{i_R}{i_Q}\right)^2\right] \qquad (4.3.1)$$

where C denotes the differential capacity, i_R and i_Q are real and quadrature (imaginary) components of the measured current, respectively. E_{ac} is the root-mean-square voltage and ω is the angular frequency of the applied alternating current perturbation.

Chronocoulometry [6] was used to measure the charge density at the MS interface. The experimental procedure of chronocoulometry is schematically outlined in Figure 4.3. A sequence of potential steps was applied to the electrode as shown in panel a. The potential was initially held at the base value E_b for a period of time t_b. Then the electrode potential was instantly elevated to the value of the variable potential E_v. This value increased from step to step with a constant increment ΔE_v, reaching the maximum E_{vN} when the last potential step was carried out. After equilibration at a variable potential E_v for a period of time t_v, the electrode potential was instantly returned to the base value E_b. The current transient was recorded during this last step. Panel b shows a diagram of a typical current transient. Integration of a current transient yielded a charge transient. Panel c presents a typical charge transient and demonstrates how one can obtain the charge density at the metal electrode at zero time (equilibrium charge density at the variable potential) by extrapolation of the linear part of the charge transient. The charge densities obtained by extrapolation were plotted

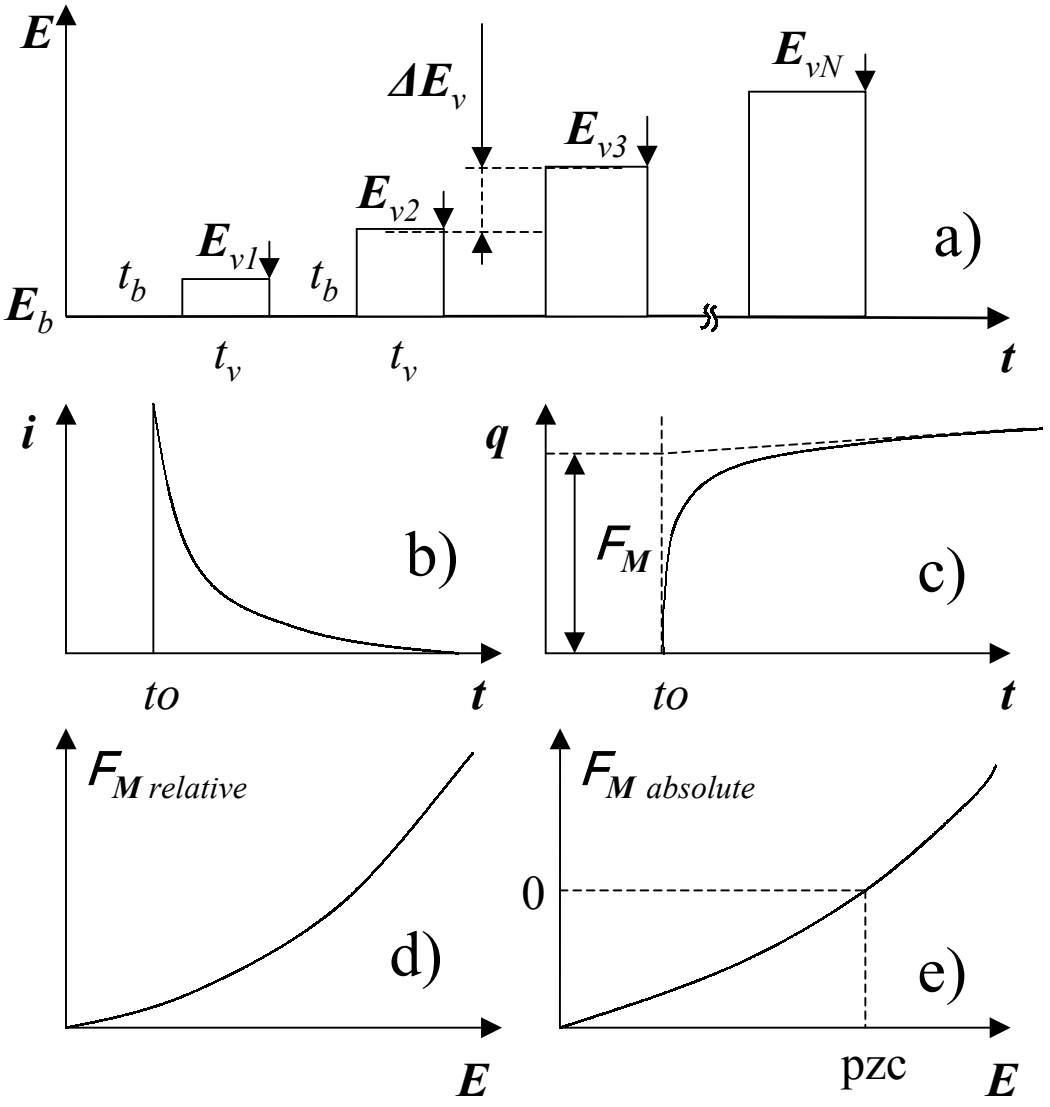

Figure 4.3 Schematic diagram of the chronocoulometric experiment.
a) anodic sequence of potential steps (current transients are measured at the time indicated by arrows);
b) typical measured current transients
c) typical calculated charge transients
d) relative and e) absolute charge densities plotted against the electrode potential.

against the corresponding values of the variable potential as shown in panel d. These data correspond to the relative charge densities (equal to zero at $E_v = E_b$) and they had to be converted to the absolute charge densities using the value of the potential of zero charge (pzc) that was determined in an independent experiment.

In this project the following settings were used to carry out chronocoulometry (for the anodic sequence of steps): the base potential E_b was -0.825 V and the equilibration time at the base potential t_b was 20 s, the first variable potential E_v was equal to the base potential and the increment of the variable potential ΔE_v was 0.025 V, the equilibration time at the variable potential t_v was 90 s and the maximum variable potential E_{vN} was 0.3 V. The current transients were sampled during 0.1 s with 20 μs sampling interval.

4.4 Equipment and Procedures used in SNIFTIRS Experiments

The SNIFTIRS spectra were measured using a NICOLET 20SX/C FTIR apparatus equipped with a MCT-B detector cooled with liquid nitrogen. The sample compartment was purged using air from a Puregas Heatless Dryer which was free of CO_2 and H_2O. The electrode potential was controlled by a PAR 173 potentiostat. A syringe-type infrared cell with a hemispherical ZnSe window was employed in these studies. The optical setup used for the *in situ* infrared spectroscopy was built using the design described by Faguy *et al.* [7]. The 8 mm diameter Au(110) working electrode was flame annealed before the experiments and pushed against the ZnSe window to form a thin layer configuration. A Pt foil cylinder was used as a counter electrode.

The angle of incidence of the infrared radiation was adjusted to be just below the

critical angle, so that the maximum surface enhancement of p-polarized photons at the electrode surface was achieved. The exact values of the angle of incidence of 28.5° and the thin layer thickness of 7.2 μm. were determined from measurements of the reflectivity of the $ZnSe/D_2O/Au$ interface following the procedures developed in this project and described in Chapter 5.

A multiple potential step routine was used to acquire the SNIFTIR spectra. The electrode potential was stepped *m* times between the base potential E_1 = -0.75 V(SCE) and a variable sample potential E_2, respectively. At each potential, *n* interferograms were collected. Data acquisition was delayed for 10 s after each potential change to allow the interface to reach thermodynamic equilibrium at the imposed polarization. A total number of $N = n \times m$ (which is 20 × 100 in our studies) interferograms were co-added, Fourier transformed and used to obtain the SNIFTIRS spectra , defined by equation (2.3.1):

$$\frac{\Delta R}{R} = \frac{R(E_2) - R(E_1)}{R(E_1)}$$

where $R(E_1)$ and $R(E_2)$ are the electrode reflectivities at the base potential E_1 and sample potentials E_2. The SNIFTIRS spectra were acquired using p-polarized radiation with a resolution of 4 cm^{-1}.

4.5 Technical Information on the PM FTIR RAS Setup

PM FTIR RAS is a new method in our laboratory. Many components of the experimental setup were designed and made as a part of the project. Therefore, it will be

described in greater detail.

4.5.1 Description of the Experimental Setup

An experimental setup similar to that described by Corn *et al.*[8][9] has been assembled and used. Figure 4.5.1 shows the top view of our setup. The layout of the optical bench and the diagram of the spectroelectrochemical cell are presented in this figure. The mechanical components of the setup are better visualized in Figure 4.5.2, which presents the side view. The collimated infrared radiation from the spectrometer (Nicolet Nexus 870) entered a port of the external tabletop optical mount (TOM) where it was redirected with a flat mirror (Nicolet) and focused onto the working electrode with a parabolic mirror (f = 6", Nicolet). Before entering the cell, the beam passed through a static polarizer (1" dia., Specac) and the photoelastic modulator (PEM) (Hinds Instruments PM-90 with II/ZS50 (ZnSe 50kHz) optical head). The beam, exiting the cell, was refocused by a ZnSe lens (f = 1", 1.5" dia. with an anti-reflective coating, Janos Technology) onto a MCT-A detector (TRS 50 MHz bandwidth, Nicolet). A bandpass optical filter (3 - 4 μm pass, Specac) was placed at the entrance window of the detector when the spectra of the hydrocarbon stretching modes were acquired.

The spectroelectrochemical cell (see Figure 4.5.1), was custom-made of glass and connected to the optical window (BaF_2 1" equilateral prism, Janos Technology) *via* a Teflon flange (see also Figure 4.5.2). Roe *et al.* [10] and Seki *et al.* [11] have described cells of similar design. The working electrode was a 15 mm disk-shaped Au(111) single crystal inserted into a glass tube, which was used to push the electrode against the optical window,

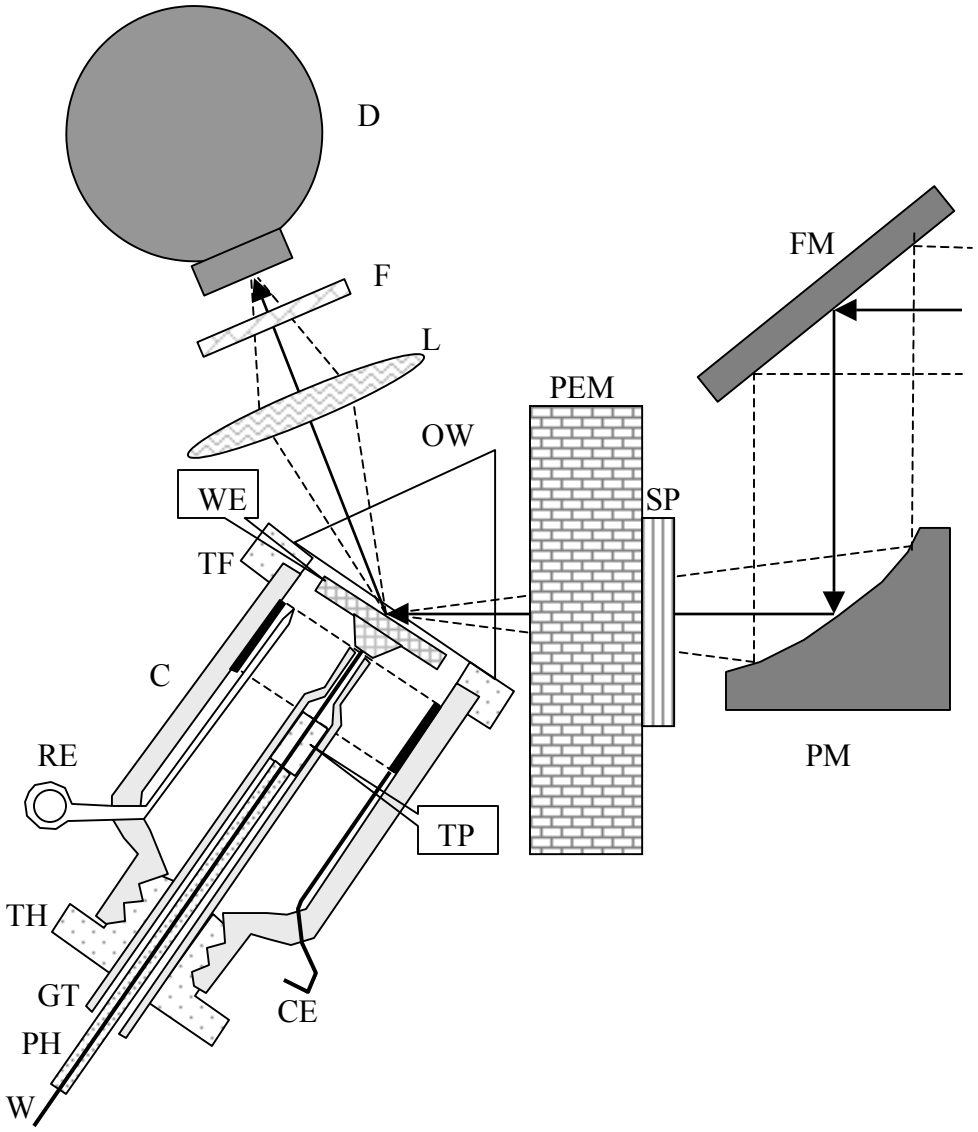

Figure 4.5.1. Illustration of the experimental PM FTIR RAS setup (top view).

FM - flat mirror
PM - parabolic mirror
SP - static polarizer
PEM - photoelastic modulator
OW - optical window
L - lens
F - optical filter
D - detector
WE - working electrode
TF - Teflon flange
C - cell
RE - reference electrode
TH - Teflon holder
GT - glass tube
PH - piston handle
W - gold wire
CE - counter electrode
TP - Teflon piston

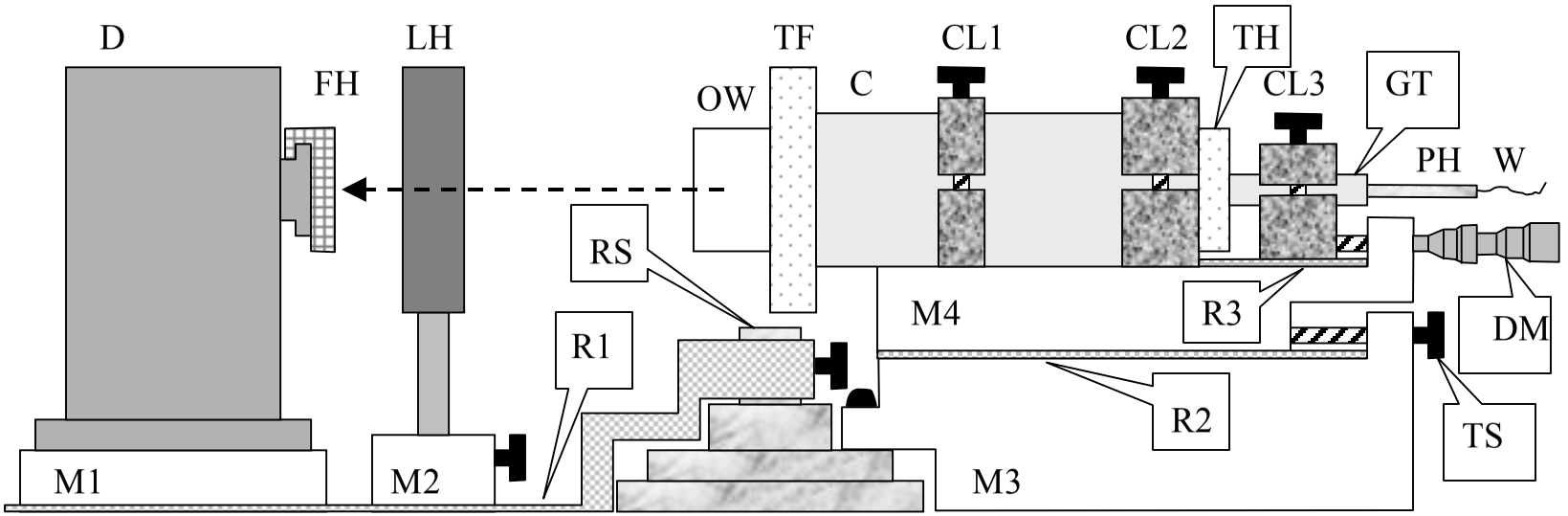

Figure 4.5.2. Illustration of the experimental PM FTIR RAS setup (positions of mechanical parts, side view).

D - detector
FH - optical filter holder
M1 - mount 1
LH - lens holder
M2 - mount 2
R1 - rail 1
RS - rotation stage
OW- optical window
TF - Teflon flange
C - cell
CL1 - clamp 1
CL2 - clamp 2
TH - Teflon holder
CL3 - clamp 3
GT - glass tube
PH - piston handle
W - gold wire
M4 - mount 4
R3 - rail 3
DM - differential micrometer
R2 - rail 2
TS - translation screw
M3 - mount 3

through a threaded Teflon holder as indicated in Figure 4.5.1. A piece of gold wire (Alpha Aesar) was used as a conductor between the potentiostat clip and the gold single crystal. It was inserted into a small orifice in a Teflon piston and placed inside the glass tube as shown in the figure. To ensure tight sealing of the cell around the gold wire the Teflon piston was pushed against the conical end of the glass tube by a hollow brass handle, attached to the piston. A Pt foil cylinder was used as a counter electrode and a glass capillary was used to connect a saturated Ag/AgCl reference electrode as shown in Figure 4.5.1.

The components of the setup were assembled on 4 mounts. Figure 4.5.2. shows the positions of these components. The detector was placed on mount 1. The lens was inserted in a lens holder (Newport) that was affixed to mount 2. Both mounts could be translated along rail 1, attached to a rotation stage (Newport). The rotation stage was affixed to the optical table such that its pivoting axis coincided with the focal point of the parabolic mirror. (When finding the location of the focal point, one should take into account the shift in its position due to the placement of the static polarizer, the PEM and the optical window into the incident beam.) The rotation stage was used to independently set both the angle of incidence and the angle of reflection. The angle of reflection was adjusted by rotation of rail 1 and the angle of incidence was changed by rotation of mount 3, which served as the base for the cell holder. The cell holder was assembled on mount 4, which could be translated with respect to mount 3 along rail 2 using the translation screw. The cell holder consisted of clamp 1 and clamp 2 that were used to attach the cell to the holder and clamp 3, used to secure the glass tube of the working electrode assembly. Clamp 3 could be translated with respect to mount 4 along rail 3 using the differential micrometer (Newport). This translation allowed one

to set the thickness of the thin layer between the electrode and the optical window.

The cell parts were assembled and the cell was placed in the cell holder as shown in Figure 4.5.2. It was then filled with electrolyte through the reference electrode capillary and purged with Ar (BOC Gases) through the inlets that are not shown on the diagrams. The Heka PG490 was connected and used to control the potential of the working electrode. The synchronous sampling demodulator (SSD) (GWC Instruments) was employed to demodulate the detector signal. It was phased with the PEM using an oscilloscope (Tektronix 2225). A Whatman FTIR pure gas generator was used to purge the spectrometer and TOM with dry and CO_2-free air.

4.5.2. List of Experimental Parameters Used in PM FTIR RAS Experiments

Optical bench: angle of incidence of 60^0 and thin cavity thickness of 3 μm (for pyridine moiety) or angle of incidence of 50^0 and thin cavity thickness of 2.5 μm (for hydrocarbon chain). These best parameters were calculated using the in-house software developed in this project and described in Chapter 5. Since the angle of incidence is distorted by the prism (if it is different from 60^0, the normal incidence with respect to front edge of the prism), the following equation was used to calculate the external angle of incidence (with respect to the metal surface normal)

$$\alpha_2 = 60^0 - \sin^{-1}\left[\sin(60^0 - \alpha_1)n_w\right] \quad (4.5.1).$$

Here, n_w is the refractive index of the optical window, α_1 and α_2 are the angles of incidence inside and outside of the optical window, respectively. It is useful to note that α_1 is calculated

by an optimization procedure, whereas α_2 is set experimentally.

Spectrometer controller (OMNIC): mirror velocity = 1.2659 cm s^{-1} (This value of mirror velocity prevents cross-talk between the Fourier frequencies of the interferogram and the PEM modulation frequency. Indeed, using equation (3.3.2), a Fourier frequency of 8.86 kHz is calculated for the wavenumber of 3500 cm^{-1}, which is about an order of magnitude less than the polarization modulation frequency, equal to100 kHz.), aperture = 86 %, sample gain = 1, high pass filter = 200 Hz, low pass filter = 11 kHz, number of scans = 400, resolution = 2 cm^{-1}, levels of zero filling = 0, sample spacing = 1, apodization = Happ-Genzel, phase correction = Mertz.

PEM controller: retardation = 0.5 λ, wavenumber of maximum efficiency = 1600 cm^{-1} (for pyridine moiety) or 2900 cm^{-1} (for hydrocarbon chain).

SSD gain: 10 (for pyridine moiety) or 5 (for hydrocarbon chain).

Potentiostat: *E*(initial) = -0.89 V, *E*(final) = 0.26V, *E*(step) = 0.05 V (from -0.89 to -0.34 V) and 0.2 V (from -0.34 to 0.26 V), number of loops = 20, delay between setting and measurement = 10 s.

4.5.3. Experimental Procedures

The initial preparations were made as follows. The cell parts were washed in a hot 1:3 mixture of nitric and sulphuric acids, rinsed in Milli Q water and dried overnight at 110 ^{0}C. The optical window was rinsed with Milli Q water and ethanol (96 %) followed by cleaning in an ozone chamber (UVO-cleaner, Jelight). The working electrode was inserted in the holder, flame-annealed, cooled in air and employed for horizontal touching deposition of a

C15-4Py film as described in Section 4.2 After transfer of the film, the electrode was placed in the cell, the optical window was attached, the cell was placed in the cell holder (see figure 4.5.2) and connected to the potentiostat and argon purge tubing. The angle of incidence and the thin cavity thickness were calculated and the angle was set to the required value. The initial thin cavity thickness was set by pushing the electrode against the window until the characteristic fringes (Newton rings) became visible through the optical window. A certain degree of skill is needed to notice a weak interference pattern. Therefore, the appreciable increase in the interferogram peak-to-peak signal can be used instead (or in addition) as a criterion of a good initial position of the electrode in the cell. After these initial cell adjustments, the thin cavity thickness was determined as described in Chapter 5 and the cell was re-aligned (sometimes several times) until the proper settings were achieved. The empirical first and second order calibration spectra were also obtained at this stage as described in Chapter 5. If the hydrocarbon region was to be investigated, the optical filter was inserted at the entrance of the detector as shown in Figure 4.5.1.

The measurements were performed in the following way. The electrode potentials and other experimental parameters were specified in the parameter file. An example of the parameter file is described in Appendix A. The Omnic macro employs this file to control the work of the spectrometer and the PEM. In addition, it uses this file to set the electrode potential *via* a digital-to-analog converter (DAQ-802, Omega) and the potentiostat. After being initiated, the program prompts for the name base of the output files, displays the used parameters from the parameter file and requests to adjust the potentiostat for the required initial electrode potential. The experiment runs automaticly for days and the operator needs

only to refill the detector with liquid nitrogen every 12 hours and to check the reference electrode for air bubbles and the cell for leaks. The electrode potential is monitored by an electronic window relay, which switches the potentiostat off if the electrode potential exceeds the manually dialed limits (as a result of a fault of the power supply, for example). If the macro stops with the message "Too many bad scans..."(which occasionally happens for an unknown reason), the operator has to press the "OK" button to proceed, record the names of files that were corrupt and acquire the missing spectra manually at the end of the experiment.

After the macro finished all the tasks, the cell thickness and the calibration spectra were measured for the second time to check whether the experimental conditions had been changed during several days of experimentation. If another part of the spectrum needed to be measured, the whole procedure was repeated with the new settings. The obtained array of experimental spectra was later processed to remove systematic errors and correct for the baseline, according to the procedures outlined in Chapter 5.

4.6 Neutron Reflectometry

Single crystal quartz substrates used for neutron reflectometry were purchased from CrysTec GmbH (Berlin, Germany) and were polished to root mean square roughness of approximately 5 Å, as verified by X-ray reflectometry. A thin layer of about 30 or 60 Å of chromium and a layer of about 74 or 103 Å of gold were sputtered on the quartz substrates in vacuum. D_2O was used as a solvent in reflectivity studies. The electrode was cleaned in warm concentrated sulfuric acid and rinsed with Milli-Q water. A film of C15-4Py was

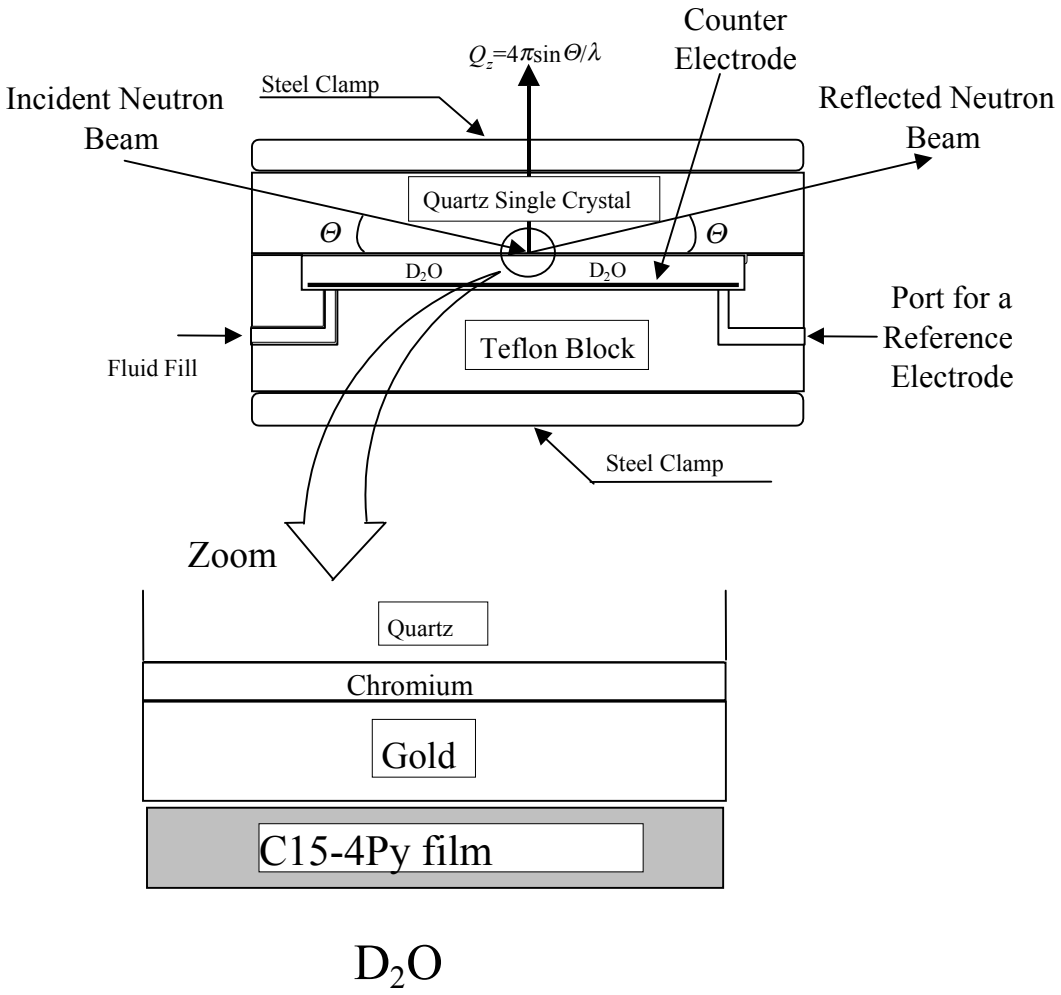

Figure 4.6 Diagram of the cell used for neutron reflectometry.
Inset: profile of the working electrode surface when a C15-4Py film is deposited using the horizontal touching technique.

transferred from the air-solution interface to a dry gold-coated surface of the quartz substrates as described in Section 4.2. The electrode was then mounted on a special cell made of Teflon, schematically shown in Figure 4.6. The cell had ports for the counter (gold foil) and reference (Ag/AgCl) electrodes. The contact between the gold-coated surface of the quartz substrate (working electrode) and a lead to the potentiostat was achieved using a spring-loaded steel bar. The resistance of the thin film of gold was of the order of a few ohms.

The neutron reflectivity measurements were made on the NG-7 reflectometer at the National Institute of Standards and Technology (NIST) [12].The neutron reflectometry measures the normalized (by the incident flux) intensity of specularly reflected neutrons, *R,* as a function of the momentum transfer vector Q_z ($Q_z = 4\pi\sin\theta/\lambda$, where θ is the angle of incidence and λ is the wavelength of the neutrons) [13]. A fixed neutron wavelength of 4.75 Å was used and Q_z was varied from ~0.0 to approximately 0.2 $Å^{-1}$ by changing the angle of incidence. Reflectivities *R* with reasonable statistics were measured down to values $R \sim 10^{-5}$. The reflected neutrons were counted using a ^{3}He proportional counter as the detector and typical counting times were 3 hours. The data were reduced, taking into account the neutron beam transmission through the quartz substrate, and corrected for the background. The error bars on the experimental results (presented in Chapter 7) represent the statistical errors in the measurements (standard deviation, σ_R). A constant instrumental resolution of $\Delta Q_z/Q_z = 0.043$ (full width at half maximum) was used throughout the scan.

References

1. D. Bizzotto, A. McAlees, J. Lipkowski, and R. McCrindle, Langmuir 11 (1995) 3243.

2. J. Richer, Ph.D. Thesis, University of Guelph, Guelph (1990).

3. I. Langmuir and V.J. Schaefer, J. Am. Chem. Soc 60 (1938) 1351.

4. T. Sagara, V. Zamlynny, D. Bizzotto, A. McAlees, R. McCrindle and J. Lipkowski, Israel J. Chem. 37 (1997) 197.

5. D. Bizzotto and J. Lipkowski, Progr. Colloid. Polym. Sci. 103 (1997) 201.

6. J. Richer and J. Lipkowski, J. Electrochem. Soc. 133 (1986) 121.

7. P.W. Faguy and N.S. Marinkovic, Anal. Chem. 67 (1995) 2791.

8. M.J. Green, B.J. Barner and R.M. Corn, Rev. Sci. Instrum. 62 (1991) 1424.

9. B.J. Barner, M.J. Green, E.I. Sáez and R.M. Corn, Anal. Chem. 63 (1991) 55.

10. D.K. Roe, J.K. Sass, D.S. Bethune and A.C. Luntz, J. Electroanal. Chem 216 (1987) 293.

11. H.Seki, K.Kunimatsu and W.G. Golden, Appl. Spec. 39 (1985) 437.

12. www.ncnr.nist.gov/instruments/ng7refl/

13. Ch.F. Majkrzak, Mat. Res. Soc. Symp. Proc. 376 (1995) 143.

CHAPTER 5

5. Development of PM FTIR RAS and SNIFTIRS

In this project, infrared spectroscopy was applied for quantitative determination of the orientation of organic monolayers at the metal-electrolyte interface. Quantitative analysis requires high quality spectra and thus, full optimization of the experimental setup was necessary. This chapter will describe how the best performance of the experimental setup used for *in-situ* IR RAS at the metal surface can be achieved. At the beginning of this chapter, the optimization of the signal-to-noise ratio (S/N) is described, followed by an explanation of the basic principles of the procedures that were used to process the raw experimental spectra in order to remove systematic instrumental errors. The methods of determination of the molecular orientation in thin organic films at the metal electrode are presented at the end. Most of the procedures that are given below are new to this field and were developed in this project. A software package was written to automate calculations that were done on an everyday basis following these procedures.

5.1.Optimization of the Experimental Setup

A number of scientists have contributed to the development of reflection absorption spectroscopy and electrochemical *in situ* FTIR RAS in particular. However, fragmentation and partial inconsistency of the published information (presented in Chapter 2) prompted us to carry out our own calculations. The novelty of our approach was that software was written that could be used to initially simulate the reflection absorption experiment and to find the optimum conditions that could be later used in real experiments.

5.1.1. Optimization of the Angle of Incidence and the Thin Cavity Thickness

The absorbance by an organic molecule in front of a metal mirror is proportional to the mean squared electric field strength (MSEFS) of the p-polarized radiation [1]. Thus, optimization of experimental conditions is equivalent to finding a global maximum of the MSEFS of p-polarized light at the electrode surface. Figure 5.1.1 shows an illustration of the model of the spectroelectrochemical cell that was used for calculations of the MSEFS. For a given wavelength, the MSEFS is a function of the angle of incidence, the angle of the incident beam convergence, the thin cavity thickness and the optical constants of all the constituents of the interface. This section will focus on optimization of the angle of incidence and the thin cavity thickness while the influence of the choice of the optical window and the incident beam collimation will be presented in the sections that follow.

CaF_2 , D_2O and Au will be used as the optical window, electrolyte solvent and working electrode, respectively, to demonstrate how the calculations for the stratified medium composed of any window, electrolyte and electrode materials can be done. The optical constants of these materials can be taken from the literature [2][3][4][5]. It is useful to present the optimization of experimental conditions for the incident beam of 2850 cm^{-1}, which corresponds to the spectral region where C-H stretching vibrations of hydrocarbon moieties are observed in the spectrum and for the incident beam of 1600 cm^{-1} which corresponds to the spectral region where the skeletal vibrations of the pyridine moiety, H-C-H bending and C = O stretching vibrations are observed.

The calculations were performed for two variables: the angle of incidence and the thin cavity thickness. Therefore, the calculated MSEFS is plotted in a three-dimensional graph as

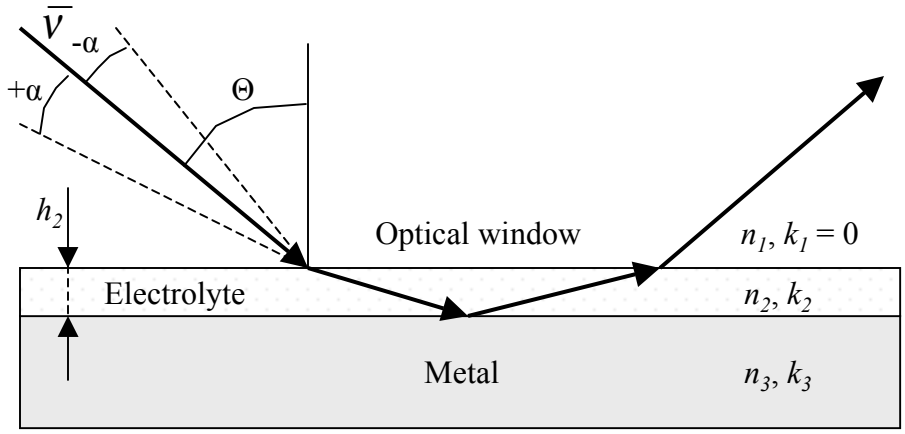

Figure 5.1.1 Stratified medium that models the experimental thin layer cell.
$\bar{\nu}$, ±α and Θ are the wavenumber, convergence and the angle of incidence of the infrared beam, respectively.
n,k and *h* are the refractive index, attenuation coefficient and thickness of the three phases that comprise the stratified medium, respectively.

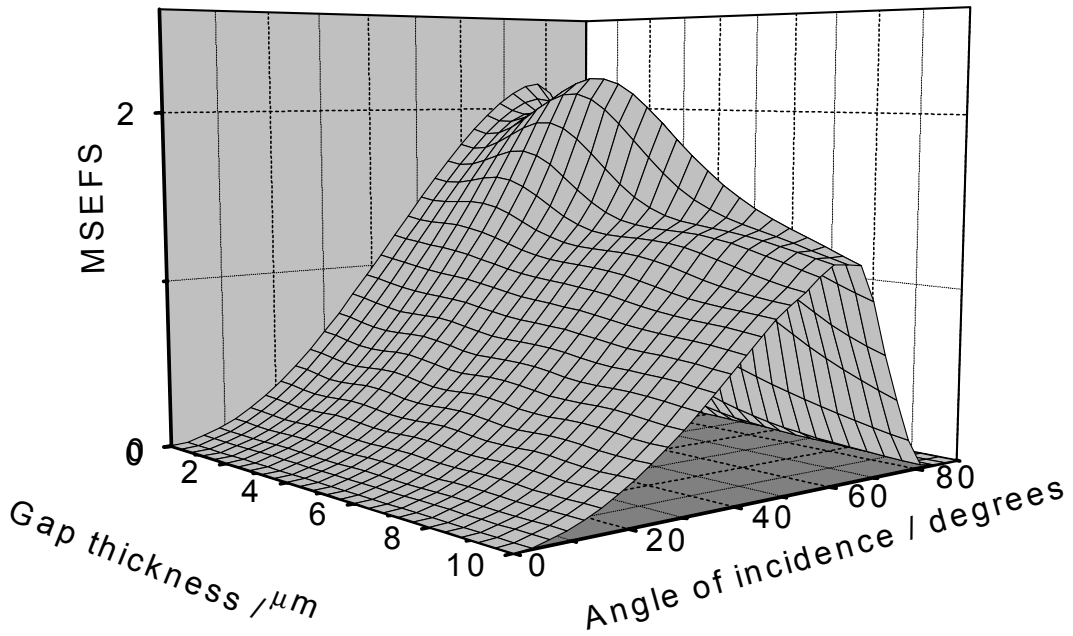

Figure 5.1.2 Mean squared electric field strength at the metal surface for a p-polarized beam as a function of the angle of incidence and the thin cavity (gap) thickness.
Calculated for the convergent ($\pm 6^0$) radiation of 1600 cm^{-1}.
For stratified medium: CaF_2 / D_2O / Au.

a function of these two variables. Figure 5.1.2 shows the MSEFS at the metal surface for the convergent ($\pm 6^0$) radiation of 1600 cm^{-1}, incident on the interface comprising CaF_2 , D_2O and Au. (To simulate the incident beam convergence, the calculations were done for several angles within the $\pm 6^0$ of convergence and then the results were averaged. Such an approach models the convergent incident beam with equal angular distribution of intensity.) The MSEFS reveals non-linear dependence on the angle of incidence and the thin cavity thickness, that displays a global maximum at the angle of 66^0 and the thin cavity thickness of 3.4 μm. Hence, these values were used during acquisition of experimental spectra in the frequency region of 1600 cm^{-1}. Figure 5.1.3 shows the angular and spatial profiles of the MSEFS surface at the global maximum. The value of the MSEFS at the maximum, equal to 2.2, indicates that the enhancement of the electric field strength is observed as the result of the constructive interference of the p-polarized light at the metal surface. This value is slightly higher than 1.84, the maximum value of the MSEFS calculated for the air-gold interface and convergent ($\pm 6^0$) radiation of 1600 cm^{-1}. The angular dependence of the MSEFS, shown in Figure 5.1.3 a, demonstrates that the electric field is reduced by about 20 % if the angle of incidence is set to 60^0, the value commonly used when the equilateral prism is employed. The spatial dependence of the MSEFS, presented in Figure 5.1.3 b, indicates that not only the angle of incidence but also the thin cavity thickness should be optimized to achieve the maximum MSEFS at the electrode.

It should be stressed that the above values of the optimum angle of incidence and thin cavity thickness are valid only for a specific frequency of the incident beam and cell configuration (window / electrolyte / metal). For example, when the electrolyte solvent is

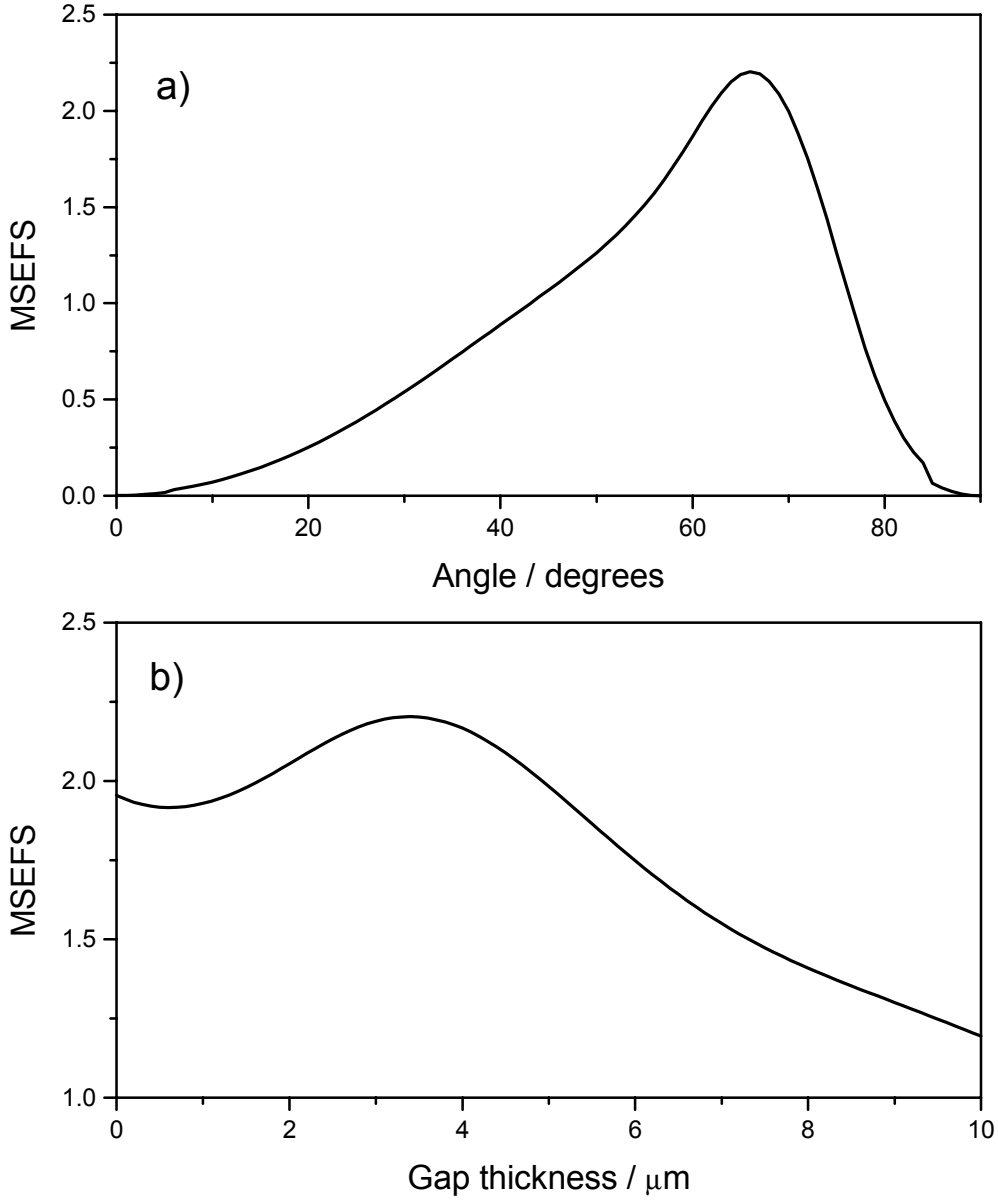

Figure 5.1.3 The mean squared electric field strength at the metal surface for a p-polarized beam as a function of:
a) the angle of incidence at the thin cavity thickness of 3.4 μm,
b) the thin cavity thickness at the angle of incidence of 66^0.
Calculated for convergent ($\pm 6^0$) radiation of 1600 cm^{-1}.
For stratified medium: CaF_2 / D_2O / Au.

changed to H_2O the calculations must be repeated and the cell realigned to attain new optimum experimental conditions. Below, the influence of the wavelength of the incident radiation will be demonstrated. Figure 5.1.4 presents the angular and spatial profiles of the MSEFS surface at the global maximum calculated for the incident radiation of 2850 cm^{-1}. Both profiles reveal profound differences from those calculated for the frequency of 1600 cm^{-1} and presented in Figure 5.1.3. The MSEFS maximum is located at the angle of 55^0 and the thin cavity thickness of 2.3 μm and attains the highest value of the MSEFS equal to 4.12. Comparison of this number with the value calculated for the air-metal interface under identical experimental conditions, equal to 1.79, clearly demonstrates the benefit of the use of the optical window. To fully utilize this advantage, however, both the angle of incidence and the thin cavity thickness should be set to the values where the maximum in the MSEFS is achieved.

Figure 5.1.4a demonstrates a very sharp decrease in the MSEFS when the angle of incidence is larger than 55^0. This behavior is typical in the proximity of the critical angle and the maximum in the MSEFS is observed "just below" the critical angle. This observation is in conflict with the conclusion given by Faguy *et al.* [6] that the maximum MSEFS is observed "just above" the critical angle. Note also that setting the angle of incidence to 60^0 would result in the loss of the MSEFS by approximately 20 %, similar value to the previous case when the incident radiation was 1600 cm^{-1}. In addition, Figure 5.1.4 b indicates that the decrease in the thin cavity thickness beyond the optimum value of 2.3 μm results in a significant reduction of the MSEFS at the electrode surface, approaching an almost twofold loss when the thin layer thickness reaches zero. Comparison of the results shown for the

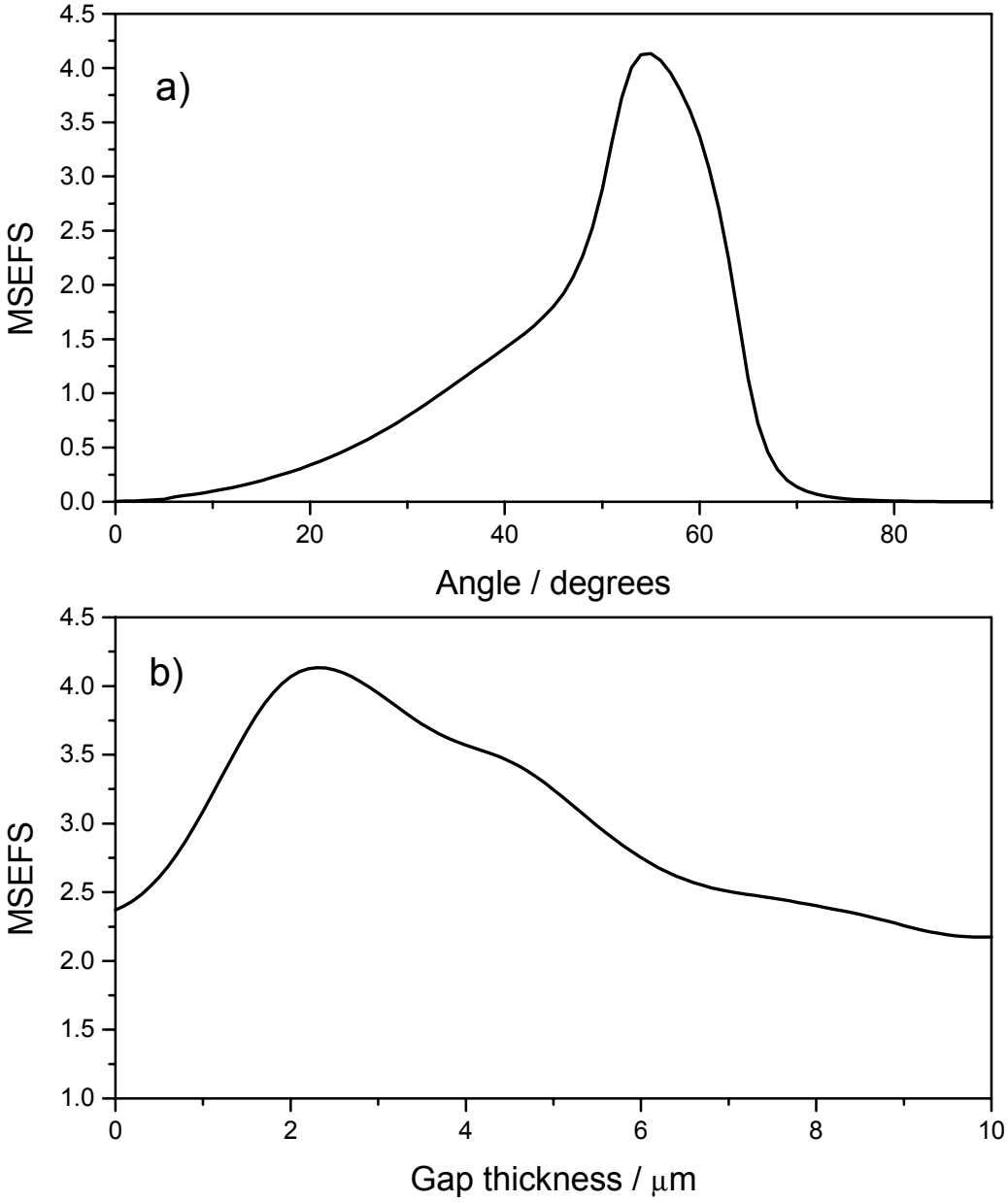

Figure 5.1.4 Mean squared electric field strength at the metal surface for a p-polarized beam as a function of:
a) the angle of incidence at the thin cavity thickness of 2.3 μm,
b) the thin cavity thickness at the angle of incidence of 55^0.
Calculated for convergent ($\pm 6^0$) radiation of 2850 cm^{-1}.
For stratified medium: CaF_2 / D_2O / Au.

frequency of the incident radiation of 1600 cm^{-1} in Figure 5.1.3 and 2850 cm^{-1} in Figure 5.1.4 clearly indicates that the experimental setup must be realigned for the data acquisition in each spectral region of interest.

5.1.2. The Choice of the Optical Window Geometry

Four types of optical windows are presently applied for electrochemical *in situ* IR RAS: flat disks, (usually equilateral) prisms, hemispheres and hemicylinders. Flat disks are disadvantegous because of significant losses in throughput (20-40 %) due to reflection from the front, air-window interface at high values of the angle of incidence. Hemispheres and hemicylinders act as lenses and can be utilized to collimate or refocus the incident beam. The difference between these two window types is that hemispheres focus the beam onto a spot while hemicylinders focus it onto a line. These focusing windows are usually made of high refractive index materials such as ZnSe, Ge or Si to achieve relatively short focal distances. (The focal distance of a hemisphere is equal to $r / (n\text{-}1)$, where r and n denote its radius and refractive index, respectively.) Even though the radiation is incident on the hemispheres and hemicylinders at the angles that approach normal incidence, the losses in throughput are still significant due to the high refractive index of the materials that are used in fabrication of these windows, reaching 30-80 % (for normal incidence). The exact values of the reflectivity at the air-window interface at normal incidence for several infrared window materials are shown in Table 5.1.1. The total losses of throughput due to reflection from the front, air-window interface are approximately twice as high as the corresponding reflectivities because the beam crosses the air-window interface twice. These losses can be significantly reduced with the help

Table 5.1.1 The refractive index, reflectance of the air-window interface (at normal incidence), the maximum MSEFS at the metal surface, the coordinates of the maximum (thin cavity thickness and the angle of incidence) and the full width at half maximum (FWHM) of the MSEFS for different optical window materials.

Material	n	R / %	MSEFS	Gap / μm	Angle / ^{0}	FWHM / ^{0}
CaF_2	1.38	2.5	2.6	4.4	69	19
BaF_2	1.44	3.2	3.6	4.3	63	10
ZnSe	2.42	17	9.8	4.1	31.8	4
Si	3.42	30	12.3	4	21.8	4.5
Ge	4.01	36	13.5	4.9	18.2	3.8

FWHM is shown for the dependence of the MSEFS on the angle of incidence.

Data in the table were calculated for a collimated (convergence $=\pm 1^0$) p-polarized radiation of 1600 cm^{-1} and stratified medium: Window / D_2O / Au.

of anti-reflective coatings. Unfortunately, anti-reflective coatings are fragile and diminish the frequency range in which the window is transparent for the incident radiation.

Prisms are made of low refractive index materials, such as CaF_2 and BaF_2 and cut to admit radiation at normal incidence. They have very small losses at the front, air-window interface (under 10 %). Although prisms do not alter the incident beam collimation, the collimated beam can be used with this type of optical window if additional lenses are utilized. Thus, in principle, the experimental setup can be assembled to use any infrared window material with either collimated or convergent incident beam, therefore the influence of the incident beam collimation on the MSEFS at the electrode surface will be considered below without reference to the particular optical window geometry.

5.1.3. The Effect of the Incident Beam Collimation

The calculation of the MSEFS was performed for incident radiation of 2850 cm^{-1} and the same stratified medium as in Section 5.1.1(CaF_2 / D_2O / Au), with the exception that the convergence of the incident beam was equal to $\pm 1^0$ instead of $\pm 6^0$. (A convergence of one degree was assumed in order to mimic the real collimated radiation rather than an ideally parallel beam.) Figure 5.1.5 shows the results of calculations in the form of the MSEFS surface profiles at the global maximum. The maximum of the MSEFS, equal to 9.0, is observed at the angle of 58^0 and the thin cavity thickness of 3.3 μm. This value is about twice as high as the value calculated for the convergent radiation (see Figure 5.1.4), indicating a significant advantage of the collimation of the incident beam. Such a gain in the MSEFS is typically observed in the proximity of the critical angle, achieved when the refractive index

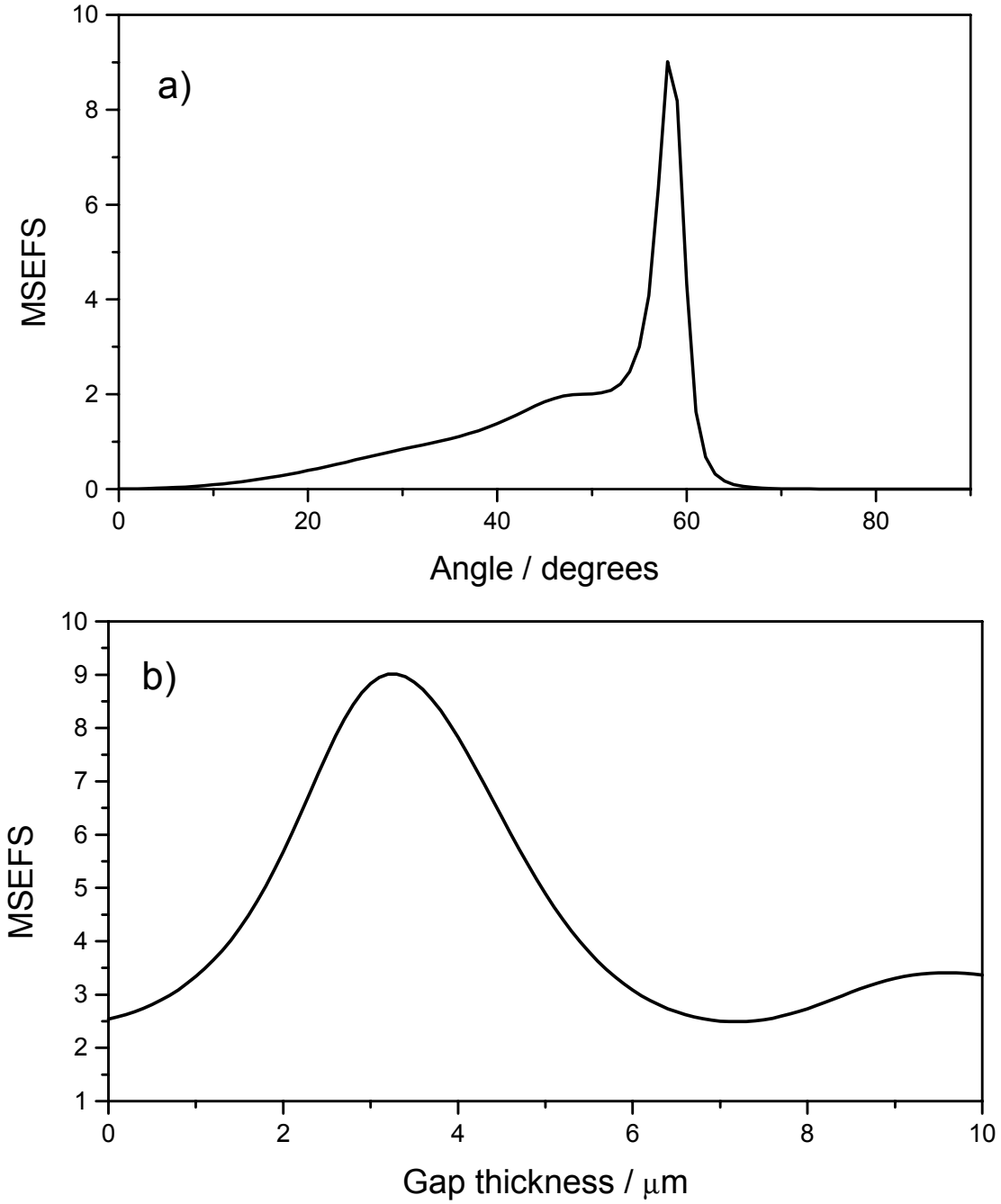

Figure 5.1.5 Mean squared electric field strength at the metal surface for a p-polarized beam as a function of:
a) the angle of incidence at the thin cavity thickness of 3.3 μm,
b) the thin cavity thickness at the angle of incidence of 58^0.
Calculated for collimated (convergence $=\pm 1^0$) radiation of 2850 cm^{-1}.
For stratified medium: CaF_2 / D_2O / Au.

of the optical window and that of the supporting electrolyte display a sharp contrast. Comparison of the MSEFS calculated for collimated and convergent radiation presented, respectively, in Figures 5.1.5 and 5.1.4 demonstrates that, in the case of the collimated radiation, the MSEFS plots display a sharper maximum, especially the dependence of the MSEFS on the angle of incidence. Since the maximum of the MSEFS is very sharp, it is more difficult to align the optical setup in order to fully utilize the benefits offered by the incident beam collimation.

5.1.4. Choice of the Optical Window Materials

Optical windows used in spectroelectrochemical cells have not only to be transparent for the infrared radiation but also to be insoluble in the supporting electrolyte. Such materials as Ge, Si, ZnSe and CaF_2 satisfy both these conditions. Application of CaF_2 has a limitation, however, because this material becomes opaque for infrared radiation in the frequency region below 1100 cm^{-1}. This drawback is removed if BaF_2, which has the absorbance cut-off at 800 cm^{-1}, is used instead. Unfortunately, it has about two orders of magnitude higher solubility in aqueous media. If, however, a moderately concentrated solution of NaF (0.1 M) is used as the electrolyte, deterioration of the window can be suppressed to such an extent that it does not exceed the dissolution rate of CaF_2 in dilute $KClO_4$ solution.

To compare the performance of different optical windows, the global maxima of the MSEFS at the metal surface were calculated for different materials and a collimated (convergence of $\pm 1^0$) radiation of 1600 cm^{-1}. The results are summarized in Table 5.1.1 (page 110). It is apparent that the larger the difference between the refractive index of D_2O (equal

to 1.32 at 1600 cm^{-1}) and the refractive indices of the window materials, the higher the values of the MSEFS at the metal surface. However, Si and Ge windows achieve the maximum of the MSEFS at very low values of the angle of incidence, rendering these materials impractical for reflection absorption spectroscopy because it is difficult to set such low angles without additional mirrors. In addition, the use of these materials may result in significant loses of total throughput due to reflection of the incident beam from the air-window interface, which exceeds 30 % from each air-window interface. Thus, it may be concluded that the best window material for reflection absorption spectroscopy is ZnSe. It allows one to achieve high values of the MSEFS, due to its high refractive index. In addition, the incident beam may be conveniently collimated if the hemisphere is used as a window in a setup described by Faguy *et al.* [6]. The reflection losses at the air-window interface for ZnSe are moderate and can be significantly reduced if an anti-reflective coating is used. The last column of Table 5.1.1 shows the values of the full width at half maximum of the MSEFS, which characterizes the sharpness of the MSEFS peak as a function of the angle of incidence. The data demonstrate that it is much more difficult to align the setup equipped with a ZnSe window, due to the very sharp maximum in the MSEFS.

While allowing the achievement of high values of the MSEFS, ZnSe has one disadvantage when employed for polarization modulation spectroscopy. The difficulty arises because of a significant difference in the reflectivities of the s- and p- polarized light at the window-electrolyte interface, which stems from the significant contrast in the refractive index of ZnSe and the aqueous electrolyte solution. Thus, only the first two materials (fluorides) are suitable for polarization modulation reflection absorption spectroscopy and BaF_2 is the

better of the two for the following reasons. Firstly, higher values of the MSEFS are attained for this material and secondly, the maximum of the MSEFS is observed at lower values of the angle of incidence. It is important to have moderate values of this angle because of a significant elongation of the footprint of the infrared beam at the electrode that occurs if the angles of incidence exceed 60^0.

The experimental evidence that demonstrates the advantages of using a ZnSe hemisphere instead of a CaF_2 prism as the optical window in SNIFTIRS studies is presented in Figure 5.1.6. The SNIFTIR spectrum of pyridine at the Au (110) electrode, acquired using a cell equipped with the ZnSe hemispherical window, is presented at the bottom of the graph and the SNIFTIR spectrum of pyridine at the Au (111) electrode, measured with the use of the CaF_2 equilateral prism. is shown at the top. The base potential E_1 = -0.75 V (SCE) is the potential of the total desorption of pyridine molecules from both electrode surfaces and the potential E_2 = 0.4 V (SCE) corresponds to the limiting surface concentration of pyridine, Γ_{max}. 6.2H10^{-10} mol cm^{-2}, at both gold surfaces. Figure 5.1.6 shows that the use of a ZnSe window allows one to record the SNIFTIR spectra in a much broader frequency range so that many more bands can be seen in the spectrum recorded with this window. In addition, consistent with the above discussion, the band at 1600 cm^{-1} is significantly stronger when the CaF_2 prism is replaced by the ZnSe hemisphere.

To verify this conclusion, the MSEFS of the p-polarized photons at the gold electrode surface were calculated for the incident radiation frequency of 1600 cm^{-1}. The calculations were performed for multilayer systems consisting of CaF_2 /D_2O/ Au and ZnSe/D_2O/Au at the angles of incidence of 60^o for the CaF_2 and 28.5^o for ZnSe and the thickness of the electrolyte

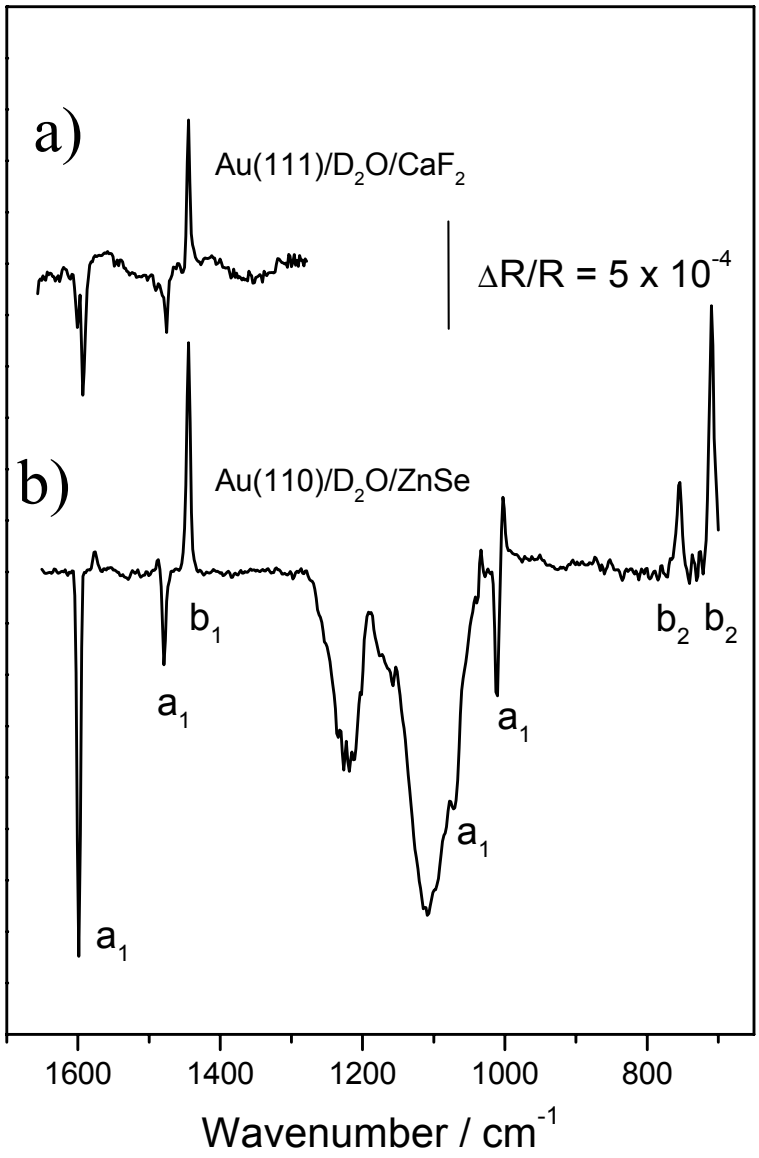

Figure 5.1.6 Comparison of the SNIFTIR spectra acquired using a cell equipped with the CaF_2 equilateral prism and the ZnSe hemisphere. Experimental cell configuration:
a) Au(111) / 0.003 M pyridine solution in D_2O / CaF_2 equilateral prism.
b) Au(110) / 0.001 M pyridine solution in D_2O / ZnSe hemisphere

For both spectra the sample potential E_2 = 0.4 V and the reference potential E_1 = -0.75 V (SCE).

layer of 7.2 μm. These values represent the conditions at which the experimental spectra were recorded. The calculated values of the MSEFS were equal to 3.6 for the ZnSe and 1.4 for CaF_2. These results suggest that a 2.6-fold enhancement of the infrared bands of the adsorbed species is expected when the CaF_2 prism is replaced by the ZnSe hemisphere. This result is consistent with approximately 2.9 times increased intensity of the a_1 mode in panel b compared to the a_1 mode intensity in panel a of Figure 5.1.6.

5.1.5. Determination of the Angle of Incidence and the Thin Cavity Thickness

In previous sections of this chapter it was demonstrated that it is important to control both the angle of incidence of the infrared beam and the thin cavity thickness of the spectroelectrochemical cell. Control of the angle of incidence is usually not associated with much difficulty, while measurement of the thin cavity thickness with a precision of fractions of a micrometer is not a trivial task. A new method of determination of these important parameters using the experimentally measured reflectivity of the thin layer cell is presented below.

The exact values of the angle of incidence and the thin layer thickness can be determined by measuring the reflectivity of the spectroelectrochemical cell and comparing this experimental reflectivity to the theoretical values simulated using Fresnel equations for the interface consisting of three parallel homogeneous phases. Figure 5.1.7 explains the principle of this method. The solid line denotes the reflectivity of the cell, equal to the ratio of the intensity of the beam reflected from the BaF_2 / D_2O / Au interface (I) and the intensity measured shortly before the electrolyte and the electrode were inserted into the cell (I_0). In

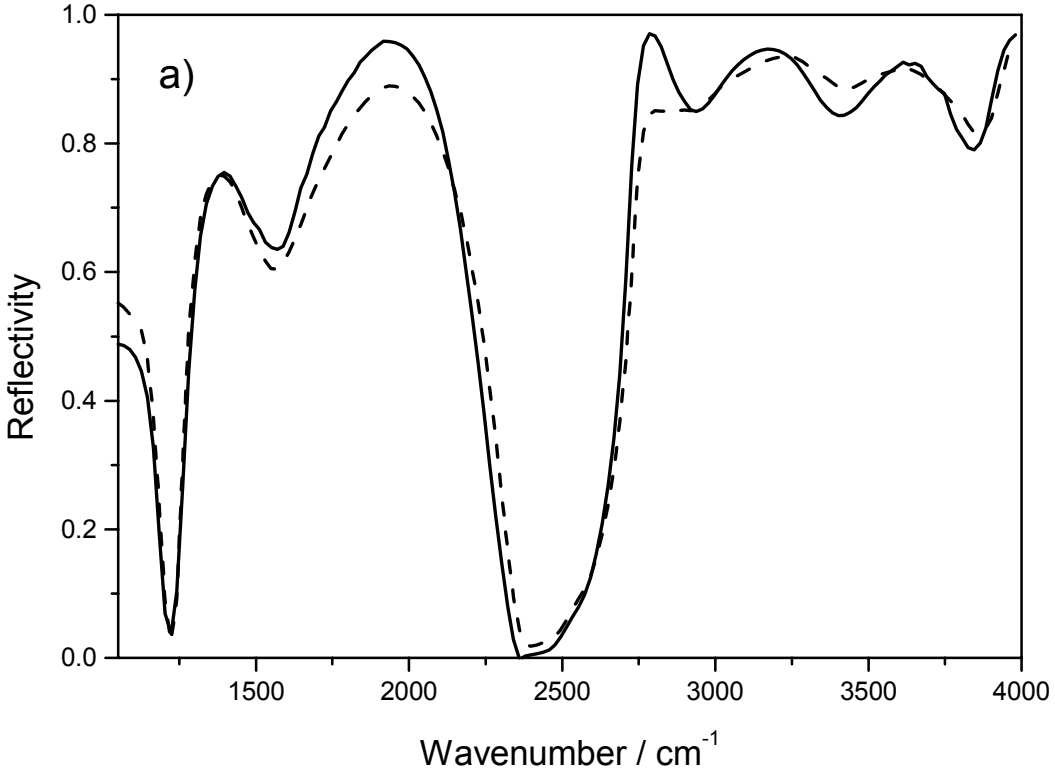

Figure 5.1.7 Reflectance spectra of the thin layer spectroelectrochemical cell composed of BaF_2 / D_2O / Au.
Solid line: experimental curve,
Dashed line: calculated curve, for the thin cavity thickness of 2.4 μm and the angle of incidence of 60^0

the absence of the electrolyte, the beam is totally reflected from the surface of the BaF_2 prism of the empty cell because the angle of incidence is above the critical angle for the BaF_2 / air interface. Hence, I_o is a good measure of the intensity of the incident beam. The dashed line in Figure 5.1.7 shows the simulated curve, calculated using the Fresnel equations in the matrix form (see Chapter 3) and the optical constants of the three parallel phases taken from the literature [2][3][4][5]. The software developed in this project altered the thickness of the thin layer of the electrolyte and the angle of incidence until the best fit of the simulated reflectivity to the experimental curve was achieved. The dashed line in Figure 5.1.7 is the best fit simulated curve obtained when the angle of incidence and the thin cavity thickness were equal to 60^o and 2.4 μm, respectively. The reasonably good match of the two curves indicates that the angle of incidence and the thin layer thickness used during simulation are close to the values that were set during the measurement of the experimental reflectivity of the thin layer spectroelectrochemical cell.

5.2. Experimental Data Processing

Raw infrared spectra collected during reflection absorption experiments are usually not suitable for direct quantitative analysis. This is because the spectra recorded using PM FTIR RAS contain artifacts imposed by the photoelastic modulator and spectra acquired using SNIFTIRS contain the optical signature of the molecules desorbed into the electrolyte bulk in addition to the response of the molecules adsorbed at the metal surface. The methods to remove these artifacts in order to obtain spectra which can be used for quantitative determination of the molecular orientation at the metal electrode are presented below.

5.2.1. PM FTIR RAS Correction

5.2.1.1.Removal of the Artifacts Introduced by the Photoelastic Modulator

Artifacts are introduced to PM FTIR spectra due to the variation of the retardation that is imposed by the PEM with the wavelength of the incident beam (see Chapter 3). As a result, the obtained PM FTIR RAS spectra have a slowly varying background that must be removed before their quantitative analysis. Buffeteau *et al.* [7] described three methods to remove this background: (i) subtraction of the mathematically modeled background, (ii) normalization of the spectrum of the interface that contains the organic film by the spectrum of a film-free interface and (iii) transformation of the PM FTIR RAS spectrum using independently obtained calibration spectra [8]. A method that is similar to the third approach was developed and used in this project. The distinctive feature of our method is that the two calibration spectra were determined experimentally and used to remove the PEM background. These spectra replace coefficients beside ΔI in either equation 3.5.16 or equation 3.5.21. (The coefficients are either Bessel functions or cosine terms, depending on the particular demodulation technique).

The correction of PM FTIR RAS spectra for the artifacts introduced by the PEM was executed in the following way. The spectroelectrochemical cell was replaced by the dielectric total external reflection mirror (a CaF_2 equilateral prism was used for this purpose). The second polarizer was inserted just after the photoelastic modulator (PEM) (see Figure 4.5.1) and set to admit p-polarized light (identical setting as that of the first polarizer). The PEM was turned off and the reference spectrum was acquired. This spectrum represents the intensity of the p-polarized light (I_p) that passes through the whole optical bench. Next, the

PEM was turned on and polarization modulation spectra were acquired. (The gain of the difference channel had to be set to unity during the acquisition of these calibration spectra.) Two spectra are obtained when the polarization modulation experiment is performed: one related to the average intensity of s- and p-polarized light $(I_s+I_p)/2$ and the other related to the difference between the intensity of the two polarizations (I_s-I_p). The first contains the zero order calibration spectrum CJ_0 while the second includes the second order calibration spectrum CJ_2. Note that theoretically zero and second order calibration spectra should be identical to zero and second order Bessel functions. The relationship between these calibration spectra and the measured intensity difference and intensity average spectra can be extracted from either equation (3.5.16) or equation (3.5.21), if the Bessel functions in equation (3.5.16) or the cosine terms in equation (3.5.21) are replaced by the corresponding calibration spectra

$$\frac{I_D(2\omega_m)}{I_D(0)} = \frac{\Delta I_\gamma \cdot CJ_2}{\langle I \rangle_\gamma + \frac{1}{2}\Delta I_\gamma \cdot CJ_0} \qquad (5.2.1).$$

Here $I_D(2\omega_m)$ and $I_D(0)$ denote the experimental intensity difference and intensity average signals after demodulation, respectively. CJ_2 and CJ_0 are, respectively, the second order and zero order calibration spectra while ΔI_γ and $\langle I \rangle_\gamma$ represent the intensity difference and the intensity average signals. The subscript γ indicates that these quantities may be different from the theoretical terms given in (3.5.16) or (3.5.21), due to the difference in the throughput of the optical bench for s- and p-polarized radiation. Since a second polarizer that admitted only

p-polarized light was used,

$$\Delta I_{\gamma} = I_p \qquad \text{and} \qquad \langle I \rangle_{\gamma} = \tfrac{1}{2} I_p \quad (5.2.2).$$

Combining equations (5.2.1) and (5.2.2), it can be demonstrated that the second order calibration spectrum can be determined *via* normalization of the experimental intensity difference signal by a reference spectrum (I_p):

$$\frac{I_D(2\omega_m)}{I_p} = \frac{\Delta I}{I_p} CJ_2 = CJ_2 \qquad (5.2.3).$$

Another calibration spectrum can be determined from the intensity average signal using a similar approach:

$$CJ_0 = 2\frac{I_D(0)}{I_p} - 1 \qquad (5.2.4).$$

Figure 5.2.1 shows the obtained calibration spectra plotted along with the theoretical Bessel functions (dotted lines), expected to be observed when the lock-in technique is used, and the cosine terms (dashed lines), that should be observed in our case because a synchronous sampling demodulator was used. Both calibration spectra show reasonable similarity in shape to the theoretically predicted dependences, yet they deviate significantly from both the Bessel functions and the cosine terms. Thus, experimental evidence demonstrates that it is better to determine the empirical calibration spectra than to rely on the theoretical functions.

Once the calibration spectra are determined, they can be employed to remove the

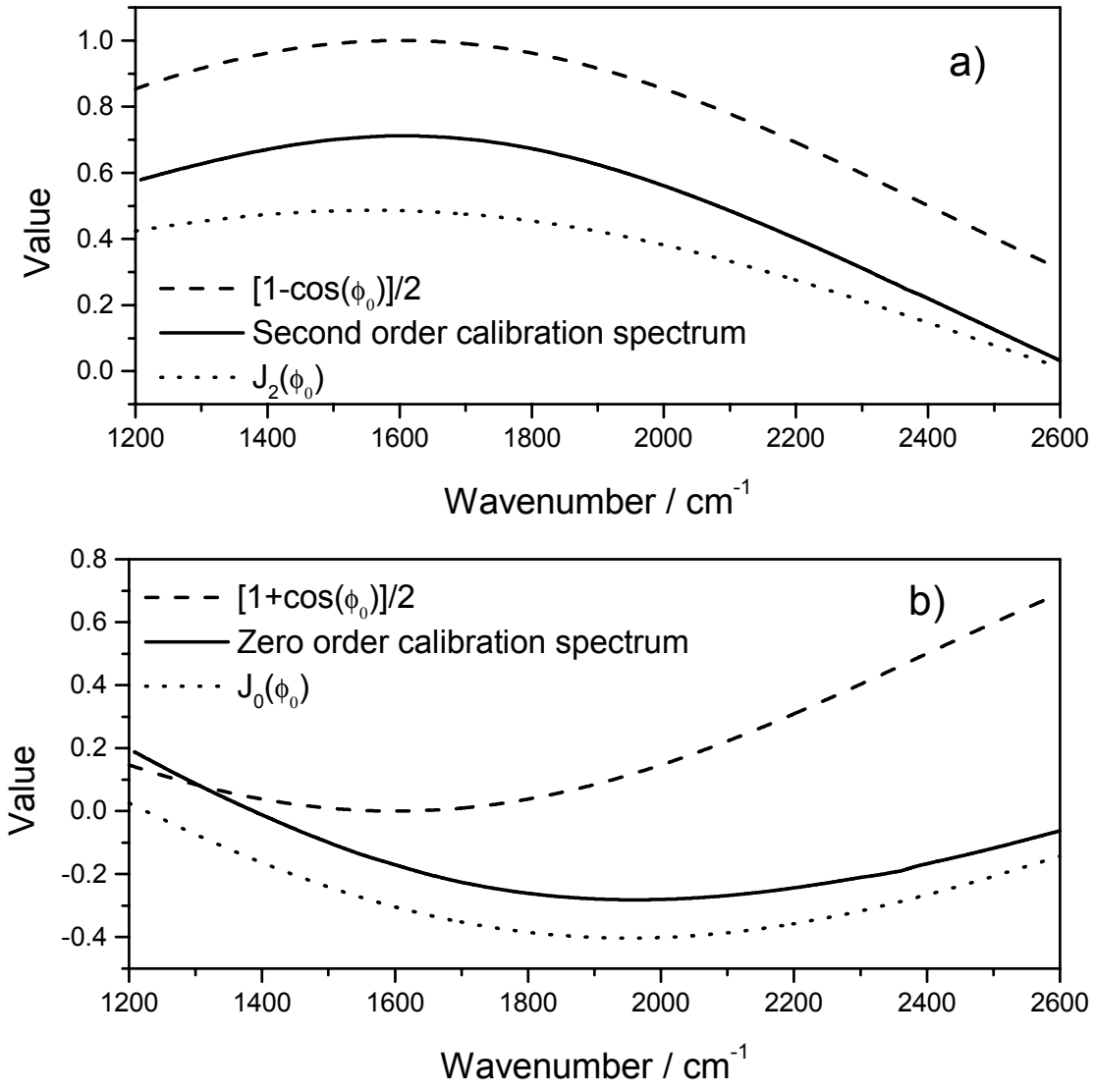

Figure 5.2.1 The theoretical response functions of the PEM and empirical calibration spectra.
a) second order and b) zero order.
Dotted line: theoretical Bessel functions,
Solid line: empirical calibration spectra,
Dashed line: theoretical cosine terms.
The PEM was optimized for 1600 cm^{-1}.

artifacts caused by the PEM from the experimental spectra. Rearrangement of equation (5.2.1) yields:

$$\frac{\Delta I_\gamma}{\langle I \rangle_\gamma} = \frac{\frac{I_D(2\omega_m)}{CJ_2}}{I_D(0) - \frac{1}{2}\frac{I_D(2\omega_m)}{CJ_2}CJ_0} \qquad (5.2.5),$$

where $\frac{\Delta I_\gamma}{\langle I \rangle_\gamma}$ is the PM FTIR RAS spectrum that was corrected to remove the artifacts introduced by the PEM, using empirical calibration spectra.

5.2.1.2 Correction for the Difference in the Optical Throughput for s- and p-polarized Radiation.

Another correction that is necessary for quantitative analysis was first pointed out by Buffeteau *et al.* [7]. It is aimed at the removal of the systematic error due to the difference in throughput of the optical setup for s- and p-polarized light. The derivation of a new procedure that was utilized in this project to perform correction for the difference in the throughput for s- and p-polarized radiation is described below.

After removal of the artifacts caused by the PEM using the technique described in the previous section, the difference ΔI_γ and the average $\langle I \rangle_\gamma$ signals become related to the

intensities of s- and p-polarized light in the following fashion:

$$\Delta I_\gamma = \left| I_s - \gamma I_p \right| \qquad \text{and} \qquad \langle I \rangle_\gamma = \frac{I_s + \gamma I_p}{2} \qquad (5.2.6),$$

where $\gamma = C_p/C_s$ is the ratio of the optical throughput of the experimental setup for p- and s-polarized radiation, respectively. After rearrangements of equations (5.2.6), one can obtain

$$I_s = \frac{\Delta I_\gamma}{2} + \langle I \rangle_\gamma \qquad \text{and} \qquad I_p = -\frac{1}{\gamma}\left(\frac{\Delta I_\gamma}{2} - \langle I \rangle_\gamma \right) \qquad (5.2.7),$$

thus the final corrected polarization modulation spectrum can be presented as

$$\frac{\Delta I}{\langle I \rangle} = \frac{I_s - I_p}{(I_s + I_p)/2} = 2\frac{(\gamma+1)\Delta I_\gamma + 2(\gamma-1)\langle I \rangle_\gamma}{(\gamma-1)\Delta I_\gamma + 2(\gamma+1)\langle I \rangle_\gamma} \qquad (5.2.8).$$

The throughput ratio $\gamma = C_p/C_s$ can be determined experimentally by taking the ratio of the two spectra acquired when the PEM is turned off and the static polarizer is set to admit p- and s-polarized radiation, respectively. (A separate experiment demonstrated that the MCT detector has a negligible difference in sensitivity to the s- and p-polarized light, hence the above procedure allows one to determine the throughput ratio due to the optical bench alone.) The measured values of the coefficient γ were close to unity. Nevertheless, they could have a significant influence on the final results because of the very low absorbance by ultrathin films of organic molecules. Thus, equation (5.2.8) was used to remove the bias imposed on the experimental data due to the anisotropy of the optical setup for the s- and p-polarized

radiation.

5.2.1.3. Background Subtraction

The last step in processing the experimental PM FTIR RAS spectra involves the subtraction of the background. When *in situ* experiments are performed, a slowly varying background is present in the PM FTIR RAS spectra because of the broad band absorbance of infrared radiation by the aqueous electrolyte. In addition, wavy patterns are sometimes visible in the experimental spectra, caused by the interference of the beam, reflected from the window-electrolyte interface, with the beam, reflected from the electrolyte-electrode interface. In contrast with *ex situ* experiments, it is very difficult (if possible) to measure the spectrum of the background alone for the spectroelectrochemical thin layer cell. This is why the procedure similar to that published by Barner *et al.* [9] was utilized to remove the baseline, created from the experimental data points using the spline interpolation. Successful interpolation requires knowledge of the exact positions of vibrations caused by the analyte and a little experience. The coordinates of the experimental data points that are to be used for building the spline are specified in a template file which is used to process the whole series of spectra, recorded at various electrode potentials. The use of the template minimizes the effect of inconsistency of the choice of the spline coordinates. Usually, several templates are tried to achieve the best results.

Figure 5.2.2 illustrates the procedure that was used to remove the baseline from the PM FTIR RAS spectrum of 4-pentadecylpyridine (C15-4Py) in the C-H stretching region. This procedure was used to process all the PM spectra that are presented in this thesis. Solid

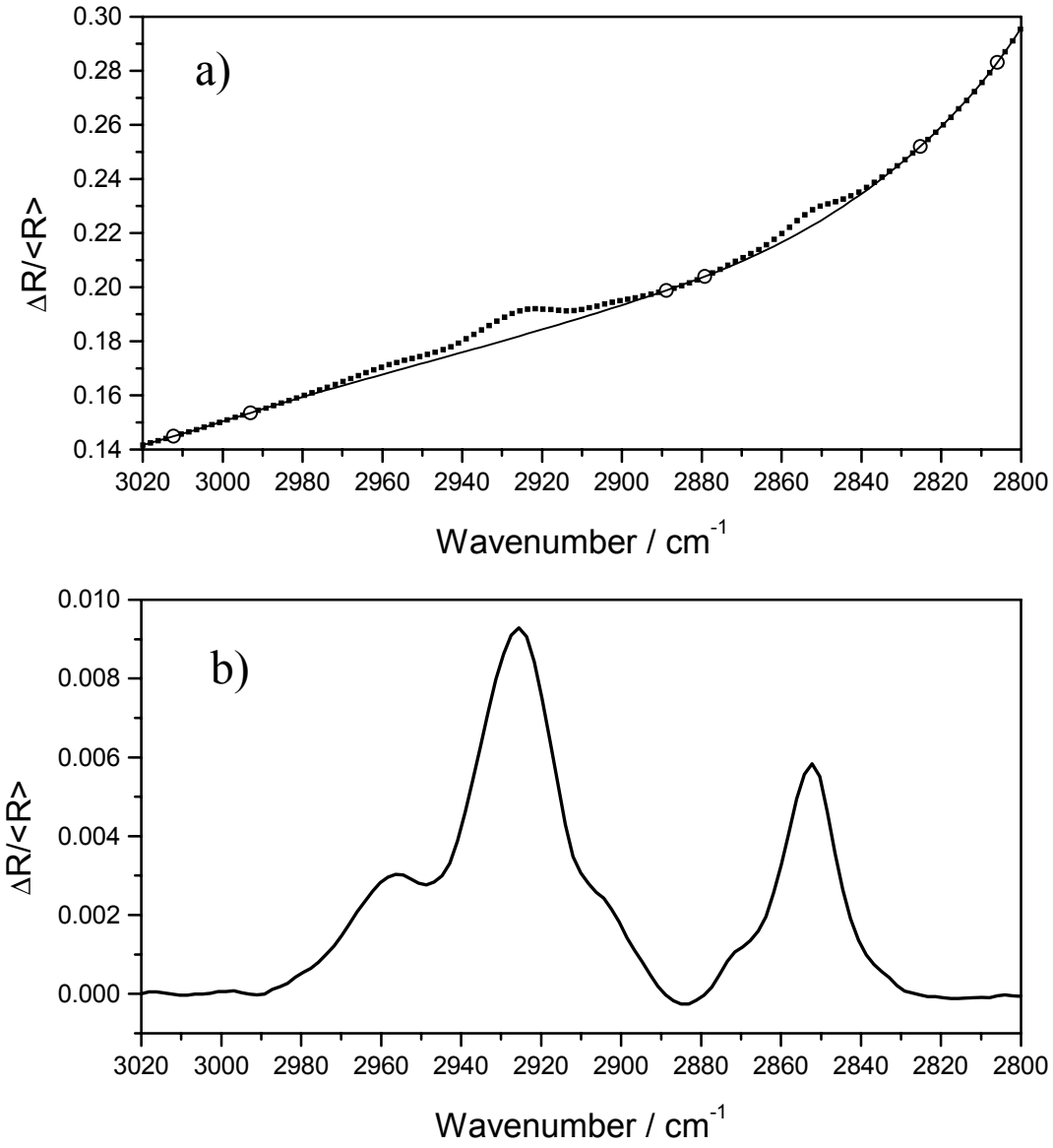

Figure 5.2.2 Baseline correction of an experimental PM FTIR RAS spectrum.
a) building the baseline from the original spectrum
Solid squares: experimental data points,
Open circles: data points used to build the spline,
Solid line: resulting background spectrum (spline).
b) the spectrum obtained after subtraction of the background
System: 4-pentadecylpyridine at the Au(111) electrode,
Electrode potential is equal to 0.1 V

squares denote the positions of the experimental points in the spectrum, open circles indicate the template data points that were used to build the spline, shown in the graph as a solid line. Subtraction of the background yields the baseline-corrected polarization modulation spectra, presented in panel b. Final spectra are proportional to absorbance, hence they display close similarity to the absorbance spectra of C15-4Py. After the above described corrections, they can be integrated and utilized to elucidate the orientation of organic molecules at the metal electrode, using the procedures described further in this chapter.

5.2.2. SNIFTIRS Decoupling

Subtractively normalized interfacial Fourier transform infrared spectroscopy (SNIFTIRS) is a technique that relies on the modulation of the electrode potential while the polarization of the incident beam is kept constant. Using this technique, the background reflectivity spectrum is recorded at very negative electrode polarizations when the analyte film is fully desorbed from the metal surface. The electrode potential is then stepped to the variable sample potential and another reflectivity spectrum is acquired. Subtraction of this background spectrum from the spectrum acquired at a variable potential followed by normalization by the background spectrum yields the SNIFTIR spectrum that contains the information about the surface concentration and orientation of the analyte at the metal surface. While SNIFTIR spectra are very important for qualitative characterization of the interfacial processes, they do not allow direct quantitative interpretation because they can be envisaged as the superposition of the spectral features of the adsorbed species acquired at variable sample potentials and the spectral signature of the molecules in the bulk recorded

when the background spectrum is acquired. In this section, a novel method is described that is used to decouple these two components of the SNIFTIR spectrum. Decoupling involves the theoretical simulation of the background spectrum (described in Section 5.3.4 of this chapter) followed by removal of the spectral signature of the background from the experimental SNIFTIR spectra. In order to calculate the background spectrum, one has to determine the angle of incidence, thin cavity thickness and the optical constants of the electrode, electrolyte and the optical window. The optical constants of the analyte were determined in an independent experiment that will be described in Section 5.3.2 of this chapter and the amount of the analyte at the metal surface is determined electrochemically [10].

As an example, Figure 5.2.3.A presents the simulated spectrum of 6.2×10^{-10} mol cm^{-2} of pyridine molecules in a 7.2 μm thick layer of D_2O between the gold electrode and the hemispherical ZnSe window. Spectrum B in this figure is the experimental SNIFTIRS spectrum. In order to compare the magnitude of the infrared bands in the SNIFTIRS spectrum and in the spectrum corresponding to the pyridine molecules inside the thin layer cavity, spectrum A and inverted spectrum B are overlaid in Figure 5.2.3 (A and -B). Finally, the bottom plot in the figure shows the spectrum of a monolayer of pyridine molecules adsorbed at the electrode as the result of SNIFTIRS decoupling. Note that one band in that spectrum, observed at ~1600 cm^{-1}, is stronger than the corresponding band in the SNIFTIRS spectrum, while the other band, located at ~1450 cm^{-1}, almost vanishes. This effect is observed because the first band arises mostly due to a preferentially aligned film of molecules adsorbed at the metal surface, while the other represents mainly the contribution of the

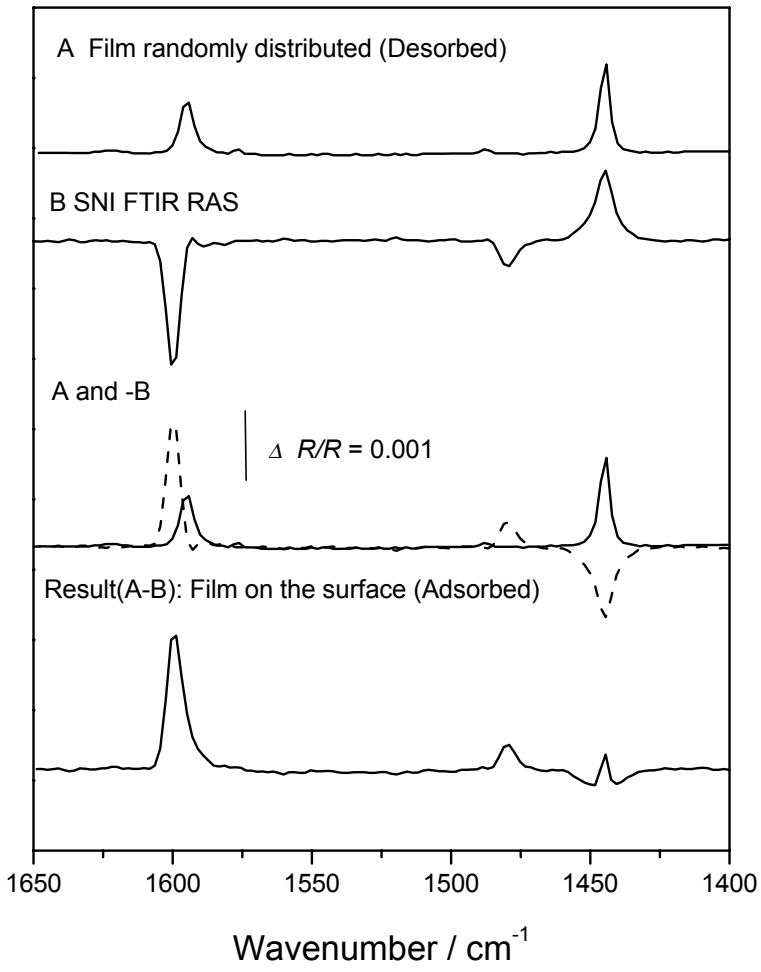

Figure 5.2.3 An illustration of the SNIFTIRS decoupling procedure.
A. Spectrum calculated for the slab of 6.2×10^{-10} mol cm^{-2} of pyridine molecules evenly distributed within the thin cavity between the optical window and the electrode.
B. SNIFTIR spectrum of 6.2×10^{-10} mol cm^{-2} of pyridine molecules.
A (solid) and –B (dashed) are, respectively, spectrum A and inverted spectrum B, overlapped.

The resulting spectrum at the bottom corresponds to the film of adsorbed pyridine molecules.
Cell configuration: ZnSe / 7.2 μm thick layer of 0.001 M solution of pyridine in D_2O /Au(110). SNIFTIR spectrum was obtained using the sample potential E_2 = 0 V and the background potential E_1 = -0.75 V (SCE).

randomly oriented desorbed species in the bulk. The bipolar features visible at the position of the second band indicate that the bands in the calculated and the SNIFTIRS spectra do not cancel each other exactly. This may be an artifact due to different values of resolution used to record the transmission spectrum, from which the optical constants for pyridine were calculated, and the SNIFTIRS spectrum, equal to 2 cm^{-1} and 4 cm^{-1}, respectively. Due to the lower resolution, the bands in the SNIFTIRS spectra are somewhat broader than the bands in the transmission spectrum. Indeed, when the band at ~1450 cm^{-1} in spectrum A-B is integrated, the integrated intensity of that band becomes close to zero.

The spectra, decoupled using the above procedure, are proportional to absorbance of a monolayer of pyridine molecules. Similarly to the processed PM FTIR RAS spectra, decoupled SNIFTIRS spectra can be integrated and used to determine the orientation of the surface species using the approach described below.

5.3. Determination of the Orientation of Organic Molecules at the Electrode Surface

After processing, the experimental spectra can be used for quantitative analysis. There are many papers that describe methods of determination of the molecular orientation from infrared spectra. A brief review of this field is given in this section first and is followed by a description of novel techniques that were used to determine the isotropic optical constants of analytes as well as to simulate PM FTIR RAS and SNIFTIRS spectra.

The most popular approach employed to determine the orientation of molecules at interfaces involves the comparison of the experimental spectra to those, simulated using the

optical constants of the analyte, determined in an independent experiment. The most widely used approach requires the determination of the anisotropic optical constants of the analyte. These constants can be calculated either from the data provided by experimental measurements [11][12][13][14] or from the isotropic optical constants [15]. Direct experiments involve measurements of a transmission spectrum of an analyte film deposited on the transparent optical window and the reflectance spectrum of the same molecules transferred to the surface of a metal mirror. The thickness of the deposits is typically measured using ellipsometry. Extreme care must be taken to preserve the orientation of films deposited on both substrates, which is sometimes difficult to achieve experimentally.

Because the electric field in the vicinity of the metal surface becomes anisotropic, the molecular orientation at the metal can be extracted using the isotropic optical constants of the analyte [15]. The approach that utilizes the isotropic constants was developed by Allara and co-workers [15][16][17][18]. The integrated absorbance of the analyte film at the metal surface (A) is proportional to the square of the dot product of the transition dipole $\vec{\mu}$ and the electric field of the photon $\vec{E}$ [1]:

$$A \propto \Gamma \left| \vec{\mu} \bullet \vec{E} \right|^2 = \Gamma \left| \mu \right|^2 \left\langle E^2 \right\rangle \cos^2 \Theta \qquad (5.3.1),$$

where ' is the surface concentration of the analyte, $|\mu|$ is the absolute value of the transition dipole moment, $\langle E^2 \rangle$ is the mean squared electric field strength (MSEFS) of the photon and Θ is the angle between the directions of the electric field of the photon and the transition dipole of a vibration in the molecule. Since, in the vicinity of a metal mirror, the electric field

is always normal to the metal surface [1], Θ always coincides with the angle between the transition dipole and the metal surface normal. Thus, equation (5.3.1) can be used to determine the orientation of molecules at the metal surface if the direction of the transition dipole can be related to the molecular geometry.

5.3.1. Two Methods Used to Determine Molecular Orientation

There are two techniques to determine the molecular orientation from equation (5.3.1). They were recently summarized by Arnold *et al.* [19]. The first approach, called the relative method, relies on availability of at least two intense absorption bands that correspond to differently oriented transition dipoles. To demonstrate how this method works, the C-H stretching region of a hydrocarbon chain is used as an example. Following equation (5.3.1), the ratio of the integrated absorbances of the CH_2 stretching bands to the integrated absorbances of the CH_3 stretching bands can be written as

$$\frac{A_{CH_2}}{A_{CH_3}} = \frac{\left|\mu_{CH_2}\right|^2}{\left|\mu_{CH_3}\right|^2} \cdot \frac{\cos^2 \Theta_{CH_2}}{\cos^2 \Theta_{CH_3}} \qquad (5.3.2).$$

Equation (5.3.2) demonstrates that the value of the surface concentration and the MSEFS is irrelevant if this method is exercised, because both bands of the spectrum are acquired simultaneously. For an isotropic sample, $\cos^2 1$ = 1/3, regardless of the vibrational mode, hence the ratio of the cosine terms in equation (5.3.2) becomes equal to unity. Thus, the ratio of the corresponding squares of the absolute transition dipole moments can be determined

from the absorbance spectra of an isotropic analyte sample. The methyl group of the hydrocarbon chain is quite mobile, hence the transition dipoles associated with this group often have no preferential orientation. In this case, one can assume that $\cos^2 \Theta_{CH_3} = 1/3$ and equation (5.3.2) then becomes transformed to

$$\frac{A^R{}_{CH_2}}{A^R{}_{CH_3}} = \frac{A^T{}_{CH_2}}{A^T{}_{CH_3}} \cdot \frac{\cos^2 \Theta_{CH_2}}{1/3} \qquad (5.3.3).$$

Here A^R and A^T, respectively, denote the integrated absorbances of a preferentially oriented analyte film at the metal mirror (obtained using the reflection absorption technique) and the absorbance of an isotropic sample of analyte (measured using transmittance spectroscopy). The relative method is very useful when either the surface concentration is not available or the MSEFS is difficult to calculate. However, this method yields the orientation of one transition dipole relative to the other, hence the absolute values of the tilt angle could be obtained only when the orientation of the transition dipole corresponding to one of the observed bands is known.

The second technique, developed by Allara *et al.* relies on calculation of the theoretical reflection absorption spectrum for the same angle of incidence and the thin cavity thickness as the values used during the collection of the experimental data. The optical constants of the window, electrolyte and metal can be taken from the literature [2][3][4][5] while the isotropic optical constants of the analyte sample are to be determined using an

independent measurement. Using equation (5.3.1) one can derive

$$\frac{A^{R}{}_{Exp}}{A^{R}{}_{Theor}} = \frac{\cos^2 \Theta}{1/3} \qquad (5.3.4),$$

where $A^{R}{}_{Exp}$ denote the experimental integrated absorbance of the analyte film at the metal, recorded using reflectance absorbance spectroscopy, and $A^{R}{}_{Theor}$ is the simulated integrated absorbance, calculated using the isotropic optical constants of the analyte film. Other terms of equation (5.3.4) (Γ , $\langle E^2 \rangle$ and $|\mu|^2$) disappear from the ratio because the simulation is done for the same Γ , the angle of incidence, the thin cavity thickness and assuming that $|\mu|^2$ is the same during measurements of the optical constants and RAS experiments. The main advantage of this method is that the absolute value of Θ can be determined directly. However, supplementary information about the surface concentration, the angle of incidence, the thin cavity thickness and the optical constants of the analyte is necessary for relevant modeling.

5.3.2. Determination of the Isotropic Optical Constants in Aqueous Solutions

The isotropic optical constants of the analyte are usually determined from the transmittance spectra. A pressed pellet, prepared by grinding the dispersion of the analyte with KBr or KCl powder is typically used as a sample. It has recently been demonstrated by

Arnold *et al.*[19] that this method may yield irreproducible results due to different histories of the sample preparation. In addition, the optical constants determined using the powder method may be quite different from the optical constants of the analyte film at the metal-electrolyte interface due to the difference in an environment. A novel technique was developed in this project that allows one to determine the optical constant of an analyte in an aqueous environment using a solution of analyte in a liquid, water-containing solvent as the sample. Such an approach should, in our opinion, yield the optical constants that would be better suited for modeling the spectra of molecules adsorbed at the metal-electrolyte interface.

The technique described by Allara *et al.* [16] was adapted to determine the optical constants of an analyte in aqueous (or binary methanol-aqueous) solution. A thin layer transmission optical cell, shown in Figure 5.3.1, was employed to obtain the experimental data. Two ZnSe or BaF_2 discs were used as windows and a 10 or 25 μm thick Teflon gasket was used as a spacer. The cell was placed in a Teflon housing, clamped between two aluminum plates and mounted inside the main compartment of an FTIR spectrometer. Teflon tubing was used to fill the cell with fluid samples. Two samples were necessary to acquire a set of experimental spectra needed for calculations: the pure solvent was used as a background sample and the dilute solution of an analyte (fractions of a percent) was used as the analyte sample. The concentration of the solution was determined using an analytical balance during their preparation. The precise value of the separation between the optical windows was determined experimentally from the number of interference fringes in the spectrum recorded when the thin layer cell was empty [20]. An interference pattern (see Figure 5.3.2. panel a) arises due to the multiple reflections from the internal walls of the cell.

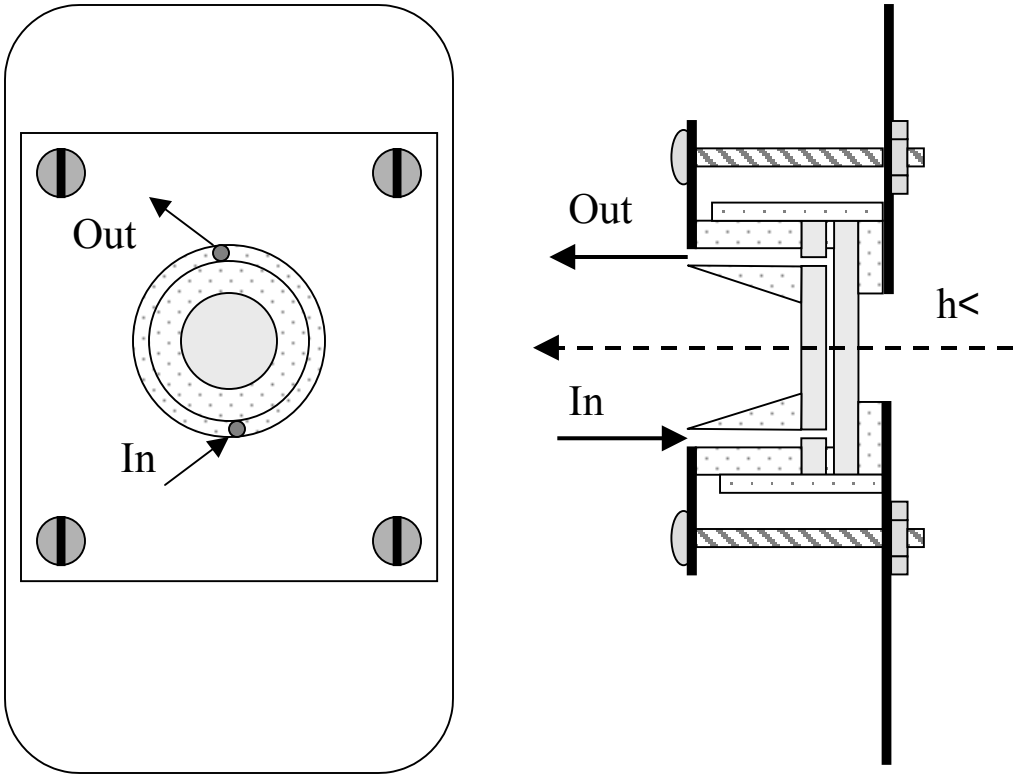

Figure 5.3.1 Schematic diagram of a thin layer flow cell used to determine the optical constants of an analyte in aqueous solution.

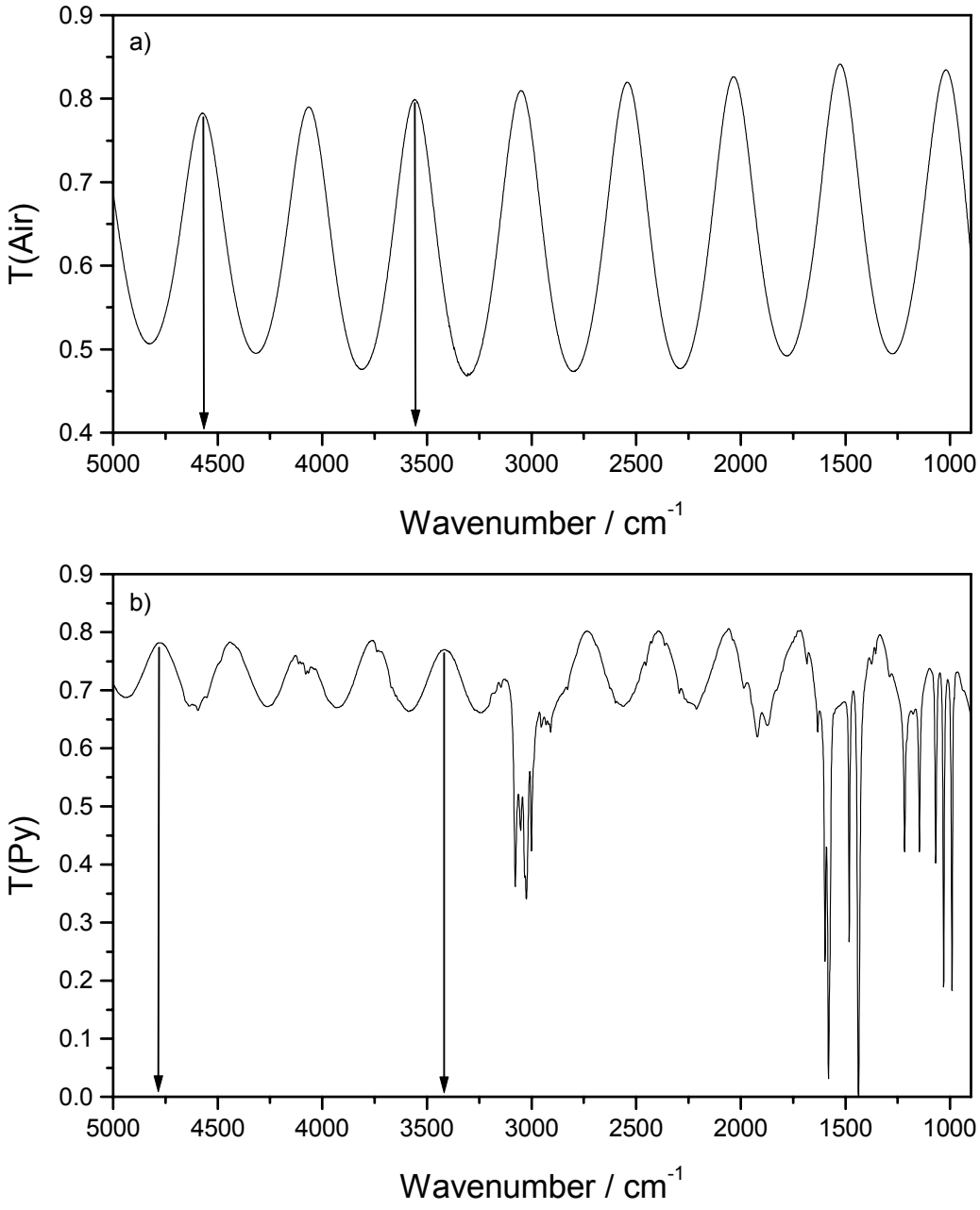

Figure 5.3.2 a) transmittance of the empty cell,
b) transmittance of the cell filled with neat pyridine.
The cell: ZnSe windows separated by a 10 μm Teflon spacer.

It can be shown [21] that the number of the interference fringes ΔN in a the frequency range $\bar{\nu}_1 - \bar{\nu}_2$ is related to the cell thickness d in the following fashion

$$d = \frac{\Delta N}{2n_\infty(\bar{\nu}_1 - \bar{\nu}_2)} \qquad (5.3.5),$$

where n_∞ is the average refractive index of the medium within the cell.

Figure 5.3.2 illustrates the principle of the method that was used to determine the thin layer cell thickness and the refractive index of liquid samples using equation (5.3.5). Panel a shows the transmittance of an empty cell (n_∞ = 1) equipped with ZnSe windows and a ~10 μm thick Teflon spacer. The arrows point to an interval (from 4575 cm^{-1} to 3557 cm^{-1}) that includes 2 full interference fringes. Using equation (5.3.5) one can calculate the exact thickness of the cell (9.82 μm). If the cell is filled with a neat analyte sample (liquid pyridine or C15-4Py for example), equation (5.3.5) can be utilized to determine the average refractive index of the analyte in the mid infrared. Panel b shows the transmittance of neat pyridine as an example. The arrows point to an interval between 4776 cm^{-1} and 3415 cm^{-1} that includes 4 fringes. Using the previously calculated value of *d,* the average refractive index of the analyte in the mid infrared can be determined (n_∞ = 1.49 for pyridine). This value is needed for calculation of the refractive index spectrum from the spectrum of the attenuation coefficient, with the help of Kramers-Krönig transformation.

The isotropic optical constants of the analyte can be calculated using the transmittance spectra of the analyte solution and pure solvent as well as the concentration and the average

refractive index of the analyte, plus the thickness of the cell and the optical constants of the optical windows and the solvent. The calculation procedure consisted of the following steps:

Step 1. The approximate values of the attenuation coefficient of the analyte k_i were determined from the two transmittance spectra using the Lambert law [22] modified to take into account dilution of the analyte (the Beer-Lambert law):

$$\frac{I}{I_0} = \exp\left(\frac{-4\pi f_i k_i d}{\lambda}\right) \quad (5.3.6),$$

where I and I_o are the intensities of radiation transmitted through the thin layer cell filled with the analyte solution and the pure solvent, respectively, d is the thickness of the thin layer cell, λ is the wavelength of the incident infrared radiation in vacuum and f_i is the volume fraction of the analyte in the sample. It can be calculated using the following equation:

$$f_i = C_i \frac{M_i}{\rho_i} \quad (5.3.7),$$

where C_i is the molar concentration, M_i is the molar mass and ρ_i is the density of the analyte in the solution. (It is important to note that such an approach allows one to determine the attenuation coefficients of the pure analyte that preserves solvent-analyte interactions taking place in aqueous environment. The obtained values of k_i for pure analyte are hypothetical quantities that are used to calculate k for analyte solutions of different concentrations.)

Step 2. Using these values of k_i as an initial estimate, the approximate values of the refractive indices of pure analyte n_i were determined using the Kramers-Krönig transformation

[23]:

$$n_i(\bar{\nu}_0) = n_\infty + \frac{2}{\pi} P \int_{\bar{\nu}_1}^{\bar{\nu}_2} \frac{\bar{\nu} k_i(\bar{\nu})}{(\bar{\nu}^2 - \bar{\nu}_0)} d\bar{\nu} \qquad (5.3.8)$$

where n_∞ is the average refractive index in the mid infrared that represents the contribution to the refractive index of regions removed from any absorption band. *P* indicates that the Cauchy principal value of the integral must be taken because of the singularity at $\bar{\nu} = \bar{\nu}_0$ and $\bar{\nu}_1$ and $\bar{\nu}_2$ are the lower and the upper limit of the spectrum of *k*, respectively.

Step 3. The refractive indices and attenuation coefficients of the solution were calculated using the following equations [24]:

$$\frac{\sum x_i M_i}{\rho} \frac{n^2 - 1}{n^2 + 2} = \sum x_i \frac{M_i}{\rho_i} \frac{n^2{}_i - 1}{n^2{}_i + 2} \qquad (5.3.9),$$

$$\frac{\sum x_i M_i}{\rho} k = \sum x_i \frac{M_i}{\rho_i} k_i \qquad (5.3.10),$$

where ρ and ρ_i denote the densities of the solution and the pure component *i* of the solution, *n, k* and n_i, k_i are the corresponding refractive indices and attenuation coefficients, x_i is the mole fraction and M_i is the molar mass of the component *i*.

Step 4. The approximate values of *n* and *k* of the solution were used as starting values

in the exact Fresnel equations (see Chapter 3) to calculate the theoretical transmittance spectrum. This spectrum was computed as the ratio of the simulated spectrum, corresponding to the analyte solution, and the simulated background spectrum of the pure solvent. Both spectra used a thin layer, sliced between the two optical windows, as the model of the transmission cell. In one case, the layer was represented by the optical constants of the pure solvent and in the other case, it had the optical constants of the solution, calculated using equations (5.3.9) and (5.3.10).

Step 5. The attenuation coefficients of the analyte k_i were perturbed at each wavelength and used to calculate the refractive indices n_i using equation (5.3.8). Both optical constants were then used to calculate the optical constants of the solution using equations (5.3.9) and (5.3.10). The attenuation coefficients of the solution were later used to calculate another theoretical transmittance spectrum using the approach, described in Step 4.

Step 6. Both theoretical transmittance spectra (obtained in Step 4 and Step 5) were compared with the experimental transmittance and a refined spectrum of attenuation coefficients k_i, was obtained. (Steps 5 and 6 implement the Newton-Raphson iterative method of numerical solutions of non-linear and transcendental equations [25].)

Step 7. Refined attenuation coefficients k_i were used to calculate the improved refractive indices n_i using equation (5.3.8) and Steps 4-7 were repeated, using the refined values of k_i and n_i as an initial estimate in Step 4, until the theoretical spectra deviated from the experimental transmittance by no more than a specified value of precision.

The procedure was highly convergent and usually two itterations were enough to achieve the final set of optical constants that yielded the theoretical spectrum within 1 %

deviation from the measured transmittance.

5.3.3. Simulation of PM FTIR RAS Spectra

Once the optical constants of the analyte are determined from the transmittance measurements, they can be used to simulate the reflectance spectra using Fresnel equations, given in Chapter 3. The angle of incidence and the thin cavity thickness were determined during the acquisition of the experimental spectra and the optical constants of the windows, metals and electrolytes were taken from the literature [2][3][4][5]. Since the optical constants of the analyte were determined using an isotropic sample, a film of randomly oriented molecules of analyte deposited on the metal surface could be modeled using these optical constants. The thickness and the surface concentration of the model film was determined experimentally using neutron reflectometry and chronocoulometry. Non-homogeneous or patchy films were modeled theoretically as homogeneous mixtures of the analyte and the solvent using equations (5.3.7.) and (5.3.9). (It was assumed that this approach is valid if the size of the defects is smaller than the wavelength of infrared radiation).

The spectra simulated using the isotropic optical constants are very convenient to use because all the transition dipoles of the analyte molecules in such films assume no preferential orientation in space. In such a case $\cos^2 1 = 1/3$ in equation (5.3.1) for all the vibrational modes and equation (5.3.4) can be applied to find the molecular orientation using any infrared band of interest. The simulated polarization modulation spectra are obtained from the calculated reflectivities of the model cell for the s- and p-polarized light (R_s and R_p) using equation (2.3.2) given in Chapter 2:

$$\frac{\Delta R}{\langle R \rangle} = \frac{\left| R_s - R_p \right|}{(R_s + R_p)/2}.$$

This equation was used for simulation of theoretical spectra that were later utilized for integration and determination of the orientation of organic molecules from equation (5.3.4).

5.3.4 Simulation of SNIFTIR Spectra

Quantitative analysis of SNIFTIRS requires two theoretical spectra to be simulated:(i) the SNIFTIR spectrum of the analyte desorbed into the electrolyte solution and (ii) the SNIFTIRS spectrum of the analyte adsorbed at the metal electrode. The first spectrum is required for SNIFTIRS decoupling and the second is needed for quantitative determination of the molecular orientation at the metal-solution interface. These two spectra can be envisaged as two components of the SNIFTIR spectrum of the Γ molecules of the analyte obtained at the base and variable potentials, respectively, where Γ denotes the surface concentration. Subtraction of the first spectrum from the second yields a full SNIFTIR spectrum. Simulation of both theoretical spectra requires knowledge of the surface concentration, angle of incidence, thin cavity thickness and the isotropic optical constants of the analyte, window material and the electrode. All these quantities can be determined experimentally.

The simulation of the first spectrum was performed using the following equation:

$$\left(\frac{\Delta R}{R}\right)_S = \frac{R(\Gamma_S) - R(0)}{R(0)} \qquad (5.3.11),$$

where $R(\Gamma_S)$ denotes the reflectivity of the stratified medium (window / electrolyte / metal) that contains a homogeneous solution of Γ molecules of the analyte in the electrolyte, and $R(0)$ is the reflectivity of the same stratified medium in the absence of the analyte. The corresponding reflectivities were calculated using the Fresnel equations in the matrix form described in Chapter 3.

The simulation of the second spectrum was performed using a similar approach:

$$\left(\frac{\Delta R}{R}\right)_M = \frac{R(\Gamma_M) - R(0)}{R(0)} \qquad (5.3.12),$$

where $R(\Gamma_M)$ denotes the reflectivity of the stratified medium (window / electrolyte / metal) that contains a film of Γ molecules of the analyte at the metal electrode. To verify that subtraction of equation (5.3.11) from equation (5.3.12) yields the SNIFTIR spectrum, one can perform the following derivations:

$$\frac{R(\Gamma_M) - R(0)}{R(0)} - \frac{R(\Gamma_S) - R(0)}{R(0)} = \frac{R(\Gamma_M) - R(\Gamma_S)}{R(0)} \qquad (5.3.13),$$

since $R(\Gamma_M) - R(\Gamma_S) << R(0)$ and $R(0) \approx R(\Gamma_S)$, one can write

$$\frac{R(\Gamma_M) - R(\Gamma_S)}{R(0)} \approx \frac{R(\Gamma_M) - R(\Gamma_S)}{R(\Gamma_S)} = \left(\frac{\Delta R}{R}\right)_{SNIFTIRS} \qquad (5.3.14).$$

These simulated spectra of desorbed and adsorbed analyte were used for SNIFTIRS decoupling and determination of the molecular orientation as described in Sections 5.2.2 and

5.3.1, respectively.

5.4. Summary

This chapter has demonstrated the influence of such parameters of the experimental setup as the angle of incidence, the collimation of the incident beam, the thin cavity thickness and the choice of the optical window on the mean squared electric field strength (MSEFS) of p-polarized radiation at the metal surface. It was shown that ZnSe and BaF_2 are the best materials for SNIFTIRS and PM FTIR RAS, respectively. In addition, it was demonstrated that collimation of the incident beam is very beneficial, especially if the critical angle can be achieved for the window-electrolyte interface. It is suggested that the best angle of incidence and thin cavity thickness should be calculated for every region of interest in the infrared spectrum. In addition, a new method was described to measure the thin cavity thickness of the spectroelectrochemical cell, which provided the key parameter of the thin layer cell needed in the quantitative analysis of the experimental spectra.

The second part of this chapter has demonstrated how to convert the experimental spectra acquired using PM FTIR RAS and SNIFTIRS into the data that can be used for quantitative analysis. Three corrections were necessary for processing the *in situ* PM FTIR RAS spectra. The first was aimed at the removal of the non-linear response of the optical bench caused by the photoelastic modulator. Measurement of two additional calibration spectra was required to achieve this goal. The second correction was designed to remove the difference in the response of the optical bench to the p- and s-polarized radiation. Finally, the third adjustment was needed to remove the broad band absorption and the interference due

to the thin layer of aqueous electrolyte.

A novel method to decouple the SNIFTIR spectra from the optical response of the analyte desorbed into the electrolyte bulk was also described. The decoupling was done by the removal of the spectrum simulated using the experimental data such as the angle of incidence, thin cavity thickness, surface concentration of the analyte and the optical constants of the metal, electrolyte and the optical window.

Two methods to determine the orientation of the analyte molecules at the metal surface were reviewed in the third part of this chapter and a novel simple technique to obtain the isotropic optical constants of the analyte from its aqueous solutions was described. In our opinion, this simple approach yields the optical constants that should aid in more relevant modeling of thin organic films at the metal-aqueous electrolyte interfaces than the optical constants determined using KCl pellets containing dispersions of the analyte. Finally, the procedures used to model the PM FTIR RAS and SNIFTIRS spectra were given at the end.

The methods described in this chapter were applied for the design of the experimental setup and for the quantitative analysis of the obtained infrared spectra that will be presented further in this thesis.

References

1. M. Moskovits, J. Chem. Phys., 77 (1982) 4408.

2. E.D. Palik (Ed.), Handbook of optical constants of solids. Academic Press, London (1998).

3. M.A. Ordal, L.L. Long, R.J. Bell, S.E. Bell, R.R. Bell, R.W. Alexander, Jr., and C.A.

Ward, Appl. Opt., 22 (1983) 1099.

4. A.N. Rusk, D. Williams and M. Querry, J. Opt. Soc. Am., 61 (1971) 895

5. J.E. Bertie, M.K. Ahmed and H.H. Eysel, J. Phys. Chem., 93 (1989) 2210.

6. P. Faguy and N.S. Marinkovi$f$, Appl. Spec. 50 (1996) 394.

7.T. Buffeteau, B. Desbat and J.M. Turlet, Appl. Spec. 45 (1991) 380.

8. T. Buffeteau, B. Desbat, D. Blaudez and J.M. Turlet Appl. Spec. 54 (2000) 1646.

9. B.J. Barner, M.J. Green, E.I. Sáez and R.M. Corn, Anal. Chem. 63 (1991) 55.

10. J. Richer and J. Lipkowski, J. Electrochem. Soc. 133 (1986) 121.

11. T. Buffeteau and B. Desbat, Appl. Spec. 6 (1989) 1027.

12. T. Buffeteau, D. Bladez, E. Péré and B. Desbat, J. Phys. Chem. B 103 (1999) 5020.

13. D. Blaudez, F. Boucher, T. Buffeteau, B. Desbat, M. Grandbois and C. Salesse, Appl. Spec. 53 (1999) 1299.

14. F. Picard, T. Buffeteau, B. Desbat, M. Auger and M. Pézolet, Biophys. J. 76 (1999) 539.

15. A.N. Parikh and D.L. Allara, J. Chem. Phys. 96 (1992) 927.

16. D. L. Allara, A. Bacca and C.A. Pryde, Macromolecules 11 (1978) 1215.

17. D.L. Allara and J.D. Swalen, J. Phys. Chem. 86 (1982) 2700.

18. D.L. Allara and R.G. Nuzzo, Langmuir 1 (1985) 52.

19. R. Arnold, A. Terfort and C. Wöll, Langmuir 17 (2001) 4980.

20. D.A. Skoog, Principles of Instrumental Analysis, third edition, CBS College Publishing, New York (1985) 341.

21. N. Li, V. Zamlynny, J. Lipkowski, F. Henglein, B. Pettinger, J. Electroanal. Chem. 524-525 (2002) 43.

22. J.D.E. McIntyre, in P. Delahay, C.W. Tobias (Eds.), Advances in Electrochemistry and Electrochemical Engineering, Vol 9, John Wiley & Sons, New York (1973) 61.
23. F. Stern, in: F. Seitz and D. Turnbull (Eds.), Solid State Physics. Advances in Research and Application., Vol 15. Academic Press, New York (1963) 299.
24. R. H. Muller, in: P. Delahay, C.W. Tobias (Eds.), Advances in Electrochemistry and Electrochemical Engineering, Vol 9, John Wiley & Sons, New York (1973) 288.
25.V.P. Diakonov, Handbook of algorithms and programs for personal computers in Basic language, Nauka, Moscow (1989) 86 (In Russian language).

CHAPTER 6

6. Interaction of the Electric Field with Small Organic Molecules

6.1. Introduction

Pyridine adsorption at gold single crystal surfaces has long been used as a model system to study co-ordination of organic molecules to metal electrode surfaces. The thermodynamics of pyridine adsorption has been thoroughly investigated with the help of the chronocoulometric technique[1][2][3][4][5][6][7][8]. The availability of the thermodynamic data has stimulated a general interest in pyridine adsorption at gold surfaces. Techniques such as ultraviolet electroreflectance spectroscopy UV-ER [9], second harmonic generation (SHG) [10], *in situ* difference frequency generation [11][12], scanning tunneling microscopy (STM) [13][14] and IR spectroscopy [14][15][16][17][18] have been employed to study the behavior of pyridine molecules at various gold surfaces. These studies demonstrated that the interaction between the pyridine molecule and the metal can involve either the delocalized π-orbitals or the lone pair localized on the nitrogen atom. As a result, the pyridine molecule can assume both $\pi-$ (flat) and N-bonded (vertical, tilted and/or rotated) orientations at gold low index surfaces. The character of the surface co-ordination of pyridine also depends strongly on the surface crystallography and the charge on the metal (static electric field at the interface).

The effect of the static electric field at the electrode surface on the orientation of pyridine molecules coordinated to the metal surface will be described in this chapter. Figure 6.1.1 explains why the Au (110) surface was selected for these investigations. Pyridine adsorption starts at $E \approx$ -0.6 V (SCE), and at $E \approx$ -0.35 V attains a limiting surface concentration of 6.2×10^{-10} mol cm^{-2} which corresponds to the packing density of a closely

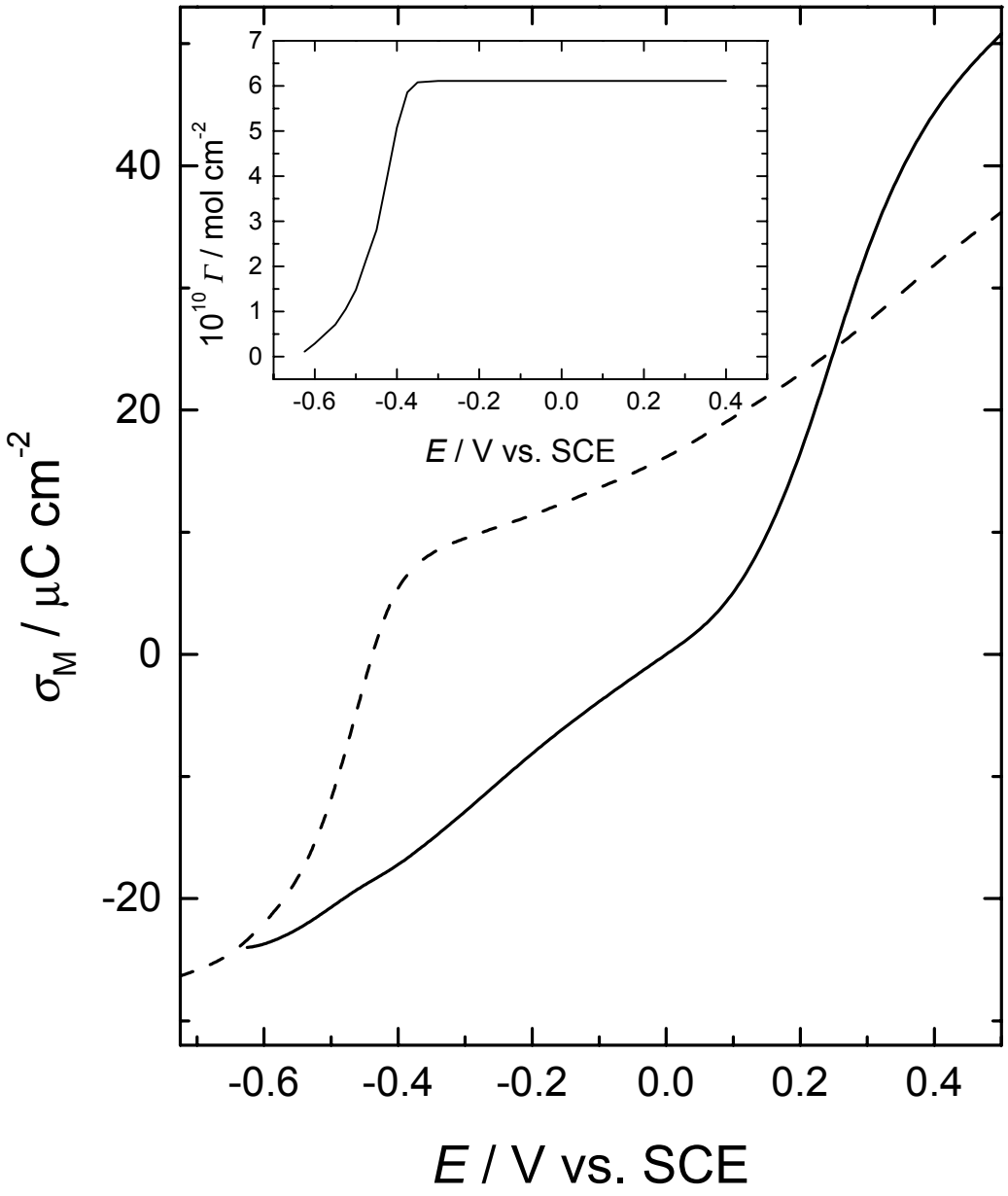

Figure 6.1.1 Charge density at the Au(110) surface plotted against the electrode potential for 0.1 M $KClO_4$ solution.
solid line: bare electrode
dashed line: with addition of 0.001 mM pyridine.
Inset: (solid line) Gibbs excess of pyridine *versus* electrode potential plot.
Electrochemical data were taken from reference [4].

packed monolayer of vertically oriented molecules. The limiting surface concentration maintains a constant value in a very broad range of electrode potentials, from $E \approx$ -0.35 V to $E \approx$ 0.55 V(SCE). The charge density at the electrode changes in this region from a value of $\sigma_M \approx 8$ μC cm^{-2} to a value of $\sigma_M \approx 35$ μC cm^{-2}. This corresponds to a change of the electric field strength at the interface from 4.5×10^{9} V m^{-1} to 2×10^{10} V m^{-1}, estimated using the Gauss's theorem ($F = (d\varphi / dx)_{x=0} = \sigma_M / \varepsilon$) and assuming that $\varepsilon = n^2\varepsilon_o$ where $n = 1.5$ is the refractive index of pyridine and $\varepsilon_o = 8.85\times10^{-12}$ C V^{-1} m^{-1} (the permittivity of vacuum).

In the plateau region, the coverage of the electrode surface by adsorbed molecules is constant, however, the static electric field at the interface changes significantly. The pyridine molecule has a rigid ring-like structure and a large dipole moment (~ 2 D) parallel to its C_2 axis. Therefore, the energy of the dipole – field interaction varies from 0.17 eV to 0.8 eV. This very significant change is shown below to have a pronounced effect on the orientation of molecules coordinated to the electrode surface.

The objectives of the research, described in this chapter, were twofold: (i) to provide direct spectroscopic information concerning the coordination of pyridine molecules adsorbed at the Au (110) electrode surface; (ii) to study the potential induced changes of the tilt angle of adsorbed pyridine molecules at potentials corresponding to the plateau on the adsorption isotherm. In addition, it will be demonstrated how the theoretical simulations of infrared spectra described in Chapter 5 can be applied for quantitative analysis of SNIFTIRS spectra.

6.2. The Shape of the SNIFTIR Spectra

To facilitate band assignment, the SNIFTIR spectrum recorded using the ZnSe

window is compared to the transmission spectrum of neat pyridine in Figure 6.2.1. In the spectral range used in our experiments, the infrared spectrum of pyridine displays several bands. The two broad bands in the SNIFTIR spectrum at ~1230 and ~1100 cm^{-1} correspond to D_2O and perchlorate, respectively. The remaining narrow bands are due to pyridine. An isolated pyridine molecule has C_{2v} symmetry. Four bands at 1581,1483, 1031 and 991 cm^{-1} have a_1 symmetry, the bands at 1438 and 1146 cm^{-1} have b_1 symmetry and the two bands at 748 and 704 cm^{-1} have b_2 symmetry [19][20]. The a_1 and b_1 bands correspond to in-plane ring deformations and b_2 bands to out-of-plane vibrations. The inset to Figure 6.2.1 shows that the a_1 bands correspond to changes of the dipole moment along the C_2 axis of the molecule and the b_1 band is due to the change of the dipole moment in the direction perpendicular to the C_2 axis. The direction of the transition dipole of the b_2 band is normal to the plane of the molecule. Therefore, using the ZnSe window one can record SNIFTIRS spectra in a sufficiently broad range of frequencies such that the spectrum encompasses bands whose transition dipole moments are directed along all three co-ordinates.

Since pyridine molecules are totally desorbed from the electrode surface at the negative extreme potential E_1, the measured change of the reflectivity ($\Delta R/R$) represents the difference between the absorption spectrum of Γ pyridine molecules desorbed from the surface into the solution, inside the thin layer cavity, at potential E_1 and the spectrum of Γ molecules adsorbed at the electrode surface at a sample potential E_2. The change of the electrode reflectivity is described by the following equation [17]:

$$(\Delta R/R) = 2.3\ \Gamma\ [g(E_1) - g(E_2)] \qquad (6.2.1)$$

where g is the decimal molar absorption coefficient and Γ is the surface concentration of the

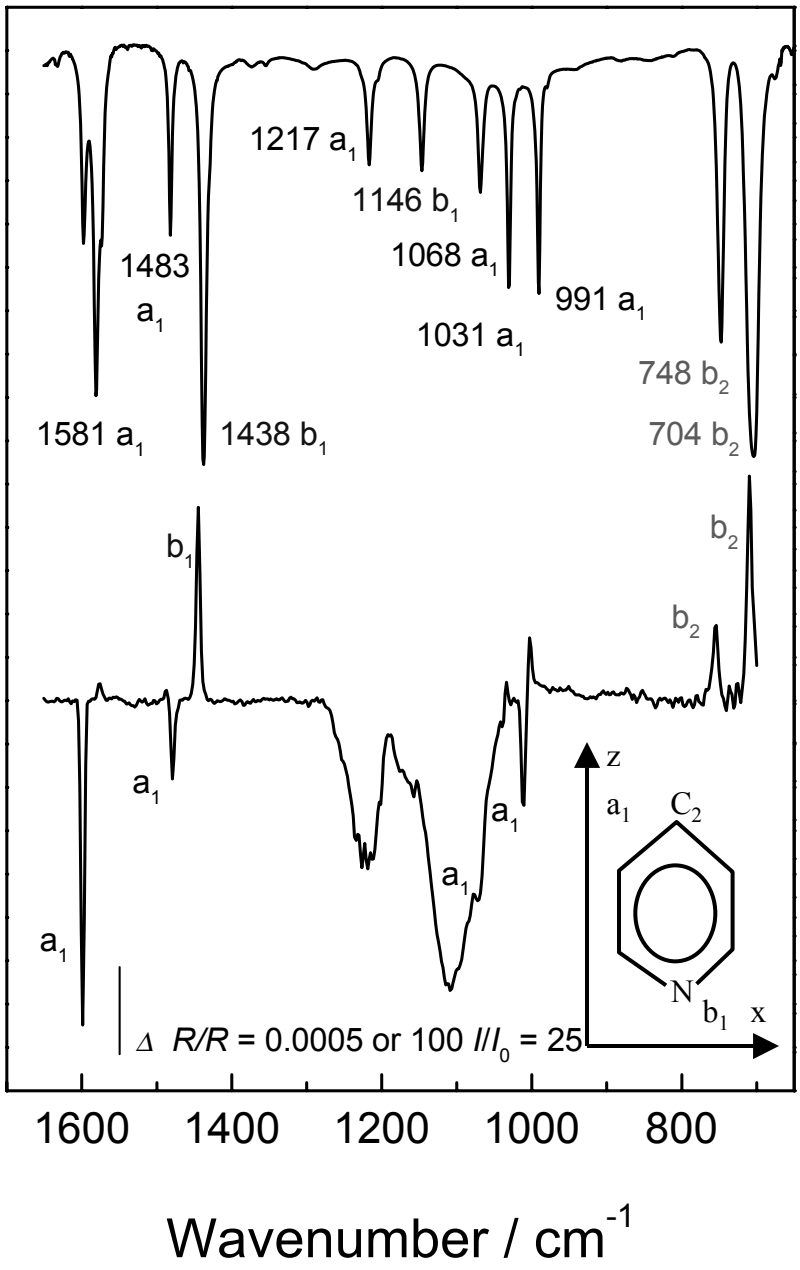

Figure 6.2.1 Comparison of the IR spectrum of neat pyridine recorded in the transmission mode with the SNIFTIR spectrum for the configuration Au(110) electrode/ 0.001 M pyridine solution in D_2O/ ZnSe hemispherical window, recorded using the sample potential E_2= 0.4 V and the reference potential E_1=-0.75 V (SCE). Inset shows directions of transition dipole moments of a_1 and b_1 bands in the IR spectrum of pyridine.

adsorbed species. Consequently, in the SNIFTIR spectrum, negative bands are observed when adsorbed molecules attenuate infrared radiation more strongly than the molecules in solution: $g(E_2)>g(E_1)$ and positive bands are present when the absorption by molecules in the solution dominates: $g(E_2)<g(E_1)$. In the spectrum shown in Figure 6.2.1, the negative bands have a_1 symmetry and the positive bands have either b_1 or b_2 symmetry.

For linearly polarized light and a single molecule adsorbed at or in front of a reflecting metal surface, equation (5.3.1) may be written as

$$\int \varepsilon \cdot d\bar{\nu} \propto \left|\vec{\mu} \bullet \vec{E}\right|^2 = \left|\mu\right|^2 < E^2 > \cos^2 \Theta \qquad (6.2.2),$$

where $\int \varepsilon d\bar{\nu}$ is the integrated molar absorption coefficient, $\vec{\mu}$ is the transition dipole, $\vec{E}$ is the electric field of the photon, Θ is the angle between the directions of the electric field of the photon and the transition dipole in the molecule, $|\mu|$ is the absolute value of the transition dipole moment and $<E^2>$ is the mean squared electric field strength (MSEFS) of the photon. The molecules desorbed into the solution at E_1 are randomly oriented with respect to the incident photon; hence, $<\cos^2\Theta> = 1/3$. In contrast, the molecules that are adsorbed at the surface assume a well-defined orientation. From equation (6.2.1) and the derivative of equation (6.2.2) with respect to $\bar{\nu}$, $(\Delta R/R)$ may be expressed as:

$$\frac{\Delta R}{R} \propto 2.3\Gamma\left[\frac{1}{3}\frac{\partial\left|\mu(E_1)\right|^2}{\partial\bar{\nu}} < E^2_{E_1}(z) > - \cos^2\Theta \frac{\partial\left|\mu(E_2)\right|^2}{\partial\bar{\nu}} < E^2_{E_2}(z=0) >\right] \qquad (6.2.3)$$

where the $\frac{\partial|\mu(E)|^2}{\partial\bar{\nu}}$ term determines the band shape, $< E_{E_1}^2(z) >$ is the MSEFS of the photon averaged over the whole thickness of the electrolyte layer and $< E_{E_2}^2(z = 0) >$ is the MSEFS of the photon at the electrode surface. When the $\frac{\partial|\mu(E)|^2}{\partial\bar{\nu}}$ terms for the adsorbed and solution species are frequency-shifted, the band in the SNIFTIR spectrum is bipolar. In the case of pyridine adsorption at gold, the frequency shift is small. For example, the tallest a_1 band in the SNIFTIR spectrum has a maximum at 1599 cm^{-1}, compared with the frequency 1594 cm^{-1} in the transmission spectrum of the pyridine solution in D_2O. This small shift in the band position indicates that the pyridine molecule is N-bonded to the Au (110) surface. It was previously shown that the frequency of this band depends somewhat on the surface crystallography of the Au electrode [17]. The frequency at the Au (110) surface is slightly lower than the 1601 cm^{-1} observed for the Au (210) electrode and slightly higher than the 1594 cm^{-1} obtained at the (111) terraces.

However, the shift in the band position is sufficiently small that the SNIFTIR spectra show unipolar rather than bipolar bands. For the purpose of further discussion, it is reasonable to assume that $\frac{\partial|\mu(E_1)|^2}{\partial\bar{\nu}}$ and $\frac{\partial|\mu(E_2)|^2}{\partial\bar{\nu}}$ have a comparable magnitude. Hence, the positive

bands in the SNIFTIR spectrum are observed when $\cos^2\Theta < \frac{1}{3}\frac{< E_{E_1}^2(z) >}{< E_{E_2}^2(z=0) >}$. It is useful to note that for p-polarized radiation $< E_{E_2}^2(z=0) >$ is significantly larger than $< E_{E_1}^2(z) >$. The positive bands are therefore observed when $\cos^2\Theta << \frac{1}{3}$ and the angle between the direction of the transition dipole and the surface normal is large. Likewise, negative bands in the SNIFTIR spectrum are observed when $\cos^2\Theta > \frac{1}{3}\frac{< E_{E_1}^2(z) >}{< E_{E_2}^2(z=0) >}$ and the angle between the transition dipole and the surface normal is small.

Consequently, the negative sign of a_1 bands and the positive sign of b_1 and b_2 bands in the SNIFTIR spectrum of pyridine at the Au (110) surface indicate that the C_2 axis of the adsorbed molecule forms a small angle with the surface normal and the in-plane and out-of-plane directions normal to the C_2 axis are parallel or nearly parallel to the surface. This behavior is consistent with a vertical or tilted surface coordination of the molecule. The infrared data are, therefore, consistent with the results of earlier chronocoulometric studies [4], which demonstrated that pyridine is N-bonded to the Au (110) surface. The present IR result provides direct, molecular level evidence of that surface coordination.

6.3. Potential-Controlled Change of the Tilt Angle

Figure 6.3.1 shows a series of SNIFTIR spectra acquired for a variable sample potential and the same reference potential equal to –0.75 V (SCE). The a_1 bands are negative, while the b_1 and b_2 bands are positive for all investigated potentials. Consistent with the previous electrochemical studies [4], this behavior indicates that, at the Au (110) surface, pyridine molecules are N-bonded in the whole range of electrode potentials.

Although all spectra in Figure 6.3.1 appear similar, the band intensities change with potential. These changes can be seen in Figure 6.3.2, where the integrated intensities of selected a_1 and b_1 bands are plotted against E_2. To facilitate discussion, the dashed line in Figure 6.3.2 shows how the Gibbs excess of pyridine changes with the electrode potential. The integrated intensities of the IR bands were multiplied by constant factors so that they could be plotted on a common scale. The results show significant differences between the potential dependence of the b_1 and a_1 bands. Apparently, the intensity of the b_1 band is independent of potential, within the region of the plateau on the Gibbs excess plot. In contrast, the intensities of the a_1 bands display a 30 % increase with potential within the plateau region. Equation (6.2.2) shows that the integrated intensity of an absorption band is proportional to $\cos^2 1$, $|\mu|^2$ and $\langle E^2 \rangle$. The transition dipole moment and the MSEFS of the photon do not depend on the electrode potential. Therefore, the trends observed in Figure 6.3.2 display chiefly the variation of $\cos^2 1$. Clearly, for the b_1 band, $\cos^2 1$ does not change with potential. In contrast, the variation of the integrated intensities of the a_1 bands indicates that the angle between the C_2 axis of the molecule and the surface normal changes with potential. The intensities of b_2 bands displayed a significant spread. The MCT detector is

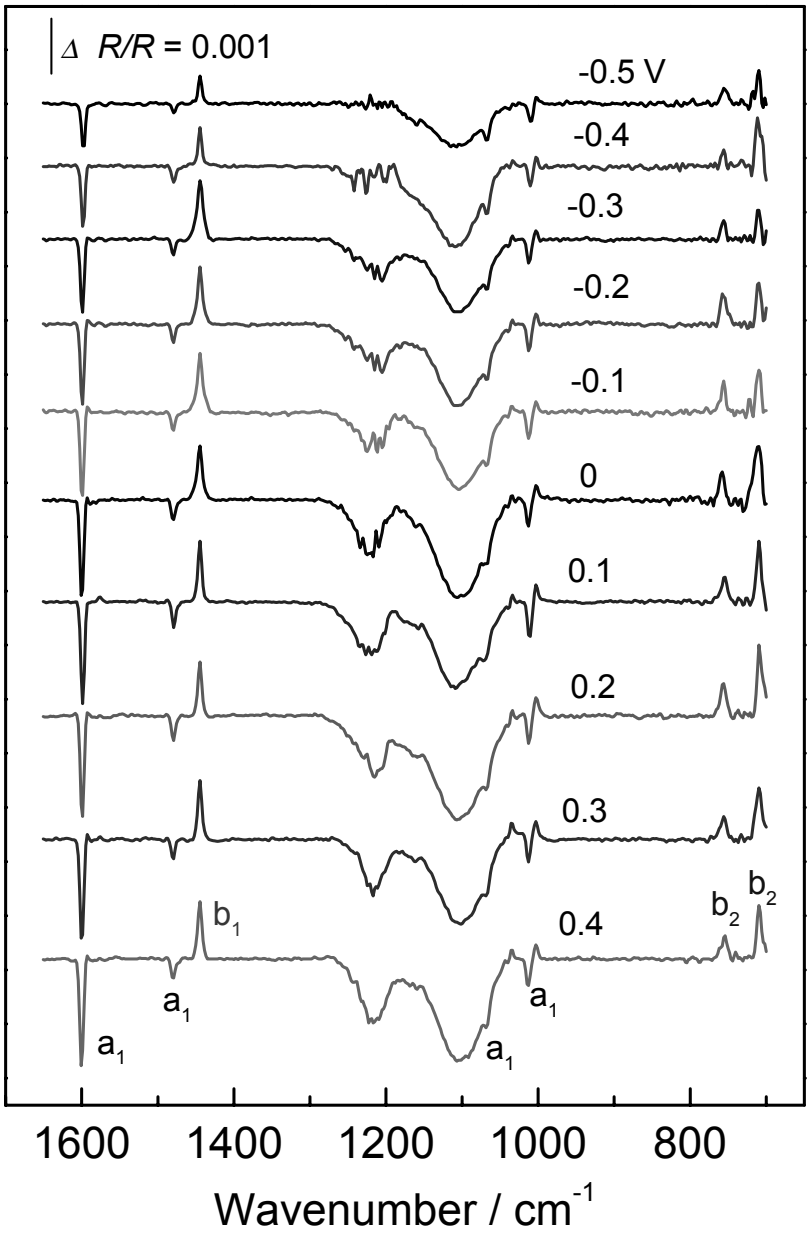

Figure 6.3.1 A series of SNIFTIR spectra recorded for pyridine adsorption at the Au(110) surface using p-polarized light.
The base potential E_1 was set to -0.75 V (SCE) and the sample potential E_2 varied. Its values are indicated at the corresponding spectrum.
The solution was 0.1 M $KClO_4$ and 0.001 M pyridine in D_2O.

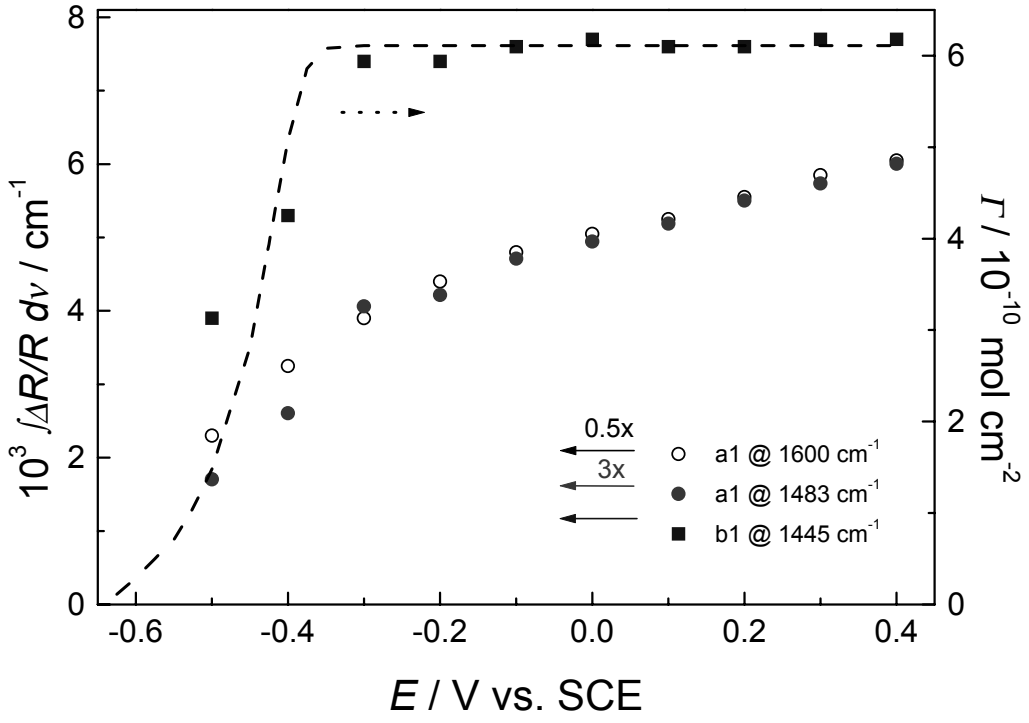

Figure 6.3.2. For the SNIFTIR spectra in Figure 6.3.1, plot of the integrated intensities of the b_1 band at 1445 cm^{-1} and a_1 bands at ~1599 and 1483 cm^{-1} *versus* the electrode potential.
Dashed line shows the changes of the Gibbs excess (data taken from reference [4]).

significantly less sensitive at frequencies below 800 cm^{-1} compared to frequencies within the 1600-1400 cm^{-1} region. For this reason, quantitative analysis of the b_2 bands was not performed.

In the plateau region, SNIFTIRS plots the difference between the absorbance of 6.2×10^{-10} mol cm^{-2} molecules desorbed into the thin layer cavity at potential E_1 and adsorbed at the electrode surface at potential E_2. To discuss the potential dependence of the a_1 bands quantitatively, it is convenient to compute the absorbance corresponding to the monolayer of adsorbed pyridine from the SNIFTIR spectrum, using the procedures described in Chapter 5. First, the optical constants of pyridine in D_2O, shown in Figure 6.3.3, were obtained as explained in Section 5.3.2. These optical constants were then used to remove the spectral signature of the desorbed species from $\Delta R/R$. The spectrum of desorbed pyridine was calculated following the procedure described in Section 5.3.4 for 6.2×10^{-10}mol cm^{-2} of pyridine molecules evenly distributed within a 7.2 μm thick layer of D_2O between the gold electrode and the ZnSe window. The SNIFTIRS decoupling procedure, explained in detail in Section 5.2.2, was employed to calculate the spectra of a monolayer of adsorbed molecules at each potential within the plateau on the adsorption isotherm. The results, plotted in Figure 6.3.4, show that the magnitude of the a_1 band at 1599 cm^{-1} progressively increases with potential, while the magnitude of the b_1 band is at the level of the subtraction error. These spectra were used to calculate the angle between the C_2 axis of the molecule and the metal surface plane (tilt angle), using the approach given in Section 5.3.1. (It is important to note that the tilt angle is reported with respect to the metal surface plane while the angle Θ used in equations denotes the angle with respect to the surface normal.) For that purpose, the

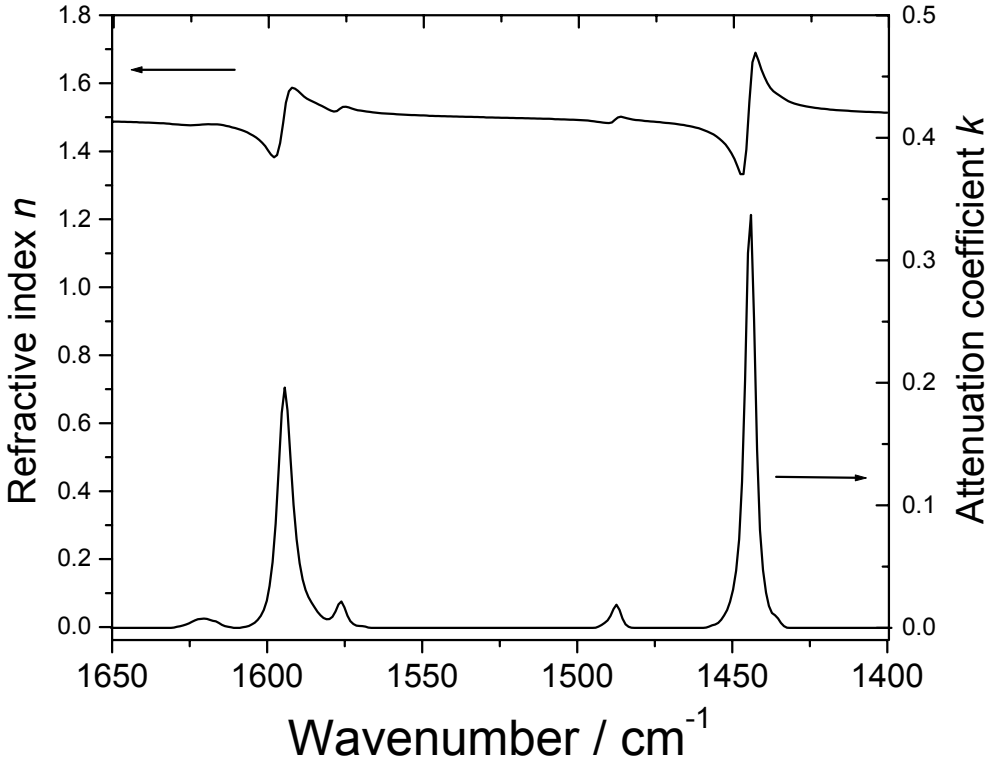

Figure 6.3.3. Optical constants of pyridine, calculated from the transmittance spectrum of a 0.1 M solution in D_2O.
n is the refractive index, *k* is the attenuation coefficient.

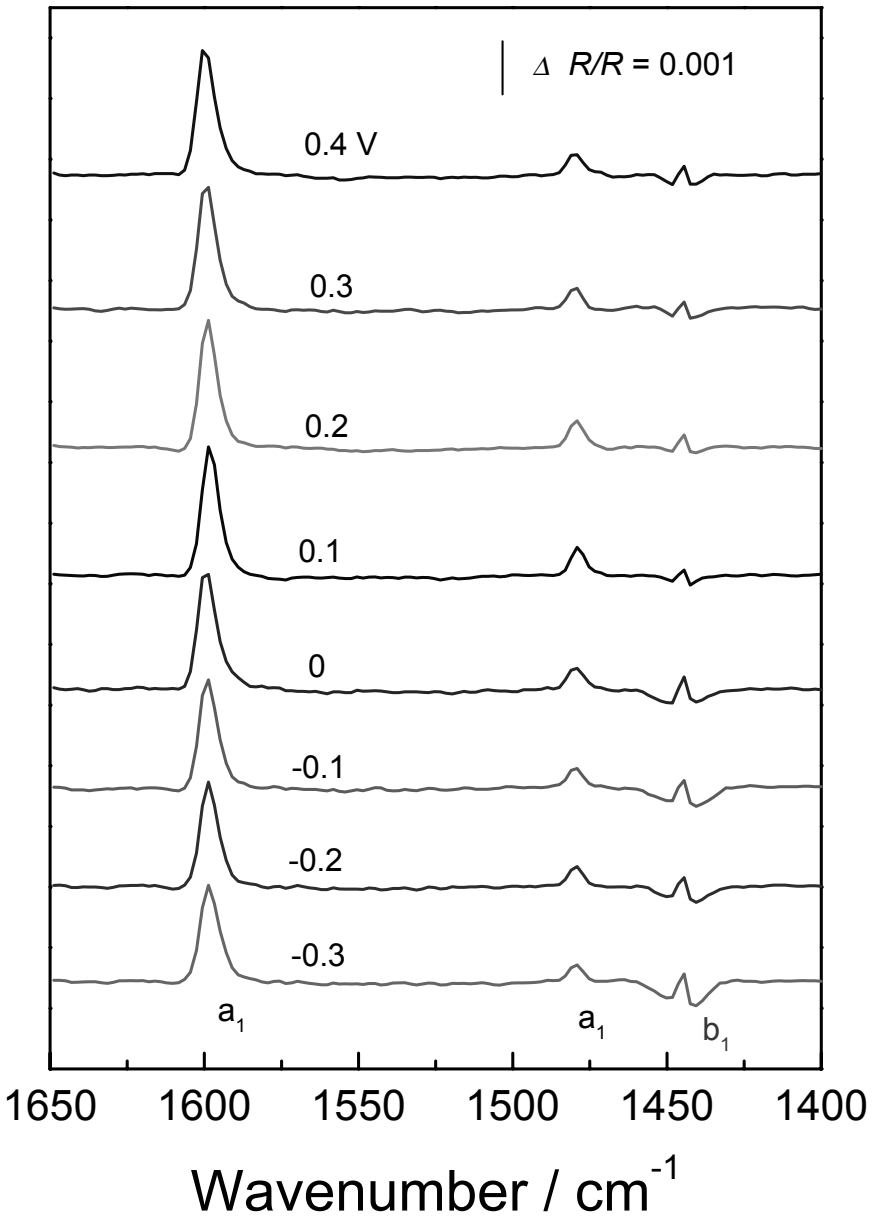

Figure 6.3.4. Infrared spectra for pyridine adsorbed at the Au(110) surface calculated from the SNIFTIR spectra after correction for the absorption of infrared radiation by molecules desorbed into the solution at the reference potential E_1.
The potentials indicated at each spectrum correspond to the sample potentials E_2.

theoretical absorption spectrum for a monolayer of 6.2×10^{-10} mol cm^{-2} molecules adsorbed at the electrode surface and separated from the hemispherical ZnSe window by a 7.2 μm layer of D_2O was computed as explained in Section 5.3.4. The tilt angles were then calculated from the integrated intensities of the a_1 bands in the spectra, presented in Figure 6.3.4, and the integrated intensity of the a_1 band in the simulated spectrum using equation (5.3.4). The results are plotted against potential in Figure 6.3.5. Their values are consistent with N-bonded coordination of pyridine to a Au (110) electrode surface.

6.4. Interpretation of the Dependence of the Tilt Angle on the Electrode Potential

To explain the observed variation of the tilt angle with potential, it is useful to recall that the energy of the dipole-field interaction for a pyridine molecule adsorbed at the Au (110) surface changes from 0.17 to 0.8 eV in this range of potentials. The strong forces of the static electric field orient the pyridine molecule such that its permanent dipole has a large component in the direction of the electric field. The dipole field interaction is opposed by the thermal movement of molecules, which disorients the film. One can envisage that the monolayer of adsorbed molecules behaves as a field of grass set into a waving motion by the wind. The energy of the dipole-field interaction restricts this movement and when the electric field increases, the amplitude of the waving motion decreases. At very large values of the static electric field, the monolayer becomes effectively frozen.

The absorption of electromagnetic radiation by molecules oriented by a static electric field was described by Kuhn *et al.* [21]. In the present case, the static electric field and the

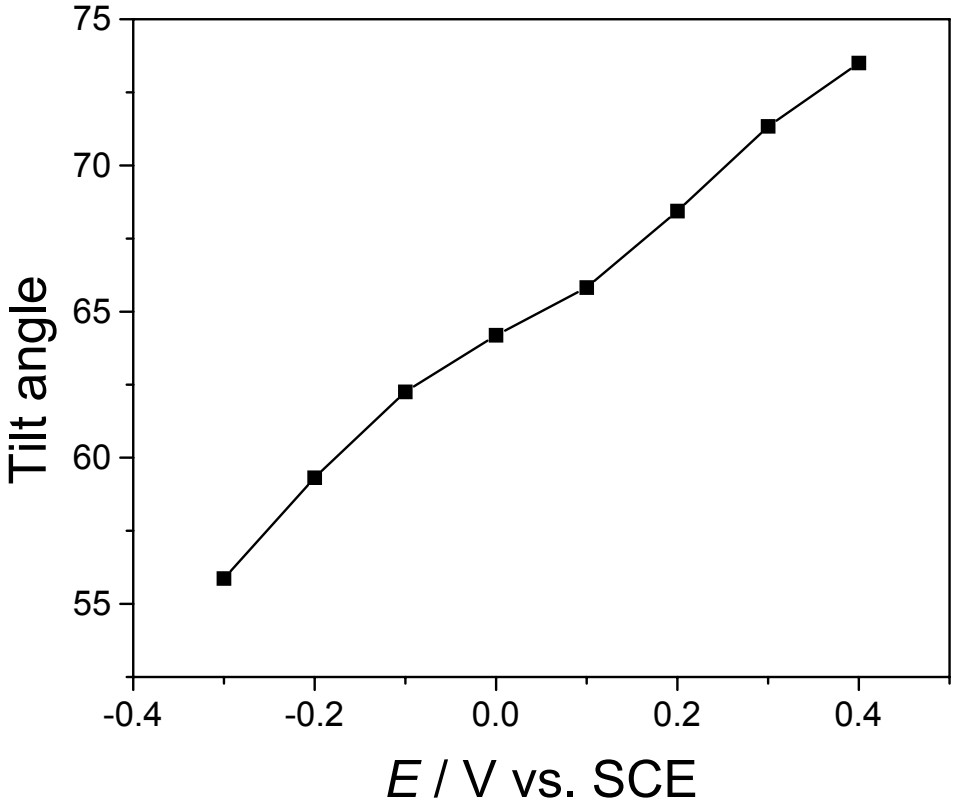

Figure 6.3.5. For pyridine adsorbed at the Au(110) surface,
plot of the tilt angle (the angle between the C_2 axis and the surface plane)
as a function of the electrode potential.

electric field of the photon at the metal surface are parallel to each other and normal to the electrode surface. When the transition and permanent dipole moments of a photon-absorbing molecule have the same direction, the dependence of $\cos^2 1$ on the static electric field is given by the Langevin function [21]:

$$\cos^2 \Theta = \left\{1 - \frac{2}{a} L(a)\right\} \qquad (6.4.1)$$

where $L(a)$ is the Langevin function defined as:

$$L(a) = \frac{e^a + e^{-a}}{e^a - e^{-a}} - \frac{1}{a} \qquad (6.4.2)$$

and $a = \frac{pF}{kT}$, where p is the permanent dipole moment of the molecule, F is the strength of the static electric field at the electrode surface and kT is the thermal energy. Using the Gauss theorem, $F = \sigma_M/\varepsilon$, a can be expressed in terms of the charge density at the metal $a = \frac{p\sigma_M}{\varepsilon kT}$.

When the dipole-field interaction energy ranges from 0.15 to 0.8 eV, the parameter a varies between 7 and 32. For such high values of the parameter a, the Langevin function may be approximated by $L(a) = 1 - \frac{1}{a}$ and the term in the curly brackets in equation (6.4.1) may be approximated by:

$$\cos^2\Theta = \left\{1 - \frac{2}{a}L(a)\right\} \approx \left\{1 - \frac{2}{a} + \frac{1}{a^2}\right\} \approx \left\{1 - \frac{2}{a}\right\} = \left\{1 - \frac{2\varepsilon kT}{p\sigma_M}\right\} \qquad (6.4.3)$$

Consequently, $\cos^2 1$ should increase linearly with $\frac{1}{\sigma_M}$. Figure 6.4.1 shows a plot of $\cos^2 1$ against $\frac{1}{\sigma_M}$. Consistent with the predictions of equation (6.4.3), the relationship is linear. In addition, according to equation (6.4.3) the change of $\cos^2 1$ caused by a change in the field is equal to:

$$\Delta \cos^2\Theta = 2\Delta\left(\frac{1}{a}\right) \qquad (6.4.4)$$

Using the values quoted above for the lower and upper limits of *a* one can calculate that the expected value of $\Delta \cos^2\Theta$ should be equal to 0.22. The overall change of $\cos^2 1$ observed in Figure 6.4.1 amounts to 0.24, in good agreement with this estimate. Therefore, a simple electrostatic model that assumes interplay between an orienting force of the dipole-field interaction and a disorienting force due to the thermal energy provides a very good description of the observed potential-dependent change in the tilt angle.

6.5. Conclusions

In situ SNIFTIRS has been employed to investigate the adsorption of pyridine on the

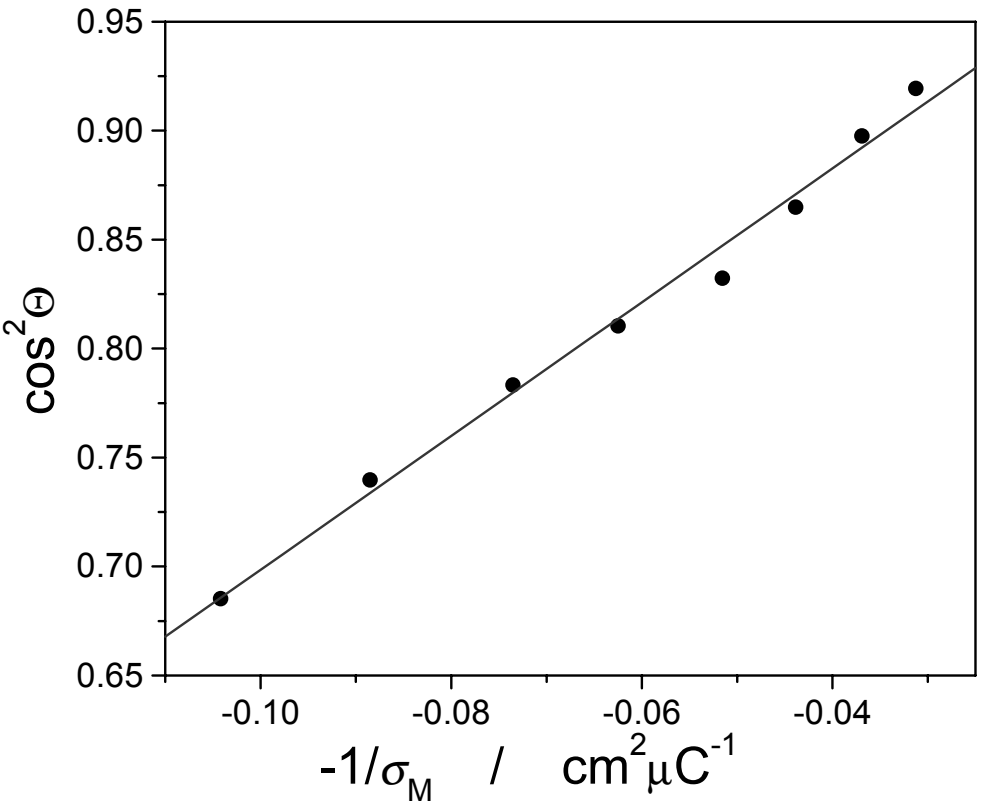

Figure 6.4.1. Plot of $\cos^2\theta = A_{exp}/A_{cal}$ *versus* inverse of the charge density at the electrode surface, where A_{exp} corresponds to the integrated intensity of the 1599 cm^{-1} band for adsorbed pyridine (Figure 6.3.4) and A_{cal} is the integrated intensity of this band calculated for the four parallel phases ($ZnSe/D_2O$/monolayer of pyridine/ZnSe) from the optical constants, using the matrix method and assuming that pyridine molecules are oriented with the C_2 axis perpendicular to the metal surface.

Au (110) surface. The infrared spectra provided direct evidence that pyridine molecules assume a vertical N-bonded state at this surface of gold in the whole range of electrode potentials investigated. The spectra also demonstrate that the tilt angle of adsorbed pyridine molecules changes with the electrode potential. These changes are described by a simple electrostatic model that assumes interplay between an orienting force from the dipole-field interaction and a disorienting force associated with the thermal energy. The spectroscopic data indicate that, driven by the thermal energy, the adsorbed molecules may display a significant waving motion when the field at the interface is small. The energy of the dipole-field interaction restricts this movement and when the field increases, the amplitude of the waving motion decreases. At very large values of the static electric field, the monolayer becomes effectively frozen. It was also demonstrated that it is feasible to remove the spectral signature of the desorbed species from SNIFTIR spectra converting them to the form that is convenient for quantitative analysis.

References

1. J. Lipkowski, L. Stolberg, D.-F. Yang, B. Pettinger, S. Mirwald, F. Henglein, D.M. Kolb, Electrochim. Acta 39 (1994) 1057.

2. L. Stolberg, J. Richer, J. Lipkowski, D.E. Irish, J. Electroanal. Chem. 207 (1986) 213.

3. L. Stolberg, J. Lipkowski, D.E. Irish, J. Electroanal. Chem. 238 (1987) 333.

4. L. Stolberg, J. Lipkowski, D.E. Irish, J. Electroanal. Chem. 296 (1990) 171.

5. L. Stolberg, J. Lipkowski, D.E. Irish, J. Electroanal. Chem. 300 (1991) 563.

6. L. Stolberg, S. Morin, J. Lipkowski, D.E. Irish, J. Electroanal. Chem. 307 (1991) 241.

7. D.F. Yang, L. Stolberg, J. Lipkowski, J. Electroanal. Chem. 329 (1992) 259.

8. J. Lipkowski and L. Stolberg in Adsorption of molecules at metal electrodes, J.Lipkowski and P.N. Ross (Eds), VCH Publishers, New York, (1992).

9. F. Henglein, J. Lipkowski and D.M. Kolb, J. Electroanal. Chem. 303 (1991) 245

10. B. Pettinger, S. Mirwald, J. Lipkowski, J. Electroanal. Chem. 329 (1992) 289.

11. Hebert, A. Le Reille, W.Q. Zheng, A. Tadjeddine, J. Electroanal. Chem. 447 (1998) 5.

12. A. Tadjeddine, O.Pluchery, A. Le Reille, C. Humbert, M. Buck, A. Peremans and W.Q. Zheng, J. Electroanal. Chem., 473 (1999) 25.

13. G. Andreasen, M.E Vela, R.C. Salvarezza, A.J. Arvia, Langmuir 13 (1997) 1317.

14. W.-B. Cai, L.-J. Wan, H. Noda, Y.-I. Hibino, K-I. Ataka, M. Osawa, Langmuir 14 (1998) 6992.

15. Y. Ikezawa, T. Sawatari, T.K.H. Goto, K. Toriba, Electrochim. Acta 43 (1998) 3297.

16. N. Nanbu, F. Kitamura, T. Ohsaka and K. Tokuda, J. Electroanal. Chem. 470 (1999)136.

17. M. Hoon-Koshla, W.R. Fawcett, A. Chen, J. Lipkowski and B. Pettinger, Electrochim. Acta 45 (1999) 611.

18. B. Pettinger, J. Lipkowski and M. Hoon-Khosla, J. Electroanal. Chem., 500 (2001) 471

19. L. Corrsin, B.J. Faxand and R.C. Lord, J. Chem. Phys. 21 (1953) 1170.

20. D.A. Long and E.L. Thomas, Trans. Faraday Soc. 59 (1963) 783.

21. W. Kuhn, H. Duhrkop and H. Martin, Z. Physik. Chem. B 45 (1940) 121.

CHAPTER 7

7. Studies of Potential-Induced Transformations in Ultrathin Films of 4-Pentadecylpyridine at the Gold-Solution Interface

7.1. Introduction

In this chapter it will be demonstrated that the concerted use of several surface analytical techniques allows one to obtain a comprehensive picture of the behaviour of insoluble surfactants at the electrified solid-liquid interface. In addition, it will be shown how the methodology described in Chapter 5 can be applied to extract a wealth of quantitative information about the mechanism underlying the potential-induced changes in a monolayer and a bilayer of 4-pentadecylpyridine, an insoluble surfactant molecule.

Electrochemical and spectroscopic methods were applied to study the spontaneous transfer of 4-pentadecylpyridine (C15-4Py) from the gas-solution (GS) interface of the electrochemical cell to the metal-solution (MS) interface of the gold electrode. Measurements of the differential capacity of the MS interface and the charge density at the metal were used to study the spontaneous formation of a bilayer of the surfactant as the result of exchange of material between the GS and the MS interfaces. Neutron reflectometry was utilized to determine the thickness and the surface concentrations of C15-4Py in the monolayer and the bilayer of the surfactant, at the Au(111) electrode surface. Polarization modulation Fourier transform infrared reflection absorption spectroscopy (PM FTIR RAS) was applied to determine quantitative information concerning the orientation of C15-4Py molecules in the films of surfactant at various potentials. These spectroscopic experiments were performed *in situ* under potential control and allowed us to better understand the mechanism of the

potential induced adsorption and desorption of the ultrathin films of insoluble surfactants at the MS interface.

7.2. Electrochemical Studies of Spontaneous Transfer of 4-pentadecylpyridine from the Gas-Solution Interface to the Metal-Solution Interface

The objective of this part of the project was to investigate the spontaneous transfer of surfactants from the GS interface to the MS interface. The solid electrode was brought in contact with the GS interface using the horizontal touching (Langmuir-Schaefer) technique and positioned in a hanging meniscus configuration (see Figure 4.2 c). In this geometry, the edge of the electrode surface forms a triple phase boundary between solid, liquid and gaseous phases and surfactant molecules must cross this triple phase line to move from the GS interface to the MS interface. The spontaneous transport of C15-4Py molecules across the triple phase line has been studied using the measurements of the differential capacity and charge density at the MS interface. It will also be shown that the slow rate of molecular migration requires over 8 h before the interface becomes covered by a bilayer of surfactant molecules. This slow rate explains why the transfer of insoluble surfactants from the GS interface to the MS interface was not detected in previous, short duration experiments [1][2][3][4][5]. An interesting case of an exchange of material between these two interfaces will be described and significant new information concerning the mechanism of spontaneous self-assembly of insoluble surfactants at the solid-liquid interface will be provided.

7.2.1. Spreading of C15-4Py onto a Monolayer-Coated Electrode Surface

The metal-electrolyte interface has the properties of a capacitor. It is well known that the capacitance of the interface decreases when organic molecules are adsorbed at the metal surface [6]. Therefore, measurement of the differential capacity provides a convenient means to study the transfer of surfactants to the surface of a metal electrode. Initially, the transfer of C15-4Py molecules from the gas-solution interface, across the triple phase line, to the metal surface coated with a monolayer of the pyridine surfactant was investigated. Effectively, a spontaneous transformation of a monolayer to a bilayer, due to the transfer of C15-4Py molecules from the GS interface to the MS interface, has been studied. This case resembled the flow of Langmuir monolayers onto the organothiol-modified gold surface described by Steel *et al.* [7].

At the beginning of the experiment, the metal electrode was coated with a monolayer of C15-4Py using the single horizontal touching procedure. Immediately after the deposition of the surfactant film, the differential capacity of the interface was measured at 0 V (SCE). The obtained values of the capacity were significantly lower (between 8 and 5 $\mu F\ cm^{-2}$) than the capacity of the film-free gold-solution interface (*ca.* 34 $\mu F\ cm^{-2}$ at 0 V and pH = 9). This behavior indicates that the film of C15-4Py is transferred to the electrode surface during the horizontal touching procedure.

A slow voltage ramp was then applied to the electrode and the capacity curve, shown as a solid line in Figure 7.2.1, was recorded. The shape of this curve is consistent with the results described earlier [8]. When the potential moves in a negative direction a maximum at E . -0.2 V can be seen. The presence of this feature indicates a phase transition in the organic

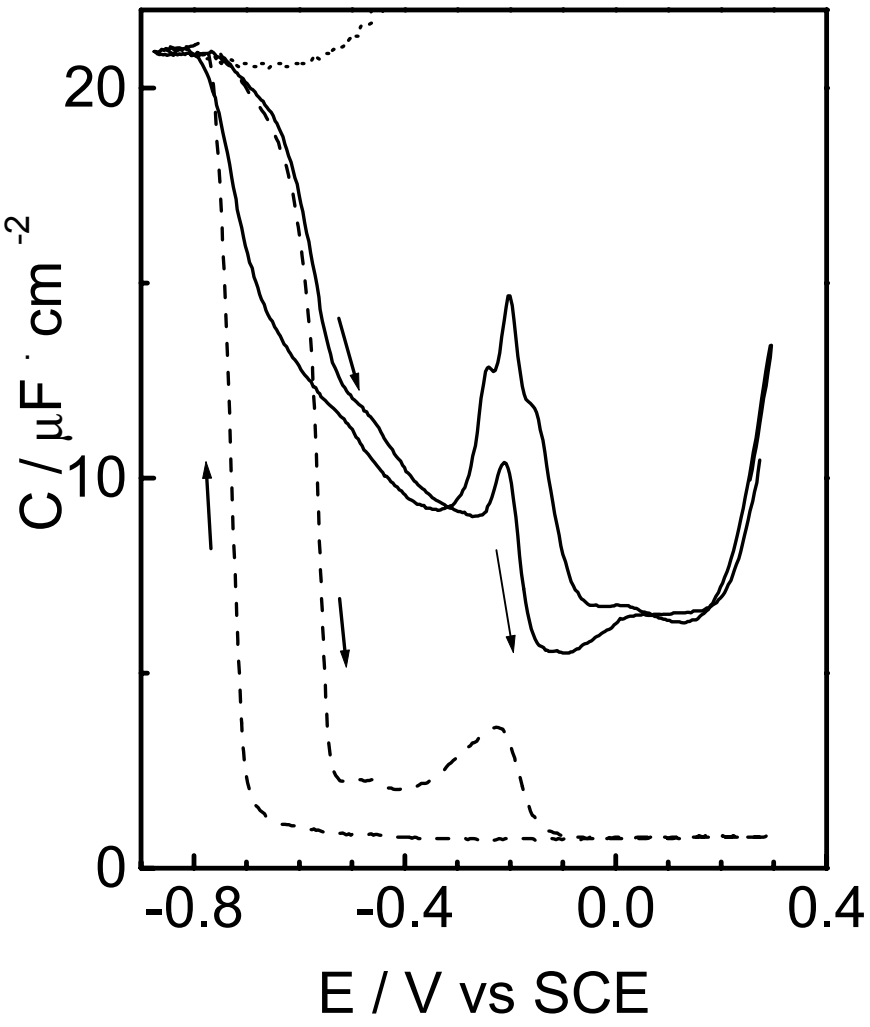

Figure 7.2.1. Differential capacity of the Au(111) electrode.
Dotted line: film-free interface,
Solid line: interface covered with a film of C15-4Py molecules deposited at E = 0 V using the single horizontal touching technique.
The curve was recorded immediately after contact between the electrode and the film-covered GS interface was established.
Dashed line: interface covered with a film produced by spontaneous transfer of C15-4Py molecules from the GS to the MS interface after 18 h of equilibration.
The electrolyte solution was 0.05 M $KClO_4$ and 0.001 M $KHCO_3$.

film. Moving the potential further in the negative direction results in additional increase in the capacity until at $E \leq$ - 0.8 V it becomes equal to the capacity of the film-free electrode. This behavior indicates that the film is desorbed from the electrode surface at negative potentials. When the direction of the voltage sweep is reversed, the capacity decreases and at E . 0 V it attains the initial value of approximately 8 μF cm^{-2}. Apparently, the film re-forms on the gold surface at this potential. At potentials higher than 0.3 V the capacity rises again. This increase indicates the onset of film desorption, most likely promoted by a competitive adsorption of hydroxide and/or bicarbonate ions ($NaHCO_3$ was added to the electrolyte to adjust the pH). Gold oxide formation prevents further extension of electrode potentials in the positive direction.

Elastic light scattering and fluorescence quenching experiments described in reference [8] demonstrated that C15-4Py, desorbed from the electrode surface at $E \leq$ - 0.8 V, is trapped in the vicinity of the electrode surface in the form of micellar-type aggregates which fuse back onto the metal surface when the electrode potential becomes less negative. The hysteresis of the differential capacity curve indicates that desorption and film re-formation processes are slow on the time scale of the voltage ramp (0.005 V s^{-1}). It may also indicate that desorption of the film from the electrode surface and fusion of aggregates at the surface may involve different mechanisms. However, independent potential step experiments indicate that the film can be re-formed completely within a time frame of 90 s [8]. For the purpose of the subsequent discussion, it is important to stress that the film, initially deposited at the gold electrode surface at E = 0 V, may be desorbed at negative potentials and then completely recovered by changing the potential back to zero volts. The film desorption and recovery

processes require time on the order of minutes. The properties of the film are not perceptibly changed by the desorption and reformation cycle.

After the initial measurement of capacity, the film-covered electrode (positioned in the hanging meniscus configuration) was allowed to equilibrate for 18 h with a monolayer of C15-4Py spread at the electrolyte surface. The differential capacity of the electrode was periodically measured at 0 V. Figure 7.2.2 shows the differential capacity curves measured at different stages of equilibration. Apparently, the capacity decreases with the equilibration time until it approaches a steady state value after 8 h. The full differential capacity curve recorded after 18 h of the experiment is plotted as a dashed line in Figure 7.2.1. The differential capacity curves determined after 8 and 18 h of equilibration are very close. The progressive decrease of the differential capacity with the equilibration time indicates that the amount of C15-4Py molecules at the metal-solution interface increases with time. This behavior strongly suggests that surfactant molecules are transferred across the triple phase line from the GS interface to the MS interface.

In fact, the differential capacity curves recorded after 8 or 18 hours of equilibration (dashed curve in Figure 7.2.1) resemble the curve recorded for the electrode, covered with a film produced by the double horizontal touching method [8][9]. This evidence suggests that a bilayer of C15-4Py is formed after a sufficiently long equilibration time. Indeed, for potentials higher than –0.1 V, the capacity of the interface recorded after 18 h of equilibration is equal to the capacity of the interface after the double horizontal touching deposition and attains a very small value of approximately 0.8 $\mu F\ cm^{-2}$, which is characteristic of a bilayer coverage. The pyridine moiety of the surfactant molecule has a relatively high affinity for gold

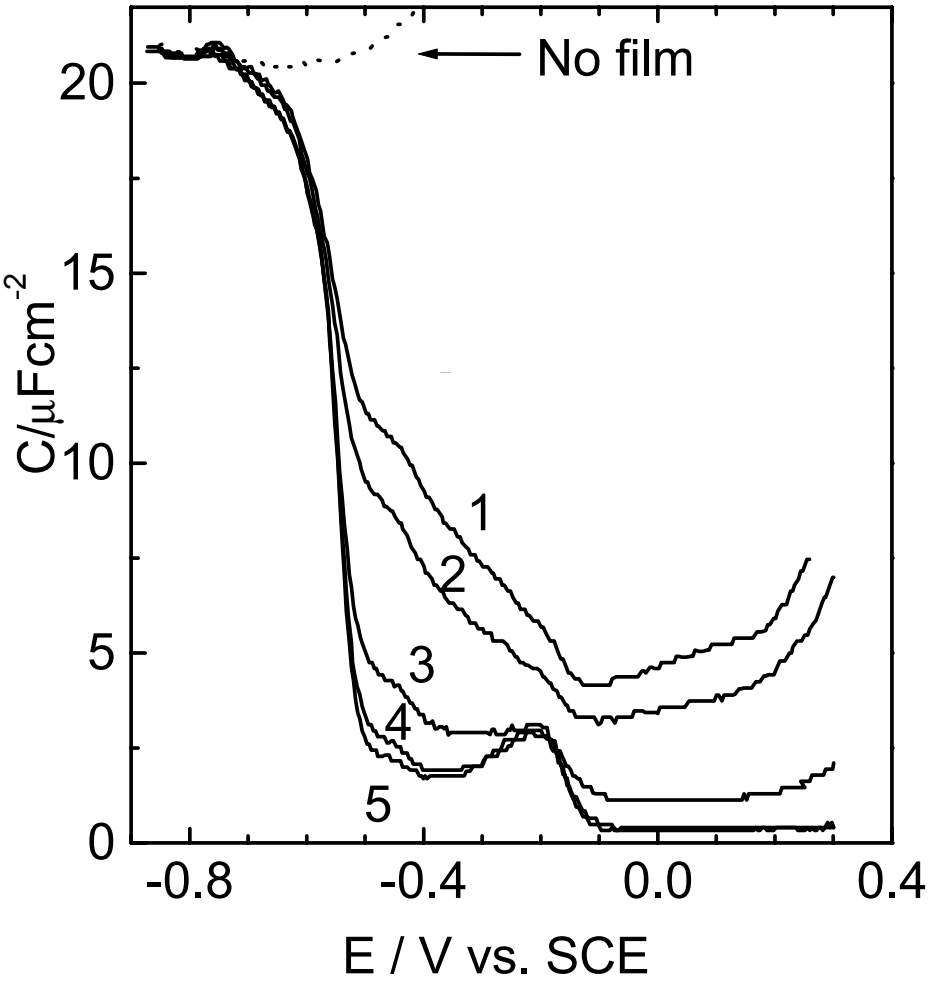

Figure 7.2.2. Evolution of the differential capacity of the Au(111) electrode covered with a film of C15-4Py.
The number associated with the curve corresponds to the following period of equilibration time:
1: 0 h, curve recorded just after the contact between the electrode surface and the monolayer-covered gas-solution interface was established,
2: 1 h; 3: 4 h; 4: 6 h; 5: 8 h .
For clarity, only the portions of the differential capacity curves recorded during the positive voltage sweep are shown.
The supporting electrolyte solution was 0.05 M $KClO_4$ and 0.001 M $KHCO_3$.

[10][11]. Consequently, in the first monolayer, C15-4Py molecules are probably oriented with the pyridine ring toward the surface and the hydrocarbon tail toward the solution, thus making the MS interface hydrophobic. The second layer of molecules diffuses or flows onto this hydrophobic substrate.

For a quantitative comparison between the film produced by the prolonged equilibration of the electrode with the surfactant spread at the GS interface and the film produced by the double horizontal touching, it is convenient to analyze the charge density data. The charge density plots determined for the Au(111) electrode covered by these two films are compared in Figure 7.2.3. The charge density curves were acquired by stepping the potential from more positive potentials, where the molecules of surfactant are spread at the metal, to a value of –0.825 V, where the desorbed surfactant molecules form micelle-like aggregates in the vicinity of the electrode surface. In the presence of the surfactant, the charge density plots display two steps. The nature of these steps has been discussed previously [8]. The first step at E = –0.6 V corresponds to the adsorption of micellar aggregates onto the electrode surface. The second step at E = –0.2 V corresponds to a phase transition in the film, which is probably due to the spreading of surface hemimicellar aggregates to form a condensed film. For the purpose of the present discussion it is important to note the remarkable similarity of the charge density curves determined for films obtained using the double horizontal touching and the prolonged equilibration procedures. The charge density measured for the film produced using the double touching method is slightly higher at potentials around –0.4 V and somewhat lower at E > 0 V. These small differences may suggest that the film formed by the spontaneous transfer of C15-4Py molecules is slightly less

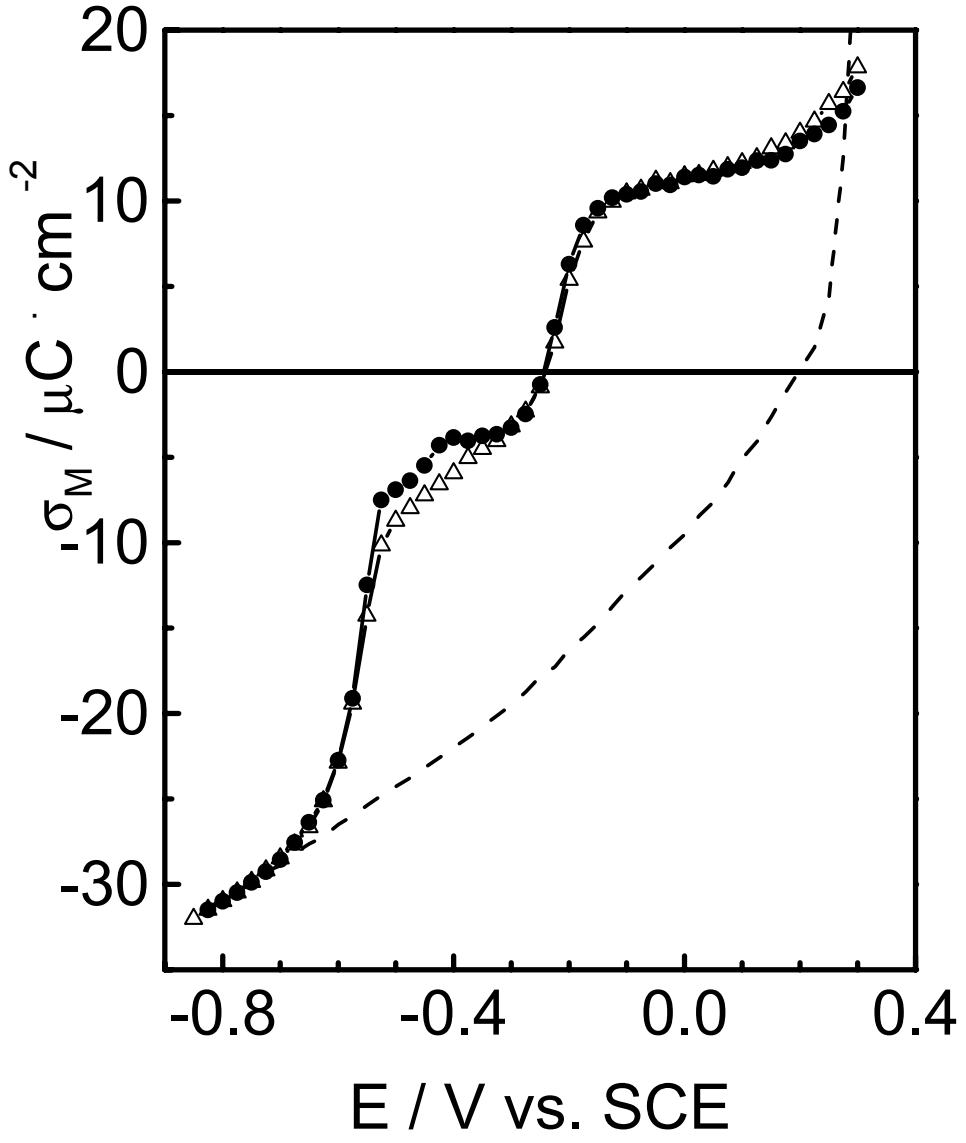

Figure 7.2.3. Charge density at the Au(111) electrode.
Dashed line: film-free interface,
Open triangles: in the presence of a film obtained using the single touching method followed by equilibration for 18 h ,
Solid circles: in the presence of a film obtained using the double touching technique.
The supporting electrolyte solution was 0.05 M $KClO_4$ and 0.001 M $KHCO_3$.

compact than the film obtained using the double touching method. Apart from these minor differences, the similarity of the two charge density curves corresponding to the two films strongly suggests that the C15-4Py molecules cross the triple phase line to form a bilayer at the gold-solution interface.

7.2.2. Spreading of C15-4Py onto the Film-Free Electrode Surface

The preceding section described the transformation of a monolayer of chemisorbed surfactant to a bilayer due to the spontaneous transfer of the surfactant molecules from the GS interface to the monolayer-covered metal. The following experiment has been performed to test whether C15-4Py molecules will also move from the GS interface to an initially surfactant-free MS interface. The Au(111) electrode was flame annealed and then quenched with water. The drop of water adhered to the clean electrode surface. This electrode was brought into contact with the film of surfactant molecules spread on the electrolyte surface. The initial presence of the water droplet prevented transfer of the surfactant film to the electrode surface. However, as soon as the contact between the MS and GS interfaces was established, the differential capacity revealed the onset of spreading of the surfactant onto the metal surface. The electrode was then allowed to equilibrate with the film at the GS interface for a period of 18 hours. The differential capacity of the gold-solution interface was recorded every few hours to monitor the transfer of C15-4Py molecules from the GS to the MS interface.

The results of these measurements are shown in Figure 7.2.4. The differential capacity of the interface recorded immediately after touching the electrolyte surface was characteristic

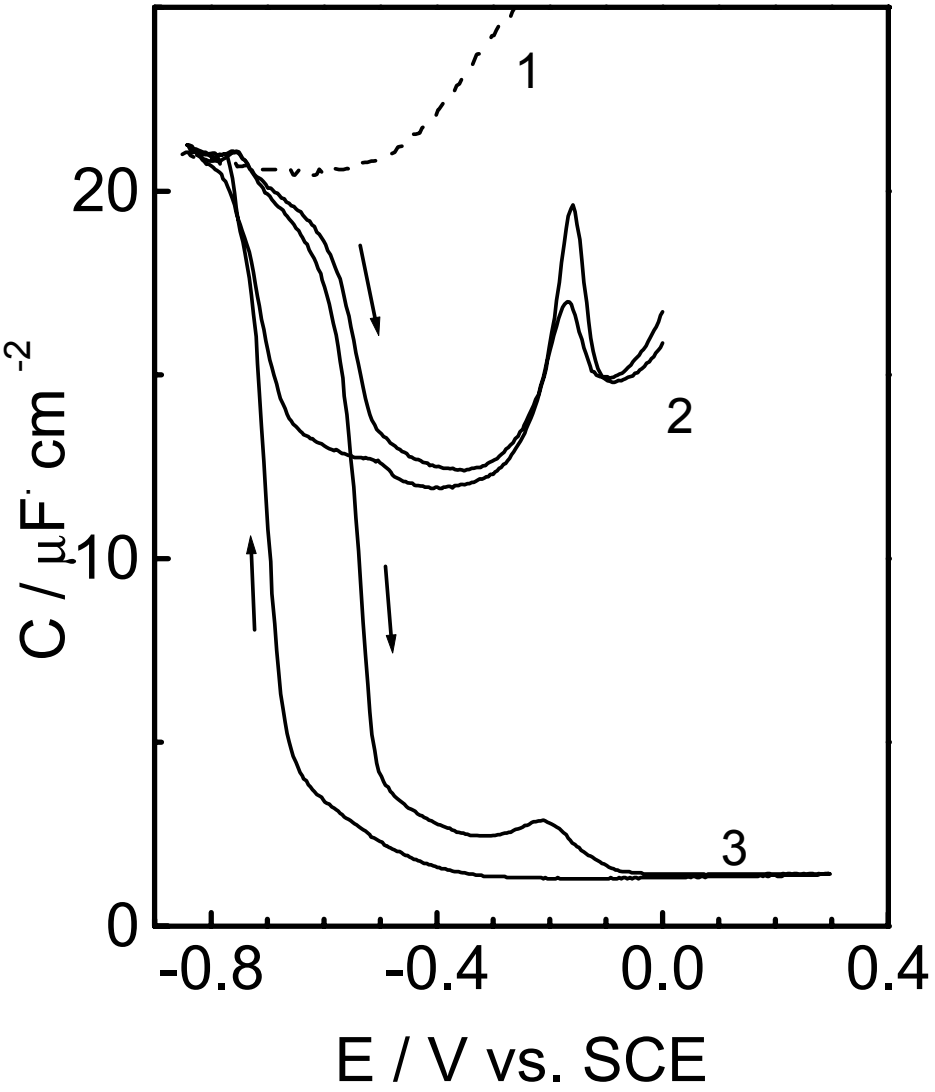

Figure 7.2.4. Differential capacity of the Au(111) electrode in contact with the surface of electrolyte, covered with a C15-4Py film at the equilibrium spreading pressure.
1: curve recorded after contact between the electrode and the GS interface was established,
2: curve recorded after 3.5 h of equilibration,
3: curve recorded after 18 h of equilibration.
The supporting electrolyte solution was 0.05 M $KClO_4$ and 0.001 M $KHCO_3$.

of a film-free Au(111) surface. However, the differential capacity curve recorded after 3.5 h of equilibration was already reminiscent of the curve recorded for the monolayer-covered surface, indicating that surfactant molecules moved from the GS interface to the MS interface across the triple phase line. After a prolonged waiting time of 18 h, the differential capacity of the MS interface decreased further until the curve became quite similar to that, characteristic of the surfactant bilayer produced by the double touching procedure. This experiment indicates that C15-4Py molecules can move from the GS interface not only to the hydrophobic MS interface but also to the film-free gold-solution interface and assemble spontaneously into a bilayer.

7.2.3. Mechanisms of Transfer of C15-4Py from the GS Interface to the MS Interface

Three mechanisms can be employed to describe the spontaneous spreading of C15-4Py molecules from the GS interface to the MS interface. The first, proposed recently by Steel *et al*. [7], assumes that spreading is caused by a viscous flow of the Langmuir monolayer across the triple-phase boundary, driven by the film-pressure of the surfactant at the GS interface. The second is the Cohen and Turnbull [12][13] free volume model of diffusion in fluids. It describes diffusion in lipid bilayers [14][15] and was recently applied by Majda and coworkers [16][17] to study lateral diffusion at the air-water interface. The two models are depicted schematically in Figure 7.2.5.A and B, respectively. We have loosely applied the phrases “collective flow” and “random walk” to differentiate between the viscous flow and diffusion models. To test these models quantitatively, one has to analyse the

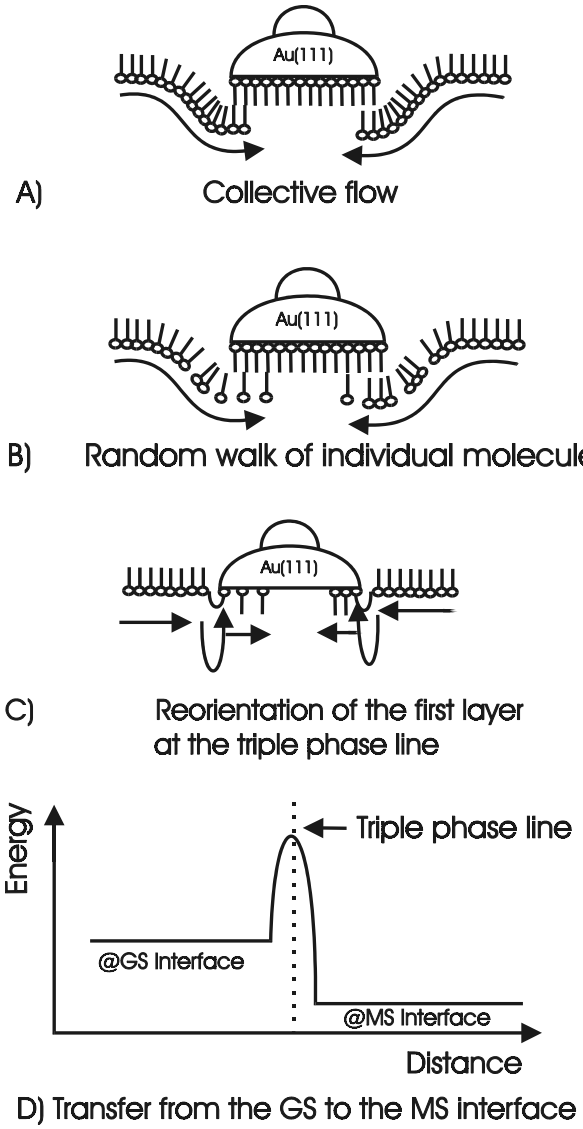

Figure 7.2.5. Schematic models of different mechanisms describing mass transfer from the GS interface to the MS interface.
A): Film-pressure-driven viscous flow of a Langmuir monolayer ("collective flow") to a hydrophobic surface.
B): Free volume model of lateral diffusion ("random walk") to a hydrophobic surface.
C): Generalized model for mass transport to a film-free surface involving re-orientation of the surfactant at the triple phase boundary.
D): Schematic description of free energy profile of a transfer of insoluble surfactant molecule from the GS to the MS interface.

dependence of the differential capacity on the equilibration time. The differential capacity curves in Figure 7.2.2 display quite a flat minimum at $E = 0$ V. At this potential, the fraction Θ of the metal-solution interface covered by the bilayer can be defined in terms of:

$$\Theta = \frac{C_0 - C_t}{C_0 - C_\infty} \approx \frac{\Gamma}{\Gamma_\infty} \qquad (7.2.1)$$

where C_0, C_t and C_4 are the differential capacities at zero equilibration time, equilibration time t and infinitely long (18 h) equilibration time, respectively. In the case of spreading on a monolayer-covered metal surface, Θ measures the extent of transformation of the monolayer to the bilayer and in the case of spreading to a bare electrode surface, Θ measures the extent of film formation. In the viscous flow model the parameter Θ is related to time t by the equation given in reference [7]:

$$\Theta = \sqrt{2k\pi_{GS}t} \qquad (7.2.2)$$

where k is a proportionality constant and π_{GS} is the surface pressure of the film at the GS interface.

The parameter Θ may also be used as a measure of Γ/Γ_4, the fraction of molecules transferred to the MS interface across the triple-phase line by diffusion, where Γ is the surface concentration of molecules transferred to the MS interface at a given equilibration time t and Γ_4 is the surface concentration after an infinitely long period of equilibration time [6]. The metal electrode is disc-shaped and characterized by a radius r_o. Initially, the surface concentration of C15-4Py, either in the second layer or at the bare gold electrode, is equal to

zero, $\Gamma(t = 0) = 0$. The diffusion from the GS interface to the MS interface is driven by the gradient of the chemical potential. The film pressure at the GS interface is equal to the equilibrium spreading pressure during the whole duration of the experiment. Consequently, the surface concentration of C15-4Py outside the disk is uniform and equal to the surface concentration at the triple-phase line $\Gamma(r = r_o)$. The formation of the bilayer is complete when the surface concentration in the second layer of the MS interface becomes equal to the surface concentration at the GS interface $\Gamma_4 = \Gamma(r = r_o)$. The number of molecules crossing a unit length of the triple-phase line during time t is given by [18]:

$$N = \int_0^t D\left(\frac{\partial \Gamma(r)}{\partial r}\right)_{r=r_0} dt \qquad (7.2.3),$$

where D is the diffusion coefficient. To calculate the surface concentration of molecules diffusing to the electrode, one has to multiply N by the length of the disc perimeter (length of the triple phase line) $2\pi r_o$ and to divide the product by the electrode area πr_o^2. The result is:

$$\Gamma = \frac{2}{r_0}\int_0^t D\left(\frac{\partial \Gamma(r)}{\partial r}\right)_{r=r_0} dt \qquad (7.2.4)$$

It is difficult to find an analytical solution of this equation. For lateral diffusion of a surfactant molecule, the diffusion coefficient depends on the surface concentration Γ. That dependence was described by Majda and coworkers [16]. In addition, the diffusion to the disc surface is

a diffusion into a limited space and solutions for diffusion under limited space conditions are complex [19]. However, one can provide an estimate of the initial rate of diffusion. At the initial stage of diffusion the disc can be treated as a semi-infinite space. In addition, at the initial stage the diffusion coefficient can be considered as coverage-independent. The flux of molecules across the disc perimeter may then be described by the Cottrell equation:

$$D\left(\frac{\partial\Gamma(r)}{\partial r}\right)_{r=r_0} = D\frac{\Gamma_{r=r_0}}{\sqrt{\pi Dt}} \qquad (7.2.5)$$

and the initial change of the fraction Θ with time may be described by:

$$\Theta = \frac{\Gamma}{\Gamma_{r=r_0}} = \frac{4}{r_0}\sqrt{\frac{Dt}{\pi}} \qquad (7.2.6).$$

According to the free volume model of diffusion [13][16], the diffusion coefficient is proportional to the free volume if the free volume is much larger than the minimum void volume necessary for diffusion. In our experiments, the free volume is proportional to (1-Θ). Therefore, the equation (7.2.6) may be used to calculate the diffusion coefficient from the initial slope of the Θ *versus* $\sqrt{t}$ plot, when Θ 6 0. Thus, the expressions for viscous flow and lateral diffusion can be used to analyze the variation of Θ with time during the spreading of C15-4Py onto both the monolayer-coated and film-free electrode surfaces. It should be noted however, that both models predict that the fraction Θ should initially vary linearly with the square root of time.

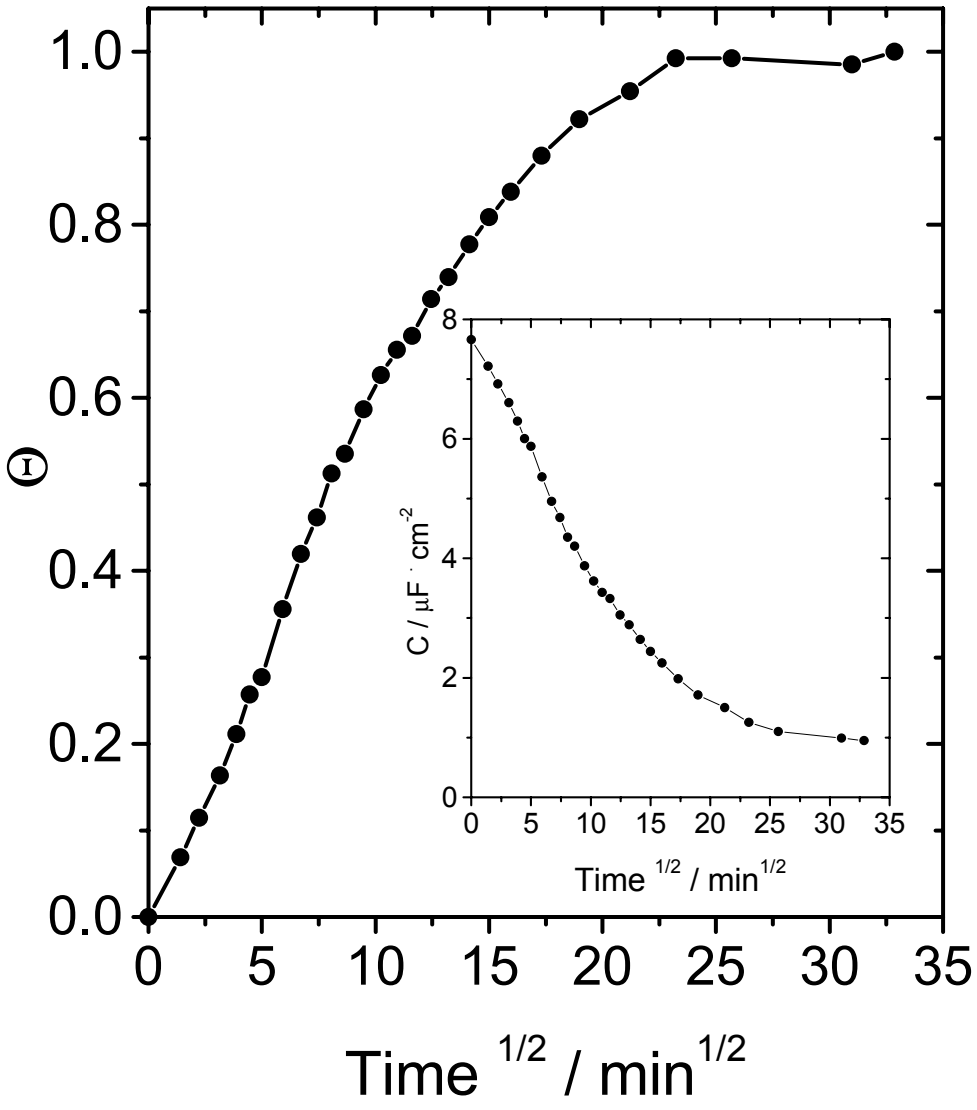

Figure 7.2.6. Extent of transformation of the monolayer into a bilayer, plotted against the square root of the equilibration time between the films spread at the MS and the GS interfaces.
Inset: dependence of the differential capacity on the equilibration time.
The supporting electrolyte solution was 0.05 M $KClO_4$ and 0.001 M $KHCO_3$.

For spreading of C15-4Py molecules onto the monolayer-covered MS interface at E = 0 V, the fraction Θ is plotted *versus* the square root of the equilibration time in the main section of Figure 7.2.6. The initial portion (Θ < 0.4) of this plot is linear. At higher fractions of Θ a deviation from a linear dependence is observed. The inset in Figure 7.2.6 shows how the capacity of the MS interface at E = 0 V changes with the equilibration time. The capacity decreases with time from a value of approximately 8 μF cm^{-2} (characteristic of a monolayer-coated gold surface) to a value of 0.08 μF cm^{-2}, representative of a metal, covered with a bilayer. It should be emphasized that in this experiment C15-4Py molecules of the monolayer that was pre-coated on the gold surface were oriented with the pyridine moiety toward the metal and the hydrocarbon tail toward the solution. Therefore, the transfer of pyridine molecules from the GS interface to the MS interface could be seen as the sliding of a slab (second monolayer) of C15-4Py molecules from the GS interface onto a slab of C15-4Py (first monolayer) attached to the gold surface. The sliding of the two slabs is opposed by frictional tail to tail interactions between the surfactant molecules in the two layers.

The kinetics of the spontaneous formation of the bilayer at the bare gold surface is described in Figure 7.2.7. Equation (7.2.1) was employed to calculate the fraction of the bilayer formation from the capacity data using C_0 to represent the capacity of the film-free MS interface. The fraction Θ is plotted *versus* the square root of the equilibration time in the main section of Figure 7.2.7. The inset in Figure 7.2.7 shows how the electrode capacity changes as a function of time. In a period of 18 h, the capacity drops from a value of approximately 34 μF cm^{-2}, characteristic of a film-free interface, to a value of 0.08 μF cm^{-2}, characteristic of a bilayer. In contrast to the previous case, it is difficult to envisage that the transfer of C15-

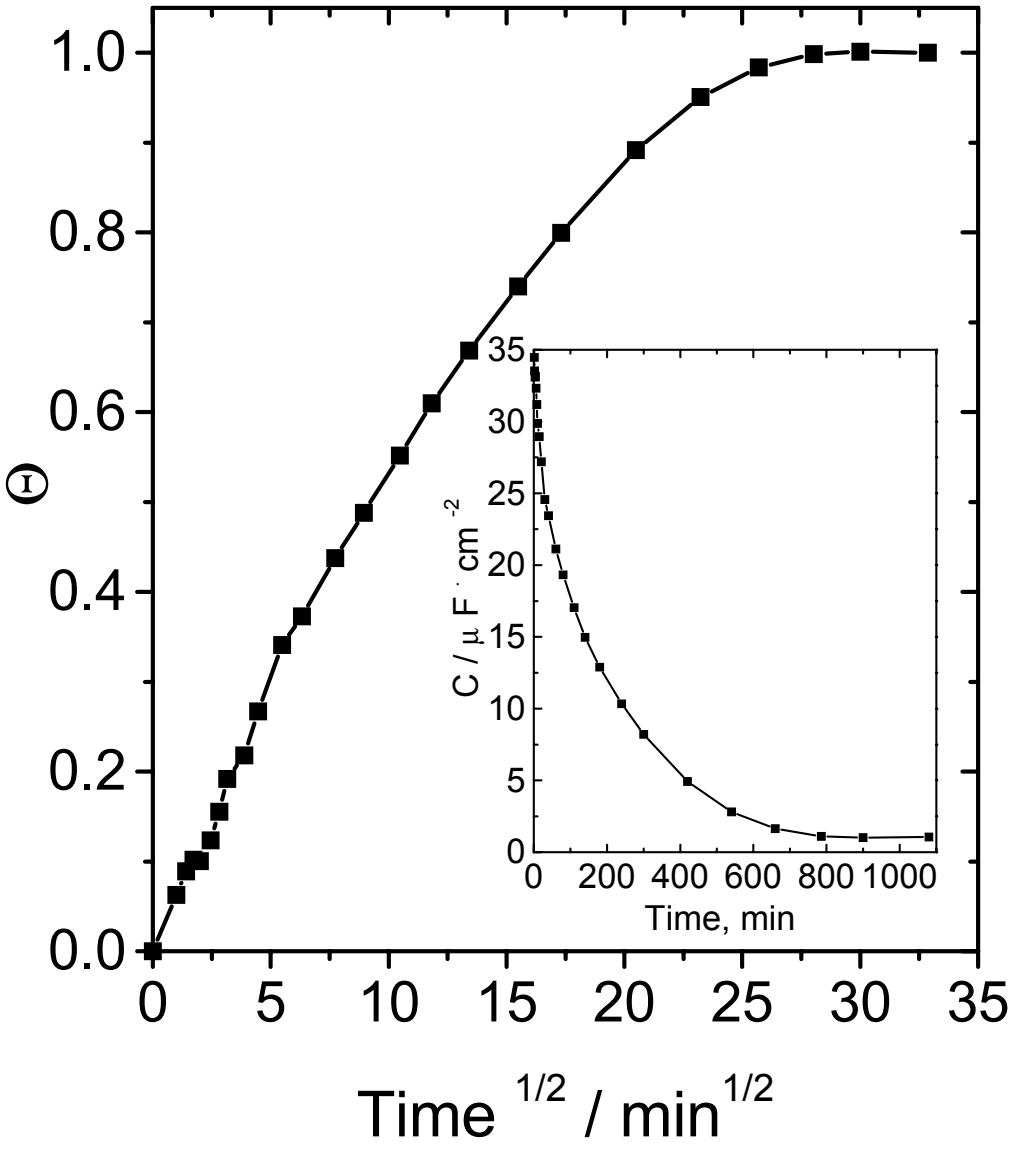

Figure 7.2.7. Extent of the bilayer formation at the initially film-free Au(111) electrode surface, plotted against the square root of the equilibration time between the films spread at the MS and the GS interfaces.
Inset: dependence of the differential capacity on the equilibration time.
The supporting electrolyte solution was 0.05 M $KClO_4$ and 0.001 M $KHCO_3$.

4Py onto the bare electrode surface involves sliding of a monolayer slab of the surfactant from the GS interface to the MS interface. The C15-4Py molecules are oriented with the pyridine moiety toward the solution at the GS interface, while in the first layer of the bilayer the pyridine moiety is turned toward the gold surface. When the first layer is formed at the MS interface, the surfactant molecules have to invert upon crossing the triple phase line, as schematically depicted in Figure 7.2.5 C. Therefore, it is quite surprising to observe that the rates of a spontaneous formation of a bilayer on the film-free electrode surface and the flow of C15-4Py onto the monolayer pre-coated electrode are nearly identical.

In the viscous flow model, the kinetics of the film transfer is described in terms of the flow parameter *FP* [7], which in the present case is given by the expression:

$$FP = \left(\frac{d\Theta}{dt^{\frac{1}{2}}} \right) r_0 \qquad (7.2.7)$$

The flow parameter may be employed to calculate the rate of flow v in cm s^{-1} using the following equation [7]

$$v = (FP)^2 / r_0 \qquad (7.2.8).$$

The initial slopes of Θ versus $t^{1/2}$ plots in Figures 7.2.6 and 7.2.7 are identical within experimental error. They give the flow parameter $FP = 1.3 \times 10^{-3}$ cm $s^{-1/2}$ and the rate of flow $v = 1.0 \times 10^{-5}$ cm s^{-1}. These numbers are lower by a factor of two relative to the values of *FP* and v reported for the flow of oleic acid on a gold surface coated by a monolayer of n-alkanethiols [7].

Alternatively, when the transfer of C15-4Py molecules from the GS interface to the MS interface is interpreted in terms of lateral diffusion, equation (7.2.6) may be used to calculate the diffusion coefficient from the initial slope of the Θ *versus* $t^{1/2}$ plot. The diffusion coefficient, calculated from the data presented in Figures 7.2.6 and 7.2.7, is equal to 3.4×10^{-7} $cm^2\ s^{-1}$. This is quite a reasonable value. It represents the diffusion of C15-4Py molecules in a slab of water next to the electrode surface. It is somewhat lower than the diffusion coefficient of pyridine molecules in the bulk of an aqueous solution (5×10^{-6} $cm^2\ s^{-1}$) and is comparable to some of the diffusion coefficients observed for surfactants in lipid bilayers [14] and for the octadecylferrocene amphiphile in Langmuir monolayers [16]. Hence, the analysis of our data gives reasonable results when both the viscous flow and the lateral diffusion models are employed.

The viscous flow and the surface diffusion models implicitly assume that the activation energy of crossing the triple phase line is negligibly small. Alternatively, one may envisage that the spreading of C15-4Py molecules is controlled by the energy barrier at the triple phase line, as shown schematically in Figure 7.2.5 D, and is essentially a first order surface reaction. In order to derive the kinetic expression for this case, it is useful to determine whether the reaction is reversible or not. To test the reversibility of the spreading of the surfactant molecules, the electrode, covered by the bilayer, was transferred to a separate cell with a surfactant-free GS interface. The film-free GS and the bilayer-covered MS interfaces were then allowed to equilibrate for about 18 h. It was expected that C15-4Py molecules would move back to the film-free GS interface, driven by the gradient of the chemical potential and/or the gradient of the film pressure. The electrode capacity was measured periodically

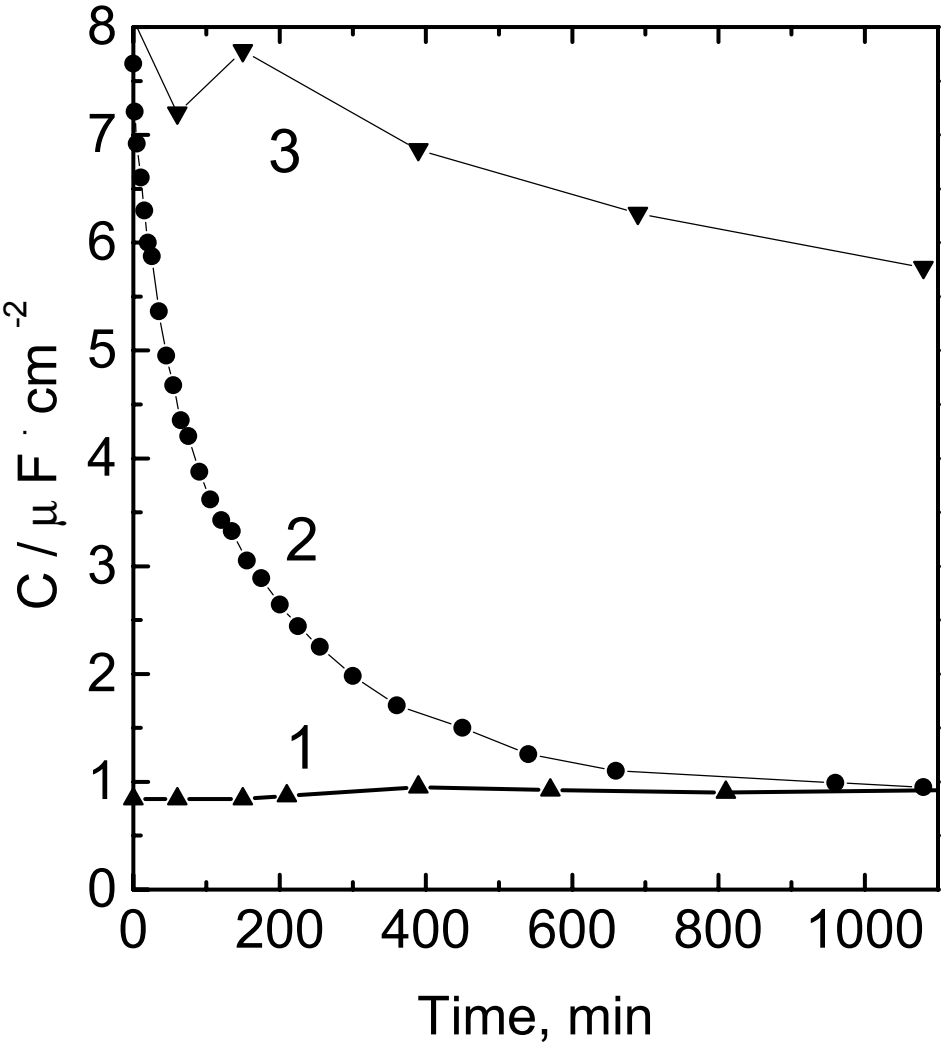

Figure 7.2.8. Dependence of the differential capacity of the electrode surface on the equilibration time.
Curve 1: MS interface covered with a bilayer of C15-4Py in equilibrium with the film-free GS interface.
Curve 2: MS interface covered with a monolayer of C15-4Py in equilibrium with the GS interface also covered with a monolayer of C15-4Py at the equilibrium spreading pressure (33 mN m^{-1}).
Curve 3: MS interface covered with a monolayer of C15-4Py in equilibrium with the film-free GS interface.
The supporting electrolyte solution was 0.05 M $KClO_4$ and 0.001 M $KHCO_3$.

during this extended equilibration time. Curve 1 in Figure 7.2.8 shows the observed changes of the electrode capacity. The changes are negligible. During the period of 18 h the electrode capacity increased only slightly. Apparently, the surfactant molecules did not move back from the MS interface to the GS interface. This behavior is in contrast to the fast transfer of C15-4Py molecules from monolayer-covered GS interface to the monolayer-covered MS interface shown by curve 2 as a rapid decay in the capacity of the MS interface. Curve 3 in Figure 7.2.8 shows the change of the electrode capacity when the monolayer-covered MS interface is allowed to equilibrate with the film-free GS interface. In contrast to our initial expectations, the capacity did not increase with time. As in the case with a bilayer, C15-4Py molecules did not move back to the film-free GS interface. (The small decrease of the capacity with time observed in curve 3 is probably the consequence of the migration of C15-4Py molecules from the gas-metal interface to the metal-solution interface.) The above experiments indicate that thermodynamically both the monolayer and the bilayer of C15-4Py molecules are more favored than the monolayer spread at the GS interface. Thus, the formation of the monolayer and the bilayer at the Au(111) surface is irreversible at $E = 0$ V.

If the transfer of surfactant from the GS interface to the MS interface is controlled by the free energy barrier at the triple phase line, the change of the coverage with time for this first order and irreversible surface reaction should be given by

$$\frac{d\Theta}{dt} = k_r(1-\Theta) \qquad (7.2.9)$$

where k_r is the rate constant, the magnitude of which depends on the activation energy barrier. Integration of this equation yields a linear relationship between the logarithm of the free area (1-Θ) and time:

$$\ln(1-\Theta) = -k_r t \qquad (7.2.10).$$

The experimental data corresponding to the transfer of C15-4Py molecules to the surfactant-free and the monolayer pre-coated MS interface are plotted as ln(1-Θ) *versus t* in Figure 7.2.9. The relationships are nearly linear in a broad range of coverages from Θ = 0.3 to Θ = 0.9. This behavior indicates that the third mechanism of spreading of the surfactant molecules is also plausible, although it does not describe the experimental results in the whole range of coverages. The rate constants calculated from the slopes of the plots in Figure 7.2.9 are 6.1×10^{-3} s^{-1} for the transfer of C15-4Py onto a pre-coated electrode and 4.5×10^{-3} s^{-1} onto the surfactant-free electrode.

7.2.4. Conclusions

In this section, it has been demonstrated that C15-4Py molecules may flow from the GS interface to the MS interface across the triple phase line formed where the solid, liquid and gas phases are in contact. The transfer of the surfactant molecules from the GS interface to the MS interface results in the spontaneous formation of a bilayer at the MS interface. The formation of the bilayer is an irreversible process. Once transferred to the MS interface, the surfactant molecules do not move back to the film-free GS interface. The formation of the bilayer due to the transfer of C15-4Py molecules to the gold surface that was (i) surfactant-

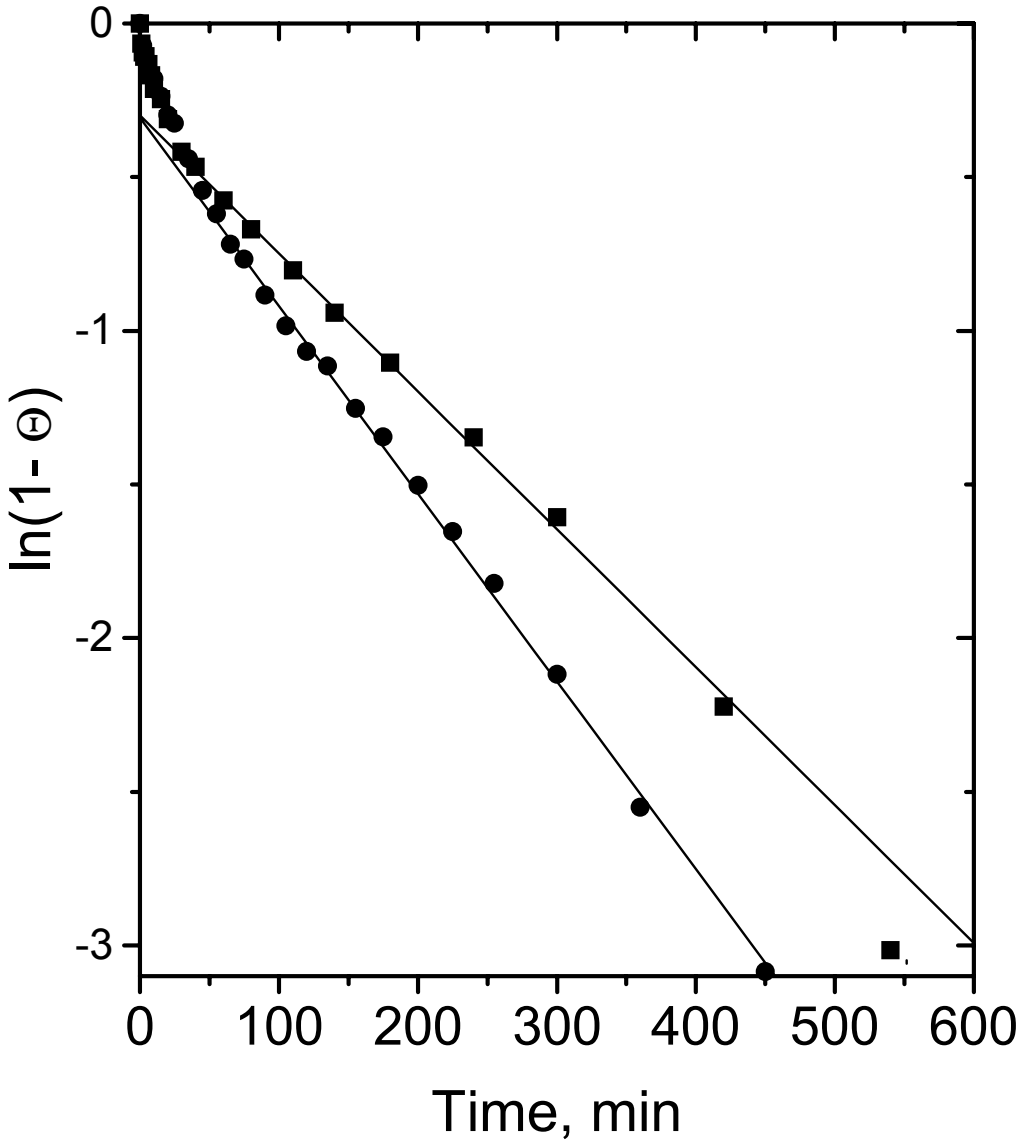

Figure 7.2.9. Dependence of the fraction of the film-free electrode area on experiment time.
Squares: transfer to the surfactant-free electrode,
Circles: transfer onto an electrode pre-coated with a monolayer of C15-4Py.

free and (ii) pre-coated by the monolayer of the surfactant molecules has been investigated. Despite significant differences in the properties of the surfactant-free and the monolayer pre-coated gold surfaces, similar flow rates were observed in the two cases. Two transfer mechanisms involving either viscous flow of a monolayer-thick slab of surfactant or lateral diffusion were used to analyze the kinetic data. The two mechanisms predict similar time dependence for the extent of the bilayer formation. The analysis of the kinetic data yields reasonable values of both the flow rates and diffusion coefficients. However, these two mechanisms do not explain the irreversibility of the transfer of the surfactant nor do they account for the similar spreading rates at the surfactant-free and pre-coated MS interfaces. Therefore, the spreading has also been considered as a first order surface reaction, controlled by the activation energy barrier of the triple phase line crossing. This third model not only gives a satisfactory description of the experimental results but also offers a better explanation of the similar rates of formation of a the surfactant bilayer at the surfactant-free and pre-coated MS interfaces.

7.3 Characterization of the Structure of 4-pentadecylpyridine Films at the Metal-Solution Interface Using Neutron Reflectometry

Neutron reflectometry has been performed in order to characterize the structure of the bilayer and the monolayer of C15-4Py at the metal-solution interface. It is difficult to apply this technique for investigation of the surfactant film that was assembled at the gold electrode *via* a spontaneous transfer from the GS interface to the MS interface. Therefore, the experiments were carried out on the monolayer and the bilayer of C15-4Py deposited onto the gold electrode surface using the single and the double horizontal touching procedures, respectively. The gold-coated quartz single crystal substrates were used as working electrodes and the measurements were carried out at a potential which was approximately equal to 0 V (SCE). Details about the experimental setup are presented in Chapter 4.

Neutron reflectometry [20] relies on measurement of the reflectivity of neutrons from an interface as a function of the momentum transfer vector Q_z. The measured reflectivity from a metal-solution interface allows one to determine the scattering length density (SLD) profile perpendicular to the metal surface. (Scattering length density is the property that characterizes the ability of materials to scatter neutrons. It is related to the refractive index of a material for neutrons.) The surface coverage and thickness as well as the relative positions of individual layers of the film can then be determined from the scattering length density profile. Unlike X-rays, which interact with the core and valence electrons, neutrons are scattered by atomic nuclei, hence the application of neutron reflectometry is not limited to atoms that have high electronic density. This advantage makes this technique particularly suitable for determination of structural information on ultrathin organic films at interfaces [21][22][23].

7.3.1. Approach and Experimental Results

The experimental cell that was used had an "inverted" geometry (shown in the inset to Figure 4.6 in Chapter 4) in which the gold-coated quartz electrode was above the D_2O phase. In this configuration, the lower medium (D_2O) has a higher SLD than the upper. Under such conditions, the reflectivity *R,* is approximately equal to unity for Q_z below a critical value $Q_c=4(\pi\Delta\beta)^{1/2}$, where $\Delta\beta$ is the SLD difference between the lower and the upper media. Above Q_c, *R* decays as a function of Q_z and the character of this decay depends on the area-averaged SLD profile normal to the interface.

The experimental neutron reflectivity data for the films of C15-4Py obtained on the gold electrode using the double and the single touching techniques are shown as solid squares in panel a and panel b of Figure 7.3.1, respectively. For technical reasons, the reflectivity studies of the bilayer and the monolayer films were performed during different neutron measurement sessions using electrodes of different thickness of gold, hence the neutron reflectivity for the two films cannot be directly compared. Consequently, the data are presented in separate panels. In order to extract structural information from these data, the reflectivities were analyzed using the iterative, dynamic method. The scattering length densities of chromium, gold and the organic layers were modeled as boxes of a specified thickness and one overall root mean square roughness factor σ was used to smear out all the interfaces. Based on known parameters of the interface (thickness of the gold and chromium layers and possible structure of the organic layer at the interface), a model scattering length density profile was generated. The dependence of the neutron reflectivity on Q_z for this model interface was then simulated using Fresnel equations and compared to the experimental

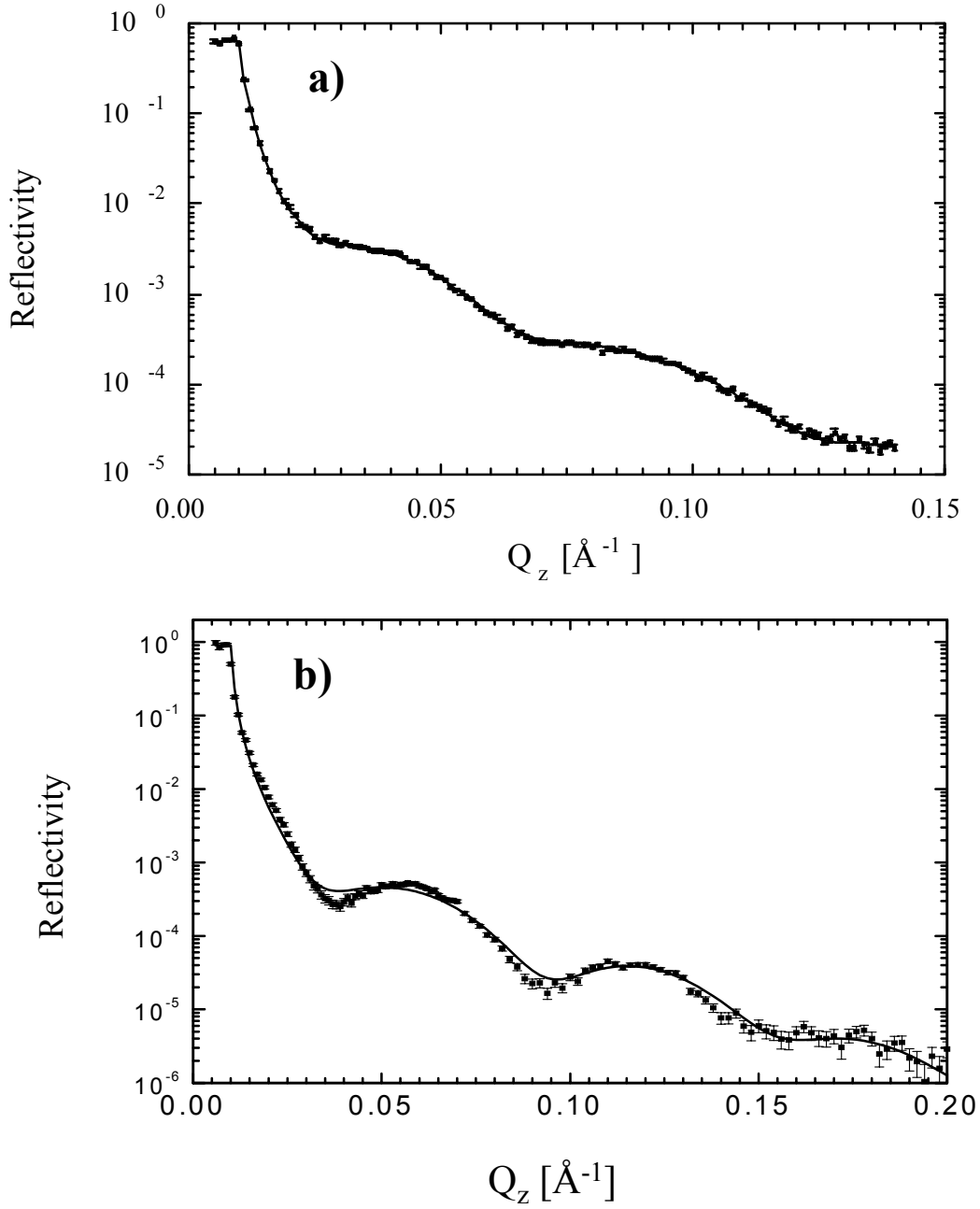

Figure 7.3.1. Neutron reflectivity of the MS interface covered with a C15-4Py film.
a): bilayer obtained using the double horizontal touching technique,
b): monolayer obtained using the single horizontal touching technique.
Solid squares: experimental data points
Solid lines: the best fit simulated neutron reflectivity curves
The numerical values of the fitting parameters are given in Table 7.3.1.

neutron reflectivity data. The model was minimized with the Marquardt-Levenburg non-linear least squares fitting routine in order to obtain the best least squares fit to the experimental data using the most physically reasonable parameters. The guideline was to use the simplest and yet most physically reasonable model to fit the experimental neutron reflectivity. Modeling began with simple one or two box models to account for the Cr and Au layers. If the simple model gave poor fit (a large χ^2 value), its complexity was increased by adding boxes to account for various layers of the interfacial film. Large variations in the parameters of the fit were allowed but the models were restricted to those that generated reasonable results based on the known thickness and SLDs of the gold and chromium layers that comprised the interface. This approach allowed the fitting of the data with a high level of self-consistency.

The best fit curves simulated using the above approach are presented as solid lines in Figure 7.3.1. They were obtained using simple, insightful models of SLD profiles of the MS interface, containing a bilayer and a monolayer of C15-4Py, presented in panel a and panel b of Figure 7.3.2, respectively. Good agreement between the experimental and simulated neutron reflectivities in Figure 7.3.1 can be taken as an argument that the models of the scattering length density profiles presented in Figure 7.3.2 correspond to the profiles of the interface of the experimental cell that contained the corresponding C15-4Py films. The parameters of the best fit for both films of C15-4Py are summarized in Table 7.3.1. In order to achieve a good fit at the higher values of the momentum transfer vector it was necessary to divide the SLD box of chromium into two parts. Table 7.3.1 shows that the values of the SLD of the chromium layers used in the fit (from 3.2×10^{-6} Å^{-2} to 3.82×10^{-6} Å^{-2}) are higher

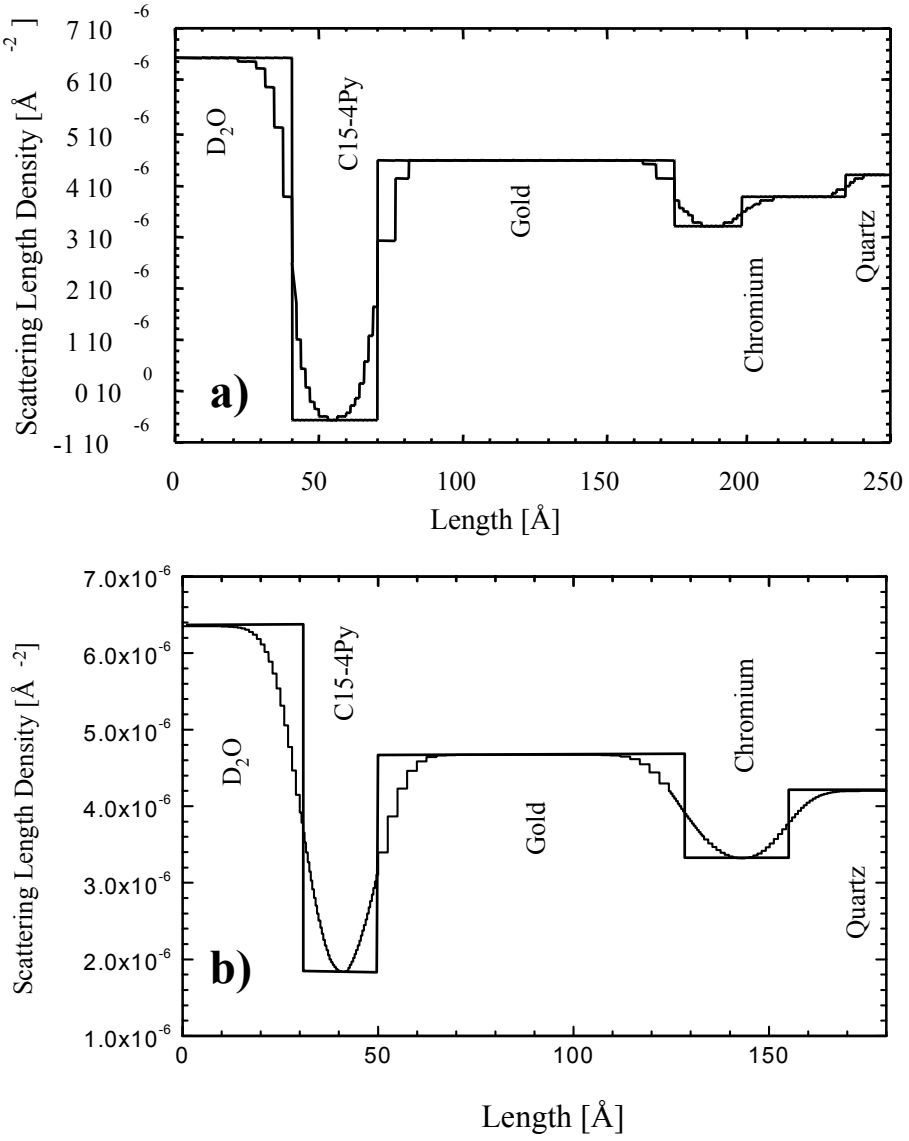

Figure 7.3.2. Scattering length density profile (smeared and unsmeared) of the MS interface covered with a C15-4Py film.
a): bilayer obtained using the double horizontal touching technique,
b): monolayer obtained using the single horizontal touching technique.
The numerical values of the fitting parameters are given in Table 7.3.1.

Table 7.3.1. Scattering length densities and thicknesses of the three layers at the interface between the quartz crystal and the electrolyte solution that were used for the simulation of the experimental neutron reflectivity curves.

C15-4Py		Gold Layer		Chromium Layers					
Scattering Length Density [10^{-6} Å^{-2}]	Thickness [Å]	Scattering Length Density [10^{-6} Å^{-2}]	Thickness [Å]	Scattering Length Density [10^{-6} Å^{-2}]	Thickness [Å]	Scattering Length Density [10^{-6} Å^{-2}]	Thickness [Å]	F [Å]	P^2
Film obtained using the DOUBLE horizontal touchning deposition.									
-0.5	31	4.50	103	3.2	24	3.7	36	5.2	1.49
Film obtained using the SINGLE horizontal touching technique.									
1.53	20	4.67	74.4	3.82	8.9	3.27	20.7	5.8	9.6

Scattering length densities of the constituents of the interface.

Quartz single crystal: $4.2 \cdot 10^{-6}$ Å^{-2}
Bulk chromium: $3.02 \cdot 10^{-6}$ Å^{-2}
Bulk gold: $4.67 \cdot 10^{-6}$ Å^{-2}
Deuterium oxide: $6.33 \cdot 10^{-6}$ Å^{-2}
Scattering length density for densely packed
$(CH_2)_n$ hydrocarbons chains is approximately $-0.4 \cdot 10^{-6}$ Å^{-2}
This value was obtained assuming that the chain area per molecule is equal to 18 Å^2.

The calculations of scattering length density of materials can be performed using the software located at http://rrdjazz.nist.gov/resources/sldcalc.html, the site maintained by the NIST Center for Neutron Research.

than the SLD of bulk chromium (3.02×10^{-6} Å^{-2}). This discrepancy can be the result of a slight mixing of gold with chromium during the gold pre-sputtering process. The gold layer is well described by a single box. A slightly lower value of the SLD of gold (4.50×10^{-6} Å^{-2}) compared to the SLD of the bulk gold (4.67×10^{-6} Å^{-2}) was used to model the interface that contained the bilayer of C15-4Py. This deviation could be due to presence of pores or voids that are sometimes found in metal films produced using the sputtering technique.

7.3.2. The Thickness, the Volume Fraction and the Surface Concentration of the C15-4Py Bilayer and Monolayer at the Metal-Solution Interface

The main objective of the neutron reflectometry was to determine thicknesses of the C15-4Py films at the MS interface. Figure 7.3.2 shows the best fit models of the SLD profiles of the MS interface containing the bilayer and the monolayer of C15-4Py. The thickness of the Au and Cr layers and their SLDs are in good agreement with the X-ray and neutron reflectivity measurements on the film-free substrates in air (for the X-ray case) and D_2O (for the neutron case). These measurements were performed as preliminary experiments before neutron reflectometry of the surfactant films. The values of the thickness of the surfactant films may be taken from either Figure 7.3.2 or Table 7.3.1. The thickness of the film deposited on the electrode by the single touching technique is equal to 20 Å. This value is consistent with the calculated length of a fully extended all-trans C15-4Py molecule that is equal to 20.6 Å, supporting a conclusion that the film of C15-4Py deposited on the electrode using the single horizontal touching technique is a monolayer. The thickness of the film that is transferred to the MS interface using the double touching method is equal to 31 Å. This

thickness is significantly larger than the length of fully extended C15-4Py molecule in the all-trans conformation, corroborating the conclusion that a film of C15-4Py produced using the double horizontal touching is a bilayer. The lower thickness of this bilayer than the total length of two all-trans C15-4Py molecules can be explained as the result of tilting of the molecules of the bilayer by approximately 61° (on average) with respect to the electrode surface plane. It may also be due to disordering of the alkyl chains of C15-4Py in the bilayer, which is expected if the adsorbed surfactant is in a liquid crystalline state.

The volume fraction of C15-4Py films at the MS interface may be determined from the SLDs of the surfactant films. Assuming that the C15-4Py layer contains only the surfactant and the electrolyte (D_2O) molecules, one can determine the volume fraction of C15-4Py in the film (f) using the following equation [21]:

$$\beta_{film} = f\beta_{C15-4Py} + (1-f)\beta_{D_2O} \quad (7.3.1),$$

where β_{film} is the SLD of the surfactant film obtained from neutron reflectometry, while $\beta_{C15-4Py}$ and β_{D_2O} are the SLDs of the bulk C15-4Py and D_2O, respectively. Using the SLDs of densely packed $(CH_2)_n$ hydrocarbon chains (as a value that mimics the SLD of C15-4Py) and D_2O that are presented below Table 7.3.1, one can obtain the volume fractions of C15-4Py in the bilayer and the monolayer of the surfactant at the MS interface equal to ~1 and 0.72, respectively. These numbers indicate that a high quality film of C15-4Py is obtained using the double horizontal touching technique while the film produced using the single

touching is quite permeable for the electrolyte solution, a conclusion that is consistent with the results of electrochemical measurements presented in Section 7.2.

The surface concentration of C15-4Py in both the bilayer and the monolayer can be evaluated using the volume fractions of the surfactant in these films and their thicknesses. Both these parameters are available from neutron reflectivity experiments. Indeed, the surface concentration (Γ) can be calculated using the equation:

$$\Gamma = f \cdot \Gamma_{max} \quad (7.3.2),$$

where f is the volume fraction of C15-4Py in the surfactant film at the MS interface and Γ_{max} is the maximum surface concentration of a densely packed film, which depends on the dimensions of the surfactant molecules and the volume that is occupied by the film spread at a 1 cm^2 area of the electrode. Γ_{max} can be estimated from the experimental value of the thickness of the surfactant film (l), the molar mass (M) and the bulk (mass) density (ρ) of the surfactant using the following equation:

$$\Gamma_{max} = l \frac{\rho}{M} \qquad (7.3.3).$$

For C15-4Py, the molar mass is equal to 289.5 g mol^{-1} and the (mass) density is equal to 0.85 g cm^{-3} (determined experimentally). Using the values of the film thicknesses of the bilayer and the monolayer of C15-4Py as equal to 31×10^{-8} and 20×10^{-8} cm, respectively, one can calculate the values of Γ_{max} and Γ for these films. The results of the calculations are shown in Table 7.3.2. (The volume fractions of C15-4Py in the bilayer and monolayer of the surfactant at the MS interface are shown in the first row of the table for convenience.) The surface

Table 7.3.2. Estimated values of surface concentration and surface pressure of C15-4Py films at the metal-solution interface.

	Bilayer	Monolayer	Units
f	1	0.72	
Γ_{max}	9.1×10^{-10}	5.9×10^{-10}	mol cm^{-2}
Γ	9.1×10^{-10}	4.2×10^{-10}	mol cm^{-2}
π_{MS}	168	155	mN m^{-1}

Data used in calculations.

Calculated molar mass of C15-4Py : 289.5 g mol^{-1}
Experimental (mass) density of C15-4Py: 0.85 g cm^{-3}

Maximum surface concentration of pyridine on Au(111): 6.7×10^{-10} mol cm^{-2}

Free energy of adsorption of pyridine on Au(111): -37 kJ mol^{-1}

Note: data on pyridine were taken from [10].

concentration of C15-4Py in a monolayer is approximately two times smaller than the corresponding value for the bilayer, which is reasonable considering the number of layers of C15-4Py in the two films. Comparing the surface concentration of a C15-4Py monolayer (4.2×10^{-10} mol cm^{-2}) to a Gibbs excess for a monolayer of densely packed pyridine molecules adsorbed on Au(111) (6.7×10^{-10} mol cm^{-2}) [10], it can be concluded that the C15-4Py monolayer is approximately 1.6 times less densely packed than the film of pyridine molecules. A slightly smaller number (1.5 times) is obtained for the bilayer of C15-4Py if the surface concentration of C15-4Py in a single leaflet is taken into account (assuming equal distribution of the surfactant between the two leaflets of the bilayer, the surface concentration of C15-4Py in a single leaflet is equal to 4.6×10^{-10} mol cm^{-2}).

The surface pressure of C15-4Py films may be estimated from their surface concentrations and the free energy of adsorption of pyridine molecules on Au (111). The surface pressure is equal to the difference between the surface energy in the absence and in the presence of the surfactant film. Assuming that the free energies of adsorption of C15-4Py and pyridine on gold are equal and neglecting the contribution to the surface energy due to interaction of the C15-4Py molecules with electrolyte solution, one can calculate the surface pressure as

$$\pi = -\Delta G_{Ads}\Gamma \qquad (7.3.4),$$

where ΔG_{Ads} and Γ denote the free energy of adsorption and the surface concentration of the surfactant, respectively. (Equation (7.3.4) can be derived from equations (3.2.13) and (3.2.14) after substitution of $X_{\text{bulk}} = 1$).Using the published value of the free energy of adsorption of pyridine on Au(111) [10], equal to -37 kJ mol^{-1} and remembering that 1 mN m^{-1} = 10^{-10} kJ

cm^{-2}, it is possible to estimate the surface pressure of C15-4Py at the MS interface. The results of this calculation are presented in Table 7.3.2. It is useful to note that the surface pressure of the C15-4Py bilayer was determined from equation (7.3.4) using Γ that is equal to one half of the surface concentration of the C15-4Py bilayer, because only one leaflet of the bilayer interacts with gold. The values of the surface pressure estimated using these reasonable, although rather crude, assumptions are quite close to the experimental value of the surface pressure of the C15-4Py bilayer at the MS interface of 150 mN m^{-1} (at the potential of maximum adsorption) determined using chronocoulometry [8]. This indicates that the data determined using neutron reflectometry are consistent with the results of the electrochemical studies presented in Section 7.2.

7.3.3 Conclusions.

Neutron reflectometry has confirmed that the film of C15-4Py deposited onto the gold electrode by the double horizontal touching technique is a bilayer while the film obtained using the single touching method is a monolayer. The calculated volume fraction of C15-4Py in the bilayer is close to unity, indicating a good quality of the film while the monolayer contains approximately 28 vol. % of electrolyte. Comparison of the surface concentrations of C15-4Py in the surfactant films at the MS interface with the surface concentration of pyridine at the Au(111) electrode indicates that C15-4Py films are approximately 1.5 times less densely packed than a monolayer of vertically oriented pyridine molecules at the maximum surface concentration. The surface pressures of a monolayer and a bilayer of C15-4Py were estimated from the surface concentrations of C15-4Py in these films. The obtained

values were approximately 12 % higher than the experimentally determined surface pressure of the C15-4Py bilayer at the MS interface. Good agreement between the quantitative data obtained using neutron and electrochemical experiments validates the data determined using neutron reflectometry. The thicknesses and the volume fractions of the C15-4Py bilayer and monolayer at the MS interface determined using neutron reflectometry were used to perform the simulations of infrared spectra of these films that are presented in the next section.

7.4. Ordering and Orientation of 4-pentadecylpyridine at the Au(111) Electrode Studied Using PM FTIR RAS

7.4.1. Introduction

Polarization modulation Fourier transform infrared reflection absorption spectroscopy (PM FTIR RAS) was used to quantitatively characterize the molecular orientation of 4-pentadecylpyridine (C15-4Py) films obtained using the single and the double touching techniques. Neutron reflectometry experiments, presented above, demonstrated that these films correspond to a monolayer and a bilayer of the surfactant at the metal electrode, respectively. The thicknesses and the volume fractions of the C15-4Py films determined using neutron reflectometry were used to simulate the infrared spectra of these films adsorbed at the gold electrode. Comparison of the experimental and the simulated spectra allowed us to derive conclusions about the influence of the electric potential on the orientation of C15-4Py molecules in both these films spread at the Au(111) electrode. To achieve our goal, an experimental setup capable of providing excellent quality infrared spectra of ultrathin films has been developed and a software package able to model infrared spectra of these films deposited onto the metal electrode has been written. Below it will be demonstrated how the procedures described in Chapter 5 can be applied to obtain the information concerning the orientation of C15-4Py molecules in a monolayer and a bilayer deposited at the Au(111) electrode.

7.4.2. Optical Constants of 4-pentadecylpyridine and Infrared Band Assignment.

The orientation of C15-4Py molecules at the MS interface was determined using the absolute method [24] (see Section 5.3.1). To apply this method, the isotropic optical constants of C15-4Py were first determined using a homogeneous solution of this surfactant and following the approach described in Section 5.3.2. Since this surfactant is insoluble in water, the experiments were carried out using a binary solvent consisting of perdeuterated methanol and deuterium oxide. Two BaF_2 disks were utilized as windows and thus, 0.1 M NaF was added to the D_2O in order to suppress the solubility of the window material. It was experimentally found that an approximately10 wt. % solution of D_2O in CD_3OD was a good solvent for C15-4Py. In addition, this binary solvent provided a sufficient amount of D_2O necessary for hydration of pyridine moieties of approximately 0.5 wt. % solution of this surfactant. Hydration of C15-4Py was necessary to ensure the relevance of the simulated and the experimental spectra. The exact composition of the solution is given in the legend to Figure 7.4.1, which presents the spectra of isotropic optical constants. Panel a shows the region of the spectra where stretching vibrations of hydrocarbon chains are observed while panel b shows the region where deformation bands of a pyridine ring and bending vibrations of aliphatic chains are observed. The spectrum of *k* in panel a reveals 4 peaks observed at 2853, 2871, 2925 and 2956 cm^{-1} that are assigned to symmetric CH_2, symmetric CH_3, asymmetric CH_2 and asymmetric CH_3 stretching vibrations of alkyl chains, respectively [25][26][27]. The spectrum of *k* in panel b displays 4 sharp peaks at wavenumbers of 1610 (a_1), 1559 (a_1), 1497 (b_1) and 1414 cm^{-1} (b_1), which are attributed to the deformational

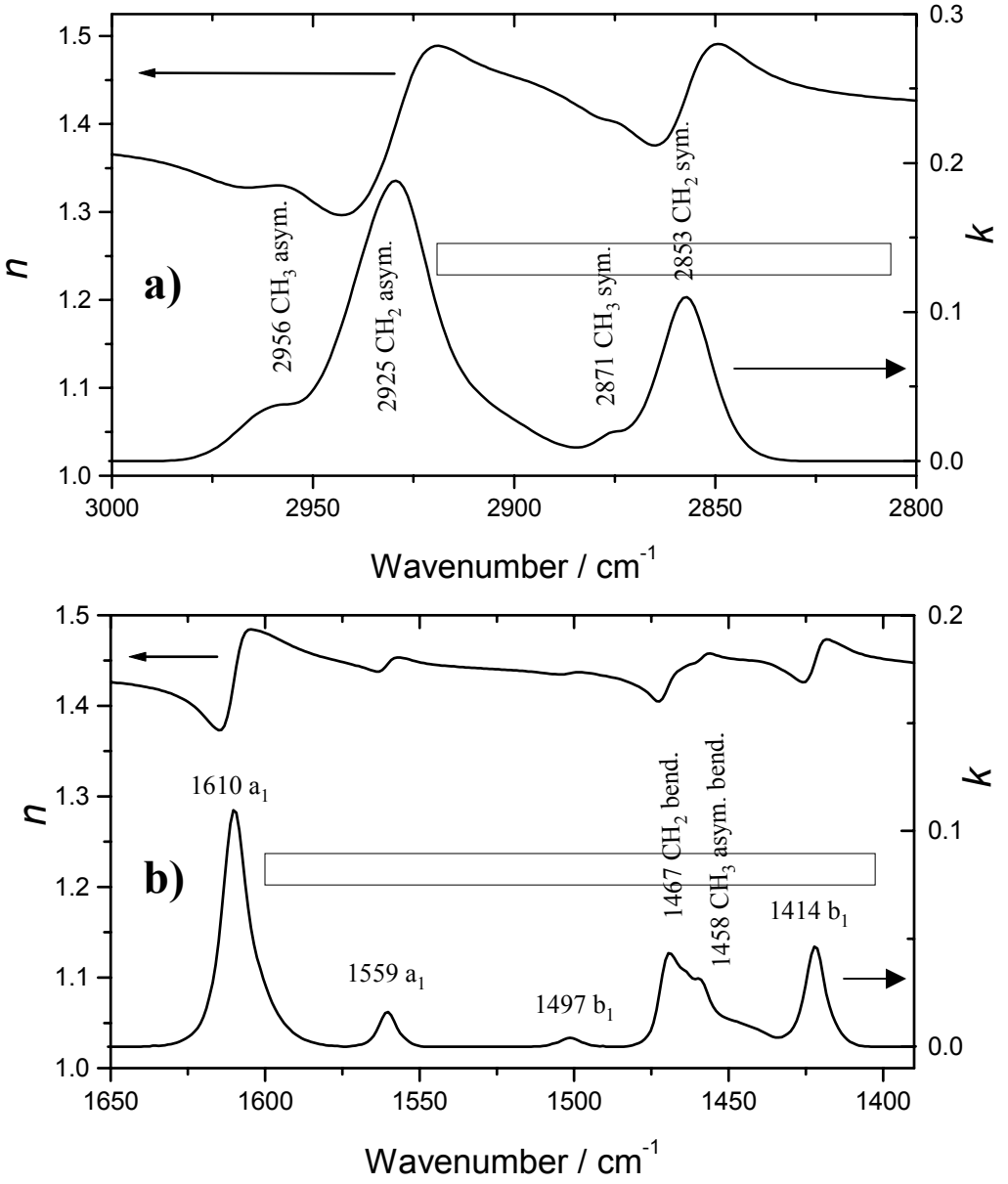

Figure 7.4.1. Optical constants of 4-pentadecylpyridine, calculated from the transmittance spectrum of its 0.5485 wt.% solution in a mixture of 12.98 wt.% of (0.1 M NaF / D_2O) in CD_3OD.
a): CH stretch region and b): HCH bending and pyridine ring vibrations region of the spectrum.
n is the refractive index, *k* is the attenuation coefficient.

vibrations of the pyridine ring of C15-4Py that have a_1 and b_1 symmetry. The orientations of transition dipoles that are associated with the major bands mentioned above are presented in Figure 7.4.2. The pyridine moiety of C15-4Py displays similar bands to those observed in spectra of 4-methylpyridine [28]. In addition, the spectrum of C15-4Py in panel b of Figure 7.4.1 shows a composite band with the most prominent features at 1467 and 1458 cm^{-1}, corresponding to the CH_2 bending and symmetric CH_3 bending vibrations, respectively [29]. (The orientation of the transition dipole of the CH_2 bending mode is parallel to the transition dipole of the CH_2 stretching vibration.) To facilitate the analysis of experimental spectra, it is important to note that transition dipoles of both symmetric and asymmetric CH_2 stretching vibrations are perpendicular to the direction of the hydrocarbon backbone in all-trans conformation.

7.4.3. Quantitative Analysis of the PM FTIR RAS Spectra

The films of C15-4Py were transferred to the Au (111) electrode using the horizontal touching technique. The electrode was then placed inside the spectroelectrochemical cell and PM FTIR RAS spectra were acquired as described in Chapter 4. The raw data were processed following the procedures reported in Chapter 5. Briefly, the experimental spectra were first corrected to remove the artifacts imposed by the PEM and to eliminate the difference in throughput of the optical bench for s- and p-polarized radiation. Next, the baseline obtained using spline interpolation was subtracted from the corrected spectra. The processed spectra were employed for quantitative analysis using the absolute method described in Section 5.3.1. This method allows one to calculate the orientation of the

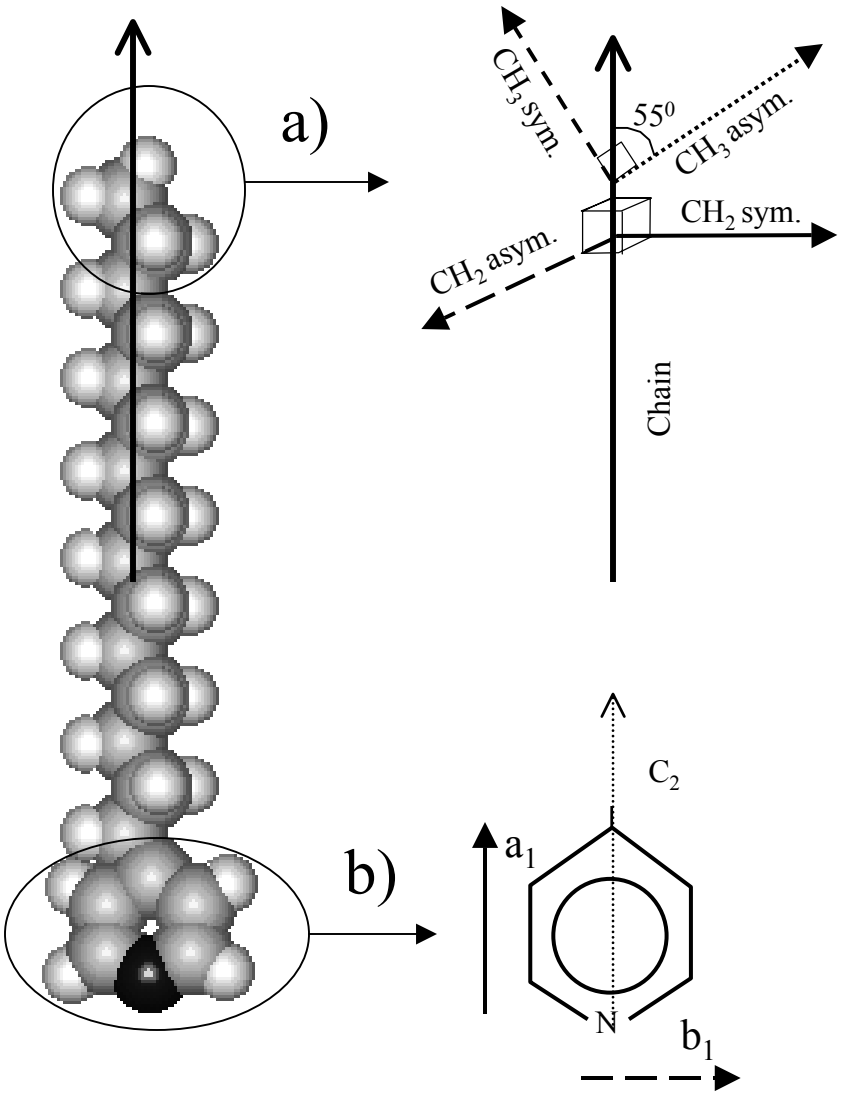

Figure 7.4.2. Orientation of major transition dipoles of 4-pentadecylpyridine.
a): stretching vibrations of the aliphatic chain
b): deformational vibrations of the pyridine moiety
Note: this is not the lowest energy conformation.

transition dipoles with respect to the normal to the metal surface and involves the integration of intensities of the corresponding infrared absorption bands. In addition, this method requires the simulation of the theoretical spectra of the surfactant with known orientations of transition dipoles. The simulated PM FTIR RAS spectra were obtained using equation (2.3.2) and procedures described in Section 5.3.3. The matrix method was utilized to obtain the reflectivities of the stratified medium that mimicked the experimental cell (BaF_2 window, D_2O solution of electrolyte, C15-4Py film, Au electrode), using the optical constants of C15-4Py presented in Figure 7.4.1 and optical constants of BaF_2, D_2O and Au published in the literature [30][31][32][33]. The simulations were performed using isotropic optical constants of C15-4Py, hence the obtained spectra denote absorbance by a disordered film. Such a film is characterized by randomly distributed (along the three coordinate axis) transition dipoles of all vibrations, hence equation (5.3.4) may be employed to determine the orientation of transition dipoles. At this point it is important to understand that the same amount of linearly polarized light is absorbed regardless of whether the light passes through totally disordered film or a perfectly ordered film with transition dipoles oriented at an angle of 55^0 with respect to the direction of the electric field of the polarized radiation. In both cases the absorption is equal to one third of the maximum absorption that is observed when the transition dipoles are aligned parallel with the direction of the field ($\Theta = 0$) because

$$\cos^2\Theta \approx \cos^2(55^0) = 1/3 \qquad (7.4.1).$$

(See also equation 5.3.1 for dependence of absorbance on $\cos^2\Theta$). Thus, without additional information, one cannot distinguish a totally disordered film from an ordered film

with transition dipoles oriented at the angle of 55^0 with respect to the direction of polarization.

The molecules of C15-4Py spread at the electrode as a film at positive and moderately negative potentials and form aggregates in the vicinity of the electrode surface when the metal electrode is polarized to negative extremes of applied potential. It is difficult to mimic the experimental cell at desorption potentials without knowing the shape and size of these aggregates. Therefore, the surfactant was modelled as a film on the metal surface and the simulated spectra were used to determine the tilt angles of C15-4Py at all the applied potentials. This model is highly relevant for the C15-4Py film in an adsorbed state only, hence orientation of C15-4Py in a desorbed state should be regarded as an approximation.

7.4.4. Ordering and Orientation of a C15-4Py Bilayer

A bilayer of C15-4Py was transferred from the GS interface to the surface of the Au(111) electrode using the double touching technique. The PM FTIR RAS was carried out as outlined in Chapter 4 and the experimental spectra were processed as described in the preceding section. The orientation of hydrocarbon and pyridine moieties as well as the conformation and packing of the hydrocarbon chains of C15-4Py film were determined at various potentials. The experimental results and discussion are presented below.

The spectra of C15-4Py bilayer at selected potentials are shown in Figure 7.4.3. The top curve represents the simulated spectrum of a 31 Å thick 100 % pure C15-4Py film deposited on gold, analogous to the bilayer studied by neutron reflectometry. The band assignment of these spectra is given in Figure 7.3.1. Comparison of the simulated and the

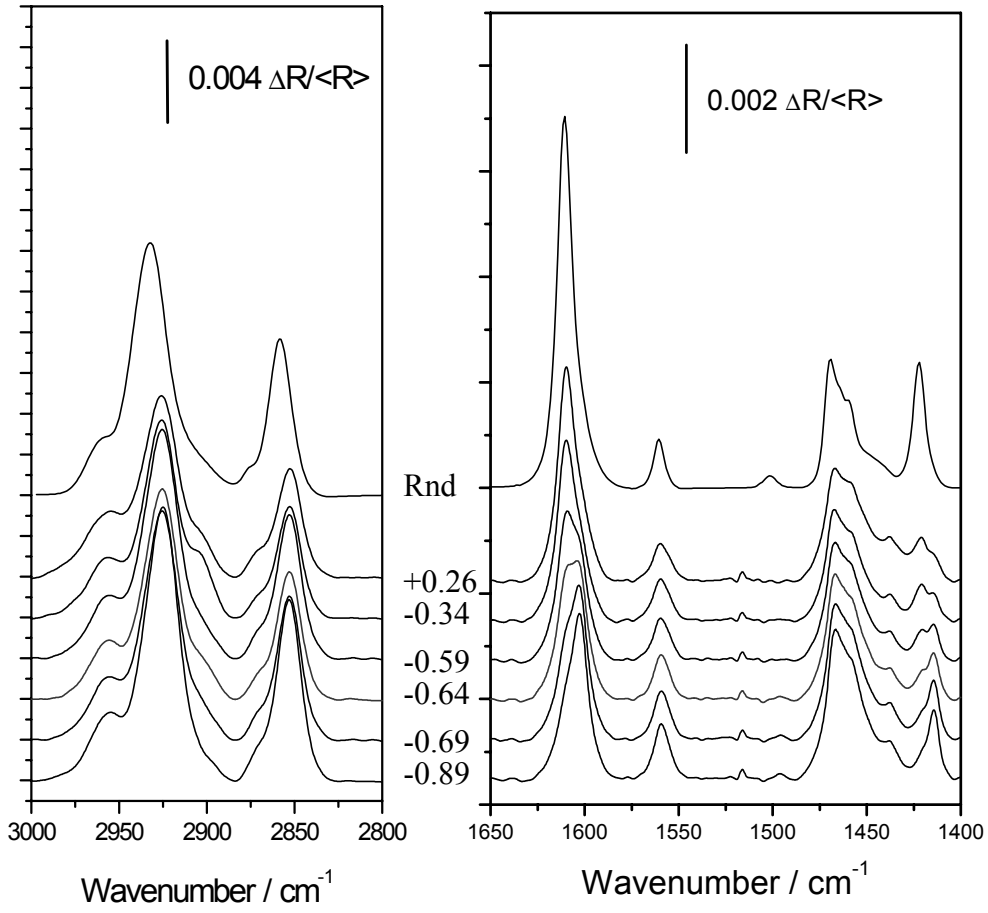

Figure 7.4.3. Spectra of a 4-pentadecylpyridine film obtained using the double touching technique.
The top spectrum (Rnd) represents a simulated spectrum of a C15-4Py bilayer (characterized by the random orientation of the transition dipoles).
Cell: BaF_2/0.1 M NaF in D_2O / Au(111)

experimental spectra presented in the left panel of Figure 7.4.3 demonstrates that at negative electrode polarizations (when the film is desorbed from the electrode surface) the experimental spectra display similar features to the absorbance of the simulated spectrum. Since the simulated spectrum was obtained using isotropic optical constants, this behaviour suggests that the alkyl chains of C15-4Py are disordered when the bilayer is desorbed. An increase in the applied potential results in a decrease of the band intensities of both symmetric and asymmetric CH_2 stretching vibrations. Because the transition dipoles associated with these modes are perpendicular to the hydrocarbon chain backbone in all-trans conformation (see Figure 7.4.2), it may be concluded that the average orientation of the hydrocarbon chains of C15-4Py molecules becomes more vertical with respect to the electrode surface when the film is adsorbed at the metal electrode at positive electrode polarizations.

Infrared spectra of hydrocarbon stretching vibrations can also be used to analyse the conformation of the alkyl chains of the C15-4Py film. It is known [34] that if insoluble surfactants are in an ordered gel state, the alkyl chains assume an all-trans conformation. When the surfactants undergo a gel to liquid crystal phase transition however, several C-C bonds change their conformation from trans to gauche. Casal *et al.* [25][26][27] demonstrated that this phase transition is accompanied by broadening and blue-shifting of CH_2 stretching vibrations. The spectra in Figure 7.4.3. indicate that the CH_2 sym. stretch is observed at 2853 cm^{-1} in the whole range of applied potentials. This value is characteristic for lipids in a liquid crystalline state [26], hence it could be concluded that the C15-4Py bilayer remains fluid at all the potentials studied.

The information about packing of the alkyl chains of a surfactant in a gel state may be derived from the shape and position of the CH_2 bending vibration shown in the right panel of Figure 7.4.3. Mendelsohn *et al.* [35][36] reported that a doublet with wavenumbers of 1472 and 1462 cm^{-1} is observed when the aliphatic chains are condensed in an orthorhombic arrangement while a single peak at 1467cm^{-1} is present if the hydrocarbon chains are arranged in a hexagonal packing. The peak position was reported to remain unchanged across the gel to liquid crystalline phase transition [36]. The experimental spectra in Figure 7.4.3 display a band with a prominent CH_2 bending peak at 1467 cm^{-1} at all the electrode polarizations, consistent with the conclusion that the bilayer of C15-4Py remains in a fluid, liquid crystalline state in the whole range of applied potentials.

Figure 7.4.2 shows that the orientation of the hydrocarbon chains can be estimated from the orientation of the CH_2 transition dipoles assuming an all-trans conformation of the alkyl chains in the surfactant film. It should be noted, however, that this assumption is accurate for ordered films in a gel state only, and the calculations of molecular orientation for films in a liquid crystalline state yield approximate results. The most convenient band to study the orientation of the alkyl chains is the peak that corresponds to CH_2 sym. stretching because it is less affected by the Fermi resonance than the CH_2 asym. peak. The Fermi resonance [37] involves a coupling between the symmetric stretching and the second harmonic of CH_2 bending vibrations, which have the same direction of their transition dipoles. As a result of coupling, a broad band appears in the region where the CH_2 asym. stretching vibration is observed. This broad band is seen in Figure 7.4.3 as a shoulder to the right of the CH_2 asym. peak (and is obscured by the CH_3 asym. peak to the left). Since it is very difficult to separate

the CH_2 asym. peak from the Fermi resonance band, the integration of the CH_2 sym. peak should yield more accurate results.

The integrated intensity of the CH_2 sym. peak observed at 2853 cm^{-1} as a function of the applied potential is shown in Figure 7.4.4 a. The magnitude of the integrated intensity decreases when the film of C15-4Py spreads onto the metal surface at potentials above -0.64 V and increases at the negative extreme of the applied potential when the film is desorbed. The hysteresis between the two curves corresponding to adsorption and desorption of the surfactant is similar to the hysteresis between the differential capacity curves presented in Section 7.1, indicating that infrared spectroscopy can be applied to study the mechanism of potential induced changes in the metal-supported surfactant films. Figure 7.4.4 b shows the average orientation of the transition dipoles corresponding to the symmetric CH_2 vibration of hydrocarbon chains with respect to the metal surface normal. (Same values of the tilt angle with respect to the metal surface plane could be estimated for orientation of hydrocarbon moieties, assuming that the chins are in an all-trans conformation.) At desorption potentials, the transition dipoles are oriented at an angle of approximately 54^0 with respect to the normal, which is close to 55^0, the value expected for totally disordered hydrocarbon chains. Considering the liquid crystalline state of the hydrocarbon chains, it is difficult to envisage that the alkyl chains of C15-4Py are ordered and tilted to yield an angle of 55^0 for transition dipoles at desorption potentials, hence the ordered state should be ruled out. Thus, it could be concluded that the hydrocarbon chains of C15-4Py molecules in a bilayer are disordered at the desorption potentials.

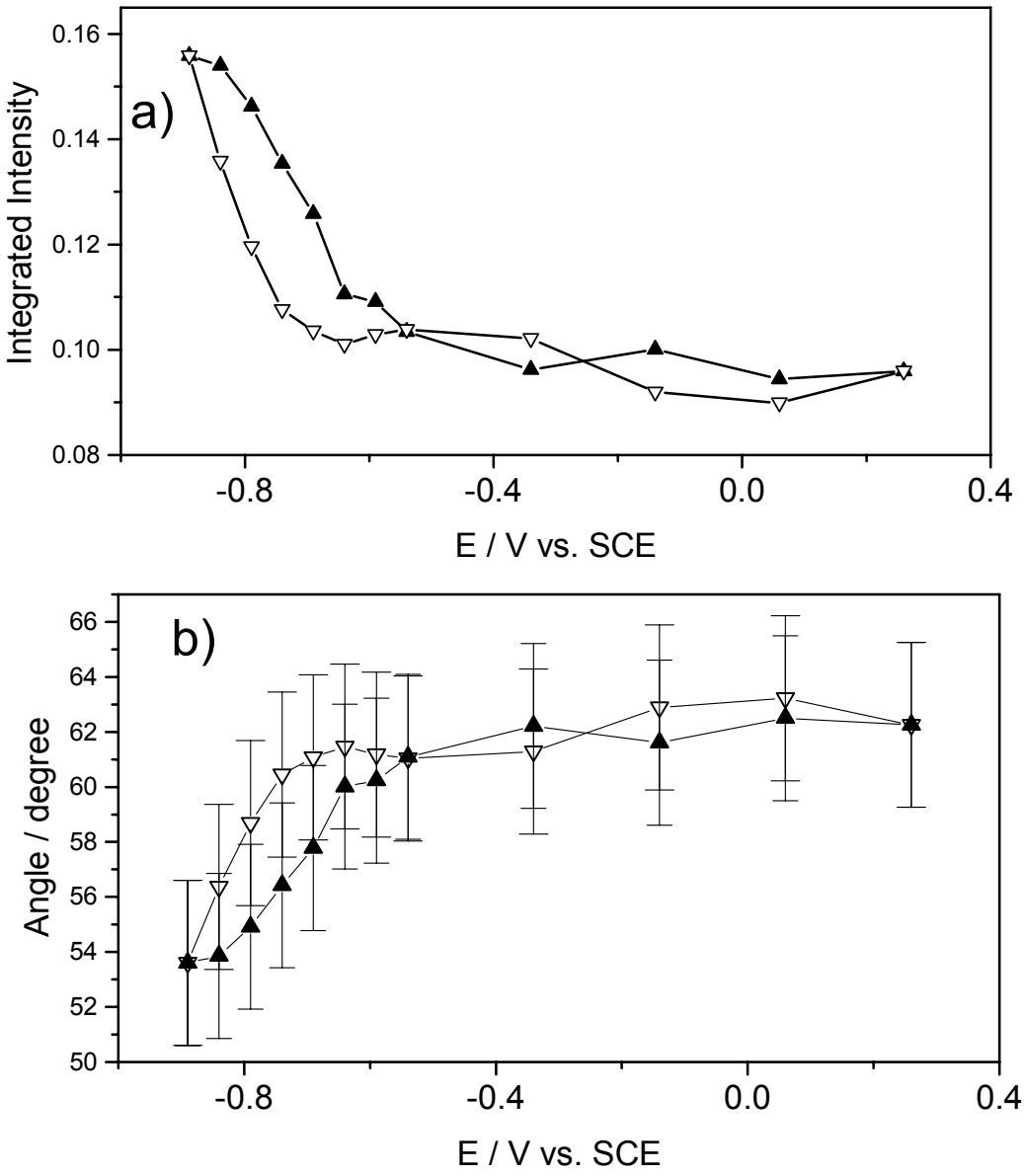

Figure 7.4.4. Variation with the electrode potential of:
a): the integrated intensity of the symmetric CH stretching vibration and
b): the average orientation with respect to the surface normal of the transition dipoles corresponding to the CH_2 sym.vibration in a film of 4-pentadecylpyridine obtained using the double touching method.
Solid triangles: positive train and Open triangles: negative train of the potential steps applied to the electrode.
The uncertainty of the tilt angle is approximately equal to $\pm 3^0$
(See Appendix B).

The molecules assume preferentially a more vertical orientation with an average orientation of transition dipoles with respect to the metal surface normal equal to 62^0 when the molecules of C15-4Py adsorb at the electrode as a film at positive polarizations. This value is consistent with the reported [38] orientation of the transition dipoles in condensed long chain surfactants adsorbed at solid substrates that typically yield the angle of 60^0. The small changes in the orientation of transition dipoles of the symmetric CH_2 vibration that occur at potentials close to -0.4V can be attributed to the transformation between the hemimicellar surface aggregates and the compact film [39]. It is not surprising that the observed changes are small since C15-4Py remains in the liquid crystalline state in the whole range of applied potentials.

The vibrations of the pyridine moiety of C15-4Py are presented in the right panel of Figure 7.4.3. In contrast to the vibrations of the hydrocarbon chain, the bands of the C15-4Py head groups reveal considerably lower intensities of the most prominent peaks at 1603-1610 cm^{-1} (a_1) and 1414 cm^{-1} (b_1), compared with the simulated spectrum shown at the top of the panel. Taking into account the orientation of the transition dipoles of a_1 and b_1 modes with respect to the direction of the C_2 axis of the molecule (presented in Figure 7.4.2), it could be concluded that the planes of the pyridine moieties of C15-4Py molecules are oriented at a relatively small angle with respect to the electrode surface in the whole range of electrode potentials. The dependence of the spectral features on the applied potential reveals two tendencies. Firstly, the b_1 peak almost vanishes from the spectra at the positive extreme of the electrode potential, indicating that the transition dipole associated with this vibration becomes oriented almost parallel to the metal surface. Secondly, the a_1 band, which includes two

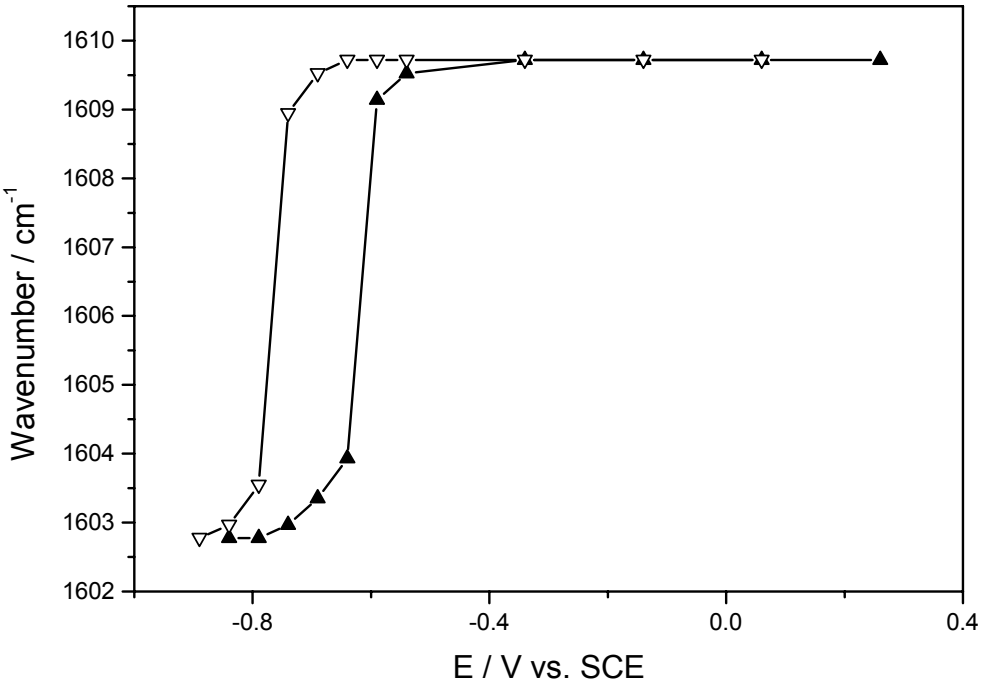

Figure 7.4.5. Change in the position of the a_1 peak of a 4-pentadecylpyridine film, obtained using the double touching method, as a function of the electrode potential.
Solid triangles: positive train,
Open triangles: negative train of the potential steps applied to the electrode.

components, displays a potential-dependent increase of its 1610 cm^{-1} component at the expense of the 1603 cm^{-1} component. Apparently, the molecules that are chemisorbed at the gold surface display a blue shift in vibrational frequency by approximately 7 cm^{-1} with respect to the frequency of the hydrated molecules in aqueous solution of electrolyte. Figure 7.4.5 demonstrates an abrupt change of the position of the maximum of the a_1 band that takes place as the result of adsorption and desorption of the surfactant film observed at approximately -0.6 and -0.8 V, respectively. The behaviour presented in this figure is consistent with the assignment of the band observed at1610 cm^{-1} to the chemisorbed C15-4Py.

Because the chemisorbed C15-4Py molecules display an a_1 mode at a different vibrational frequency from the hydrated molecules, the 1603-1610 cm^{-1} band can be deconvoluted to two peaks. For the positive sequence of potential steps, such deconvolution is valid in the potential region from -0.54 V to 0.26 V, where the molecules of C15-4Py are adsorbed at the gold surface. To a first approximation, the adsorbed film may be treated as a bilayer in this potential region. (Figure 7.2.1 shows that the C15-4Py film forms a bilayer in the region between -0.05 and 0.3 V, and in the region between -0.54 and -0.05 V the film is likely to form an array of surface aggregates of hemimicellar or hemicylindrical type. Hence, the bilayer state of the film in the potential region from -0.54 V to 0.26 V is an approximation). The inner leaflet of such a bilayer is chemisorbed at the gold surface and the outer leaflet is hydrated by the aqueous electrolyte solution. Figure 7.4.6 a demonstrates the change in the shape of the 1603-1610 cm^{-1} band with the electrode potential on an expanded scale. It is evident from this graph that the shape of the band depends on the intensity of two components with maxima at 1603 and 1610 cm^{-1}. These components were deconvoluted by

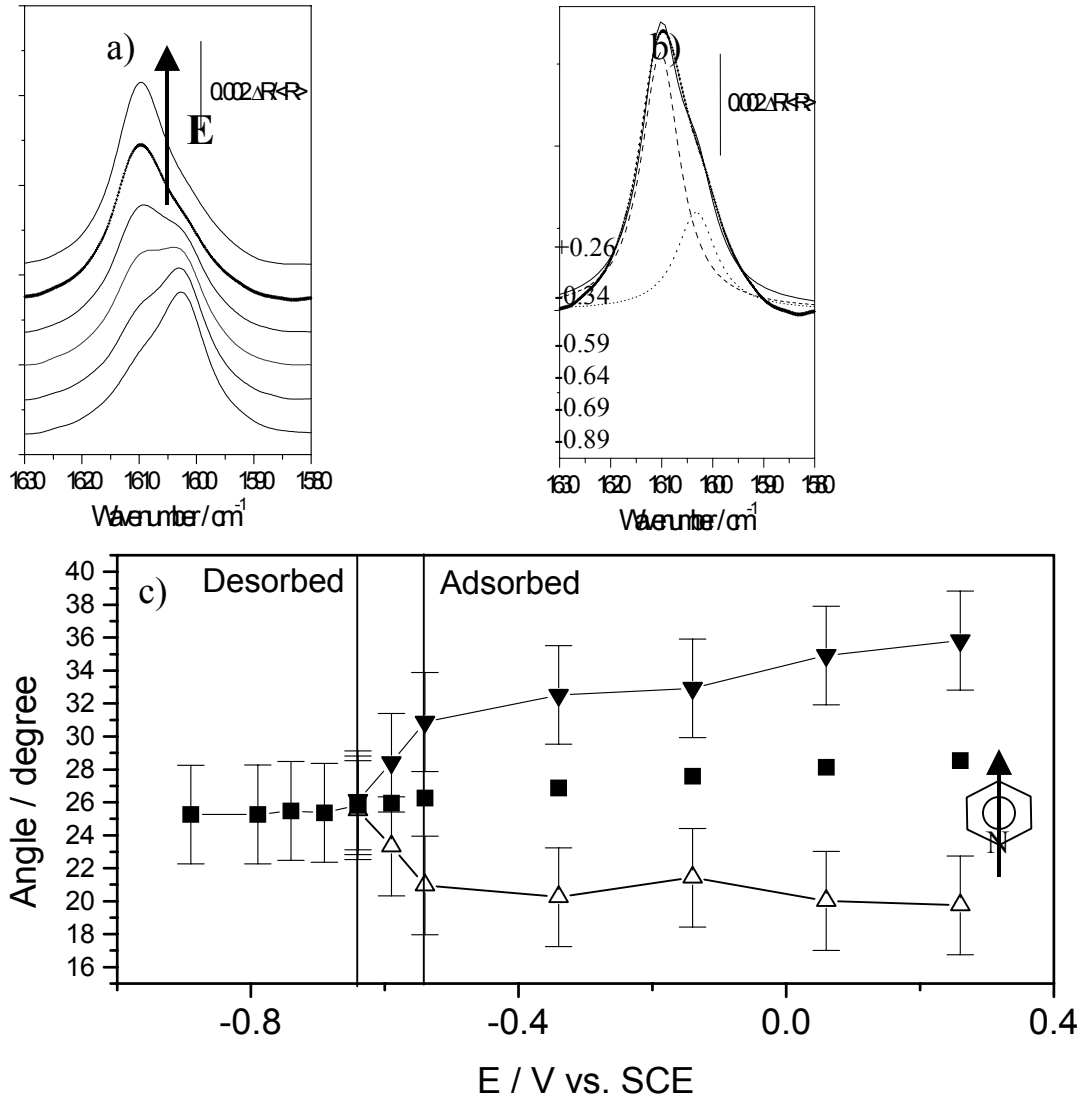

Figure 7.4.6. Spectra and orientation of the head groups of a C15-4Py bilayer.
a): the shape of the a_1 band at selected potentials.
b): an example of deconvolution of an experimental spectrum (crosses) to two components with maxima at 1610 cm^{-1} (dashed line) and 1603 cm^{-1} (dotted line). (Solid line denotes the spectrum obtained by recombination of the two components)
c) Orientation of the C_2 axis of the pyridine moieties
Solid squares: determined using the total integrated intensity of both 1610 cm^{-1} and 1603 cm^{-1} components of the a_1 band.
Solid triangles: determined using the integrated intensity of the 1610 cm^{-1} component
Open triangles: determined using the integrated intensity of the 1603 cm^{-1} component
The angles are reported with respect to the surface plane.
The data represent the positive sequence of potential steps.
The uncertainty of the tilt angle is approximately equal to $\pm 3^0$
(See Appendix B).

fitting two Lorentzian peaks into the a_1 band. Figure 7.4.6 b shows an example of the deconvolution procedure. The experimental spectrum (acquired at -0.34 V) was separated into two peaks at 1610 cm^{-1} (dashed line) and 1603 cm^{-1} (dotted line), which represent the spectral signatures of the inner and the outer leaflet of the bilayer, respectively. A good fit of the spectrum obtained by the recombination of these two components (solid line) and the experimental spectrum (crosses) indicates that the 1603-1610 cm^{-1} band can indeed be derived from two Lorentzian peaks.

The two bands, obtained by deconvolution, were integrated and the integrated intensities were used in equation (5.3.4) to determine the orientations of the head groups of C15-4Py in two separate leaflets of a C15-4Py bilayer. The theoretical integrated intensity for a single leaflet of the bilayer was calculated assuming an even distribution of C15-4Py molecules between the outer and the inner leaflets. The obtained value was equal to one half of the theoretical integrated intensity of a bilayer determined by integration of the a_1 band in a simulated spectrum shown at the top of Figure 7.4.3. The potential-dependent change in the orientation of the head groups of C15-4Py determined using deconvolution is shown in Figure 7.4.6 c. The orientation of the pyridine groups in the outer and the inner leaflets is denoted by solid and open triangles, respectively. Solid squares show the orientation of pyridine moieties determined using the experimental (convoluted) spectrum and represent the average orientation of the head groups of C15-4Py molecules in the whole range of applied potentials. Since deconvolution is valid only in the region where the C15-4Py film is adsorbed at the metal, the orientation of the pyridine moieties in the inner and the outer leaflets is shown only for the electrode potentials above -0.64 V. Figure 7.4.6 c demonstrates that the pyridine

moieties are oriented at an average angle of 25^0 with respect to the electrode surface at the negative extreme of the electrode polarizations and the average tilt angle (solid squares) slowly increases with potential to attain 28^0 at the positive extreme. In an adsorbed state, the pyridine groups of the inner leaflet assume higher values of the tilt angle (*ca.* 35^0) than the groups of the outer leaflet (*ca.* 20^0). In addition, a progressive increase of the tilt angle from 31^0 to 35^0 with the applied potential is observed for the head groups of the inner leaflet while the orientation of the pyridine moieties of the outer leaflet remains practically unchanged.

To explain the above observations it is useful to recall [10] that pyridine undergoes a rapid change from horizontal to nearly vertical orientation (with respect to the electrode surface), when the electrode potential becomes positive. The surface concentration increases from 1.4×10^{-10} to 6.7×10^{-10} mol cm^{-2} during this phase transition, which corresponds to the change in the mean molecular area (MMA) from 119 to 25 $Å^2$. Experimental results indicate that in contrast to the pyridine molecules, the pyridine surfactant displays only a small increase in the tilt angle of the pyridine moiety in the proximity of 0 V, where the phase transition from hemimicellar (or hemicylindrical) surface aggregates to the bilayer takes place. The results also show that the tilt angle of C15-4Py molecules in the inner leaflet remains within the limits of 25^0 to 35^0 in the whole range of electrode polarizations. Apparently the alkyl chains, attached to the pyridine groups, hinder the reorientation of the head groups and preserve the tilt angle within the above limits.

Studies of compression isotherms at the GS interface in the Langmuir trough [8] demonstrate that the MMA of C15-4Py at equilibrium spreading pressure is equal to 30 $Å^2$. Using one half of the surface concentration of C15-4Py molecules in the bilayer at the MS

interface determined using neutron reflectivity (from Table 7.3.2), it is possible to calculate the MMA of C15-4Py at the MS interface. The obtained value is equal to 36 $Å^2$. Hence, it could be concluded that the closest packing of C15-4Py films is achieved when the MMA attains values in the region from 30 to 36 $Å^2$. These values are larger than the MMA for a densely packed film of pyridine (25 $Å^2$), suggesting that the closest packing of the pyridine surfactant is determined by the area needed to accommodate its hydrocarbon tails. The pyridine heads of the surfactant apparently cannot achieve separation distances of less than 5 Å in order to form vertically oriented stacks, similar to those observed using STM for pyridine on Au(111) by Cai *et al.* [40]. Experimental evidence demonstrates that the molecules can however, come close enough to form tilted rather than horizontal arrangements at the metal surface.

A more horizontal orientation of the pyridine head groups in the outer leaflet compared to the orientation in the inner leaflet of the bilayer apparently assists in the compensation of the dipole moments of individual C15-4Py molecules in order to decrease the net dipole moment of the outer leaflet. Similar behaviour has been observed for bilayers of lipids [41]. It was reported that the head group dipoles are oriented parallel to the plane of a bilayer. The low values of the average tilt angle of the pyridine moiety at the negative extreme of applied potentials suggests that C15-4Py may form flat aggregates (flakes or bilayers) rather than spherical micelles when the film is desorbed. The decrease in the tilt angle of the head groups of the outer leaflet that occurs when the film becomes adsorbed may be due to a partial screening of the electrode by the chemisorbed inner leaflet. The rapid increase in the tilt angle of the pyridine moieties of the inner layer that takes place during adsorption

is apparently the result of chemisorption. It should be noted, however, that the angle determined for a desorbed C15-4Py film denotes the average values for both leaflets, hence it is difficult to derive accurate conclusions about the changes in molecular orientation in separate leaflets that occur as a result of adsorption. The progressive increase of the tilt angle of the pyridine moieties of the inner leaflet with the applied potential indicates that, due to dipole- field interaction, the electric field tends to align the head groups of the adsorbed C15-4Py molecules in a similar fashion as it orients pyridine molecules at the Au(110) electrode (see Chapter 6).

Low values of the average tilt angle of pyridine moieties are consistent with the estimated average orientation of hydrocarbon chains in the C15-4Py bilayer. It was shown at the beginning of this section that the average tilt angle of the alkyl chains may be estimated to attain values from 60 to 62^0 with respect to the metal surface when the bilayer is adsorbed at the electrode. Figure 7.4.7 demonstrates that one could expect the tilt angles from 25 to 27^0 for the pyridine moiety in its adsorbed state, assuming the lowest energy conformation of the C15-4Py molecule. Thus, the orientation of the head groups and the orientation of the hydrocarbon tails are related.

The orientation of the transition dipole of C15-4Py head groups associated with the b_1 mode (see Figure 7.4.2) can be determined using the integrated intensity of this mode. Figure 7.4.8 shows the results of calculations. At the negative extreme of the electrode potential, the b_1 transition dipole is tilted at an the angle of almost 35^0 with respect to the metal surface which corresponds to an angle of 55^0 with respect to the surface normal, a value characteristic of random orientation of transition dipoles. This observation implies that the

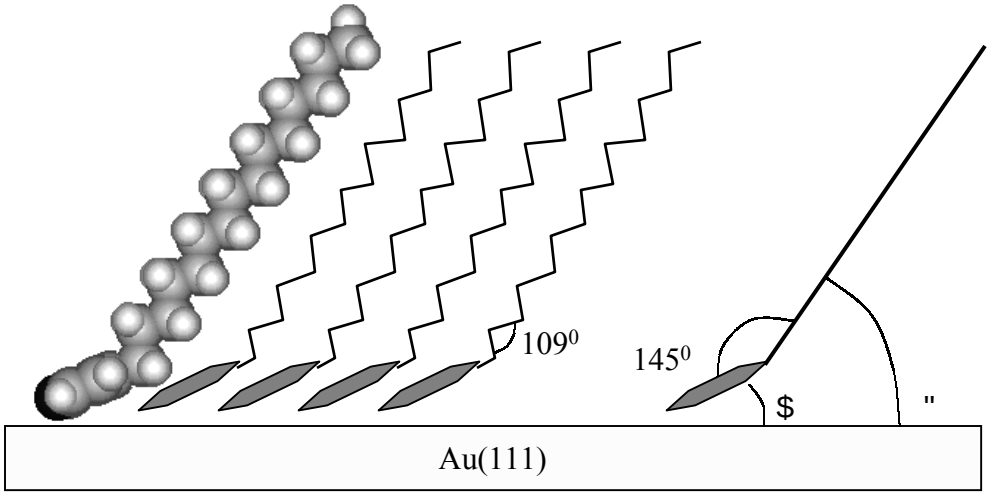

Figure 7.4.7. Orientation of the pyridine moiety and the hydrocarbon chain in a C15-4Py film adsorbed at a gold electrode. (Lowest energy conformation).
$\$ = " - (180^0 - 145^0) = " - 35^0$

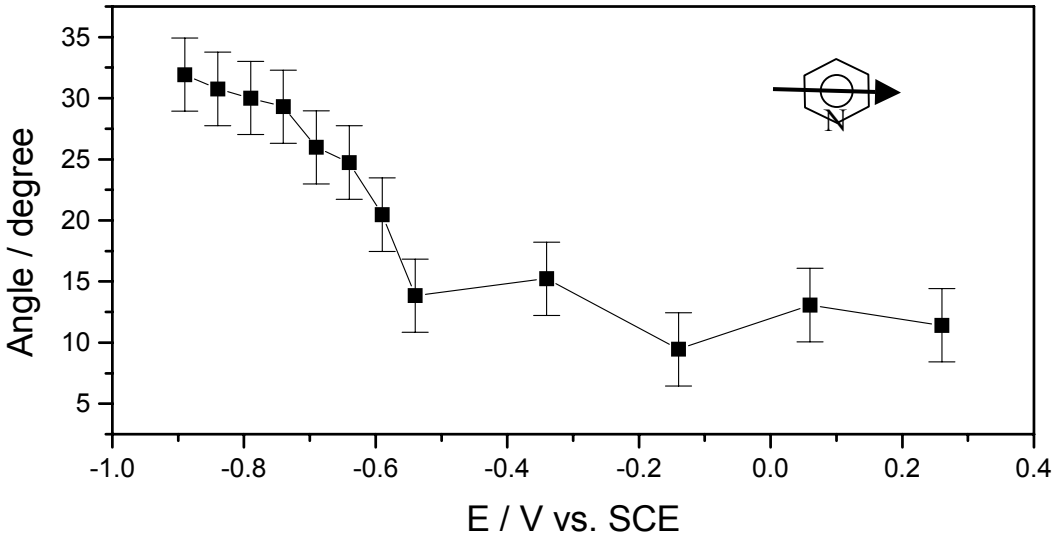

Figure 7.4.8. Orientation of the b_1 transition dipoles of the pyridine moieties (shown in the drawing) in a 4-pentadecylpyridine film obtained using the double touching technique.
Determined from the integrated intensity of the peak observed at 1415 cm^{-1}.
The angle is reported with respect to the surface plane.
The uncertainty of the tilt angle is approximately equal to $\pm 3^0$
(See Appendix B).

pyridine moiety can rotate relatively freely with respect to the C_2 axis when the C15-4Py film is desorbed. In an adsorbed state, however, the orientation becomes hindered at an angle of approximately 10^0 with respect to the metal surface. A nearly parallel orientation of the b_1 transition dipole of adsorbed C15-4Py molecules is consistent with infrared measurements of pyridine adsorption on Au(111) performed earlier in our laboratory [42] and elsewhere [40].

7.4.5. Ordering and Orientation of a C15-4Py Monolayer

The monolayer of C15-4Py was transferred from the GS interface to the surface of the Au(111) electrode using the single horizontal touching technique. The PM FTIR RAS spectra were acquired using the setup and procedures described in Chapter 4 and processed using the approach described in Section 7.4.3. The experimental results and discussion are presented below.

The infrared spectra of C15-4Py monolayer at selected potentials are presented in Figure 7.4.9. The stretching vibrations of the hydrocarbon tail and the pyridine moiety of the molecule are shown in the left and the right panel of the figure, respectively. The left panel also shows the bending vibrations of the hydrocarbon tail. The band assignments are presented in Figure 7.4.1 which shows the isotropic optical constants that were used to obtain the simulated spectrum of the C15-4Py monolayer, shown in Figure 7.4.9 at the top. The monolayer was modelled as a 20 Å thick film with the volume fraction of C15-4Py (in D_2O) equal to 0.72. The simulation was performed using the data obtained from neutron reflectometry and presented in Section 7.3. Experimental spectra in Figure 7.4.9 reveal an approximately twofold decrease in the intensity of most of the infrared bands compared with

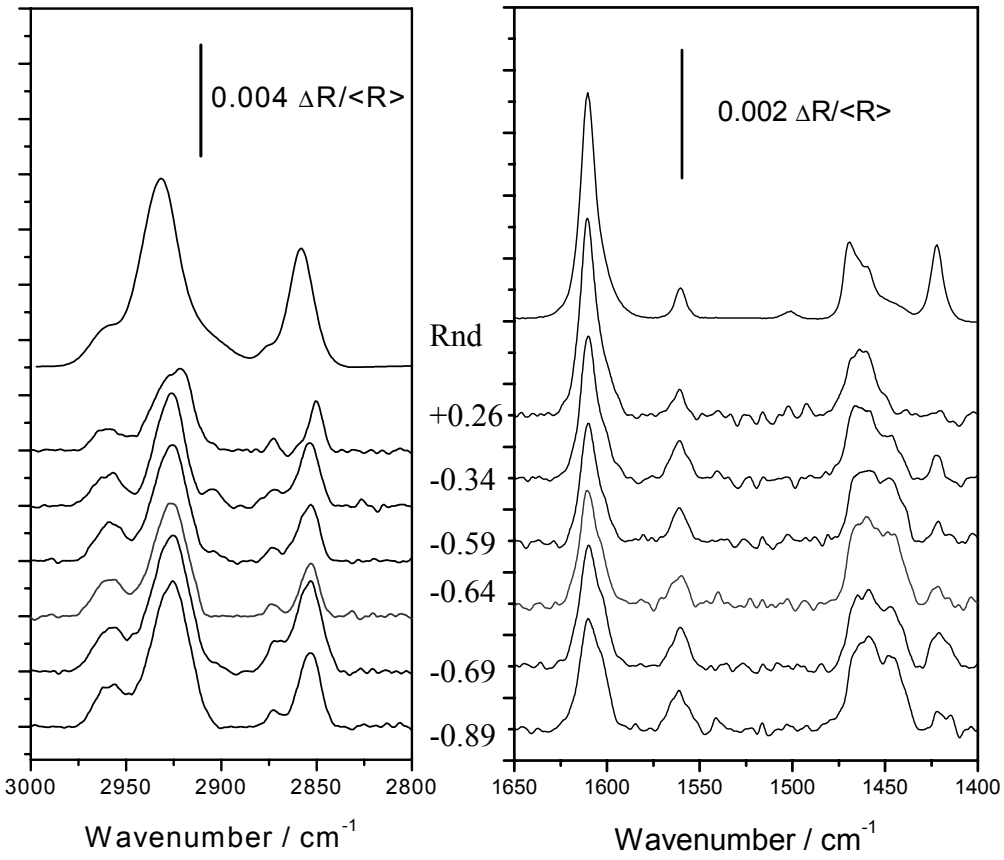

Figure 7.4.9. Spectra of a film of 4-pentadecylpyridine obtained using the single touching technique.
The top graph (Rnd) represents a corresponding simulated spectrum, characterized by the random orientation of the transition dipoles.
Cell: BaF_2/0.1 M NaF in D_2O/Au(111)

the spectra of the C15-4Py bilayer in Figure 7.4.3. This behaviour is consistent with a monolayer coverage of the electrode. There are several distinct features characteristic of a monolayer spectrum of this surfactant.

First, the average orientation of the hydrocarbon chains is much more vertical in the monolayer, observed in Figure 7.4.9 as a significant reduction in the intensity of the CH_2 stretching vibrations relative to the CH_3 stretching modes of the alkyl chains. Second, the hydrocarbon moieties become so well aligned at positive electrode polarizations that a phase transition from the liquid crystalline to gel state occurs. This phase change is indicated by a shift of the maxima of the CH_2 sym. stretching vibrations from 2853cm^{-1} to 2850cm^{-1}, the value characteristic for all-trans conformation of the hydrocarbon chains observed for lipids in a gel state [26]. It should be noted, however, that this phase transition is not accompanied by the splitting of the CH_2 bending mode to a doublet with wavenumbers of 1472 and 1462 cm^{-1}, which is expected when the aliphatic chains become closely packed in an orthorhombic arrangement. The maximum of the band 1466 cm^{-1} indicates that the alkyl chains are arranged in a hexagonal packing arrangement. Another principal difference between the spectra of the bilayer and the monolayer of C15-4Py is the significant decrease in the intensity of the b_1 mode of the surfactant head group. This vibration almost entirely disappears from the spectrum at all the electrode polarizations, indicating a parallel orientation of the transition dipole associated with this mode with respect to the electrode surface.

To perform quantitative analysis of the orientation of C15-4Py molecules at Au(111), the intensities of the peaks assigned to the CH_2 sym. stretching vibration and the a_1 mode of pyridine ring deformation were integrated and used, together with the corresponding

integrated intensities of the simulated spectrum, to calculate the orientation of the transition dipoles hydrocarbon chain and pyridine heads in the monolayer, respectively. The absolute method, described in Section 5.3.2, was used to calculate the angles. Figure 7.4.10. a shows the average orientation with respect to the metal surface normal of the transition dipoles corresponding to the symmetric CH_2 stretching vibration of the hydrocarbon chains in a monolayer of C15-4Py as a function of applied potential. The average orientation of the transition dipoles with respect to the metal surface normal is approximately equal to 68^0 at the desorption potentials and approaches 76^0 when the film is adsorbed. (The estimated tilt angles of the hydrocarbon chains with respect to the metal surface plane would assume the same values if all-trans conformation of the hydrocarbon backbone is assumed.)

More horizontal orientation of the transition dipoles at the negative extreme of the electrode polarizations compared with the orientation of the transition dipoles in the bilayer (55^0, disordered film) suggests that the C15-4Py monolayer forms a different type of aggregates in the desorbed state. It is quite possible that, due to a lack of material, the monolayer forms incomplete aggregates with hydrocarbon chains exposed to the electrolyte solution and the repulsion of the hydrophobic alkyl chains from the electrolyte causes them to be more ordered and assume a relatively more vertical orientation. This explanation is consistent with more horizontal orientation of the transition dipoles in C15-4Py monolayer observed at adsorption potentials (from 0.54 to 0.26 V) compared with the corresponding values for the surfactant molecules in the bilayer (62^0) at these potentials. It is known from the measurement of the differential capacity of the interface (see Section 7.2) that the C15-4Py monolayer has poor barrier properties, due to presence of the pores in the film.

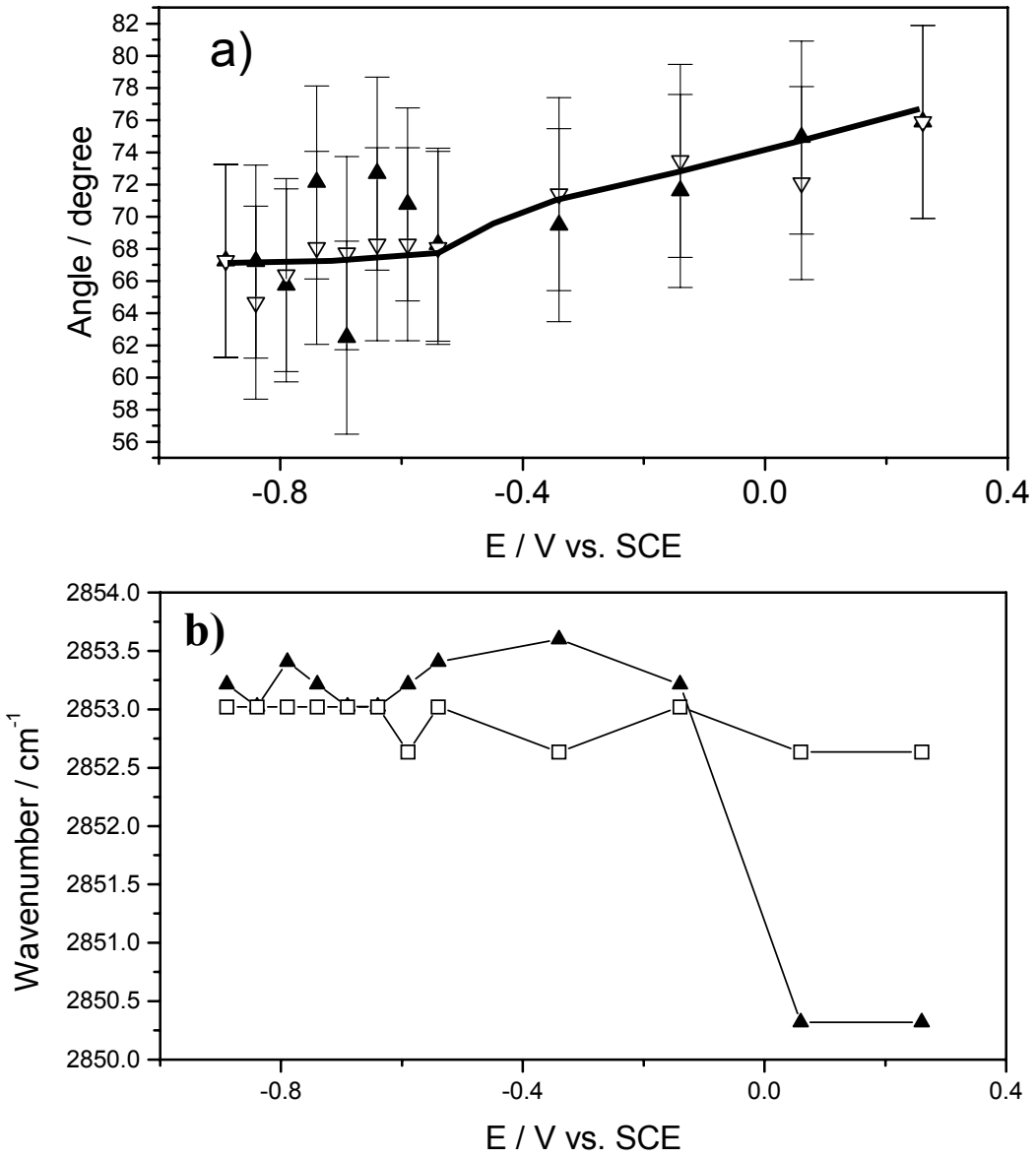

Figure 7.4.10. Potential induced changes in the orientation and the conformation of the hydrocarbon chains of a monolayer of C15-4Py.
a): the average orientation with respect to the surface normal of the transition dipoles corresponding the CH_2 sym. vibration of the hydrocarbon chains
Solid triangles: positive train and Open triangles: negative train of the potential steps applied to the electrode.
b): the change in the position of a symmetric CH stretch peak as a function of the electrode potential observed for
Solid triangles: monolayer , Open squares: bilayer of C15-4Py.
The uncertainty of the tilt angle is approximately equal to $\pm 6^0$
(See Appendix B).

Apparently, penetration of the electrolyte into a C15-4Py monolayer also causes a more vertical alignment of the hydrocarbon chains in the adsorbed monolayer due to repulsion between the alkyl chains and an aqueous electrolyte. Finally, the potential-induced increase of the angle of the transition dipoles with respect to the surface normal in a C15-4Py monolayer, from 62^0 to approximately 74^0, may be explained as the result of a better ordering of the film that is adsorbed at the surface compared with the arrangement of molecules in the aggregates that are separated from the electrode by a layer of electrolyte (at desorption potentials).

The influence of the electrode potential on the conformation of hydrocarbon moieties in a C15-4Py monolayer can be elucidated from the position of a maximum of a peak corresponding to the CH_2 sym. stretching vibration. Panel b of Figure 7.4.10 shows the change in the position of this peak observed for the monolayer of C15-4Py (solid triangles) compared with the bilayer of the surfactant (open squares) as a function of the applied potential. Unlike the bilayer, the monolayer of the surfactant undergoes the liquid crystalline to gel phase transition when the electrode potential becomes positive. A comparison of panel a with panel b of Figure 7.4.10 demonstrates that this phase transition takes place when the angle between the transition dipoles of the alkyl chains and the normal reaches values above 72^0. Apparently, the observed phase transition is assisted by a more vertical orientation of the hydrocarbon chains. The observed phase transition is very interesting because, in principle, the electric potential should not have a direct influence on the conformation of the non-polar hydrocarbon moieties.

In order to find the cause of the liquid crystal to gel phase transition that takes place in a C15-4Py monolayer, the orientation of the pyridine moieties was analysed. The intensity of the a_1 mode of the pyridine head groups was integrated and used to determine the orientation of the C_2 axis of the pyridine moieties with respect to the electrode surface. Figure 7.4.11 shows the change of the tilt angle of the C_2 axis of the pyridine moiety with the electrode potential. (The C_2 axis is oriented as schematically shown in Figure 7.4.11). The graph demonstrates that the head groups are tilted by $24\text{-}25^0$ when the surfactant is desorbed at the negative extreme of the electrode polarizations and undergo a change in orientation to reach tilt angles of approximately 29^0 when the electrode potential becomes more positive than -0.14 V. This behaviour is similar to the trend displayed by the inner leaflet of the bilayer (see Figure 7.4.6), except that the change in the orientation of the head groups in a monolayer occurs at more positive values of the applied potential. Hence, a similar explanation may be offered to interpret the experimental results. The head groups of the neighbouring molecules apparently tend to assume the orientation that results in a minimum net dipole moment of an array of C15-4Py molecules in an aggregate, causing the tilt angle to assume lower values at negative potentials. The pyridine moieties assume a more vertical orientation at adsorption potentials, due to chemisorption. The hydrocarbon chains prevent the head groups from coming close enough together to form the stacks of vertically aligned molecules observed for pyridine molecules, hence a tilt angle of $\sim 29^0$ is observed at positive potentials.

In contrast to the bilayer, the orientation of pyridine heads and the tilt angle of the hydrocarbon tails in the monolayer of C15-4Py do not tend to assume lowest energy configuration shown in Figure 7.4.7. This behaviour suggests that the orientation of the

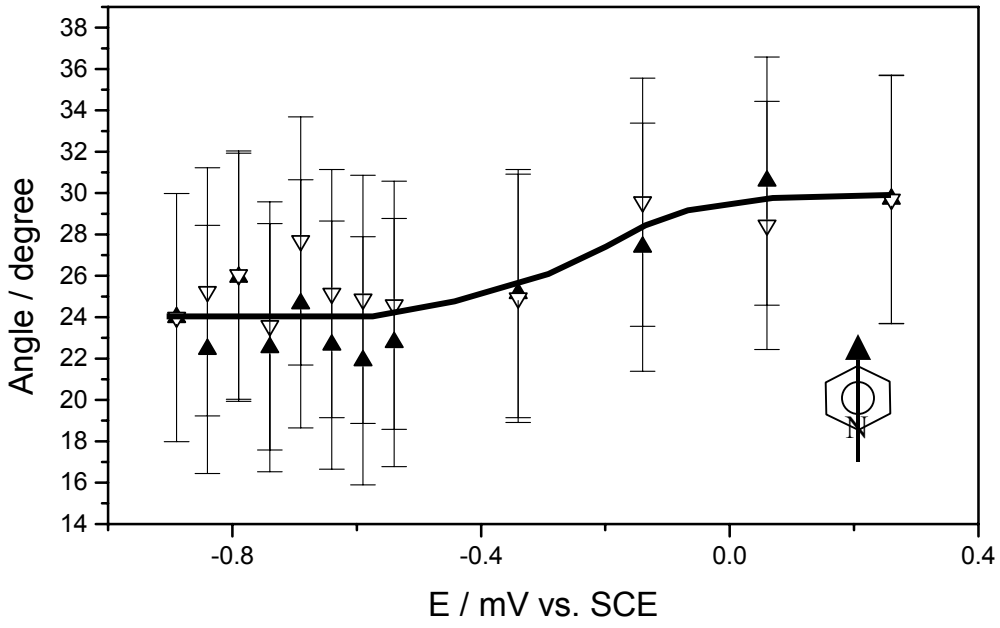

Figure 7.4.11. Potential induced changes in the orientation of the C_2 axis of the pyridine moieties in a monolayer of C15-4Py.
Solid triangles: positive train and Open triangles: negative train of the potential steps applied to the electrode.
The angles are reported with respect to the surface plane.
The uncertainty of the tilt angle is approximately equal to $\pm 6^0$
(See Appendix B).

pyridine moieties of both films adsorbed at the electrode is determined by the electrode potential. However, when the films are desorbed to form aggregates in the vicinity of the electrode surface, the dipole-dipole interactions between the neighbouring pyridine moieties prevail. The role of the hydrocarbon tail in the orientation of the pyridine moieties is apparently limited to hindering of the tilt angle of pyridine moieties within the limits of 24^0 and 35^0. Comparison of the orientation of the pyridine heads shown in Figure 7.4.11 and the position of the CH_2 sym. stretching vibration shown in Figure 7.4.10 b indicates that the liquid crystal to gel phase transition takes place after the reorientation of the head groups. This observation suggests that the potential-induced reorientation of the pyridine moieties may serve as a trigger for the phase transition of the hydrocarbon chains. Hence, it can be concluded that the orientation and conformation of the hydrocarbon tails is determined by two factors: the orientation of the pyridine moieties and the repulsion of the alkyl tails from the aqueous electrolyte, characteristic for the monolayer of C15-4Py.

Finally it is useful to note that the component of the a_1 band that is observed at 1610 cm^{-1} does not completely disappear from the spectra of both a monolayer and a bilayer of C15-4Py at desorption potentials. Since this band is associated with the vibrations of C15-4Py molecules chemisorbed on the electrode, it can be concluded that some material may remain at the electrode surface when the electrode is polarized to -0.89V (SCE). It is possible that some molecules remain attached to the electrode surface at the defect sites of the Au(111) electrode since it is known that pyridine interacts more strongly with the high index planes of Au [43].

7.4.6. Summary and Conclusions

It has been demonstrated that, due to the improvements of the electrochemical *in situ* PM FTIR RAS made as a part of this project, one can obtain excellent quality spectra of ultrathin insoluble surfactant films at the MS interface that can be utilized for quantitative analysis of the potential-induced changes in the orientation, conformation and packing of surfactant molecules. The observed changes in the orientation of C15-4Py films are summarized in Figure 7.4.12. As a result of the potential-induced adsorption of the bilayer, C15-4Py molecules undergo a change from the disordered state, characterized by an angle between the metal surface normal and the transition dipoles corresponding to the symmetric CH_2 vibration of the alkyl chains equal to 55^0 to a state characterized by the angle of the transition dipoles of approximately 62^0 with respect to the metal surface normal. The head groups of the surfactant change the tilt angle from 25^0 to 36^0 in the inner leaflet and from 25^0 to 20^0 in the outer leaflet of the bilayer. The film remains fluid in the whole range of electrode polarizations.

In the monolayer, the average orientation of the hydrocarbon chains is more vertical yielding larger values of the angle between the normal and the corresponding transition dipoles, equal to 62^0 in desorbed state and 76^0 in adsorbed state, compared with the bilayer of C15-4Py. In addition, the alkyl chains attain an all-trans conformation at positive values of the electrode potential where the monolayer becomes condensed in a gel state. The pyridine part of the molecule, however, behaves in the a similar fashion as the inner leaflet of the C15-4Py bilayer showing a slight increase in the tilt angle from 25^0 to 30^0 when the film becomes chemisorbed at the electrode.

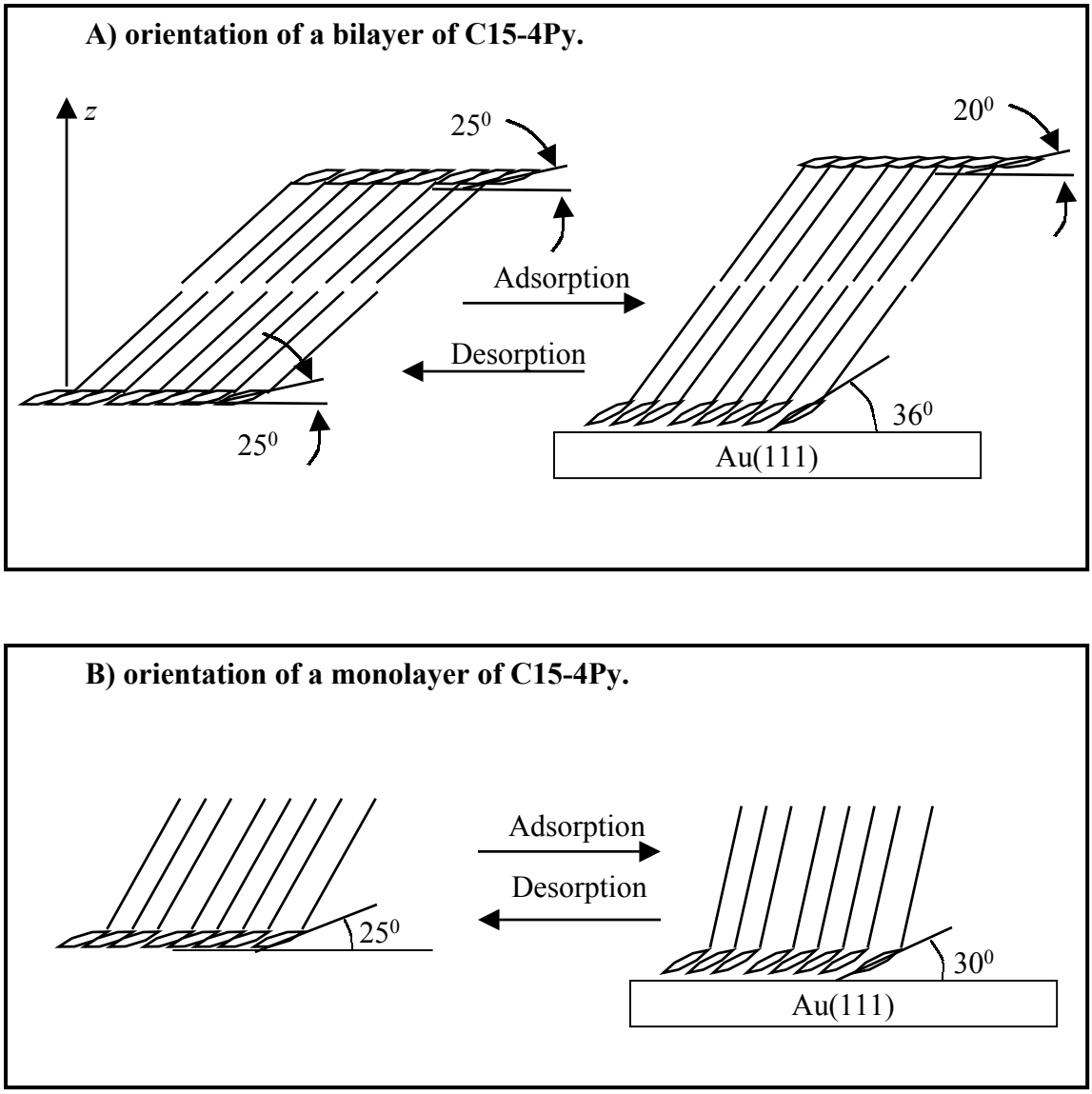

Figure 7.4.12. Orientation of films of C15-4Py at Au(111) at negative (desorption) and positive (adsorption) potentials.

The observed changes in orientation of C15-4Py molecules with the applied potential were explained in the following way. In the desorbed state, the pyridine moieties of C15-4Py tend to attain a parallel orientation with respect to the surface of the electrode. In an adsorbed state the pyridine moieties that are chemisorbed onto the gold surface prefer a vertical orientation at positive electrode polarizations while the head groups of the outer leaflet of the bilayer prefer a parallel orientation. Due to limitations imposed by the closest packing of the hydrocarbon tails, the alkyl chains restrict the above tendencies to occur within the limits of the tilt angles from 20 to 35^0. The orientation and conformation of the hydrocarbon chains is determined by the orientation of the head groups and the repulsion of the alkyl tails from the aqueous electrolyte. When desorbed, the bilayer of C15-4Py apparently forms flat aggregates (flakes of bilayers) in the vicinity of the electrode surface. These aggregates are characterized by disordered alkyl chains. In contrast, the monolayer of C15-4Py probably forms incomplete aggregates with hydrocarbon chains exposed to the electrolyte solution.

The information about orientation conformation and packing of the monolayer and bilayer of C15-4Py at the MS interface derived using the PM FTIR RAS is in good agreement with the results of electrochemical and neutron experiments. Thus, quantitative analysis of the data provided by electrochemical infrared spectroscopy allows one to obtain complementary information about the behaviour of insoluble surfactants at an electrified MS interface.

7.5. Conclusions of the Chapter

In this Chapter it was demonstrated that a combination of classical electroanalytical techniques with modern *in situ* methods such as neutron reflectometry and polarization

modulation infrared spectroscopy allowed one to present a complete picture of the processes that take place at electrified interfaces. The transfer of C15-4Py, an insoluble surfactant, from the GS interface to the MS interface was discovered and studied using electrochemical techniques. Measurements of the differential capacity demonstrated that the surfactant spontaneously crosses the triple phase line, formed at the junction of the gaseous liquid and solid phases, to form a compact bilayer at the metal surface. Chronocoulometry showed that this bilayer is analogous to the film produced using the double touching deposition procedure. The studies of kinetics of the bilayer formation demonstrated that this process is controlled by the rate of the triple phase line crossing by the molecules of the surfactant. Thus, its kinetics is best described by the mechanism that regards the transfer of C15-4Py as a first order surface reaction.

The bilayer state of the surfactant film obtained using the double touching method, and consequently the final state of the film after transfer of C15-4Py from the GS interface to the MS interface, was confirmed using neutron reflectometry. In addition, this technique has demonstrated that the film obtained using the single touching method is a monolayer.

The orientation of C15-4Py molecules in the monolayer and the bilayer was quantitatively determined using PM FTIR RAS. It was found that the bilayer is fluid in the whole potential range studied, while a monolayer becomes condensed to a gel state at the positive electrode polarizations. The results obtained using electrochemical PM FTIR RAS are consistent with the conclusions derived from electrochemical and neutron reflectometry techniques as well as derived from infrared studies of similar systems. Thus, it could be concluded that the PM FTIR RAS technique and the methodology developed during this

project have a tremendous potential in application for *in situ* characterization of ultrathin organic films at a molecular level.

References

1. D. Bizzotto, J. NoNl and J. Lipkowski, Thin Solid Films 248 (1993) 69.

2. D. Bizzotto, J. NoNl and J. Lipkowski, J. Electroanal. Chem. 369 (1994) 259.

3. D. Bizzotto, J. Lipkowski, J. Electroanal.Chem. 409 (1996) 33.

4. D. Bizzotto, J. Lipkowski, Progress Surf. Sci. 50 (1996) 237.

5. D. Bizzotto, J. Lipkowski, Progr. Colloid Polym. Sci. 103 (1997) 201

6. B.B. Damaskin, O.A. Petrii, V.V. Batrakov, " Adsorption of organic compounds on electrodes", Plenum Press, New York (1971).

7. A.B. Steel, B.J. Cheek and C.J. Miller, Langmuir 14 (1998) 5379.

8. T. Sagara, V. Zamlynny, D. Bizzotto, A. McAlees, R. McCrindle and J. Lipkowski, Israel. J. Chem. 37 (1997) 197.

9. D. Bizzotto, A. McAlees, J. Lipkowski and R. McCrindle, Langmuir 11 (1995) 3243.

10. L. Stolberg, S. Morin, J. Lipkowski and D.E. Irish, J. Electroanal. Chem. 307 (1991) 241.

11. J. Lipkowski and L. Stolberg, Molecular adsorption at gold and silver electrodes, in Adsorption of molecules at metal electrodes, J. Lipkowski. and P.N. Ross, (Eds.), VCH Publisher, New York (1992) 171.

12. M.H. Cohen and D. Turnbull, J. Chem. Phys. 31(1959) 1164.

13. D. Turnbull and M.H. Cohen, J. Chem. Phys. 52 (1970) 3038.

14. H-J. Galla, W. Hartmann, U. Theilen and E. Sackmann, J. Membrane Biol. 48 (1979)

215.

15. W.L.C. Vaz, R.M. Clegg and D. Hallmann, Biochemistry 24 (1985) 781.

16. D. H. Charych, E.M. Landau and M. Majda, J. Am. Chem. Soc. 113 (1991).3340.

17. W-Y. Lee, M. Majda, G. Brezesinski, D. Moebius, J. Phys. Chem. B 103 (1999) 6950.

18. C. Buess-Herman, Dynamics of adsorption and two-dimensional phase transitions at electrode surfaces in Adsorption of molecules at metal electrodes, J. Lipkowski. and P.N. Ross (Eds.), VCH Publisher, New York (1992) 79.

19. Z. Galus, Fundamentals of Electrochemical Analysis, 2nd ed., Ellis Harwood Ltd., Chichester, UK (1994) 211.

20. Ch.F. Majkrzak, Mat. Res. Soc. Symp. Proc. 376 (1995) 143.

21. R.K. Thomas, Progr. Colloid Polym. Sci. 103 (1997) 216.

22. D.C. McDermott, J.R. Lu, E.M. Lee, R.K. Thomas and A.R. Rennie, Langmuir 8 (1992) 1204.

23. B.W. Koenig, S. Krueger, W.J. Orts, C.F. Majkrzak, N.F. Berk, J.V. Silverton and K. Gawrisch, Langmuir 12 (1996) 1343.

24. R. Arnold, A. Terfort and C. Wöll, Langmuir 17 (2001) 4980.

25. D.G. Cameron, H.L. Casal and H. H. Mantsch, Biochem. 19 (1980) 3665.

26. H.L. Casal and H.H. Mantsch, Biochim.Biophys. Acta 737 (1983) 387.

27. H.L. Casal and H.H. Mantsch, Biochim. Biophys. Acta 779 (1984) 381.

28. DMS Working Atlas of Infrared Spectroscopy, Butterworth & Co. London (1972) 244.

29. A. Parikh, J.D. Beers, A.P. Shreve and B.I. Swanson, Langmuir 15 (1999) 5369.

30. E.D. Palik (Ed.), Handbook of optical constants of solids. Academic Press, London

(1998).

31. M.A. Ordal, L.L. Long, R.J. Bell, S.E. Bell, R.R. Bell, R.W. Alexander, Jr. and C.A. Ward, Appl. Opt. 22 (1983) 1099.

32. A.N. Rusk, D. Williams and M. Querry, J. Opt. Soc. Am. 61 (1971) 895

33. J.E. Bertie, M.K. Ahmed and H.H. Eysel, J. Phys. Chem. 93 (1989) 2210.

34. R.R.C. New (Ed.), Liposomes. A practical approach. Oxford University Press, Oxford (1990).

35. R.G. Snyder, G.L. Liang, H.L. Strauss and R. Mendelsohn, Biophys. J. 71 (1996) 3186.

36. C.R. Flatch, A. Gericke and R. Mendelsohn, J. Phys. Chem. 101 (1997) 58.

37. R.G. Snyder, S.L. Hsu and S. Krimm, Spectrochim. Acta, 34A (1977) 395.

38. I. Pelletier, H. Bourque, T. Buffeteau, D. Blaudez, B. Desbat and M. Pézolet, J. Phys. Chem. B 106 (2002) 1968.

39. I. Burgess, C.A. Jeffrey, X. Cai, G. Szymanski, Z. Galus and J. Lipkowski, Langmuir 15 (1999) 2607.

40. W.B. Cai, L.J. Wan, H. Noda, Y. Hibino, K. Ataka and M. Osawa, Langmuir 14 (1998) 6992.

41. H. Hauser and M.C. Philips, Prog. Surf. Membr. Sci. 13 (1979) 297.

42. M. Hoon-Khoshla, W.R. Fawcett, A. Chen, J. Lipkowski and B. Pettinger, Electrochim. Acta 45 (1999) 611.

43. D.F. Yang, L. Stolberg and J. Lipkowski, J. Electroanal. Chem. 329 (1992) 259.

CHAPTER 8

8. Summary and Future Directions

The main achievement of this project is the development and successful application of procedures that allow quantitative determination of the influence of electric potential on orientation of organic molecules in ultrathin films deposited at metal electrodes. SNIFTIR has been in use for about two decades and yet has been chiefly employed as a qualitative tool. This thesis describes the first successful application of this technique for quantitative surface analysis. PM FTIR RAS has already been successfully employed for quantitative studies of the gas-liquid and gas-solid interface and this project expands the application of this technique for quantitative analysis of electrified solid-liquid interfaces**.**

This thesis has described a novel approach in optimization of the modern electrochemical *in situ* infrared spectroscopic techniques such as SNIFTIRS and PM FTIR RAS, from the acquisition of raw spectra to the processing of experimental data in order to obtain the spectra suitable for quantitative analysis. It has also been demonstrated that the developed methods can be applied to determine the orientation of small organic molecules as well as molecules of insoluble surfactants at the electrified metal-solution interface. The information derived from infrared spectroscopy was combined with the results provided by electrochemical and neutron experiments to unfold a comprehensive picture concerning the potential-induced changes in a monolayer and a bilayer of 4-pentadecylpyridine at the Au(111) electrode.

Quantitative analysis demands good quality high resolution spectra. It was demonstrated that to achieve this requirement, such experimental conditions as the angle of

incidence and the thin cavity thickness should be optimized before acquisition of raw spectra in each frequency region of interest. The optimization is achieved taking into account the collimation of the incident beam and the optical constants of materials that constitute the thin cavity cell (the optical window, electrolyte and the electrode). It was suggested that the best window materials for SNIFTIRS and PM FTIR RAS are ZnSe and BaF_2, respectively. In addition, an original method to determine the thin cavity thickness of the spectroelectrochemical cell was developed in this project.

The raw spectra must be processed in order to be suitable for quantitative analysis. This thesis described a novel method to convert bipolar SNIFTIRS spectra to unipolar data as well as a new approach to remove the artifacts introduced to PM FTIR RAS spectra due to: (i) the photoelastic modulator, (ii) the difference in throughput of the optical bench to s- and p-polarized light, (iii) the interference of the infrared radiation within the thin cavity of the spectroelectrochemical cell and (iv) the absorption of radiation by the aqueous electrolyte. In order to determine the orientation of molecules of adsorbate at the metal electrode it is necessary to obtain a simulated spectrum of the adsorbed species using their optical constants and the optical constants of other components of the interface. An original simple technique to determine the isotropic optical constants of the adsorbate using its aqueous or binary (aqueous-organic solvent) solutions has also been described in this thesis.

The developed methods were combined with established techniques to elucidate the influence of the electric potential on the orientation of ultrathin organic films at the gold-electrolyte interface. An advanced approach allowed us to apply SNIFTIRS for the quantitative determination of the influence of the electrode potential on orientation of pyridine

molecules at a Au(110) electrode. It has been demonstrated that the change in the tilt angle of pyridine molecules occurs as a result of an interplay between the disorienting force associated with the thermal energy and the orienting force that is caused by the dipole-field interaction of pyridine molecules and the electric field at the metal-solution interface.

The orientation of C15-4Py molecules in the monolayer and the bilayer of the surfactant at Au(111) was determined from the PM FTIR RAS data using the methods developed in this project. Neutron reflectometry was employed to determine the thickness and the surface concentration of C15-4Py films and electrochemical methods were utilized for studies of the mechanism of the potential-induced transformations that occur in the adsorbed film, In addition, electrochemical techniques were used for kinetic studies of the transfer of a C15-4Py film from the gas-solution interface to the metal-solution interface. Combining the data determined using the above three techniques the following conclusions were derived.

The monolayer of C15-4Py can be deposited at the metal electrode using the single horizontal touching technique. However, the barrier properties of this monolayer are poor. A good quality bilayer can be deposited at the metal, either using the double touching technique or *via* transfer of C15-4Py molecules from the GS interface to the MS interface, achieved by prolonged equilibration of the electrode in contact with the GS interface. It is interesting that the bilayer is formed regardless whether the electrode is initially film-free or pre-coated with a monolayer of the surfactant. The transfer of C15-4Py from the GS interface to the MS interface is a spontaneous and irreversible process. Studies of the transfer kinetics suggest that the crossing of the triple phase line by the surfactant molecules is the rate-limiting step.

Studies of the mechanism of the potential-induced transformations that take place in the deposited film demonstrated that the surfactant film can be detached from the surface of the electrode if the metal is polarized to sufficiently negative potentials. The film is converted to micellar type aggregates, probably flakes, that remain in the proximity of the electrode surface and can be readily re-spread onto the metal if the potential is made less negative. Immediately after the re-spreading, the molecules apparently form hemimicellar or hemicylindrical aggregates that can be transformed to the compact film at potentials close to the potential of zero charge. The hysteresis between the potential-driven adsorption and desorption of the surfactant film suggests that rather complex mechanisms are involved in these processes.

A similar hysteresis was followed by the changes in the orientation of C15-4Py molecules at (or in the vicinity of) the metal electrode. The changes in the orientation were most pronounced in the potential region where the adsorption and desorption of both the monolayer and the bilayer of C15-4Py takes place. It has been demonstrated that pyridine moieties of the surfactant molecules tend to attain a more parallel orientation with respect to the electrode surface when they are exposed to the electrolyte solution and the tilt angle of the pyridine rings increases when C15-4Py is chemisorbed at the metal. The hydrocarbon tails restrict the changes of the tilt angle within the limits from 20 to 35^0. The orientation of the hydrocarbon chains depends on two factors: (i) the orientation of the pyridine moieties and (ii) the repulsive interactions with the aqueous solution of electrolyte. The bilayer of C15-4Py contained no electrolyte, hence the first factor was dominant, whereas the orientation and the conformation of the hydrocarbon tails of the C15-4Py monolayer was more strongly affected

by the second factor. The electrode potential was shown not only to cause adsorption of C15-4Py molecules but also to orient the pyridine moieties chemisorbed at the electrode surface in a similar fashion as it orients pyridine molecules adsorbed at Au(110). The potential-induced phase transition from liquid crystal to gel state was observed for the monolayer of C15-4Py while the bilayer remained fluid in the whole range of the electrode potentials studied.

Based on the information presented above, it can be concluded that 4-pentadecylpyridine is an excellent adhesive material for applications in biomimetic research or fabrication of biosensors. Due to its high mobility at the metal electrode, it is able to spontaneously repair defects that may be introduced during deposition of a film that mimics a cell membrane. Due to the fluid state of the C15-4Py films, the obtained model membranes should provide an adequate environment for polypeptides and other components of natural cell membranes.

The methodology developed in this project to study the orientation of organic molecules at the metal surfaces has the potential to be applied to study the influence of electric field on complex molecules that are constituents of natural cell membranes such as phospholipids, cholesterol and membrane polypeptides. It has already been applied recently to study the potential-controlled transformations of phospholipid layers on a Au(111) electrode [1] and information about the conformation, orientation and hydration of phospholipid molecules was determined for these systems. In the near future this methodology will be applied to study hybrid films composed of C15-4Py and phospholipids. Such assemblies bear a close resemblance to natural biological cells and should be useful for

biomimetic research. Hybrid films should adhere to the gold electrode well and be quite robust if the provisions for self-healing are made. A preliminary electrochemical experiment has already been carried out using the hybrid C15-4Py-lipid film. Figure 8.1. shows the capacity of the MS interface containing the film deposited on the Au(111) electrode using the single horizontal touching of C15-4Py followed by another touching to a monolayer of a phospholipid at the GS interface. The formation of the hybrid film is evident from the emerging pseudo-capacitance peak at approximately -0.7 V and lower values of the capacity in the potential region between -0.2 and -0.4 V, compared with the capacity of the MS interface in the presence of a C15-4Py monolayer (dashed line). Hybrid films obtained from C15-4Py and lipid should exhibit a fascinating mechanism of the potential induced desorption and readsorption because the C15-4Py molecules have an affinity for gold while phospholipid molecules do not. The difference in the affinity should result in spontaneous separation of the two leaflets of the bilayer at the electrode potentials close to the potential of zero charge, while at the desorption potentials the film could form either common or separate aggregates.

The separation of aggregates and the orientation of the lipid and the surfactant in the mixed films can be studied in the future using PM FTIR RAS combined with neutron reflectometry and electrochemical techniques. Further advances in this field will involve incorporation of trans-membrane polypeptides in the C15-4Py or hybrid films to study the influence of electric field on functioning of these constituents of the natural membranes that play a key role in many important life processes that are not yet well understood on a molecular level. The information gained in this project and in its future developments could be very useful for fabrication of novel molecular recognition devices.

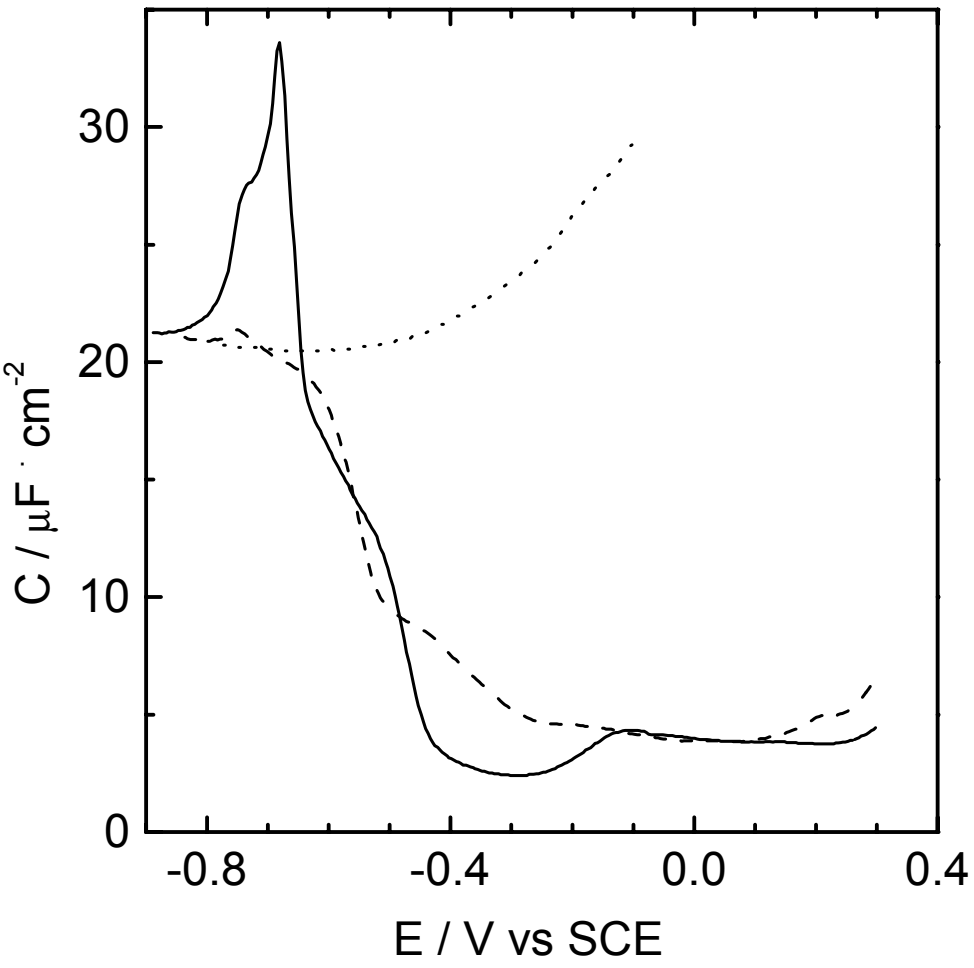

Figure 8.1. Differential capacity of the Au(111) electrode covered with a hybrid C15-4Py-lipid film.
(dotted line) film-free interface,
(dashed line) interface covered with a monolayer of C15-4Py deposited using the single horizontal touching technique,
(solid line) interface covered with a hybrid film obtained using the single horizontal touch of C15-4Py followed by another touch to the phospholipid monolayer at the GS interface.
Only negative scans of the electrode potential are shown for clarity.
The electrolyte solution was 0.05 M $KClO_4$ + 0.001 M $KHCO_3$.

References

1.S.L. Horswell, V. Zamlynny, H.-Q. Li, A.R. Merrill and J. Lipkowski, Faraday Disc. (2002) accepted.

APPENDIX A

Example of the Parameter File that was Used by the Omnic Macro to Run the PM FTIR RAS Experiment.

The parameter file was used by the Omnic macro to run the PM FTIR RAS experiment automatically. Four potential ramps may be specified allowing for variation of the potential increments if necessary. The macro changes the electrode potential in cycles such that the potentials in the negative sequence of potential steps coincide with the potentials in the positive sequence. The contents of the parameter file are presented below (explanations are added in italics).

[Parameters]
Config= C:\Vlad\Param\VZ_PMRAS_BaF2.con - *OMNIC configuration*
Exp= C:\Vlad\Param\VZ_PMRAS_BaF2.exp - *OMNIC experiment*
PEM_Frequency= 1600 - *PEM frequency (cm^{-1})*
Equilibration_Time= 0 - *Equilibration time minus 10 s (s)*
Number_Of_Potential_Loops= 20 - *Number of potential loops*
Time_To_Collect_Spectrum= 307 - *Time necessary to collect a specified number of interferograms (s)*
Diff_Gain= 10 -*Total gain in the difference channel of the SSD*
Reserved= Reserved - *Reserved space*
[Potentials] - *Electrode potentials*
E1i= -850 - *Initial value of the first potential ramp (mV)*
E1f= -500 - *Final value of the first potential ramp (mV)*
E1s= 50 - *Increment of the first potential ramp (mV)*
E2f= -300 - *Final value of the second potential ramp (mV)*
E2s= 200 - *Increment of the second potential ramp (mV)*
E3f= -100 - *Final value of the third potential ramp (mV)*
E3s= 200 - *Increment of the third potential ramp (mV)*
E4f= 300 - *Final value of the forth potential ramp (mV)*
E4s= 200 - *Increment of the forth potential ramp (mV)*

APPENDIX B

Estimate of Uncertainities in the Tilt Angle.

Several factors contribute to the net error in determination of the tilt angle using the approach described in Chapter 5. Equation (5.3.4):

$$\frac{A^{R}{}_{Exp}}{A^{R}{}_{Theor}} = \frac{\cos^2 \Theta}{1/3}$$

demonstrates that the net error in the tilt angle depends on the error in the absorbance A^{R}_{Exp} measured in reflection absorption spectroscopy and the error in absorbance A^{R}_{Theor} calculated using the experimentally determined optical constants. Since it is difficult to estimate how well the theoretical model describes the conditions used during an experiment, the error associated with the calculated absorbance is difficult to determine. The transmittance spectra that were used to determine the optical constants were of much better signal-to-noise ratio than experimental reflection absorption spectra and every effort was made to approach highly relevant modeling of the experimental setup. Thus, it is reasonable to assume that the error associated with calculation of the theoretical spectra does not exceed the error of the absorbance determined from reflection absorption experiments. Hence, the net precision of the tilt angle to a large extent depends on the precision of A^{R}_{Exp} that was obtained experimentally.

Below, the estimate of the uncertainities in the tilt angle is given based on the calculated random errors in absorbance determined from reflection absorption spectra. The following procedure was utilized to determine these errors. For a chosen infrared band (symmetric CH_2) of the C15-4Py bilayer spectrum recorded at a chosen potential (0.06 V *versus* SCE) in a positive train of potential steps the tilt angle was calculated for each of 20 potential loops. (Usually, 20 potential loops were performed during every experiment and the acquired spectra were averaged before further processing.) Figure App.B shows the values of the tilt angle of the hydrocarbon chain for the bilayer of C15-4Py determined using equation (3.5.4). Application of statistical analysis of these data yields the mean value of the tilt angle of 61^0 and the standard deviation of 2.8^0. Because the angles presented in this thesis were determined using the average value of A_{Exp}^{R} for 20 potential loops, the confidence interval (*CI*) can be calculated using the following equation [1]:

$$CI = \frac{ts}{\sqrt{N}},$$

where t is the Student's coefficient, s is the standard deviation and N is the number of averaged spectra. Using the tabulated value of Student's coefficient [1] equal to 3.153 at 99.5% confidence level, one can find that the confidence interval for the determined tilt angle is equal to $\pm 3^0$. A similar approach was used to determine the confidence interval for the orientation of the hydrocarbon chain of the monolayer of C15-4Py. The obtained value was $\pm 6^0$ which is a reasonable number since the absorbance of a monolayer is approximately equal to one half of the absorbance of the bilayer of C15-4Py.

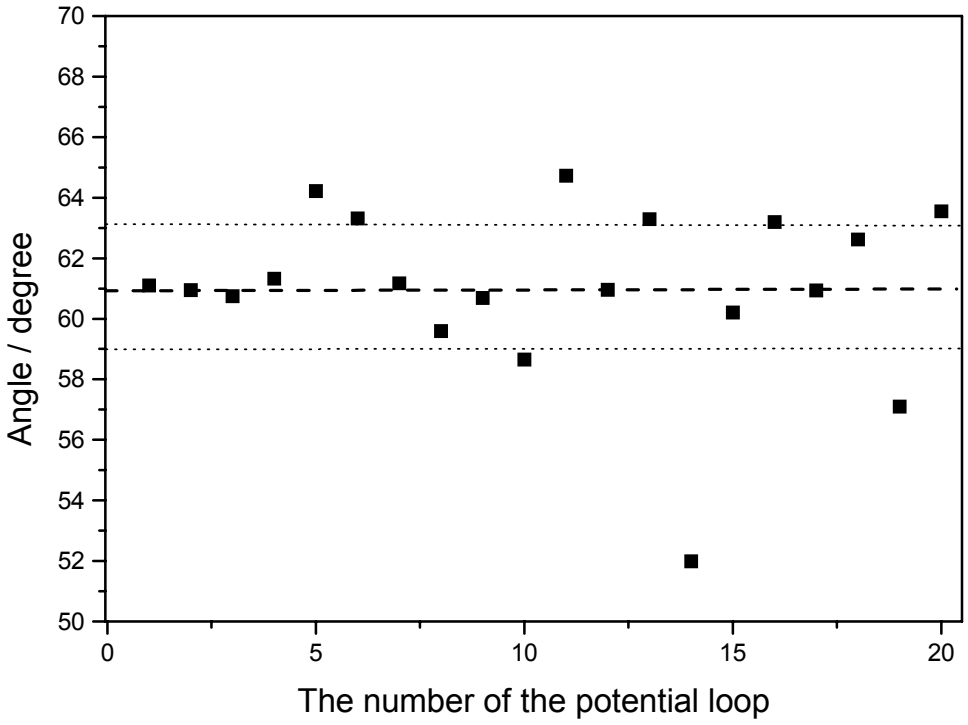

Figure App.B. The tilt angle of the hydrocarbon chains of C15-4Py bilayer. The dependence of the calculated value of the angle on the particular number of 20 potential loops that were collected during a PM FTIR RAS experiment. Electrode potential was 0.06 V *versus* SCE (positive train of potential steps), infrared band was symmetric CH_2 stretching.

Since it is probable that the error in absorbance A_{Theor}^{R} calculated using the experimentally determined optical constants has a small contribution to the net error in the tilt angle, the values of confidence levels determined above suggest that the error associated with the tilt angles should not be significantly larger than $\pm 3^0$ for the bilayer of C15-4Py and to $\pm 6^0$ for the monolayer of the surfactant. These numbers and the consistency of results derived from infrared spectroscopy with the observations made using other techniques present evidence that polarization modulation infrared spectroscopy can be utilized for quantitative characterization of ultrathin organic films such as munolayers and bilayers of surfactants as well as biomimetic films of lipids.

References

1. D.C. Harris, Quantitative Chemical Analysis, 5th Ed., W.H. Freeman Co. New York (1999) 74.